

INAUGURAL - DISSERTATION

zur

Erlangung der Doktorwürde

der Naturwissenschaftlich-Mathematischen Gesamtfakultät

der Ruprecht-Karls-Universität Heidelberg

vorgelegt von

Dipl.-Phys. Alice Zimmermann

aus Bad Kreuznach (Rheinland-Pfalz)

Tag der mündlichen Prüfung:

26. Oktober 2016



Production of strange hadrons in charged jets  
in Pb–Pb collisions  
measured with ALICE  
at the LHC

Gutachter:

Prof. Dr. Johanna Stachel

Prof. Dr. Stephanie Hansmann-Menzemer



# Abstract

First measurements of the baryon-to-meson ratio in heavy-ion collisions at the Relativistic Heavy Ion Collider (RHIC) showed an relatively enhanced baryon production at intermediate transverse momentum ( $p_T \approx 3$  GeV/c) [1, 2] relative to pp collisions. Measurements at much higher energy at the Large Hadron Collider (LHC) at CERN corroborated this observation [3, 4]. Although the mechanisms of this enhanced baryon production is not yet known, there are several scenarios proposed to explain this. These are e.g. collective effects and string fragmentation in a hydro-dynamically expanding environment [5]. These collective phenomena, like the particle flow [6], are a characteristic feature of the Underlying Event (UE) in Pb–Pb collisions. Partons that are produced by hard parton scatterings in an early stage of the heavy-ion collision and which can be measured as a collimated spray of particles, a particle jet, are assumed to hadronise via fragmentation.

The production of the particles from the Underlying Event (UE) is in principle independent of the fragmentation process but could have a possible impact on the jet fragments. In this way it is possible that interactions between partons that stem from the fragmentation and those inside the hot and dense medium created in heavy-ion collisions, could change the jet pattern. So far several measurements observed these medium-modifications in terms of jet quenching [7, 8]. Furthermore a modification of the fragmentation functions in Pb–Pb collisions was lately seen by the CMS [9] and the ATLAS [10] experiment. There are models that consider alternative hadronisation mechanisms to explain the baryon anomaly. They expect hadrons at low  $p_T$  to be produced via “recombination” [11], which is a soft process that is expected to favour baryon over meson production. Particles with a momentum larger than  $p_T = 4\text{--}6$  (GeV/c) would, on the other hand, be produced in hard processes via fragmentation, that does not lead to an enhanced production of baryons (compared to production in vacuum). The study of identified particle yields and ratios like  $\Lambda(\bar{\Lambda})$  and  $K_S^0$  in jets in Pb–Pb collisions will help to disentangle energy loss and hadronisation scenarios and their  $p_T$  dependence. For the analysis presented in this thesis, the  $p_T$  spectra of strange particles associated with jets are studied for the 10% most central events in Pb–Pb collisions at  $\sqrt{s_{NN}} = 2.76$  TeV. Furthermore they are compared to the inclusive particle measurement and the  $(\Lambda + \bar{\Lambda})/2K_S^0$  ratio in jets in p–Pb collisions at  $\sqrt{s_{NN}} = 5.02$  TeV. For the particles within jets, that are produced via hard parton fragmentation, the  $(\Lambda + \bar{\Lambda})/2K_S^0$  ratio is found to be much less enhanced than the corresponding ratio for inclusive particles. Within uncertainties, it is furthermore consistent with a reference measurement in jets in p–Pb collisions. The measured  $\Lambda + \bar{\Lambda}$  and  $K_S^0$   $p_T$  spectra however give strong hints about possible modifications. The comparison to

the scaled  $V^0$   $p_T$  spectra in jets in p–Pb collisions indicates medium-modifications of the spectra in Pb–Pb collisions. The  $K_S^0$  yields seem to be enhanced in Pb–Pb for all hadron  $p_T$  intervals w.r.t. the reference. The  $\Lambda$  yields at low hadron  $p_T$  indicate an enhancement while for higher hadron  $p_T$  they hint on a suppression of the yields.

This could point to a modification of the fragmentation pattern similar as observed by CMS and ATLAS. Furthermore the observation raises the question whether there could be a particle-species dependent strength of the medium-modification of the fragmentation functions and probably also as a function of the jet  $p_T$ .

---

# Zusammenfassung

Nachdem Messungen des Verhältnisses von Baryonen zu Mesonen in Schwerionenkollisionen am Relativistic Heavy Ion Collider (RHIC) eine erhöhte Produktion von Baryonen bei mittleren Transversalimpulsen (ca. 2-5 GeV/c) im Vergleich zu Messungen in Proton-Proton-Kollisionen gezeigt hatten, konnte diese Beobachtung am Large Hadron Collider (LHC) am CERN bei viel höherer Strahlenergie bestätigt werden. Die Ursache dieser Baryon Anomalie ist bis heute nicht eindeutig geklärt, aber eine Anzahl möglicher Interpretationen existiert, die u.a. kollektive Effekte oder die Fragmentation sogenannter Farbstrings in einem sich hydrodynamisch expandierenden Medium (das sogenannte Quark-Gluon-Plasma), das sich in ultrarelativistischen Schwerionenkollisionen bildet, zur Erklärung heranziehen. Kollektive Effekte, wie z.B. direkter und elliptischer Teilchenfluß, sind charakteristisch für die Vielzahl von niederenergetischen Teilchen, die bei der Hadronisierung des Quark-Gluon-Plasmas entstehen und weisen eine Abhängigkeit bezüglich der Teilchenmasse auf, was zu der Ausbildung der beobachteten Baryon Anomalie führen könnte. Alternative Erklärungskonzepte betrachten Teilchen die aus der Streuung hochenergetischer Partonen in einer frühen Phase der Blei-Blei-Kollision hervorgehen. Diese können im Experiment als ein kollimierter Strahl von Teilchen (sogenannter "Jet") mit überwiegend hohen Teilchenimpulsen nachgewiesen werden. Die Jet-Konstituenten werden durch die Hadronisierung von Farbstrings produziert. Diese entstehen durch Fragmentation der hochenergetisch gestreuten Partonen. Es wird angenommen, dass der große Untergrund von niederenergetischen Teilchen aus der Blei-Blei-Kollision unabhängig von der Jetproduktion entsteht.

Allerdings besteht die Möglichkeit dass Wechselwirkungen zwischen Partonen aus dem Plasma und aus der Fragmentation (also schon vor der Hadronisierung) das Fragmentationsmuster beeinflussen könnten. Dafür gibt es mehrere experimentelle Hinweise aus Messungen am RHIC und am LHC, die zum einen eine signifikante Abschwächung von Jets in Schwerionenkollisionen gegenüber Jets aus Proton-Proton-Kollisionen zeigen (das sogenannte "Jet-Quenching") [7], zum anderen aber auch deutliche Hinweise auf eine Modifikation der Impulsverteilung von Jet-Konstituenten ("Fragmentationsfunktionen") geben [9, 10]. Demnach werden im Jet mehr niederenergetische Teilchen gebildet während Teilchen mit mittlerem Transversalimpuls ( $p_T$ ) weniger häufig zu finden sind.

Ein anderer Ansatz zur Erklärung der Baryon Anomalie betrachtet den Hadronisierungsprozess von Teilchen aus verschiedenen Bereichen des Impulsspektrums. Hadronen mit einem  $p_T$  von ca. 4-6 GeV/c würden demnach vorwiegend aus dem Zusammenschluss von Quarks aus dem dichtbesetzten Phasenraum innerhalb des heißen und dichten Plasmas

produziert. Dieser statistische Prozess begünstigt die Baryonproduktion gegenüber der von Mesonen. Für Teilchenproduktion im Bereich ab ca. 4-6 GeV/c hingegen dominiert perturbative Stringfragmentation als Hadronisierungsmechanismus, bei dem Baryonproduktion nicht in der Weise bevorzugt wird, wie es bei der “Rekombination” von quarks z.B. erwartet würde.

Die vorliegende Arbeit untersucht die Transversalimpulsspektren von neutralen Kaonen und Lambda-Baryonen in Jets in der 10% zentralsten Klasse von Blei-Blei Kollisionen bei  $\sqrt{s_{NN}} = 2.76$  TeV. Die gemessenen Spektren und das  $(\Lambda + \bar{\Lambda})/2K_S^0$  Verhältnis wird mit den bereits gemessenen inklusiven Teilchen (d.h. alle Teilchen innerhalb der Messakzeptanz) sowie mit den Resultaten aus der Analyse dieser Teilchen in Jets in Proton-Blei-Kollisionen bei  $\sqrt{s_{NN}} = 5.02$  TeV verglichen. Das gemessene Baryon-zu-Meson-Verhältnis in Jets ist weit weniger erhöht als in den inklusiven Teilchenspektren. Es weicht zudem nicht signifikant von dem Verhältnis ab, welches in Proton-Proton Kollisionen gemessen wurde. Dies weist darauf hin, dass die Baryon Anomalie ein Charakteristikum des niederenergetischen Untergrunds in den Blei-Blei-Kollisionen ist und könnte beispielsweise durch verschiedene Hadronisationsmechanismen im Untergrund und in Jets erklärt werden.

Die gemessenen  $\Lambda + \bar{\Lambda}$  und  $K_S^0$  Transversalimpulsspektren hingegen geben mehr detaillierte Information über mögliche Abweichungen von den Referenzmessungen in Proton-Blei-Kollisionen. Kaonen in Jets in Blei-Blei-Kollisionen scheinen demnach häufiger produziert zu werden. Der Vergleich der Spektren von Lambda-Baryonen in Jets in Blei-Blei-Kollisionen mit den Spektren in Proton-Blei-Kollisionen zeigt, dass Lambdas mit mittlerem Impuls (2-4 GeV/c) leicht häufiger, bei höheren Impulsen (4-10 GeV/c) mit leicht geringerer Häufigkeit produziert werden. Diese Beobachtungen könnten auf eine Medium-Modifikation der Fragmentationsfunktionen der Jets hinweisen und deutet auch auf eine mögliche Abhängigkeit der Modifikation von der Masse der identifizierten Jet-Konstituenten hin.

# Contents

<b>1</b>	<b>Introduction</b>	<b>13</b>
1.1	The standard model of particles and interactions	13
1.2	Quark-Gluon interactions	16
1.3	The Quark Gluon Plasma formation	21
1.4	Particle flow	25
1.5	Particle jets as hard probes	28
1.6	Jet quenching	30
1.7	Modification of jet observables in heavy-ion collisions	35
1.7.1	A model for jet quenching and its impact on the jet hadrochemistry	38
1.8	Identified light-flavour particle production in heavy-ion collisions	41
1.9	Analysis of identified particles in a jet-like environment	47
<b>2</b>	<b>Experimental access</b>	<b>53</b>
2.1	The Large Hadron Collider	53
2.2	ALICE at the LHC	55
2.3	Inner Tracking System (ITS)	56
2.4	Time Projection Chamber	59
2.5	VZERO detector	60
2.6	Zero Degree Calorimeters (ZDC)	62
2.7	Detectors for Particle Identification	62
2.8	Centrality determination	62
2.9	Event plane determination	64
2.10	Track reconstruction	65
2.11	Reconstruction of secondary vertices	67
<b>3</b>	<b>Analysis of strange particles in jets in Pb-Pb collisions</b>	<b>69</b>
3.1	Reconstruction of the $V^0$ particles	69
3.1.1	Analysis software	69
3.1.2	Data	70
3.1.3	Event selection	70
3.1.4	$V^0$ particle reconstruction	72
3.1.5	Signal extraction	76
3.1.6	Uncorrected $p_T$ spectra	81
3.1.7	Analysis workflow	82

3.2	Reconstruction of jets from charged particle tracks . . . . .	84
3.2.1	Some aspects of the jet reconstruction . . . . .	84
3.2.2	Contribution from the Underlying Event and background fluctuations . . . . .	86
3.2.3	Track selection . . . . .	89
3.2.4	Combinatorial jets . . . . .	89
3.2.5	Statistics after jet selection . . . . .	91
3.3	Identification of V0 particles in jet cones . . . . .	92
3.4	Corrections on inclusive and intra-jet V <sup>0</sup> particles . . . . .	94
3.4.1	V0 reconstruction efficiency . . . . .	95
3.4.2	Acceptance correction . . . . .	97
3.4.3	Subtraction of particles from the Underlying Event . . . . .	103
3.4.4	Subtraction of decay products (“feed-down”) . . . . .	105
3.4.5	Correction of the jet transverse momenta . . . . .	107
3.5	Impact of Underlying Event fluctuations on the measurements . . . . .	108
3.5.1	Embedding of PYTHIA jets into PbPb events . . . . .	109
3.5.2	Datasets . . . . .	109
3.5.3	Jet matching . . . . .	111
3.5.4	PYTHIA embedded jet spectrum . . . . .	113
3.5.5	Results for the charged tracks as a crosscheck . . . . .	114
3.5.6	Development of a precise V <sup>0</sup> background estimation derived from PYTHIA embedding . . . . .	116
3.5.7	Impact of PYTHIA $p_T^{\text{jet}}$ spectral shape on V <sup>0</sup> background estimation . . . . .	121
3.5.8	Event-plane dependence of the V <sup>0</sup> background . . . . .	123
3.5.9	Estimation of the systematic uncertainties . . . . .	129
<b>4</b>	<b>Results and discussion</b> . . . . .	<b>143</b>
4.1	Inclusive particles . . . . .	143
4.2	$(\Lambda + \bar{\Lambda})/2K_S^0$ ratio in jets in Pb–Pb collisions . . . . .	143
4.3	$K_S^0$ , $\Lambda$ and $\bar{\Lambda}$ hadrons in “no-jet” events in Pb–Pb collisions . . . . .	145
4.4	Comparison of $\Lambda + \bar{\Lambda}/2K_S^0$ ratio to other measurements . . . . .	149
4.5	$K_S^0$ and $\Lambda + \bar{\Lambda}$ $p_T$ spectra in jets in Pb–Pb collisions . . . . .	152
<b>5</b>	<b>Conclusions</b> . . . . .	<b>157</b>
5.1	Physics conclusions . . . . .	157
5.2	Conclusions on the analysis strategy . . . . .	158
	References . . . . .	161
	List of Tables . . . . .	173
	List of Figures . . . . .	175
<b>A</b>	<b>Hadronisation mechanisms</b> . . . . .	<b>189</b>
<b>B</b>	<b>Signal extraction for inclusive V<sup>0</sup> particles</b> . . . . .	<b>191</b>
<b>C</b>	<b>Signal extraction in jet cones</b> . . . . .	<b>197</b>

<b>D</b>	<b>Signal extraction in the Underlying Event</b>	<b>207</b>
<b>E</b>	<b>Technical details jet reconstruction</b>	<b>213</b>
E.1	Cut selection on tracks used for jet reconstruction . . . . .	213
E.2	Jet reconstruction settings . . . . .	214
<b>F</b>	<b>Methods to estimate <math>V^0</math> <math>p_T</math> spectrum in the Underlying Event</b>	<b>215</b>
<b>G</b>	<b>Scaling of reference measurement in p–Pb collisions</b>	<b>219</b>
<b>H</b>	<b>Preliminary version of the <math>(\Lambda+\bar{\Lambda})/2K_S^0</math> ratio</b>	<b>223</b>



# Chapter 1

## Introduction

### 1.1 The standard model of particles and interactions

From the ancient times on the concept of the building blocks of matter present in our universe was investigated and it was tried to achieve a deeper understanding of physics on microscopic scales. In the past century, the elementary particles and their way to interact have been explored and arranged in the Standard Model of Fundamental Particles and Interactions (SM) [12, 13]. The SM is a collection of related theories including Quantum Electrodynamics (QED), the Glasgow-Weinberg-Salam theory of electro-weak processes and Quantum Chromodynamics (QCD). In this way, it can describe strong, electromagnetic and weak interactions and could explain most of the experimentally observed phenomena in particle physics. However, it does not include a theory of gravity, the fourth known type of interaction. The SM knows three kinds of elementary particles: the quarks and leptons (which are fermions) and the bosonic mediators of the different forces. An overview of the particles is given in Fig. 1.1. The fermions have spin  $\frac{1}{2}$  and are considered to be point-like objects. The mediators are bosons and carry spin 1. To each particle also exists one antiparticle. Unlike leptons (that do not interact via the strong force), the quarks participate in strong, electromagnetic and weak interactions. They are grouped into three families (the up and down, the charm and strange, the top and bottom quark each build one family). Each quark can exist in three equivalent states that are characterised by the “colour” quantum number, that comes in three possible states (green, red and blue). The antiparticles carry anticolour (antigreen, antired and antiblue).

The quark masses, as shown in Fig. 1.1, are the “current” masses, that are used for perturbative QCD (Quantum Chromo Dynamics) calculations (QCD is explained later in more detail). Considering how light e.g. u and d quarks are, it seems surprising how the proton e.g. can obtain its experimentally found rather large mass of  $938.272 \text{ MeV}/c^2$ . Since the mass generation by the Higgs mechanism only could explain the current quark masses, which is only a small fraction of the observed proton mass, the quarks must gain a much larger mass, when contained in a hadron. These are usually called the quark constituent masses, of which a large contribution to the quark mass is produced by the spontaneous symmetry breaking of the chiral symmetry [14] of QCD.

Also the leptons are grouped in three flavour families: one for the electron, the muon and

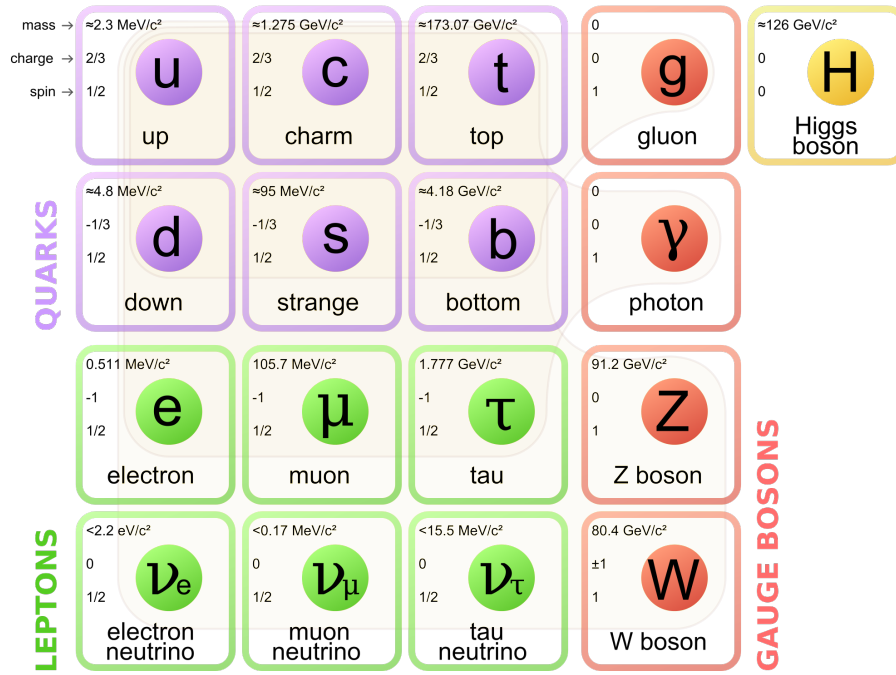


Figure 1.1: The standard model of elementary particles. (Figure adapted from [15]).

the tau particle. The second member of each family is a neutrino, which plays a special role among the elementary particles. Three flavours observed so far, the  $\nu_e$ , the  $\nu_\mu$  and the  $\nu_\tau$ .

Neutrinos have been proposed by Pauli in 1930 to explain energy, momentum, and spin conservation in the weak decay of the neutron  $n \rightarrow p^+ + e^- + \bar{\nu}_e$ . Experimentally it is confirmed that they play a role in charged or neutral current electroweak processes. Although according to the standard model these particles are massless, a small lower bound for the neutrino mass was assigned. This non-zero neutrino mass prediction is a consequence of the experimental discovery of neutrino oscillations by Super-Kamiokande [16] and the Sudbury Neutrino Observatory [17]. They measured the flux of atmospheric neutrinos and solar electron neutrinos and discovered that neutrinos change their flavour over long distances.

The four different kind of interactions are illustrated in Fig. 1.2. Each interaction between quarks or leptons is mediated by the exchange of bosons. The massless photon ( $\gamma$ ) is the mediator for the electromagnetic force. The  $W^\pm$  and  $Z^0$  bosons mediate the weak interaction and couple to all known fermions.  $W^\pm$  enable quarks to change their flavour in weak decays.

The massless gluon (g) mediates the strong interaction and also carries colour. Furthermore it causes the binding of nucleons in atomic nuclei according to the Yukawa potential, which is a residual interaction among the nucleons of the form  $V(r) = -g^2 \frac{e^{-kmr}}{r}$  with the strength obtained from a massive exchange particle (with the mass  $m$ ). In this way it acts against the repulsive Coulomb force that is caused by the positively charged protons inside the nucleons via their electro-magnetical interaction. The Yukawa coupling was proposed in 1935 and describes the interaction between a scalar field  $\phi$  and a Dirac field  $\psi$  of the

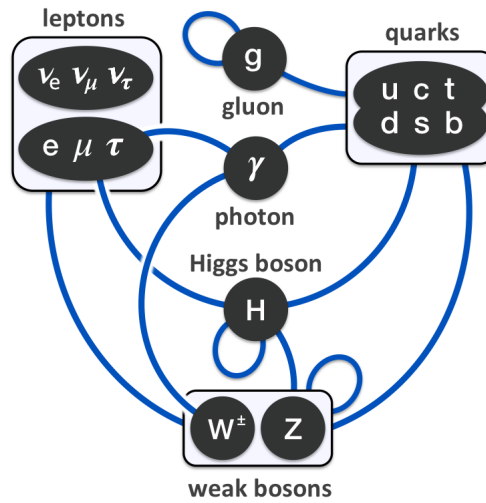


Figure 1.2: Interactions of the standard model. Figure adapted from [15].

form  $V \sim g\bar{\psi}\phi\psi$ , which can explain the binding of the nucleons inside the nucleus with carriers of the strong force being massive particles, for which a new particle, the pion, was proposed. The pion was indeed discovered in 1947 [18], quickly followed by the discovery of many more and heavier particles in cosmic ray measurements and at the first built accelerators. The numerous particles motivated the concept of the building blocks of the hadronic matter, that were later found to be the quarks and the gluons. They are the smallest constituents of matter that are known so far, furthermore they are stable and don't exist in excited states. The first hint for the existence of quarks and gluons, which are commonly referred to as partons, was seen in Deep Inelastic Scattering (DIS) of leptons off protons (and as described in [19]).

The structure functions of the proton  $F_2(x, Q^2)$  was measured over a large energy range of  $2 \text{ (GeV/c)}^2 < Q^2 < 18 \text{ (GeV/c)}^2$  (see Fig. 1.3) and as a function of the Bjorken scaling variable  $x = \frac{1}{n} \frac{Q^2}{2Pq} = \frac{Q^2}{2M\nu}$  which is a measure of the inelasticity of the scattering process. The Lorentz-invariant quantity  $\nu = \frac{P \cdot q}{M}$  is the energy transfer between the projectile and the target, while  $P$  is the four-momentum of the target and  $q$  the four-momentum of the exchanged photon during the projectile-target interaction.  $n$  is the number of nucleon constituents. The fact that only a weak dependence on  $Q^2$  was found, leads to the conclusion that the electrons scatter off a point-like target<sup>1</sup>. For an elastic scattering  $x = 1$ . When considering the broad peak at  $x \sim \frac{1}{3}$ , one can conclude therefore that the nucleons have three constituents [19]. The width of the peak is determined by the Fermi motion of the partons inside the nucleon.

The Higgs boson  $H^0$  (a spin 0 particle with a mass  $\sim 125 \text{ GeV}$  and even parity, that decays (among other channels) into a pair of  $\gamma\gamma$ ,  $ZZ$  or  $WW$  particles) was discovered [20],[21]

<sup>1</sup>For the case of an elastic scattering, the form factor  $f(x, Q^2)$  is defined as the Fourier transform of the charge distribution. In case of a constant (i.e. independent of  $Q^2$ ) it corresponds to a point-like charge distribution. For an inelastic scattering,  $f(x, Q^2)$  turns into the structure functions  $F_2(x, Q^2)$ . Since protons are extended objects, and their structure functions don't show a dependence on  $Q^2$ , they must consist of point-like constituents.

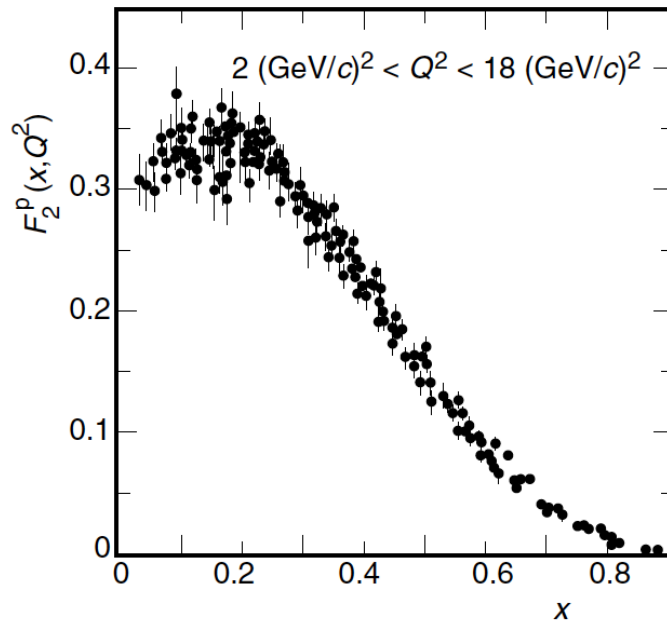


Figure 1.3: The proton structure function  $F_2$  as a function of  $x$  and for  $Q^2$  between  $2 \text{ (GeV/c)}^2$  and  $18 \text{ (GeV/c)}^2$ . No dependence on  $Q^2$  is found, which indicates a scattering off point-like targets and thus leads to the understanding that the proton consists of point-like constituents (Fig. adapted from [19]).

at the LHC in July 2012. It is a quantum excitation of the Higgs field. The Higgs field causes e.g. the large mass of the  $Z$  and  $W^\pm$  bosons [22] which is in contrast to the photon or gluon that are massless bosons. On larger (spatial) scales also the gravitational force<sup>1</sup>, plays an important role, but it is rather negligible for microscopic processes. However it is not described by the standard model but by the theory of general relativity.

## 1.2 Quark-Gluon interactions

Gluons (as described in more detail in [19]) are coloured objects, they carry colour and anti-colour and couple in this way to other coloured particles. From the colours (and anticolours) a gluon carries a colour-singlet  $\sqrt{1/3}(r\bar{r}+g\bar{g}+b\bar{b})$  (which is invariant under rotations in colour space and therefore cannot be exchanged in a strong interaction) and an octet can be formed. The octet serves as a basis from which all other colour states can be constructed, one possible choice is [19] is:  $(r\bar{g}, r\bar{b}, g\bar{b}, g\bar{r}, b\bar{r}, b\bar{g}, \sqrt{1/2}(r\bar{r}-g\bar{g}), \sqrt{1/6}(r\bar{r}+g\bar{g}-2b\bar{b}))$ .

Gluons can be emitted, absorbed and be annihilated and created in pair production processes.

The gluon self-coupling is possible because of the colour-changing interactions that the gluons do and that is not possible for the photons since they have no such charge. The hadrons, which are made of the partons, however, have to be colour-singlets. Otherwise

<sup>1</sup>e.g. the gravitational pressure in the solar envelope, that is due to the enormous amount of helium and hydrogen, provides the environmental conditions in which the burning processes inside the sun take place

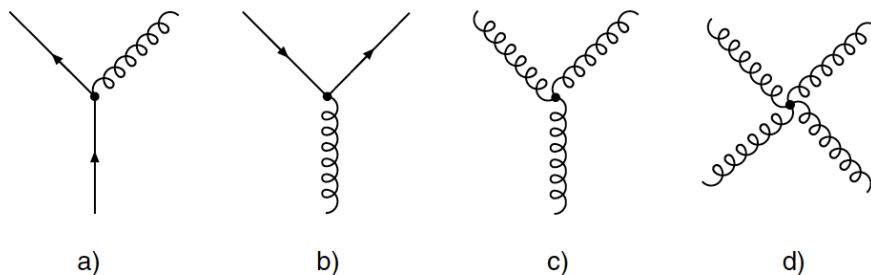


Figure 1.4: Fundamental types of the strong interaction. a) shows a quark emitting a gluon, in b) a gluon splits into a quark-antiquark pair and c),d) demonstrate the self-coupling of gluons. (Figure adapted from [19]).

each hadron could exist in many equivalent types, which was not measured in nature since each hadron type (consisting of a particular quark flavour composition) was found to be unique. To form a colour-neutral hadron either all three colours have to be combined, or colour and anti-colour are needed. A charged pion, for example, has three possible combinations of colour to form a colour-singlet:

$$|\pi^+\rangle = \begin{cases} |u_r \bar{d}_{\bar{r}}\rangle \\ |u_b \bar{d}_{\bar{b}}\rangle \\ |u_g \bar{d}_{\bar{g}}\rangle \end{cases} \quad (1.1)$$

The pion in nature is a mixture of all these possible combinations. QCD, the theory describing strong interactions, is a remarkably precise theory that is able to describe numerous experimental results. Its only free parameters are the current quark masses and the coupling  $\alpha_s$ . Like Quantum Electrodynamics (QED), which describes interactions between electrically charged particles, it is a gauge theory in which currents and charges are conserved. With the perturbative calculations all strong (interaction) processes with large momentum transfer (such as jets) can be described. Strong interactions also show some interesting parallels to interactions in QED. When in electromagnetic interactions leptons exchange photons to undergo an interaction, the photon mediates the momentum and energy exchange. Gluons are (like the photons) massless  $J^P = 1^-$  field particles but they can also interact among themselves (see Fig. 1.4 in c) and d)). Furthermore they can be emitted by quarks (as shown in a) ) or produce a quark-antiquark pair (as shown in b) ). The character of the strong force can phenomenologically be described by the picture of the quark-antiquark potential for quarks that are separated by a certain distance  $r$  as

$$V(r) = -\frac{4}{3} \frac{\alpha_s}{r} + k \cdot r \quad (1.2)$$

in which  $k$  is the (linear) string tension parameter (which is around 1 GeV/fm) and  $\alpha_s$  the strong coupling constant. The form of this potential can explain the feature of confinement for large distances (i.e. at low  $Q^2$ ). It also gives a simple picture of how quarks can be produced by string breaking at high energies, when a quark antiquark pair is separated from each other and a coloured string forms out between both quarks. For larger separation

distance the string energy achieves such high values that the string breaks up and a new quark-antiquark pair is created that builds new hadrons together with the initial quarks. This concept of string breaking is used in Monte Carlo event generators (as e.g. PYTHIA [23], HIJING [24]) to model the particle production in nucleon-nucleon (nucleus-nucleus) collision processes.

In QCD as well as in QED, the coupling constant describes the strength of the interaction and depends on the energy scale  $Q^2$ . However,  $\alpha_{\text{em}}$  only shows a very weak dependence on  $Q^2$  and is  $\alpha_{\text{em}} \propto 1/137$ , while  $\alpha_s$  strongly depends on the scale  $Q^2$  and is much more complicated to measure accurately. The lower panel in Fig. 1.5 shows a comparison of the electromagnetic and the strong coupling constant. The difference between the two couplings can be explained by the different character of the QED and QCD exchange bosons (upper panel). Fluctuations of gluons into a pair of quark anti-quark leads to screening of strong charge (colour screening). Electron-positron pair production in QED causes screening of electric charges. For larger  $Q^2$  the distances between the interacting partons are very small, therefore the effective charge of the interacting particles increases and the coupling gets stronger.

However gluons can couple to themselves, for higher  $Q^2$  they fluctuate into (additional) gluons as illustrated in the upper panel of Fig. 1.5 which acts like an effective “gluonic cloud” around a coloured (test) charge. That causes an “anti-screening” effect and makes the coupling small for high  $Q^2$ . The anti-screening effect turns out to be much stronger than the screening effect in QCD (caused by fluctuations of gluons into quark-antiquark pairs). This causes the strong coupling to get smaller with increasing  $Q^2$  and larger for decreasing  $Q^2$ .

The first order of a perturbative QCD calculation gives for the strong coupling constant  $\alpha_s$ :

$$\alpha_s(Q^2) = \frac{12\pi}{(33 - n_f) \cdot \ln\left(\frac{Q^2}{\Lambda_{\text{QCD}}^2}\right)} \quad (1.3)$$

Where  $\Lambda_{\text{QCD}}$  is a scale (around 250 MeV/c) which provides a limit on the applicability of perturbative QCD calculations [25].  $n_f$  is the number of active quark flavours (which is around 3-6, depending on the energy scale). At the energy scale around the mass of the Z boson ( $M_Z \sim 91$  GeV)  $\alpha_s(M_Z^2)$  is around 0.12, which is compared to the fine-structure constant (with  $\alpha_{\text{em}}(M_Z) \sim \frac{1}{128}$ ) still about 15 times larger at that energy scale. That is much above the scale at which the quark confinement dominates (which is from around  $Q \sim 1$  GeV on) [26]. At very high values of  $Q^2$  the strong coupling constant becomes very small, which implies that quarks and gluons at these energy scale are quasi-free. This high energy limit of  $\alpha_s$  is called the “asymptotic freedom” [27], whose discovery by Wilczek, Gross and Politzer in 1973 was awarded the nobel prize in 2004.

Figure 1.6 shows the results of several measurements in which the running of  $\alpha_s(Q^2)$  over a large range of momentum transfer was determined. The measurements confirm the character of the strong force at high and low energies as described before. Strong

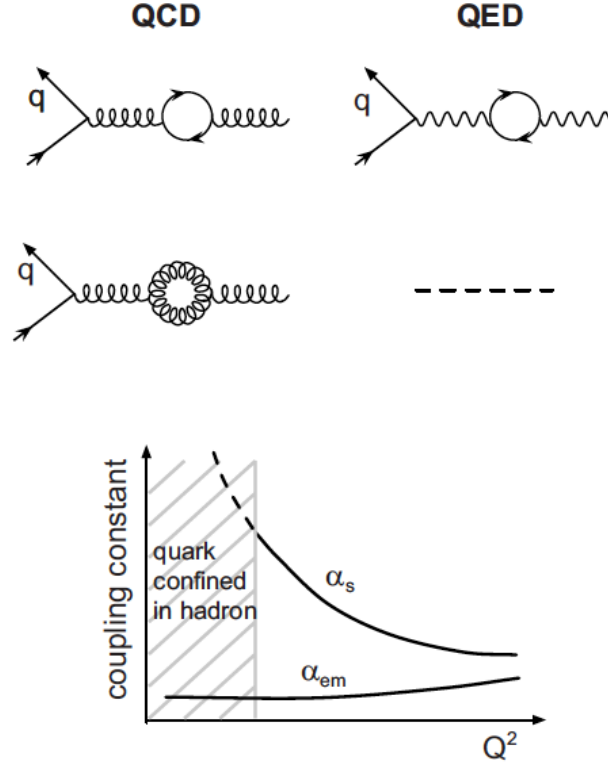


Figure 1.5: (Upper figure) Fluctuations of gluons into a pair of quark anti-quark leads to screening of strong charge (colour screening). Electron-positron pair production in QED causes screening of electric charges. The gluon self-coupling however leads to anti-screening effect. (Lower figure) Comparison of the electromagnetic and the strong coupling. (Figure adapted from [19]).

interactions are described by the fundamental Lagrangian of QCD:

$$\mathcal{L} = -\frac{1}{4} \sum_a F_{\mu\nu}^a F^{a\mu\nu} + \sum_f \bar{\psi}_f (i\gamma^\mu \partial_\mu - g\gamma^\mu \sum_a A_\mu^a \frac{\lambda^a}{2} - m_f) \psi_f \quad (1.4)$$

where  $\psi_f$  are the quark fields (with the quark masses  $m_f$  and the quark flavour index  $f = u, d, s, c, b, t$ ) and  $A_\mu^a$  are the gluon fields ( $a = 1, \dots, 8$  is the gluon colour index and  $\mu = 0, \dots, 3$ ).  $g$  is the strong coupling constant (with  $\alpha_s(Q^2) \equiv \frac{g^2(Q^2)}{4\pi}$ ),  $\gamma^\mu$  are the Dirac matrices and  $\lambda^a$  the Gell-Mann matrices, that are the generators of the SU(3). The gluon field tensor  $F_{\mu\nu}^a$  in equation 1.4 is defined as

$$F_{\mu\nu}^a = \partial_\mu A_\nu^a - \partial_\nu A_\mu^a - g_s f_{abc} A_\mu^b A_\nu^c. \quad (1.5)$$

$f_{abc}$  are the structure constants of the Lie algebra, that is defined by the commutation relations of the Gell-Mann matrices

$$\left[ \frac{\lambda_a}{2}, \frac{\lambda_b}{2} \right] = i f_{abc} \frac{\lambda_c}{2}$$

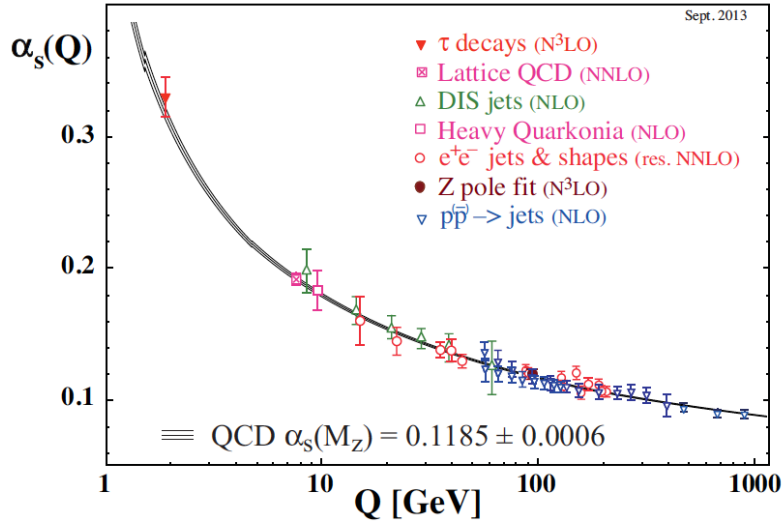


Figure 1.6: Experimental measurements of  $\alpha_s$  by different experiments and at different scales  $Q = \sqrt{Q^2}$  [22]).

The discovery of numerous new particle types with increasing collision energy motivated particle production models, like the “statistical bootstrap” model by Hagedorn [28]. He interpreted the increase of particle resonance and bound states in a hadron resonance gas model as a function of a certain mass interval in a thermodynamical picture. With increasing energy the number of particle types increases exponentially while the temperature is limited by a certain value. The “Hagedorn” temperature was determined to be  $T_H \approx 160$  MeV. This was the first prediction of a characteristic temperature limit up to which a stable description of a hadron gas by statistical mechanics is possible. Remarkable is that this first estimate for the critical temperature ( $T_c$ ) is not very far away from the current best estimated value [29] of  $T_c$  which is around 155 MeV as calculated in lattice gauge theory (see e.g. [30]). At very high temperature, due to the large value of the strong coupling, perturbative calculations are not applicable. This requires alternative approaches, such as the lattice QCD calculations [31], which are numerical Monte Carlo methods, aiming to solve the QCD theory of quarks and gluons but are requiring huge computational power. Indeed lattice QCD calculations firstly predicted a phase transition of the hadronic matter to a new phase of QCD matter. Afterwards also alternative concepts such as *AdS/CFT correspondence* have been used to explain aspects of the the Quark Gluon Plasma (QGP). It provides a non-perturbative description of string theory under certain boundary conditions. The calculations showed e.g. that the ratio of the plasma shear viscosity  $\eta$  and the entropy (volume) density  $s$  has a lower limit of  $\frac{\eta}{s} \approx \frac{\hbar}{4\pi k_B}$  [32]. Furthermore *AdS/CFT* calculations [33] provide a description for the transport coefficient  $\hat{q}$ , that describes the observed quenching of jets and high- $p_T$  particles inside the plasma. In the BDMPS model [34],  $\hat{q}$  relates the energy loss to the square of the distance that has been traveled by the parton inside the medium. More about the energy loss of particles and jets in the medium is discussed later in this chapter.

The phase transition around  $T_c$  (or equivalently the critical energy density  $\epsilon_c$ ) can be seen as a rise in the energy density and pressure as shown in Fig. 1.7. The results are

obtained from QCD calculations by the Wuppertal-Budapest group on a discretised lattice of the euclidean spacetime of temperature  $T$  and three-volume  $V$ , using physical quark masses and  $N_t = 4, 6$  and  $10$  lattices ( $N_t$  is the number of time points on the lattice grid). The results predict a rapid rise of the pressure and energy density of hadronic matter for increasing temperature. Both energy density and pressure are increasing towards the Stefan Boltzmann limit<sup>2</sup> but at  $T = 1000$  MeV it is still around 20% below.

In the phase diagram of QCD (see Fig. 1.8) the QGP is located at very high temperature ( $T$ ) or baryo-chemical potential ( $\mu_B$ ) (which is a function of the net baryon density in the thermodynamical system). At low temperature and low density the normal hadronic matter, of which most of the matter present in the universe consists of, is located. Furthermore a hint for a critical point was found in [35], at which the transition into the QGP might be of second order.

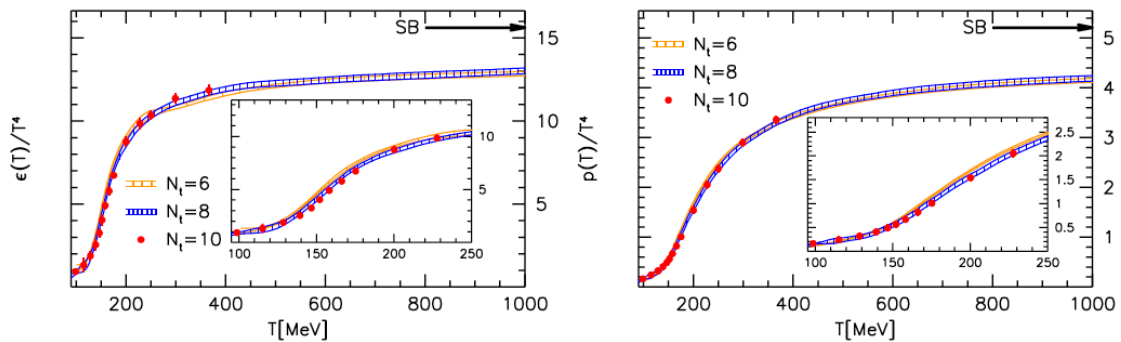


Figure 1.7: QCD calculations [36] on a discretised (hypercubic) lattice (of the euclidean spacetime of temperature  $T$  and three-volume  $V$ ) predict a rapid rise of the pressure and energy density of hadronic matter for rising temperature on  $N_t = 4, 6$  and  $10$  lattices.  $N_t$  is the number of time points on the lattice grid. The Stefan-Boltzmann (SB) limits are marked with arrows.

### 1.3 The Quark Gluon Plasma formation

The prediction of this new state of matter led to the idea of heavy-ion collision studies, for which numerous experiments have been setup at several accelerator facilities since 1970, such as the Relativistic Heavy Ion Collider (RHIC) [38] in Brookhaven (US), the SPS [39] at CERN or the SIS accelerator at GSI [40] (Darmstadt, Germany) and at the LHC at CERN [41], each of them measuring at different collision energies and studying different regions of the QCD matter in terms of the temperature and the net baryon density. The time development of the quark gluon plasma is sketched in Fig. 1.9 as a function of the time-axis  $t$  with the different stages that the plasma experiences.

The collision process starts with the two colliding nuclei approaching each other with approximately the speed of light. Each nucleus is lorentz-contracted (in perpendicular direction w.r.t. the beam axis  $z$ ) from its previously spherical shape to a thin disc with

<sup>2</sup>Which is the result of thermodynamical calculations of an ideal black body and given by  $p_{SB}(T) \approx 5.209 \cdot T^4$

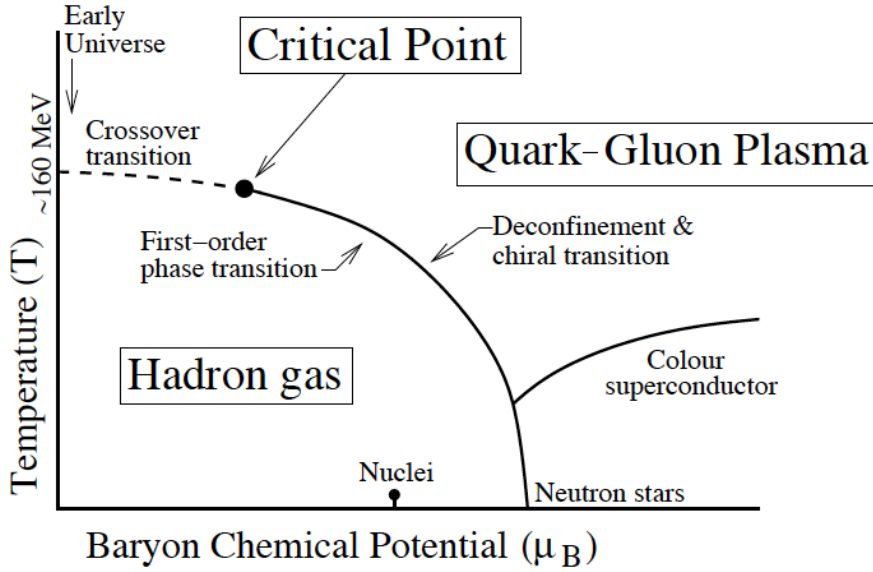


Figure 1.8: QCD phase diagram of hadronic matter as a function of temperature and baryo-chemical potential. The current LHC experiments measure at very low net baryon densities and very high energy. At these values the phase transition from normal hadronic matter to the quark gluon plasma is a continuous crossover, at higher baryo-chemical potential a transition of 1st order is expected to take place. Figure from [37].

a thickness of about 1 fm. At such high energies (like at the LHC) the nucleon Parton Distribution Functions<sup>3</sup> (PDFs) are dominated by the gluon PDF (see HERA measurement in Fig. 1.10). The proton PDFs [43] have been measured at the HERA [44] accelerator (Deutsches Elektronen-Synchrotron, Germany) using data from Deep Inelastic Scattering (DIS) of electrons off protons. At small Bjorken  $x$  (at high momentum transfer  $Q^2$ ) the gluon PDF dominates the distribution and contributes the largest fraction of the proton momentum.

At these high energies the discs of the nuclei are expected to be contained in a colour Glass Condensate (CGC) state [45] (not shown in timeline of QGP), composed of a coherent cloud of partons. In the CGC the gluons have a maximal occupation number and have reached a "saturation" (energy) scale in the transverse dimension (w.r.t. the disc), that turns the proton discs into dense many-body systems of gluons which show non-perturbative phenomena. Once the discs have smashed into each other a region of very high energy-density is built up, the Glasma. The system is then in a state of non-thermalized partons (i.e. it is far off equilibrium and not characterised by hadronic degrees of freedom anymore). They are undergoing multiple scatterings, what is commonly described by relativistic kinetic theory. The wounded nucleons, which did not participate in the inelastic collision process continue their way along the beam axis  $z$  and strong longitudinal colour electric and magnetic fields are formed. After a very short time in the order of  $\mathcal{O}(1\text{fm})$ , a locally thermalized plasma of partons has been formed by rescattering of the partons in

<sup>3</sup>The PDF describes the probability for finding a parton as nucleon constituent with a certain momentum fraction of the nucleon momentum

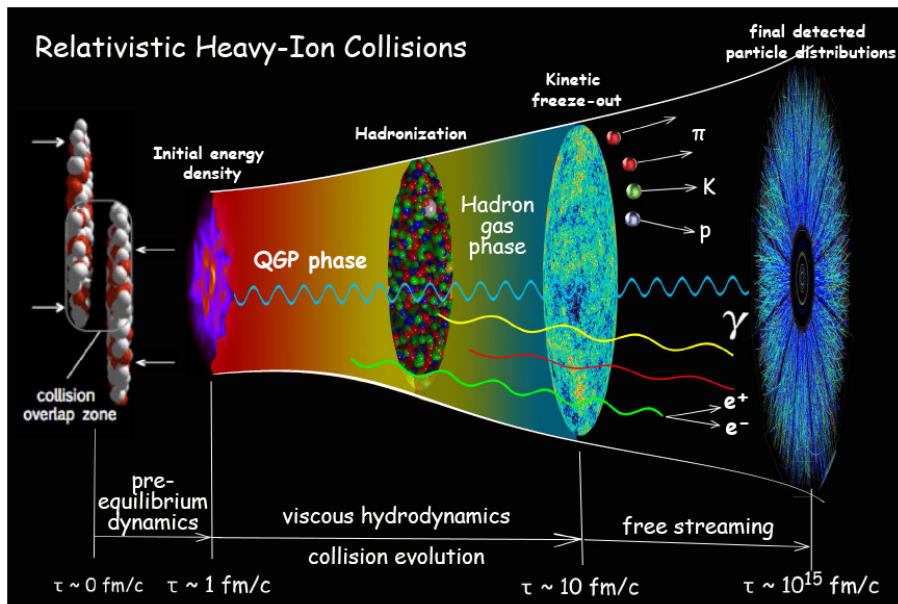


Figure 1.9: Different stages of the Quark Gluon Plasma formation. Figure adapted from [42].

the glasma, the QGP is created and exists for around  $\tau_{QGP} \sim 10 \frac{\text{fm}}{c}$  (which corresponds to around  $3 \cdot 10^{-23}$  seconds). Assuming local thermal equilibrium of the system, it can be described by relativistic ideal hydrodynamics [46, 47]. These models consider the collision geometry and the dynamics of the fireball. After its creation, the high density and temperature act with a high inner pressure so that the plasma undergoes a fast spatial expansion and cools down rapidly. After the critical temperature of around  $T_c \sim (154 \pm 9)$  MeV (or equivalently the critical matter density  $\rho_c \sim 1 \text{ GeV}/\text{fm}^3$ ) is reached, partons hadronise into baryons and mesons. This transition at vanishing baryo-chemical potential is a smooth crossover (see Fig. 1.8 at high  $T$  and low  $\mu_B$ ). At higher  $\mu_B$  the phase transition is expected to be of 1st order and at the critical point of 2nd order. When the plasma is expanding to larger volumes, temperature and energy density are decreasing accordingly until the critical values ( $T_c, \mu_c$ ) are reached. Since quarks are coloured objects, they cannot exist freely in a QCD confined phase and are recombining to final state hadrons. The hadronisation process is not well known up to know and since it takes place in the non-perturbative regime it requires phenomenological approaches with guidance from experimental measurements. Commonly used is the Lund string model, that is employed for Monte Carlo event generators like e.g. PYTHIA [48] to model nucleon-nucleon collisions or HIJING [24] (Heavy-ion Jet Interaction Generator) to model nucleus-nucleus collisions. It uses the idea of separated charges, which are connected by colour field lines over a certain distance. With increasing separation the field lines are compressed into strings that are breaking by non-perturbative string fragmentation as soon as the energy density exceeds a certain limit. In this way numerous partons are produced. At low energies the string fragments are identified with hadrons.

After the hadronisation, the particles follow the expansion behavior of the matter while

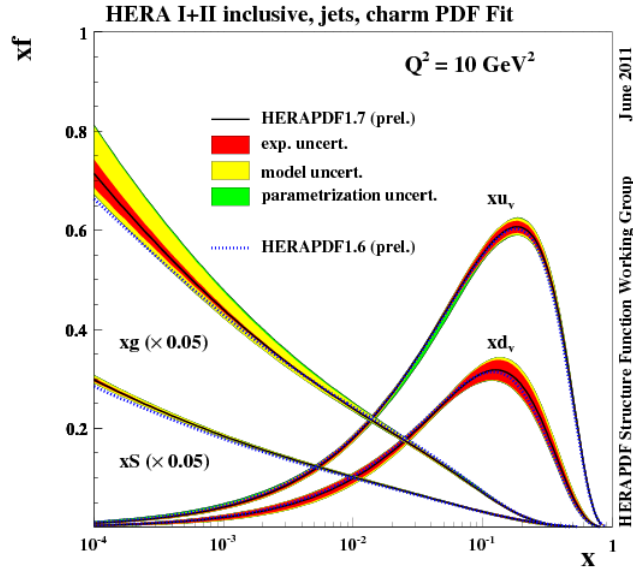


Figure 1.10: Parton distribution functions (PDFs) [43] as measured at HERA. At small Bjorken  $x$  (at high momentum transfer  $Q^2$ ) the gluon PDF contributes the largest fraction of the proton momentum and dominates over the valence quark PDFs.

colliding with each other until first the chemical freeze-out and then also the thermal (kinetic) freeze-out is reached. The chemical freeze-out takes place, when particles do only elastic scatterings and no more inelastic scatterings which change the particle composition of the collision. Then the average free path-length of the hadrons is larger than the distances over which the hadrons are colliding (or in a more simple approach, at almost the size of the system). When also the elastic scatterings are stopping the momentum composition of the primary particle spectra is determined. Heavy and unstable particles start eventually to decay into lighter ones, producing secondary particles.

Hadron multiplicity measurements are one of the basic measurements that are made for different collisions systems and can be successfully described by statistical models (that are inspired by hydrodynamical models) [49–51]. They aim to access plasma properties like temperature or the baryo-chemical potential at the chemical freeze-out conditions. In the statistical models the partition function  $Z(T, V)$ , formulated in the Grand Canonical (GC) ensemble of thermodynamics, is the starting point of the model description.  $Z(T, V)$  describes the set of possible states that a system of many particles in thermodynamical equilibrium can have and is given by

$$Z^{GC}(T, V, \mu_Q) = Tr[e^{-\beta(H - \sum_i \mu_{Q_i} Q_i)}] \quad (1.6)$$

where  $H$  is the Hamiltonian (using the description of a hadron resonance gas),  $\mu_{Q_i}$  are the chemical potentials and  $Q_i$  are charges that are conserved in the whole system on average.  $\beta$  is connected to the temperature of the system  $\beta = 1/T$ . For the simpler assumption of a static fireball, the particle multiplicities e.g. are obtained from the thermodynamic

relation in Eq. 1.7 in which an integration over the momentum space is carried out

$$N_i = g_i \int \frac{d^3p}{(2\pi)^3} [e^{\frac{E_i(p)-\mu_i}{T}} - \epsilon]^{-1} \quad (1.7)$$

$N_i$  is the hadron multiplicity of hadron type  $i$ , the factor  $\epsilon$  is -1 for bosons and +1 for fermions,  $g_i$  is the spin-isospin degeneracy factor, and  $\mu_i$  is the chemical potential that ensures charge conservation for Strangeness  $S_i$ , Baryon number  $B_i$  and the electric charge  $Q_i$ . The temperature is related to the energy density in the system and the chemical potential to the particle number, the integrand of Eq. 1.7 describes the density of states in phase space times their occupation number. The integration is carried out separately for each hadron type  $i$  and  $E_i$  the particle energy is given by  $E = \sqrt{p^2 + m^2} \sim p$  in the ultra-relativistic limit.

This description is done for hadrons up to a certain mass (e.g. mesons up to 1.5-2 GeV) and delivers good accuracy to describe the fireball consisting of hadrons and higher resonances (firstly the light resonances  $\phi$  and  $\rho$  are included, additionally also more heavy resonances are included in some models) in thermal and chemical equilibrium. In this way particle abundances and ratios can be fitted with good accuracy by a certain choice of the parameters ( $T_{\text{chem}}$  and  $\mu_{\text{chem}}$ ) of this model and tuned in order to fit many different particle types simultaneously (see Fig. 1.11 for a comparison to NA49 (at the SPS) data and Fig. 1.12 for a comparison of the model to ALICE data).

## 1.4 Particle flow

The bulk of particles produced in heavy-ion collisions carries away some collective (i.e. non-local) features, that have been determined by the plasma itself. One typical feature are collective effects, like the particle flow [53], which lead to modifications of the momentum distribution of the final state hadrons. The flow has its origin in the dense and hot confined medium of the participants (the nucleons which have actively participated in the collision process) directly after the collision, in which strong pressure gradients push with different strength into the different directions (e.g. into the reaction plane "in-plane" or into the direction perpendicular to the reaction plane "out-of-plane"). An illustration of this scenario is given in the left panel in Fig. 1.13 in which the reaction plane is defined by the  $z$  and  $x$  direction. The flow is furthermore affected by the initial asymmetry of the overlapping zone of both nuclei (more details about the event centrality are given in section 2.8) and can therefore contain asymmetrical shapes.

In general the particle flow, measured by the azimuthal distribution of the observable  $r(\phi)$  (e.g. the azimuthal momentum distributions of the particles  $dp_T/d\phi$ ) can be expressed by a Fourier expansion [56]:

$$r(\phi) = \frac{x_0}{2\pi} + \frac{1}{\pi} \sum_{n=1}^{\infty} [x_n \cos(n\phi) + y_n \sin(n\phi)] \quad (1.8)$$

with the Fourier coefficients  $x_0$ ,  $x_n$  and  $y_n$ , for the  $n$ th order of the expansion coefficient. For a finite number of particles they are calculated as the following sums over the particles,

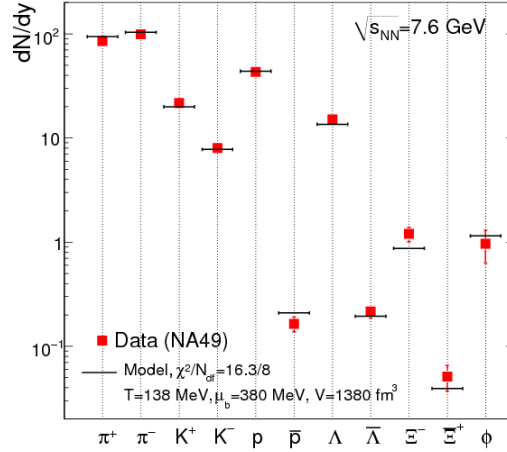


Figure 1.11: Comparison of prediction by the thermal model and the SPS data for central Pb–Pb collisions at  $\sqrt{s_{\text{NN}}} = 7.6$  GeV. Figure adapted from [49].

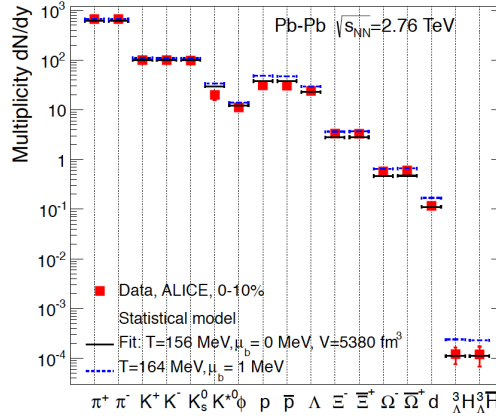


Figure 1.12: Statistical hadronisation model fitted to hadron yields measured by ALICE. The fit yields  $T_c = 156$  MeV while also fit results for slightly higher  $T = 164$  MeV are shown (blue dotted lines). Figure adapted from [52].

with  $\phi_\nu$  being the azimuthal angle of particle  $\nu$ :

$$x_n = \sum_{\nu} [r_{\nu} \cos(n\phi_{\nu})] \quad (1.9)$$

$$y_n = \sum_{\nu} [r_{\nu} \sin(n\phi_{\nu})] \quad (1.10)$$

In the absence of fluctuations and flow all coefficients are zero except  $x_0$ . For non-zero values of  $x_n$  and  $y_n$  each combination gives another order of the harmonic  $v_n$ :

$$v_n = \sqrt{x_n^2 + y_n^2} \quad (1.11)$$

The different orders are identified with the measured direct flow ( $v_1$ ), elliptic flow ( $v_2$ ) and triangular flow ( $v_3$ ). Experimentally the anisotropic flow [57] is measured as the anisotropy

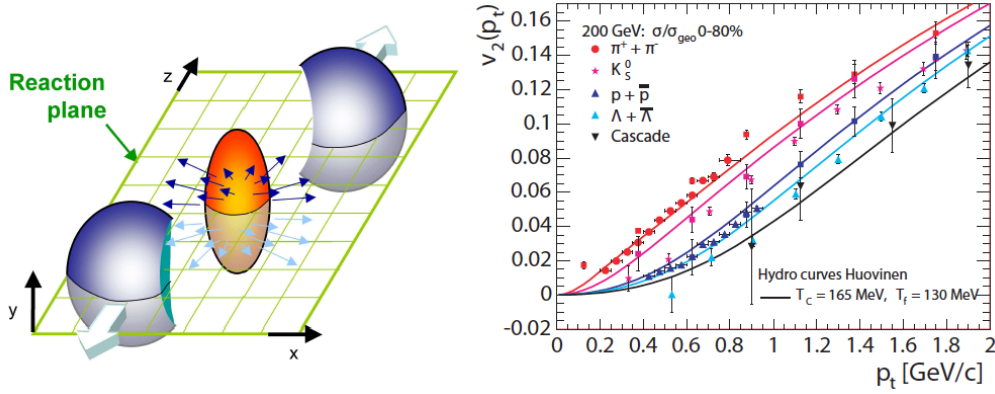


Figure 1.13: Left panel: Spatial asymmetry in the reaction plane of the collisions in a peripheral heavy ion collision. Right panel: Measured elliptic flow parameter  $v_2(p_T)$  for soft particles ( $p_T < 2$  GeV/c) measured by PHENIX [54], the comparison to hydrodynamical predictions show good agreement. Figures adapted from [55].

of differential momentum distributions

$$E \frac{d^3N}{d^3\mathbf{p}} = \frac{1}{2\pi} \frac{d^2N}{p_T} \left( 1 + 2 \sum_{n=1}^{\infty} v_n \cos[n(\phi - \psi_{\text{RP}})] \right) \quad (1.12)$$

where  $E$  is the particle energy,  $p$  the momentum,  $p_T$  is the transverse momentum,  $\phi$  the azimuthal angle,  $y$  the rapidity (which is defined as  $y = \frac{1}{2} \ln(\frac{E+p_z}{E-p_z})$  with  $p_z$  being the momentum component along the beam axis  $z$ ).  $\psi_{\text{RP}}$  is the reaction plane. The flow coefficients  $v_n(p_T, y)$  are given by

$$v_n(p_T, y) = \langle \cos[n(\phi - \psi_{\text{RP}})] \rangle \quad (1.13)$$

where the angular brackets represent an average over the particles and the sum over all events, measured for each  $p_T$ - $y$  interval separately.

The impact of the flow on the shape of the particle  $p_T$  spectra as a "blueshift" is investigated i.a. by the analysis of particle ratios in heavy-ion collisions (discussed later in this chapter).

Figure 1.13 (right panel) shows an example for the elliptic flow parameter  $v_2(p_T)$  for soft particles ( $p_T < 2$  GeV/c) measured by PHENIX [54]. The measurement is compared to hydrodynamic models (with a certain choice of  $T_c$  and  $T_f$ , the temperature at *freeze-out*) that can well describe the  $p_T$  dependence of  $v_2$  for the different particles species.

Apart from this soft particle production in nucleus-nucleus collisions, hard scatterings of partons occur at the early stages of the collision process. They are produced independently from the plasma formation but might interact to some extent with the partons of the medium and therefore appear modified in the final state.

## 1.5 Particle jets as hard probes

It is possible to experimentally probe the QGP and study its thermodynamical properties in hard-scattering processes ( $p_T$  at several  $\text{GeV}/c \gg \Lambda_{\text{QCD}}$ ), like particle jets and particles with high transverse momentum ( $p_T$ ). These hard probes, as tools to study the QGP, provide several advantages. Firstly, parton scattering processes<sup>4</sup> with large momentum transfer  $Q^2$  can only take place in a very early phase of the nucleus-nucleus collision (in which the energy density is at maximum) and thus "experience" all phases of the heavy-ion collisions. Since they have to traverse the hot and strongly-coupled medium, they can undergo interactions with the surrounding medium. Therefore they might provide information on the thermodynamical properties of the plasma (like the medium viscosity  $\eta$  or its transport coefficients  $\hat{q}$ ). And secondly, since  $\alpha_s$  is small for low high  $Q^2$  the jet cross-sections can be precisely predicted by pQCD calculations, which makes any modification (in the measurements w.r.t. predictions or a reference) of these precise "vacuum-like" calculations a tool to study the medium-modifications of various physics observables.

Jets are observed in particle-collider experiments as collimated bunches of particles. The theoretical description of jet production is done with the parton model [58], in which nucleons are made up of a number of point-like colour-charged constituents, which are quarks and gluons. It furthermore treats hard parton interactions independently from the nucleons (the other partons are considered as spectators) in which they are confined and from soft QCD processes that are following the parton shower evolution.

Jet production starts with a parton-parton scattering with a large momentum transfer  $Q^2$  between the two colliding nuclei. Both partons can undergo an elastic ( $2 \rightarrow 2$ ) or an inelastic scattering ( $2 \rightarrow 2 + X$ ), in the latter case numerous partons in the final state can be produced. In both cases the outgoing scattered partons carry a large virtuality  $Q^2$  that is reduced by radiation of soft gluons or producing quark-antiquark pairs, building up a parton cascade. This parton shower evolution is described in perturbative QCD (pQCD) by the Dokshitzer-Gribov-Lipatov-Altarelli-Parisi (DGLAP) equations [59]. The shower evolution stops at virtualities  $\mathcal{O}(1\text{GeV}^2)$ , and the partons are dressed by soft QCD processes and turn into observable colour-neutral hadrons. The hard parton shower process and the following hadronisation are called *fragmentation* process. The probability to produce a hadron in the final state by a hard parton scattering (as here for the example of an hadron-hadron collision) is given by the production cross section  $d\sigma_{AB \rightarrow h}^{\text{hard}}$  as given in Eq. 1.14 (for more details see [60]). For high  $Q^2$  it can be calculated in perturbative QCD and factorized into the cross section of the partonic scattering [61], the non-perturbative parton density functions (PDFs)  $f_{a/A}(x_1, Q^2)$ , measured at a scale  $Q^2$ , and the fragmentation functions (FF)  $\mathcal{D}_{c \rightarrow h}(z, Q^2)$ . This QCD factorisation scheme (that is applicable in the high energy regime due to the small  $\alpha_s$ ) is required to describe the process which cannot be calculated by using a huge set of Feynman diagrams. The hard scattering process is

---

<sup>4</sup>Hard parton scatterings take place in a very small time-scale  $\tau$  approx.  $1/p_T$  after the collision took place.

illustrated in Fig. 1.14 and shows the different components used in the factorisation.

$$d\sigma_{AB \rightarrow h}^{hard} = f_{a/A}(x_1, Q^2) \otimes f_{b/B}(x_2, Q^2) \otimes d\sigma_{ab \rightarrow c}^{hard}(x_1, x_2, Q^2) \otimes \mathcal{D}_{c \rightarrow h}(z, Q^2) \quad (1.14)$$

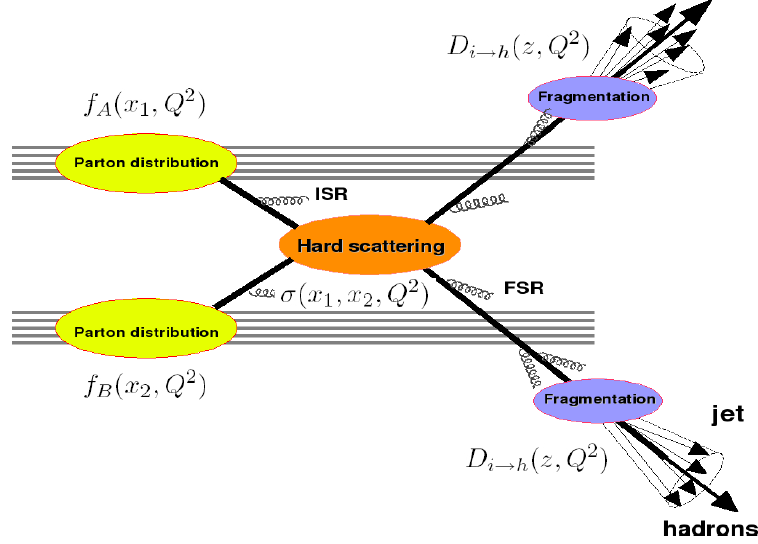


Figure 1.14: Sketch of dijet production and pQCD collinear factorisation in hadronic collisions:  $f_{a/A}(x_1, Q^2)$  are the PDFs.  $\mathcal{D}_{c \rightarrow h}(z, Q^2)$  are the fragmentation functions (FFs) and ISR (FSR) represents initial (final-) state radiation. Figure and caption adapted from [55].

In which  $d\sigma_{ab \rightarrow c}^{hard}(x_1, x_2, Q^2)$  is calculable in perturbative QCD up to a given order in  $\alpha_s$ . The other two expressions for the PDFs and the FFs are non-perturbative terms and to be determined independently (from experimental measurements e.g. by DIS of electrons on protons or in  $e^+e^-$  collisions): The FFs  $\mathcal{D}_{c \rightarrow h}(z, Q^2)$  give the fragmentation probability of the outgoing parton into the final state hadron  $h$  with a certain momentum fraction  $z$  of the initial parton momentum. The PDF  $f_{a/A}(x_1, Q^2)$  encode the probability to find a parton (of flavour  $a$ ) of a certain momentum fraction  $x$  inside the nucleon. It is an intrinsic property of the nucleon and expected to be independent from any experimental process. For the case of a nucleus-nucleus (with the mass number  $A$  and  $B$ ) scattering, the factorisation scheme follows as for  $A$  independent nucleon-nucleon collisions:

$$d\sigma_{AB}^{hard} = A \cdot B \cdot d\sigma_{pp}^{hard} \quad (1.15)$$

This is commonly expressed by the measurements of invariant yields as:

$$dN_{AB}^{hard}(b) = \langle T_{AB}(b) \rangle \cdot d\sigma_{pp}^{hard} \quad (1.16)$$

The nuclear overlap  $\langle T_{AB}(b) \rangle$  at a given impact parameter  $b$  can be determined by the Glauber model [62] as described in section 2.8.

In a parton-parton hard scattering two or more jets can be formed as observed by previous collider-experiments. In collision events in which 3 jets appear in the final state e.g. the

first hint on the gluon was found.

## 1.6 Jet quenching

“Hard probes”, i.e. high- $p_T$  jets or heavy particles ( $p_T, m > 2 \text{ GeV}/c^2$ ), present very useful tools to study the QGP from the earliest phase of its creation.

In the following (and according to the description in [12]) we are focusing on jets that are produced by partonic scatterings with a large momentum transfer  $Q^2$  at very short timescales ( $\tau \sim 1 / p_T \sim 0.1 \text{ fm}/c$ ) after the collision process started, allowing them to propagate through the plasma and strongly interact with the medium constituents. Via their medium interaction they suffer energy loss that can be measured and compared to “vacuum-like” jets or by the study of more sophisticated techniques like e.g. hadron-jet,  $\gamma$ -jet or photon-jet correlations. Therefore one of the most interesting observables in the context of jet production in heavy-ion collisions is jet energy loss and the modification of jet observables.

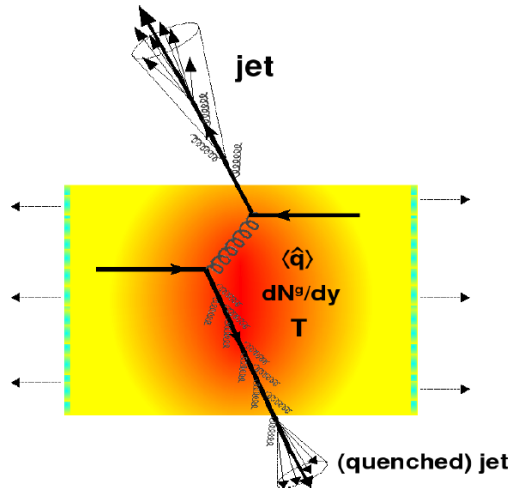


Figure 1.15: Two quarks suffer a hard scattering: one goes out directly into the vacuum, radiates a few gluons and hadronises, the other goes through the dense plasma created (characterised by the transport coefficient  $\hat{q}$ , the gluon density  $dN^g/dy$  and temperature  $T$ ), suffers energy loss due to medium-induced gluonstrahlung and finally fragments outside in a (quenched) jet. Figure and caption adapted from [60].

Figure 1.15 illustrates a typical scenario for jet quenching: There are two quarks that undergo a hard scattering. One quark directly escapes the medium and enters into the vacuum. It radiates a few gluons and hadronises. The other quark has a long path-length within the dense plasma (that is characterised by the transport coefficient  $\hat{q}$ , the gluon density  $dN^g/dy$  and a temperature  $T$ ) and suffers energy loss due to medium-induced gluonstrahlung. It finally fragments outside the plasma into a “quenched” jet [60]. Quenched jets therefore may appear attenuated or can even completely disappear in the experiment.

Jet quenching as a tool to study the QGP was first considered by Bjorken in 1982 [63], where he predicts sizable quenching effects up to completely “extinguished” jets in hadron-

hadron collision experiments. Instead of studying reconstructed jets the first measurements used single high- $p_T$  particles that are expected to be one of the leading particles inside a jet and therefore serve as a "proxy" for jets.

A common observable to study medium-modifications in heavy-ion collisions is the *Nuclear Modification Factor*  $R_{AA}$ , which is defined as

$$R_{AA} = \frac{1}{\langle T_{AA} \rangle} \frac{dN_{AA}/dp_T}{d\sigma_{pp}/dp_T} \quad (1.17)$$

where  $\langle T_{AA} \rangle$  is the nuclear thickness function as calculated with the Glauber<sup>5</sup> model [62].  $dN_{AA}/dp_T$  is the differential yield in nucleus-nucleus collisions and  $d\sigma_{pp}/dp_T$  the differential cross section in pp collisions.  $R_{AA} = 1$  would indicate that the particle  $p_T$  spectrum is the superposition of all binary nucleon-nucleon collisions which take place during one nucleus-nucleus interaction. In case of  $R_{AA} < 1$  the (high- $p_T$ ) particle production in Pb–Pb shows a relative suppression w.r.t. the production in pp collisions, an  $R_{AA} > 1$ , on the other hand, a relative enhancement. The interpretation of the  $R_{AA}$  (for  $p_T \gtrsim 2$  GeV/c) as a measure of a possible medium-modification (of a measured observable) assumes binary collision scaling<sup>6</sup> (i.e. considering the collision process as a superposition of multiple nucleon-nucleon scatterings). Every deviation from unity (for a hadron  $p_T \gtrsim 2$  GeV/c) would therefore indicate a suppression or enhancement of the particle production. For  $p_T \lesssim 2$  GeV/c  $N_{part}$  scaling is expected, that leads to  $R_{AA} < 1$  even when there is no suppression of particles (or jets).

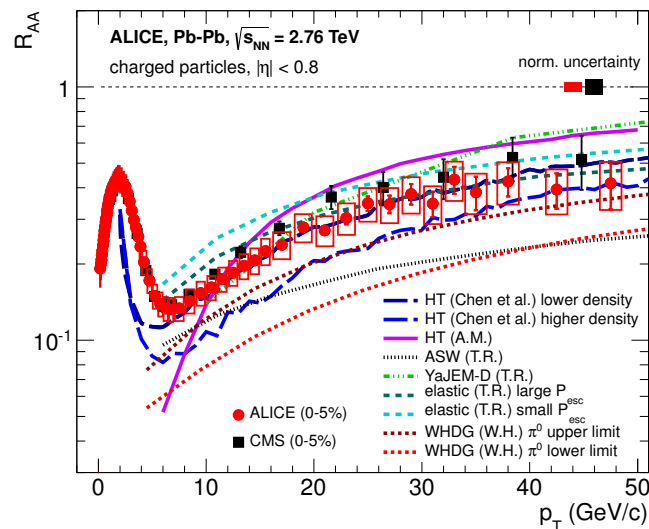


Figure 1.16: Nuclear modification factor  $R_{AA}$  measured at the LHC for the 5% most central events compared to theoretical model predictions [67–69]. Figure adapted from [70].

The expectation of jet energy loss was then confirmed in the year 2000 by measurements

<sup>5</sup>The Glauber model is used for the calculation of geometrical quantities in nucleus-nucleus collisions, like the impact parameter  $b$ , the number of participating nucleons  $N_{part}$  and the number of binary nucleon-nucleon collisions  $N_{coll}$ .

<sup>6</sup>This concept of binary scaling was tested and confirmed e.g. by the  $R_{AA}$  for direct photons [64],  $W^\pm$  [65] and the  $Z^0$  [66], that is unity as expected (since they do not interact via the strong force).

of high- $p_T$  particles [70] at RHIC and also later at much higher energies at the LHC (see Fig. 1.16). Several predictions by energy loss models [67–69] can describe the high- $p_T$  particle suppression.

The total amount of the jet energy loss  $\delta E$  depends on the jet properties (energy  $E$  and mass  $m$ ) and on the medium properties (plasma temperature  $T$ , thickness  $L$  and the particle-medium interaction coupling  $\alpha$ ) [12]. The jet energy loss along an in-medium path-length can be characterised by the following observables of the medium (as described by [60]):

- The *mean free path length*  $\lambda = 1/(\rho\sigma)$ , that depends on the medium density  $\rho$  ( $\propto T^3$  for an ideal gas) and the integrated particle-medium cross section  $\sigma$ ,
- The *opacity* (corresponding to the number of scattering centers)  $N = \frac{L}{\lambda}$  along a path  $L$ ,
- The Debye mass  $m_D(T) \sim g \cdot T$  (where  $g$  is the coupling strength) that is the inverse of the screening length of the chromo-electric fields in the QGP, the effective masses of the plasma constituents are of the order of  $\mathcal{O}(m_D)$ ,
- The transport coefficient  $\hat{q} = m_D^2/\lambda$ , which determines the average transverse momentum  $p_T$  transferred to the quenched parton per unit path-length,
- The *diffusion* constant  $D$  characterises heavy particles (with mass  $m$  and speed  $v$ ) crossing the QGP and is defined as  $D = 2T^2/\kappa = T/(M\eta_D)$ ,
- $\kappa$  is the average momentum the particle gets per unit time and is related to the transport coefficient as  $\kappa \propto \hat{q} \cdot v$ , and with the *momentum drag coefficient*  $\eta_D$ .

The two main mechanisms of parton in-medium energy loss are the *collisional* and the *radiative* energy loss. They add up to the total lost energy  $\Delta E = \Delta E_{coll} + \Delta E_{rad}$ . Figure 1.17 (left side), shows a quark in an elastic collision process with a quark from the surrounding medium (red quark line), an process that dominates at low particle  $p_T$ . By this scattering on average a total energy loss of

$$\langle \Delta E_{coll}^{1scat} \rangle \sim \frac{1}{\sigma T} \int_{m_D}^{Q_{max}^2} Q^2 \frac{d\sigma}{dQ^2} dQ^2$$

is caused.

$Q^2$  is the squared momentum transfer of a quark in the medium of temperature  $T$ . At higher particle  $p_T$  energy loss via inelastic collisions with the medium (as illustrated on right side in Fig. 1.17), followed by the emissions of gluons, plays an important role. The corresponding total energy loss (per scattering process  $E^{1scat}$ ) is given by the *gluon bremsstrahlung* spectrum  $\omega(dI_{rad}/d\omega)$ :

$$\Delta E_{rad}^{1scat} = \int^E \omega(dI_{rad}/d\omega)d\omega \quad (1.18)$$

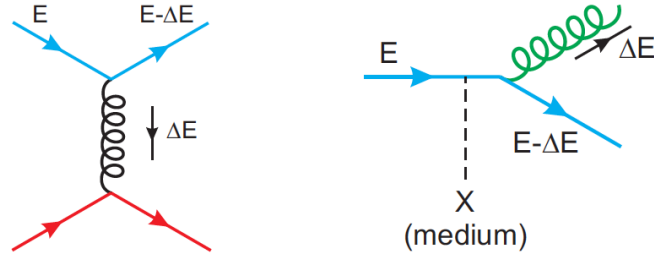


Figure 1.17: Left side: Quark energy loss in the medium via elastic collisions, Right side: Inelastic scatterings with the medium results in radiative energy loss. Figure adapted from [60].

In the case of incoherent scatterings, i.e. in absence of interference effects, these two contributions simply add up like  $\Delta E^{tot} = \frac{L}{\lambda} \cdot \Delta E^{1scat}$ . The *stopping power* of the medium per unit length  $l$  is then given by

$$-\frac{dE}{dl} = \frac{\langle \Delta E^{tot} \rangle}{L} \quad (1.19)$$

The QCD energy loss for  $\Delta E_{coll}$  and  $\Delta E_{rad}$  can be expressed (in analogy to the QED energy loss for leptons) as follows in the equations below.  $C_R$  is the "colour" factor<sup>7</sup> and  $\omega$  is the frequency of the radiated gluons.  $\omega_c$  is the characteristic gluonstrahlung energy  $\frac{1}{2}\hat{q}L^2$ , that is proportional to the average energy lost in the medium (for  $\omega_c < E$ ).

- Collisional energy loss:

- for light quarks or gluons:  $-\frac{dE_{coll}}{dl}|_{q,g} = \frac{1}{4}C_R\alpha_s(ET)m_D^2\ln(ET/m_D^2)$
- for heavy quarks:  $-\frac{dE_{coll}}{dl}|_Q = -\frac{dE_{coll}}{dl}|_q - \frac{2}{9}C_R\pi T^2[\alpha_s(M^2)\alpha_s(ET)\ln(\frac{ET}{M^2})]$

- Radiative energy loss:

- *Bethe-Heitler* regime ( $L \ll \lambda$ ):

$$\Delta E_{rad}^{BH} \approx \alpha_s \hat{q} L^2 \ln(E/(m_D^2 L)) \quad (1.20)$$

- *Landau-Pomeranchuk-Migdal* regime ( $L \gg \lambda$ ):

$$\Delta E_{rad}^{LPM} \approx \alpha_s \cdot \begin{cases} \hat{q} L^2, & (\omega < \omega_c) \\ \hat{q} L^2 \ln(E/(\hat{q} L^2)), & (\omega > \omega_c) \end{cases} \quad (1.21)$$

The Landau-Pomeranchuk-Migdal effect (as already described in QED) for thin media ( $L \ll \lambda$ ) describes how the destructive interference of the emitted gluons suppresses the effective<sup>8</sup> radiative energy loss for small  $\omega$  (in the infrared) as  $\frac{1}{\sqrt{\omega}}$  relative to the Bethe-Heitler gluon radiation spectrum (that is valid for thick media  $L \gg \lambda$ ) as  $\frac{1}{\omega}$ . The dominant

<sup>7</sup>The "colour" factor  $C_R$  is  $C_F = \frac{N_c^2 - 1}{2N_c} = \frac{4}{3}$  for the case of gluon emission by a quark. In case of a gluon emission by a gluon the colour factor is given by  $C_A = N_c = 3$ .

<sup>8</sup>The *LPM* effect lets the radiating medium particles effectively act as one single scattering centre.

energy loss mechanism of a parton traversing a coloured dense medium is caused by the radiation of gluons and not so much via collisions with partons from the medium [71–73]. However the collisional energy loss starts to be important for slow moving heavy quarks (charm and bottom) that cross the medium. For heavy quarks another interesting feature exists, the *dead cone effect* [74], which describes the reduction of gluon radiation. In case of a gluon with  $\omega$  and a transverse momentum  $k_T$  for angles  $\theta$  smaller than  $k_t \approx \omega\theta$  this effects decreases the gluon radiation by a factor of  $\approx \omega \frac{dI_{rad}}{d\omega dk_T^2} \cdot (1 + \frac{\theta_0^2}{\theta^2})^{-2}$  compared to the standard gluon bremsstrahlung spectrum. In a simplified picture description this reduction depends on the properties of the quark ( $E, M$ ) and the medium ( $L$ ) and is of the order  $\mathcal{O}(m_D/M)$ <sup>9</sup>. This furthermore leads to the expectation that the energy loss of quarks traversing the medium shows a kind of ordering related to the quark mass ( $q$  is a light quark u,d):  $\Delta E_{rad} > \Delta E_q > \Delta E_c > \Delta E_b$ . The reason why gluons are expected to suffer stronger in-medium energy loss compared to quarks is due to the fact, that gluons couple stronger to the medium and the probability for a gluon to radiate a gluon is proportional to  $C_A = 3$  while the one of a quark is smaller with  $C_F = \frac{4}{3}$ . These parton energy loss considerations motivate the following expectations w.r.t. "vacuum-like" fragmentation processes:

- Suppression of the transverse momentum  $p_T$  spectra of high- $p_T$  hadrons and suppression of jet  $p_T$  spectra (see e.g.  $R_{AA}$  measurements in Fig. 1.16 and Fig. 1.19)
- Imbalances of di-jets (see e.g. event display from CMS in Fig. 1.20) and di-hadron correlations in azimuthal direction  $\delta\phi$  in A+A collisions (as observed e.g. in di-jet asymmetries at CMS, see Fig. 1.21 (as described in text), Dijet imbalance was also measured by ATLAS [75])
- Softening of jet constituent spectra, larger multiplicity of jet constituents, angular broadening of jets (as measured by CMS [9] and shown in Fig. 1.22)

In this simplified picture (i.e. using one path-length for all partons, not considering fluctuations of this stochastic energy loss process, etc.) the average transport coefficient  $\hat{q}$  of the plasma is related to the suppression of high- $p_T$  hadrons and jets in the  $R_{AA}$  measurements as  $\Delta E_{medium} \propto \alpha_s \langle \hat{q} \rangle L^2$  (as derived from the equations in 1.21 and 1.20). A recent development [76] (made by the JET collaboration) for energy loss modeling, that employs (experimentally constrained) hydrodynamic models to describe the medium expansion, studied the suppression of high- $p_T$  single inclusive hadrons measured in heavy-ion collisions at RHIC and LHC. It is based on several existing parton energy loss models ([77–79] et al., for more details about the models see also [80]) that are constrained with new data available from RHIC and LHC. The models aim to extract the transport coefficient (that is also called *jet transport parameter*)  $\hat{q}$  at the center of the most central collisions. Since  $\hat{q}$  is a function of the temperature ( $\propto \alpha_s \cdot T^3$ ) it is expected to change during the expansion of the plasma. The exact proportionality factor of  $\hat{q}$  w.r.t. the temperature is not clearly known and slightly differently assumed in the different calculations [76, 80]. Therefore

<sup>9</sup>For a plasma with  $m_D = 1 \text{ GeV}/c^2$  this leads to a charm quark ( $m \sim 1.3 \text{ GeV}/c^2$ ) energy loss of around 25%.

it is estimated for an early time in these calculations and for a given temperature. For a quark with the initial energy of 10 GeV e.g. the model extracts a transport coefficient of  $\hat{q} \approx 1.2 \pm 0.3 \text{ GeV}^2/\text{fm}$  at an initial time  $\tau_0 = 0.6 \text{ fm}/c$  (and for  $T = 370 \text{ MeV}$ ) for Au+Au collisions at  $\sqrt{s_{\text{NN}}} = 200 \text{ GeV}$ . For Pb–Pb collisions at  $\sqrt{s_{\text{NN}}} = 2.76 \text{ TeV}$  the calculation leads to a  $\hat{q} \approx 1.9 \pm 0.7 \text{ GeV}^2/\text{fm}$  (and for  $T = 470 \text{ MeV}$ ). The ratio  $\hat{q}/T^3$  was found to be slightly larger at RHIC than at the LHC what might indicate a hotter medium at LHC. A hotter medium also causes particles to be stronger suppressed. On the other hand, the stronger suppression at LHC could be also explained by a slightly smaller value of  $\alpha_s$ .

## 1.7 Modification of jet observables in heavy-ion collisions

As discussed already before, the physics of hard parton scatterings, i.e. at high momentum transfer  $Q^2$ , can be well described by perturbative QCD (at Next-to-Leading-Order (NLO)) due to the small coupling constant  $\alpha_s(Q^2)$ . The hadronisation however needs to be described and modeled by non-perturbative QCD estimates, e.g. the Lund string model, that is used in the Monte Carlo event generators like PYTHIA [48],[23]. Figure 1.18 shows the inclusive jet production cross sections ( $R = 0.2$ ) measured with ALICE. NLO (next-to-leading order) pQCD predictions (calculations done by G. Soyez [81] and by N. Armesto, the latter one based on [81, 82]) are superimposed with the data. The ratio of the simulation and the results are shown in the lower panel. They show that the pQCD calculation including hadronisation effects show good agreement with the measurements. Jet cross section measurements in more elementary systems like in pp collisions help to test standard model predictions, but also serve as a reference for medium-modified measurements.

In the environment of a hot and dense medium, already numerous observations have been made, that indicate modifications w.r.t. measurements in pp collisions. Figure 1.19 shows the  $R_{\text{AA}}$  [84] for jets, reconstructed from charged and neutral particles, as measured by ALICE. The  $R_{\text{AA}}$  is defined as described in the previous section. The left plot shows the  $R_{\text{AA}}$  for the 10% most central events, the right plot in the centrality interval (10 - 30)%. The results indicate that for both centrality intervals a huge suppression of the jet production is present in heavy-ion collisions at  $\sqrt{s_{\text{NN}}} = 2.76 \text{ TeV}$  what is similar to the charged particle  $R_{\text{AA}}$  measured earlier (see Fig. 1.16). The suppression of jets with energies in the interval  $p_{\text{T}}^{\text{jet}} = 40\text{-}60 \text{ GeV}/c$  is stronger than for jets with higher energies (around 100 GeV/c). This suppression seems to be slightly larger for the 10% most central events than for the more peripheral data. Models like JEWEL [85] and YaJEM [86], (which simulate a pQCD jet evolution together with a modification by the medium present in heavy-ion collisions in a perturbative picture and model the non-perturbative hadronisation into the experimentally observable jet) are compared to the measurement. As can be seen from the comparison of experiment and theoretical prediction JEWEL shows a good agreement throughout the full  $p_{\text{T}}^{\text{jet}}$  interval.

Jet quenching effects have been also measured by the analysis of dijet events. While one

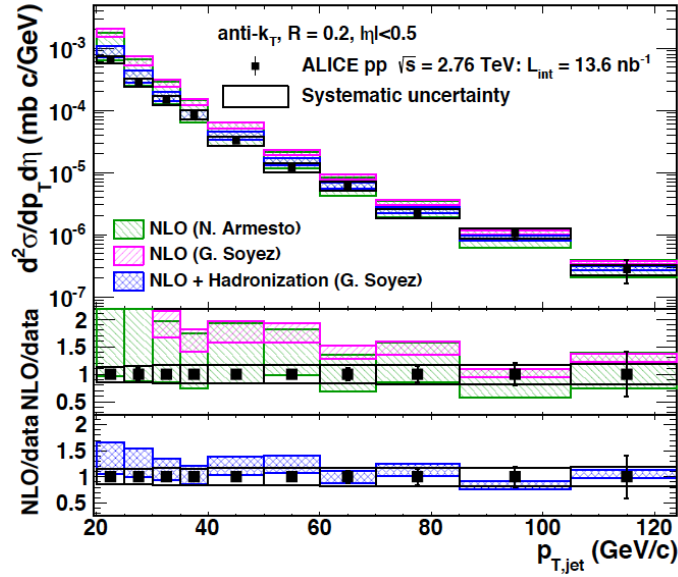


Figure 1.18: Inclusive jet production cross sections ( $R = 0.2$ ) measured. NLO pQCD predictions [81, 81, 82] are superimposed with the data and show good agreement when hadronisation effects are included. The ratio of the simulation and the results are shown in the lower panel. Figure adapted from [83].

high- $p_T$  jet is reconstructed, a strongly suppressed back-to-back jet on the opposite side in azimuth ( $\phi$ ) is observed as e.g. visible on the event display from ATLAS (see Fig. 1.20). By measuring both jet transverse momenta one can define an related observable, the dijet asymmetry:

$$A_J = \frac{p_{T,1} - p_{T,2}}{p_{T,1} + p_{T,2}} \quad (1.22)$$

where  $p_{T,1}$  and  $p_{T,2}$  are the transverse momenta from leading jets (with jet  $p_{T,1} > 120$  GeV/c) and sub-leading jets (with jet  $p_{T,1} > 30$  GeV/c) with an azimuthal distance  $\Delta\phi_{1,2} > \frac{2}{3}\pi$ .

Fig. 1.21 shows a measurement of the dijet asymmetry by CMS as a function of the event centrality (from left upper side to right lower side with increasing event centrality) [7]. The measurement (as black points) are compared to PYTHIA dijets, that are reconstructed after they have been embedded into HYDJET simulated (PbPb) events to "model" the impact of the background in Pb–Pb collisions on the jet reconstruction (see following chapter for more details) and the jet constituent spectrum (the PYTHIA dijets are indicated as a red histogram).

The rightmost panel on the lower row shows the asymmetry in Pb–Pb collisions for the 10% most central events. The leftmost upper panel shows the measurement in most peripheral events (70-100%) and in pp events in which the asymmetry  $A_J$  is almost identical for data and the PYTHIA comparison. The comparison to the PYTHIA dijets indicates a much more pronounced energy imbalance (see distribution of black points exceeding the red area at high values of  $A_J$ ) than for more peripheral events.

A more differential analysis, related to the work presented in this thesis, considers the jet

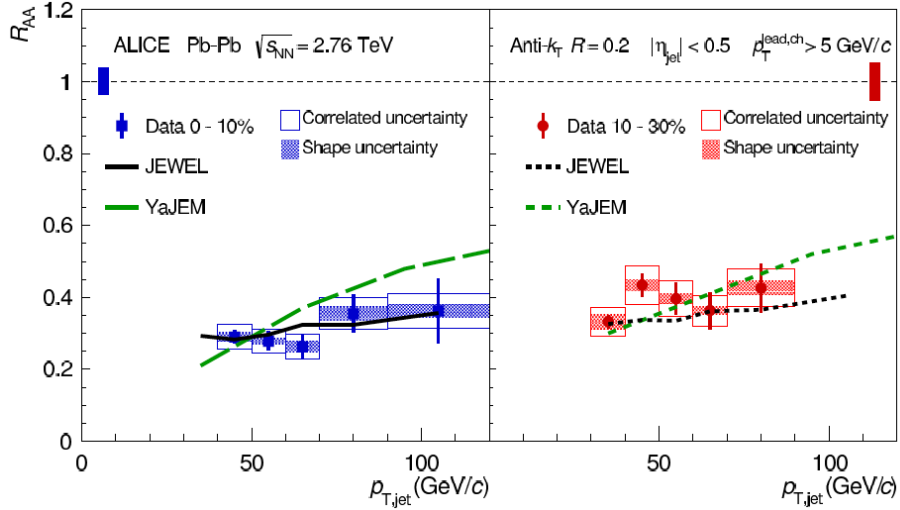


Figure 1.19:  $R_{AA}$  of jets [84] reconstructed from charged and neutral particles indicates a strong suppression in Pb–Pb collisions. The left plot shows the jet suppression for the 10% most central events, the right plot for 10–30% event centrality.

constituents with the measurement of the jet fragmentation functions [87] as measured by CMS in Pb–Pb and pp collisions at  $\sqrt{s_{NN}} = 2.76$  TeV. The modification of the jet fragmentation is shown in Fig. 1.22. The fragmentation functions (FFs) and the ratio to the FFs in pp collisions (PbPb/pp) at the same collision energy are shown. For the jet reconstruction neutral and charged particles are used. The fragmentation function is defined as

$$\frac{1}{N_{\text{jet}}} \frac{dN_{\text{track}}}{d\xi} \quad (1.23)$$

and presented as a function of the variable  $\xi$  that expresses the jet constituent fraction of the jet momentum  $p^{\text{jet}}$ :

$$\xi = \ln\left(\frac{1}{z}\right) \quad (1.24)$$

with the component  $z$  of the jet constituent momentum along the jet axis:

$$z = \frac{p_{\parallel}^{\text{track}}}{p^{\text{jet}}} \quad (1.25)$$

where  $p^{\text{jet}}$  is the magnitude of the jet momentum. Small  $\xi$  corresponds to high- $p_T$  jet constituents and large  $\xi$  to the soft jet constituents. The FFs are normalised to the number of jets  $N_{\text{jet}}$ . The upper panels show the FFs as measured in the Pb–Pb collisions, the lower panels contain the ratio w.r.t. the measurement in pp collisions. As can be seen from the bottom rightmost panel, the 10% most central Pb–Pb events exhibit a clear modification of the fragmentation pattern. A clear enhancement at the highest values of  $\xi$  (which corresponds to the softest jet constituents) can be seen. At intermediate  $\xi$  a depletion of the ratio is visible while for small values of  $\xi$  the ratio is in agreement with unity. It can be concluded from this observation that the medium modification softens the jet fragmentation in a significant way. The jet constituents with large  $p_T$  however seem to

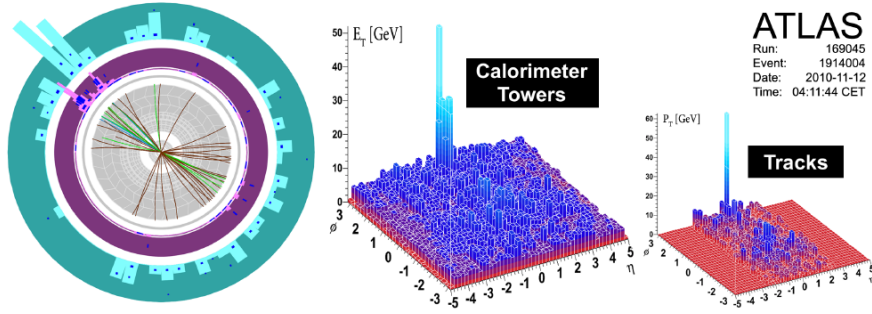


Figure 1.20: Event display by CMS experiment showing a dijet event (left panel). The right panels show the calorimeter towers that measure the total jet energy and the distribution of charged tracks over the acceptance  $\eta \times \phi$  both are indicating one high- $p_T$  jet and an almost vanished ("quenched") back-to-back jet appearing on the opposite side in azimuthal direction. Figure adapted from [75].

remain mostly unaffected.

For a more detailed understanding of these medium effects and their mechanisms it is interesting to study identified particles inside jets, which is the topic of the analysis presented in this thesis.

### 1.7.1 A model for jet quenching and its impact on the jet hadrochemistry

A phenomenological model [88] has been developed that consider these medium modifications via an enhanced parton splitting in the hard parton shower leading to the final state hadrons, while the hadronisation process remains unmodified.

The model describes the fragmentation process that leads to the hadronic distributions  $D_{q,g}(\xi, \tau, \lambda)$  inside the jet (with  $\xi = \ln(\frac{1}{z}) = \ln(\frac{E_{\text{jet}}}{p_{\text{hadron}}})$ ,  $\tau = \ln(\frac{Q}{\Lambda})$  and  $\lambda = \ln(\frac{Q_0}{\Lambda})$ ) by making use of the MLLA formalism [89] (modified leading logarithmic approximation) in order to make a perturbative calculation of the parton distribution inside a quark or gluon jet (i.e. a parton shower which is initialised by a quark or gluon). The hard parton shower calculation is based on leading order parton splitting functions. It furthermore uses an energy scale  $Q \sim E_{\text{jet}}$  as a starting point to model the parton shower. At a certain scale  $Q_0 = \lambda$  ( $Q_0$  is like  $\Lambda$  a fit parameter of the order of  $O(\Lambda_{\text{QCD}})$  that is approximately at the value of the hadron mass (for the case of identified particles) the evolution is stopped. The typical "hump-back" shape (see e.g. Fig. 1.22, upper panels) of the fragmentation function is caused by destructive quantum interference. At small values of  $z$  this causes an angular ordering of the parton cascade. This characteristic shape of the FF from a parton showering process in vacuum (studied in high energy pp and  $e^+ + e^-$  collisions) is well understood. Any modification from this shape might therefore hint on a distortion of the standard QCD radiation pattern induced by medium-interactions.

Figure 1.23 shows a sketch from a parton shower of gluons. In the large  $N_c$  (= number of colours) limit, the gluons can be represented as pairs of  $q\bar{q}$  fermion lines.

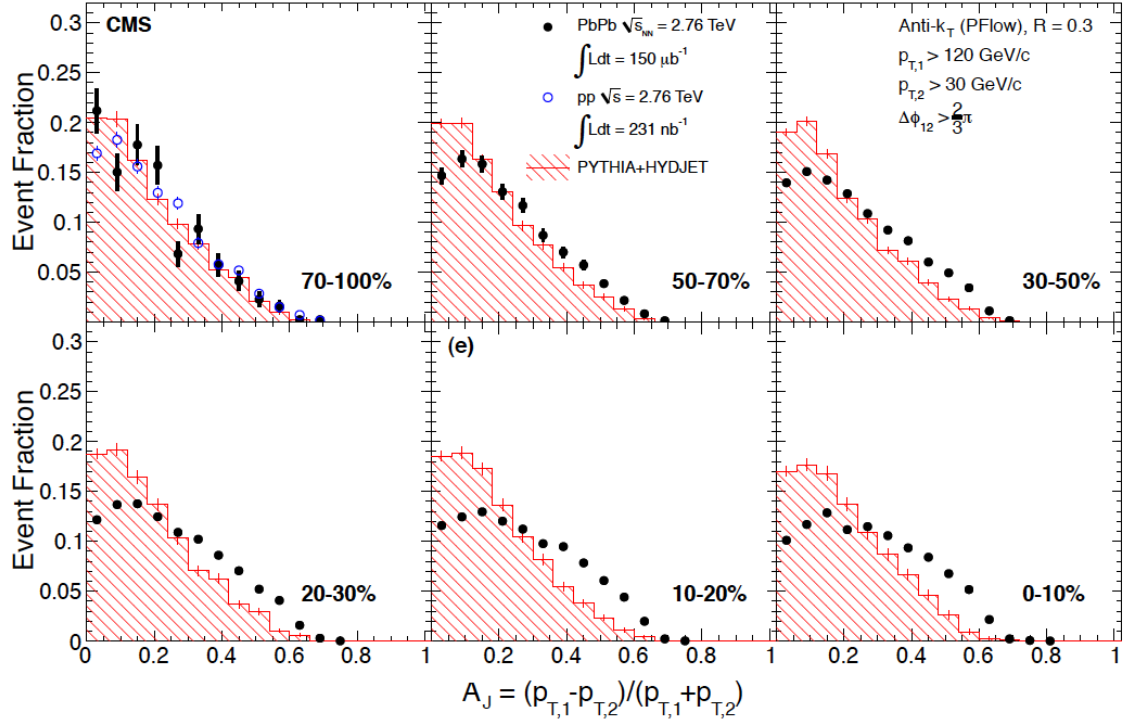


Figure 1.21: Dijet asymmetry measurement [7] by CMS collaboration as a function of event centrality (from left upper side to right lower side with increasing event centrality).  $p_{T,1}$  and  $p_{T,2}$  are the transverse momentum from leading and sub-leading jets with an azimuthal distance  $\Delta\phi_{1,2} > \frac{2}{3}\pi$ . The measurement (as black points) are compared to PYTHIA dijets, that are embedded into HYDJET simulated (Pb–Pb) events (red histogram). The different panels correspond to different centrality intervals.

The picture on the left side represents a parton shower evolution taking place in vacuum, while a shower inside the medium is shown on the right side. Partons inside the shower which interact with a medium parton via an exchange of momentum, flavour or colour modify the shower pattern and can lead to an increased particle multiplicity in the final state. It may also change the particle composition of the jet when colour charge is transferred by a single gluon exchange (as drawn in the right panel) and after the hadronisation took place.

This medium-induced parton splitting is included in the model as a constant factor for leading partons in the shower as well as for sub-leading parton splitting processes. For the modeling of the hadronisation the concept of local parton-hadron duality [90] (LPHD) is used, which assumes that the transformation of partons into final state hadrons takes place at a low virtuality scale (to energy scales at the order of the pion mass) in order to translate the partonic observables into those of the hadrons.

Furthermore a dependence of the fragmentation function on the particle species has been studied employing this model (and as adapted from [88] as well).

How the increase of the gluon splitting may affect the resulting hadron type content of the jets is illustrated in Fig. 1.24. Shown are the identified (hadron) fragmentation functions as a function of  $\xi$  and for three different particle types.

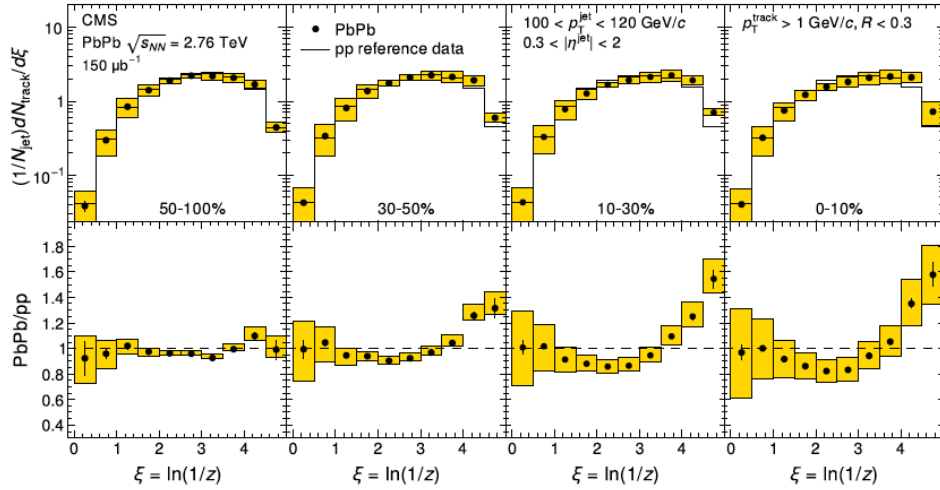


Figure 1.22: Modification of the jet fragmentation pattern for different event centrality intervals as measured by the CMS experiment. The fragmentation functions (FF) for jets, for the interval  $100 < p_T^{\text{jet}} < 120$  GeV/c and for a fragmentation radius of  $R = 0.3$ , are shown in the panels above while the ratio to the FFs in pp collisions at the same energy are shown below [87].

The solid lines show the outcome of this calculations for a fragmentation in vacuum while the dotted lines show the result in the presence of a medium. The calculation shows an increased particle multiplicity in the presence of a medium relative to the case of vacuum fragmentation. This effect is stronger for more massive particles (this we will see more clearly for the particle ratios presented in the following). It furthermore predicts a softening of the jet constituent spectrum in the medium case w.r.t. to the vacuum case as indicated by a shift of the maximum of the distribution to larger values of  $\xi$ .

How this increased parton splitting affects the particle ratios is shown in Fig. 1.25 for jet fragmentation in vacuum and medium and for different jet energies ( $E_{\text{jets}} = 50, 100$  and  $200$  GeV/c). The left panel shows the  $K^\pm/\pi^\pm$  ratio while the right panel the results for the  $p(\bar{p})/\pi^\pm$  ratio. The results for a fragmentation within the medium show an enhancement compared to the results from a fragmentation in vacuum (using no enhanced parton splitting). It furthermore suggests that the particle ratio enhancement is stronger for more massive particles. This can be seen in the larger difference between the medium and the vacuum result for the  $p(\bar{p})/\pi^\pm$  ratio and compared to this difference seen for the  $K^\pm/\pi^\pm$  ratio. This effect seems to be largest for the uppermost panels that correspond to  $E_{\text{jet}} = 50$  GeV while it is smaller for higher energetic jets (lower panels). This motivates to experimentally study particle ratios using particles with a larger mass difference (e.g.  $\Lambda$  and  $K_S^0$  hadrons as used in the analysis presented in this thesis) in jets with low energies. The basic idea of this model, the increased (via multiplication of a small constant factor) parton splitting (into quarks or gluons), leads to a modification of the jet shower even if no medium is present anymore at the time of the hadronisation of quarks into final state hadrons. Although it does not make any further effort to describe the exchange of momentum, colour or baryon number, mentioned before, what would be a difficult and

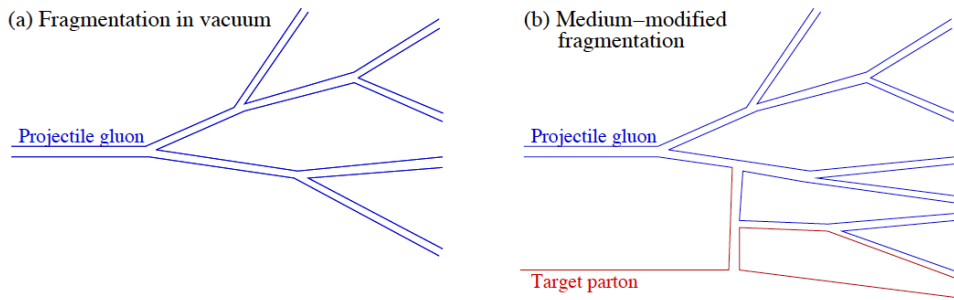


Figure 1.23: In the large  $N_c$  approximation, gluons are represented as pairs of  $q\bar{q}$  fermion lines. This sketch shows a gluonic parton shower, taking place in vacuum (left) and in the medium (right). Partons that interact with a medium parton via momentum, flavour or colour exchange (e.g. by hadronising with a medium parton via recombination) modify the shower pattern and can lead to an increased particle multiplicity, a shower softening and widening and may furthermore change the particle composition of the jet in the final state (after hadronisation) [88].

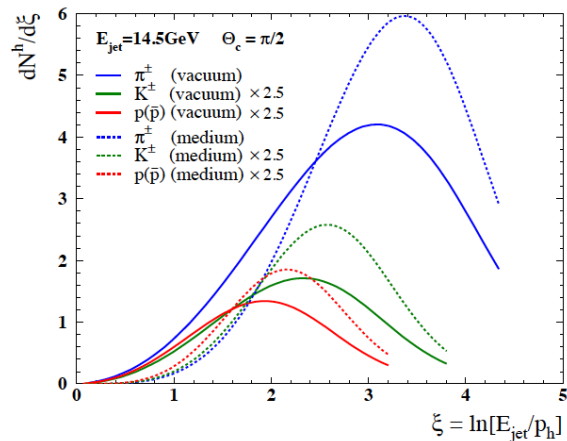


Figure 1.24: Shown are the results of a perturbative parton shower calculation in the MLLA formalism and using the model of Sapeta, Wiedemann [88]. Figure adapted from [88].

complex description with only little guidance from theory, it can demonstrate in a simplified way how medium-modifications could express themselves for jet observables and when considering results for identified particles.

In the following section we review several existing results in heavy-ion collisions that consider identified light-flavour particle production. Afterwards a brief outlook on existing measurements of identified hadrons in the environment of jets is given.

## 1.8 Identified light-flavour particle production in heavy-ion collisions

Several kind of analysis techniques, that are using identified particles, are able to give insight into medium-modifications in heavy-ion (HI) collisions.

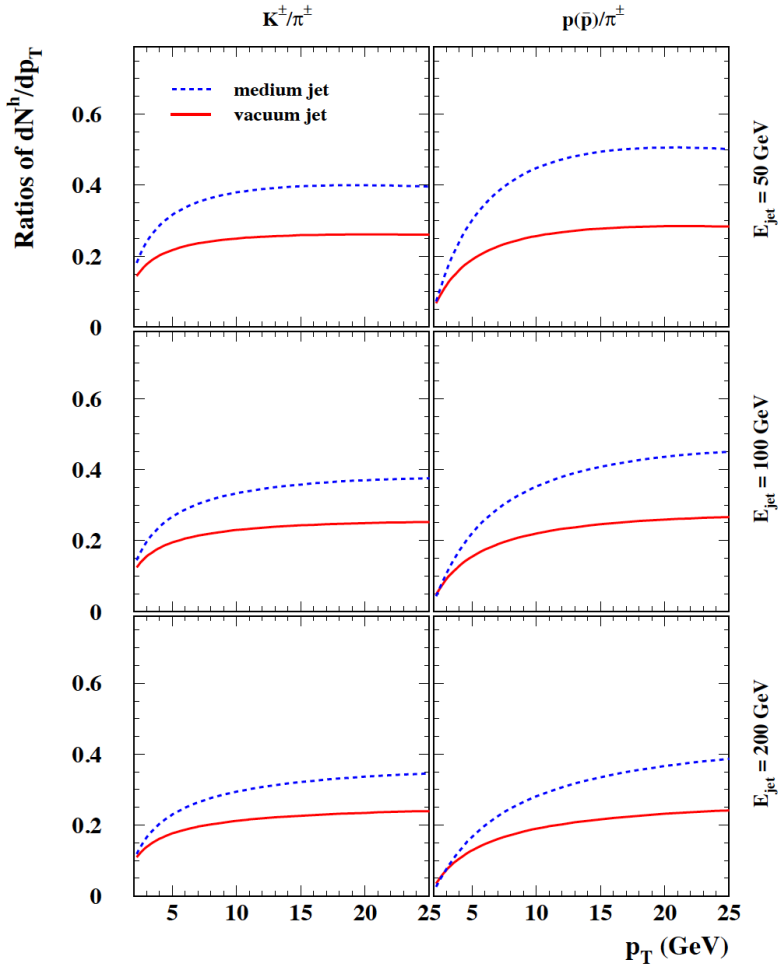


Figure 1.25: Results of the MLLA+LPHD formalism for the particle ratios  $K^\pm/\pi^\pm$  and  $p(\bar{p})/\pi^\pm$  in jets as obtained from enhanced parton splitting [88]. Figure adapted from [88].

One possible way is to study ratios of particle  $p_T$  spectra, like the baryon-to-meson ratios, which exhibit a high enhancement around intermediate ( $p_T \sim 2\text{--}5$  GeV/c) values of the hadron transverse momentum. The first observation of this effect was made in the STAR experiment at the RHIC collider, which collides gold nuclei at  $\sqrt{s_{NN}} = 0.2$  TeV, (see right plot in Fig. 1.26).

At the LHC this baryon-to-meson enhancement was seen as well at much larger energy  $\sqrt{s_{NN}} = 2.76$  TeV (see same Fig. left plot). When measuring the ratio in different centrality intervals, the enhancement is larger for the most central collisions (red markers), while it is less pronounced for the most peripheral collisions (black markers) or when obtained from pp data (purple markers). However at high- $p_T$  ( $\gtrsim 6\text{--}8$  GeV/c) the particle ratios among the different centrality intervals and also between Pb–Pb and pp are in agreement. From this one would conclude that hard parton fragmentation is not sizably affected by medium-modifications. The measurements are compared to model calculations (right plot) from a hydrodynamic model [93] that includes recombination [95] and the EPOS<sup>10</sup> model [96].

<sup>10</sup>EPOS a is an energy conserving mechanical multiple scattering approach that is based on an initial parton model [97, 98]. It describes jets, hydrodynamically expanding bulk matter and the interaction

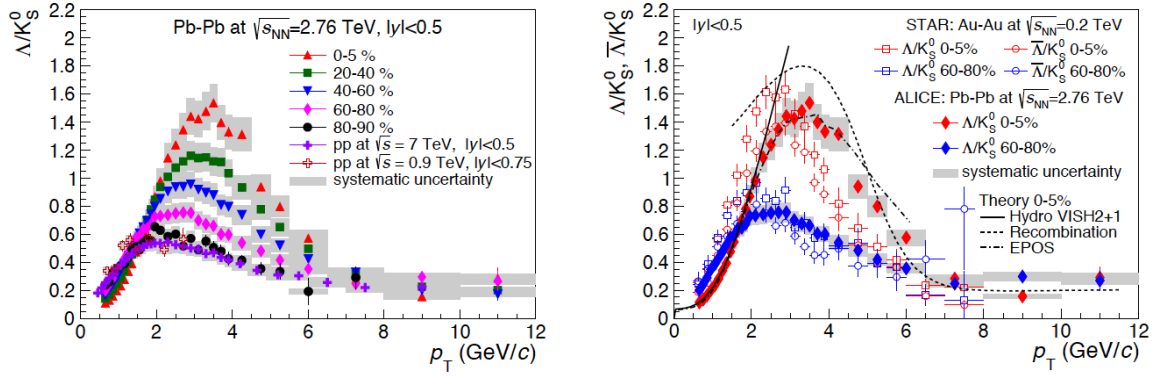


Figure 1.26: Inclusive  $\Lambda/K_S^0$  ratio as measured by the STAR [91] experiment (right side, open markers) and by ALICE at the larger energy of  $\sqrt{s_{NN}} = 2.76$  TeV (left side) [92]. Compared are the measurements to model calculations from a hydrodynamical model [93, 94], one describing recombination [95] and the EPOS model [96].

At low  $p_T$  (until  $\sim 2$  GeV/c) the hydrodynamic model gives a good description of the  $\Lambda/K_S^0$  ratio, for higher  $p_T$  (from around 2 GeV/c until upper limit of model calculations) however it is far away from the measurement.

Figure 1.27 shows the  $p/\pi$  ratio (left panel for the particles, right panel for the anti-particles) in the 0-12% central (black filled markers) and 60-80% peripheral (triangular red markers) Au+Au collisions and in d+Au collisions (blue open markers) at  $\sqrt{s_{NN}} = 200$  GeV measured by PHENIX [99, 100]. At intermediate  $p_T$  the ratios strongly depend on the event centrality. The most central collisions reveal the known baryon enhancement and are above unity, while the (60-80%) peripheral collisions show a less pronounced enhancement and are in agreement with the ratio from d+Au collisions. At high  $p_T$  ( $> 5$  GeV/c) the ratio from central collisions in Au+Au decreases and is also in agreement with the result from d+Au collisions. The dashed-and-dotted line is the  $(p+\bar{p})/(\pi^++\pi^-)$  ratio from light quark jets in  $e^++e^-$  collisions at  $\sqrt{s} = 91.2$  GeV, as measured by DELPHI [101], which is far below all measured ratios in Au+Au and d+Au collisions. It is slightly closer to the measurements at RHIC at the highest  $p_T$  intervals but is still below and not in agreement. Several model calculations are compared to the measured data. The fine-dotted (pink) line is from a parton *recombination* model [102] and the (black) dotted line from a calculation that models the hadronisation as *coalescence*, while also considering jet quenching and using a parametrisation of *KKP* fragmentation functions (FFs) by [104], that are leading and next-to-leading order particle identified FFs (driven by measured data from ALEPH [105], DELPHI [106], OPAL [107] and SLD [108]). As can be seen, the recombination and coalescence models are able to describe the baryon enhancement, while they don't give a good description at higher  $p_T$  (starting from around  $p_T > 5-6$  GeV/c).

An idea to explain the baryon-to-meson ratio enhancement via different hadronisation mechanisms for the low and high- $p_T$  particle range is presented in appendix A. This model [109] by R. J. Fries, B. Müller and C. Nonaka considers particle production for hadrons with  $p_T \lesssim 4-5$  GeV/c to be dominated by recombination of quarks from the

between them.

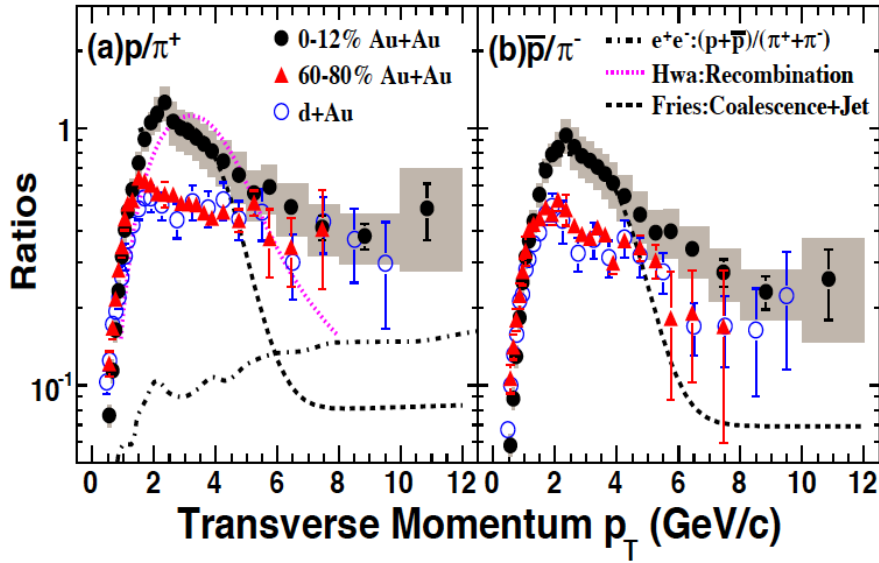


Figure 1.27:  $p/\pi$  ratio in d+Au and Au+Au collisions at  $\sqrt{s_{NN}} = 200$  GeV measured by PHENIX [99, 100]. Dotted line is the  $(p+\bar{p})/(\pi^++\pi^-)$  ratio from light quark jets in  $e^++e^-$  collisions at  $\sqrt{s} = 91.2$  GeV [101]. Dashed-and-dotted line is a model calculation by [102, 103] for central Au+Au events.

densely populated phase-space within the plasma. For hadrons with higher  $p_T$  ( $\gtrsim 5$  GeV/c) the model assumes string fragmentation as the dominant hadronisation mechanism. The particles at low  $p_T$  follow a thermal momentum distribution while at larger  $p_T$  they are distributed according to a perturbative power law function. A combination of these two could describe measured data by PHENIX at  $\sqrt{s_{NN}} = 200$  GeV/c and reproduce e.g. the characteristic shape of the proton-to-pion ratio.

Fig. 1.28 shows the centrality dependence of the primary charged (identified) particle  $R_{AA}$  [70] as measured by ALICE. The left side shows the  $R_{AA}$  measurements from Pb–Pb collisions at  $\sqrt{s_{NN}} = 2.76$  TeV in 0-5% central events for different identified particles. On the right side the results for more peripheral (60-80% centrality) events are shown. The upper plot shows the  $R_{AA}$  for charged pions, for protons and kaons and also for all charged particles. In the bottom plot the  $R_{AA}$  for kaons and the one for protons is shown. The  $R_{AA}$  shows the largest particle suppression ( $\sim 0.13$ ) for the most central collisions, while for more peripheral collisions particles seem to be less suppressed ( $\sim 0.6$ - $0.7$ ) for  $p_T \gtrsim 4$ - $5$  GeV/c. Concerning the shape of the  $R_{AA}$  in the most central collisions, hadrons with  $5 \gtrsim p_T \gtrsim 10$  GeV/c appear to be highly suppressed, while at very high  $p_T$  ( $> 15$  GeV/c) particles partially recover from the suppression. The latter observation could hint on the scenario that particles at very high momentum are almost entirely produced by fragmentation in which baryon production is not enhanced (supporting the model picture of R. J. Fries, B. Müller and C. Nonaka [109]). One furthermore can see that baryons at intermediate  $p_T$  seem to be less suppressed compared to mesons what leads to the baryon anomaly seen in the particle ratios.

The charged particle  $R_{AA}$  (in Fig. 1.28) for  $p_T \gtrsim 2$  GeV/c in the most central events

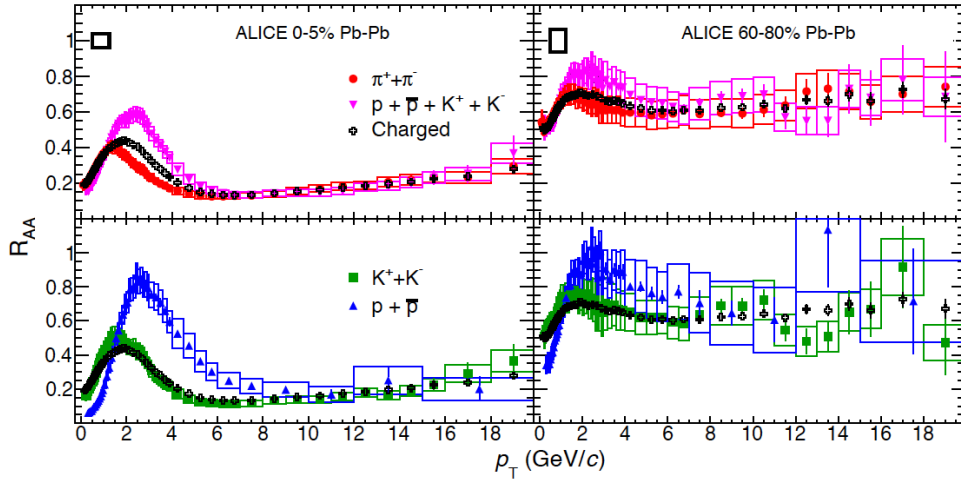


Figure 1.28: Light flavour  $R_{AA}$  measurements from Pb–Pb collisions at 2.76 TeV in 0-5% central and 60-80% peripheral events for identified particles and different particle types shows a dependence on the particle mass [110]. For the most central collisions and at intermediate hadron  $p_T$  the mesons show a stronger suppression than the baryons.

indicates a large suppression which might hint on a huge energy loss for all hadrons in the first place. The suppression at higher hadron  $p_T$  ( $\gtrsim 8-10$  GeV/c) could be also attributed to jet quenching, i.e. high- $p_T$  particles stemming from fragmentation of hard scattered (initial state) partons, that have suffered energy loss while traversing the medium. On the other hand, this could also be due to reduced particle production in this  $p_T$  interval or absorption within the medium. Interestingly the particle-type dependence of the  $R_{AA}$  seems to be absent for the high- $p_T$  interval, while for smaller  $p_T$  a clear mass-ordering is observed. One has to keep in mind that the values of  $R_{AA}$  at very low particle  $p_T$  ( $\lesssim 2$  GeV/c), which are smaller than 1, are expected since soft particle production scales rather with  $N_{\text{part}}$  than with  $N_{\text{coll}}$  (see also [111] for more details).

Contemplating these results, one needs to keep in mind for any interpretation that the measurements are considering hadronic observables, which are not straight forwardly transferable into those of partons that are governing the situation before the freeze-out and the hadronisation took place. Therefore realistic hydrodynamical expansion models and transport models need to be developed, which enable to extract the characteristic thermodynamic properties of the plasma.

Figure 1.29 presents predictions from a viscous hydrodynamic model [112] that can well reproduce the ALICE measurements of  $v_2$  in 40-50% central events for different particle types. It confirms the measured mass ordering of the strength of  $v_2$  at low hadron  $p_T$ . The same mass dependent effect was also seen in the  $R_{AA}$  measurements of  $\Lambda$  baryons and  $K_S^0$  mesons as measured in [113]. To study this mass difference, various particle types have been compared to each other [110], as can be seen in Fig. 1.28. The particle ratio measurements are motivated by the following idea: In case the hydrodynamical flow might cause the baryon enhancement it should act differently on the particle mass and modify the spectral shapes accordingly, this in turn should be also visible in the shape of the particle ratios. If collective flow "shifts" e.g.  $\Lambda$  particles to higher  $p_T$  but  $K_S^0$  particles to

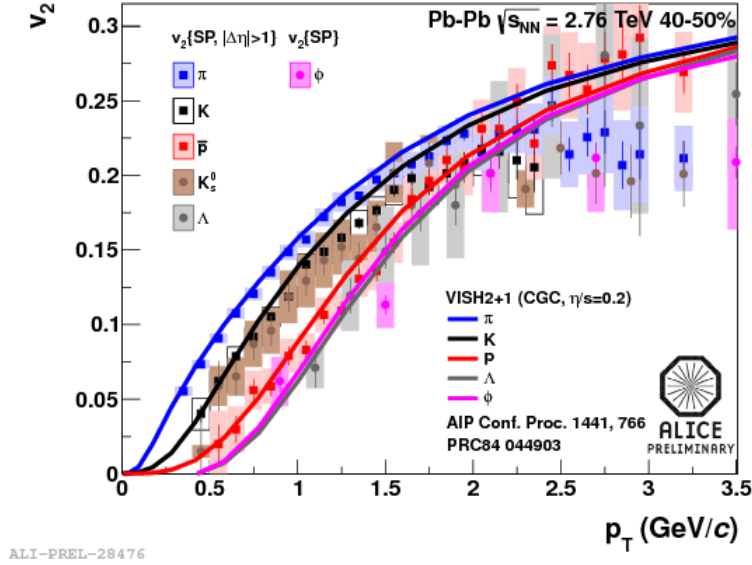


Figure 1.29: Elliptic flow measurement in 40-50% central events for different particle types can be well described by viscous hydrodynamical models [112].

a less strong extent (due to the smaller mass) the ratio from particles with more equal masses should be less affected by  $v_2$ , which indeed can be seen in the ALICE particle ratio measurements shown in Fig. 1.30 (for a better comparability the  $p/\phi$  ratio is multiplied by 0.1). This could hint at the scenario that the baryon enhancement (up to  $p_T \sim 2.5$  GeV/c) is (partially or fully) due to collective effects.

In summary, the observed suppression of particle production in heavy-ion collisions at RHIC and LHC show both a strong dependence on the hadron transverse momentum and, at intermediate  $p_T$ , also a dependence on the hadron mass. To explain these different measurements several interpretations are possible that are considering different ranges of the hadron  $p_T$ . Among these interpretations there is the proposal of different hadronisation mechanisms, the mass-ordering caused by collective flow and energy loss of hard partons in the medium, that suppresses particle production at larger  $p_T$ . In order to disentangle these ideas more differential studies are required what can be e.g. provided by the study of identified particles in the environment of a jet. The observation by CMS [9] and ATLAS [10] of medium-modified fragmentation functions (of unidentified particles) was seen for the first time. It indicates that jets are not only suppressed but the fragmentation pattern is also affected. By studying these modifications more information about the surrounding medium might be achieved. An even more differential analysis could study e.g. a modification of the jet constituents concerning their hadrochemical composition and compare among the different collision systems. This follows the idea of a model by S. Sapeta and U. Wiedemann that showed a modification of the particle type composition inside a jet via increased parton splitting in presence of a medium [88]. A brief overview about already existing measurements in this field are presented in the following section.

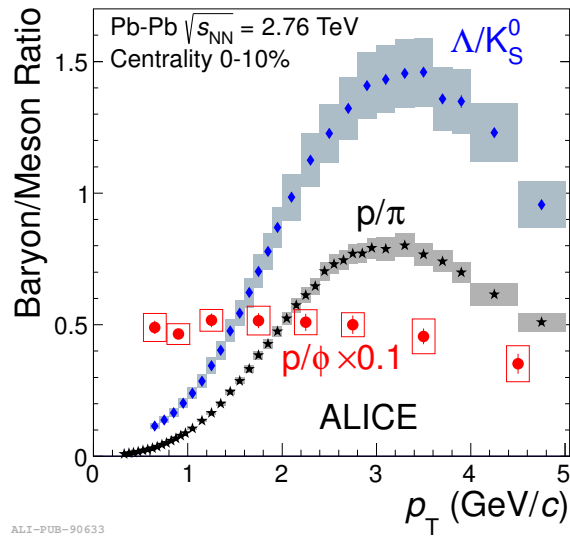


Figure 1.30: Comparison of  $p_T$ -dependent baryon-to-meson ratios measured in central (0-10%) Pb–Pb collisions at  $\sqrt{s_{NN}} = 2.76$  TeV:  $\Lambda/K_S^0$  [92],  $p/\pi$  [4, 114] and  $p/\phi$  [115]. Figure adapted from [116].

## 1.9 Analysis of identified particles in a jet-like environment

From the various measurements like the nuclear modification factor  $R_{AA}$ , elliptic flow  $v_2$  and particle ratios from A+A collisions it becomes evident that final state effects in heavy-ion collisions have a huge impact on the physics observables. So far hints on the origins of these modifications are found but no clear picture is yet gained.

The observations of the modified FFs by CMS and ATLAS [10] raise the question how the modifications might change for different particle species in jets. Since in the  $R_{AA}$  measurements at low particle  $p_T$  the huge contribution of hadrons from the Underlying Event (i.e. not produced via fragmentation of hard scattered partons) makes the study of modifications in this energy range impossible, other analysis techniques are needed. The observed baryon enhancement in inclusive A+A collisions leads to the question whether this enhancement is still visible inside a jet, where particle production via fragmentation is dominating and flow effects are expected to be absent. This motivates further analysis, studying more differential observables like identified hadron  $p_T$  spectra in jets or hadron-jet correlation techniques to disentangle hadronisation mechanisms.

The analysis technique of particle correlations provides an alternative to analyses that employ jet reconstruction and is used so far in several existing measurements at RHIC and the LHC.

Jet reconstruction provides a measure that is "closer" to the initial (hard-scattered) parton observables concerning transverse momentum (corresponding to  $p_T^{\text{jet}}$ ) and angular direction (in terms of  $\eta$  and  $\phi$  of the reconstructed jet axis) than requiring a single high- $p_T$  particle as a "proxy" for the jet. The high- $p_T$  particle serves to trigger on "jet-like" regions inside the event and is therefore also called "trigger" (particle). With respect to this trigger other

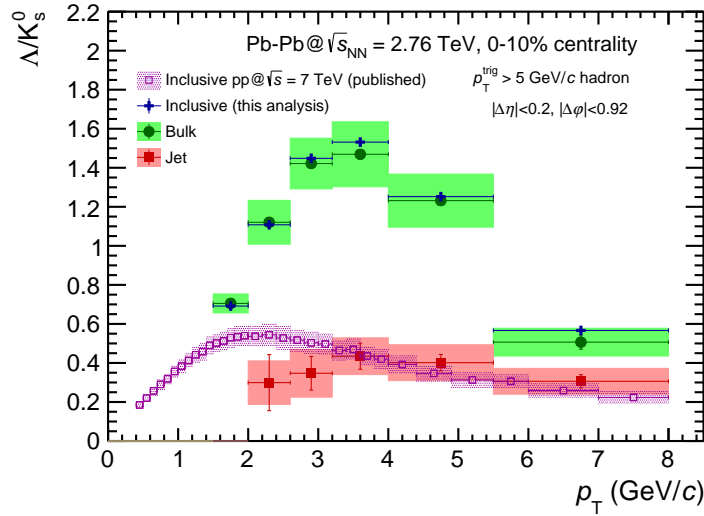


Figure 1.31:  $\Lambda/K_S^0$  ratio as a function of the  $V^0$   $p_T$  with *eta-gap* correlation technique that associates  $\Lambda$  and  $K_S^0$  particles with high- $p_T$  trigger hadrons. (Figure adapted from T.Richert, thesis [117]).

identified hadrons can be reconstructed and selected according to a certain geometrical requirement close to the trigger (“near-side”) or on the opposite side in azimuthal direction (“away-side”).

This correlation technique however is a more simple approach that does not require jet reconstruction and the corresponding necessary corrections (see section 3.2 for more details about jet reconstruction and the corrections). But it also might impose a bias on the selection of “jet-like” regions, in which a high- $p_T$  “trigger” particle is found. Furthermore the “trigger” could select preferably jets fragmenting with a certain pattern (“fragmentation bias”) and therefore (quenched) jets consisting of only soft constituents are not selected. One such study is currently under preparation for publication, using data from ALICE. Figure 1.31 shows the  $\Lambda/K_S^0$  ratio in a jet-like environment from the so-called “ $\eta$ -gap” method as described in [117]. The study is based on the same data set that was used also for the analysis presented in this thesis. The red markers describe the  $\Lambda/K_S^0$  ratio in the environment of the high- $p_T$  trigger ( $p_T^{\text{hadron}} > 5$  GeV/c) with a distance between  $V^0$  hadron and trigger particle of  $|\Delta\phi| = |\phi_{V^0} - \phi_{\text{trig}}| < 0.92$ . The Underlying Event  $V^0$  subtraction is done by reflecting the  $V^0$  sampling region (w.r.t.  $|\eta_{\text{trig}}|$ ) in  $\eta$  and sampling  $V^0$  candidates in a window with the same size.

The resulting particle ratio in the near-side of the trigger hadron (red markers, referred to as “Jet”) is shown in red markers. The one measured “away-side” is shown in green markers and labeled as “Bulk”.

Another hadron- $V^0$  correlation study (using charged high- $p_T$  hadrons with  $3 < p_T < 6$  GeV/c as trigger particles) was recently published by the STAR collaboration (see Fig. 1.32). The obtained data point for the  $(\Lambda + \bar{\Lambda})/2K_S^0$  ratio in jet-like correlation in the 60% most central events in Cu+Cu collisions shows no significant deviation from the inclusive measurement in pp collisions (at the same energy). This provides evidence that this correlation is dom-

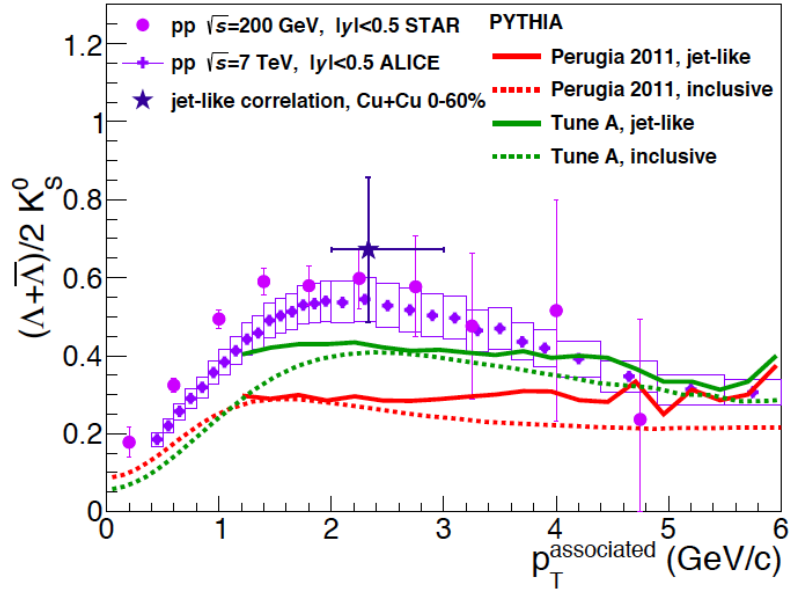


Figure 1.32:  $(\Lambda + \bar{\Lambda})/2K_S^0$  ratio measured by STAR in di-hadron correlations with identified strange associated particles in 0-60% most central Cu+Cu collisions at  $\sqrt{s_{NN}} = 200$  GeV. Figure adapted from [118].

inated by particle production via fragmentation.

A first measurement in ALICE using reconstructed jets, instead of single high- $p_T$  trigger, was made by combining charged reconstructed jets together with a method to identify particle types inside the jet:

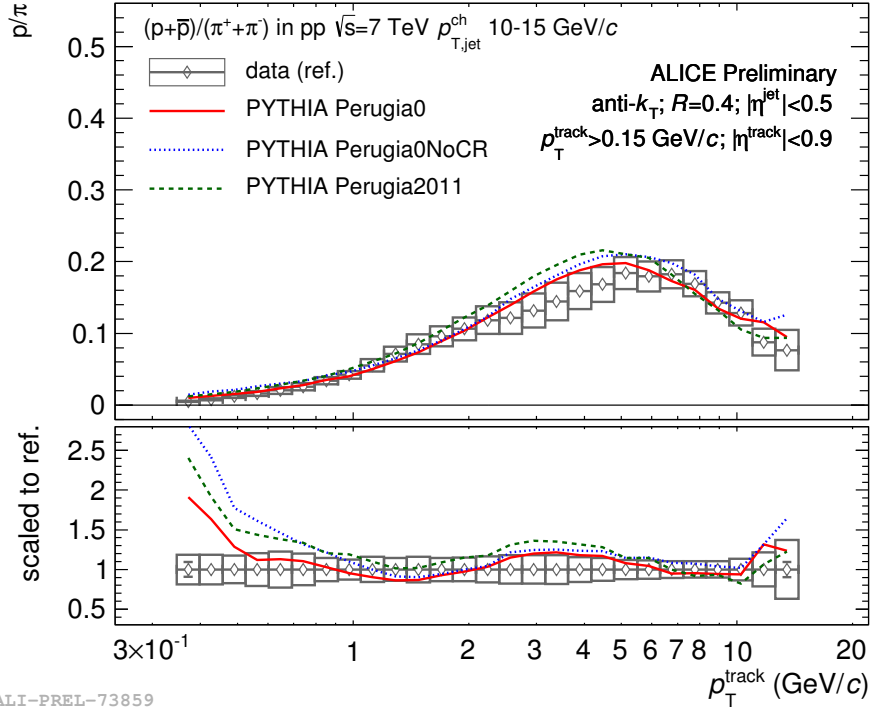
Figure 1.33 shows the first measured  $p/\pi$  particle ratio in jets [119, 120] in pp collisions at  $\sqrt{s} = 7$  TeV with ALICE.

The  $p/\pi$  particle ratio is plotted as a function of  $p_T$  in charged jets from the interval  $10 < p_T^{\text{jet}} < 15$  GeV/c. The particle identification is made using the TPC  $dE/dx$  information of the charged (identified) hadrons and associating them with reconstructed jets from charged tracks.

Such measurements will serve as a reference for future analyses of this kind in Pb–Pb collisions and could be carried out for all charged particle types, that provide a TPC  $dE/dx$  signal.

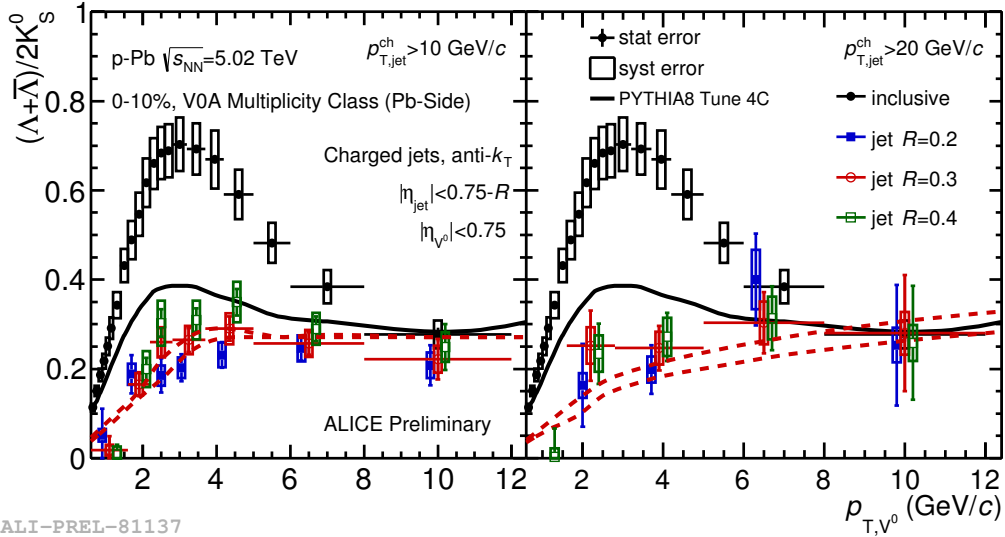
The analysis presented in this thesis focuses also on particle identification (PID) inside cones around reconstructed charged jets. The measurement is made by the analysis of the  $K_S^0$ , the  $\Lambda$  and  $\bar{\Lambda}$  hadrons inside and outside the jet in the 10% most central Pb–Pb events at  $\sqrt{s_{NN}} = 2.76$  TeV. It is the first measurement of identified particles inside jets in Pb–Pb collisions at such high energies.

A very similar analysis strategy was already used for the ALICE measurement of the  $(\Lambda + \bar{\Lambda})/2K_S^0$  ratio in jets in p–Pb collisions. The analysis uses events in the 0-10% “V0A” multiplicity class interval (Pb-Side) of p–Pb data measured at  $\sqrt{s_{NN}} = 5.02$  TeV. Figure 1.34 shows the result of this analysis in p–Pb events at 5.02 TeV and in the 10%



ALI-PREL-73859

Figure 1.33:  $p/\pi$  particle ratio as a function of  $p_T$  in charged jets from the interval  $10 < p_T^{\text{jet}} < 15$  GeV/c and measured in pp collisions at  $\sqrt{s} = 7$  TeV. The result is compared to PYTHIA simulations. Figure adapted from [119, 120].



ALI-PREL-81137

Figure 1.34:  $(\bar{\Lambda}+\Lambda)/2/K_S^0$  ratio in jets in p–Pb collisions (for different values of  $R$ ) for  $p_T^{\text{jet}} > 10$  GeV/c (left panel) and  $p_T^{\text{jet}} > 20$  GeV/c (right panel) and compared to inclusive particle ratio in the 0-10% V0A multiplicity class interval (Pb-Side) in p–Pb collisions (black markers) and to the expectation from a PYTHIA 8 4C simulation at 5.02 TeV (dotted lines, showing spread for the used values of  $R$ ) [121, 122]. Figure adapted from [123].

highest multiplicity class. It is compared to the inclusive  $\Lambda/K_S^0$  ratio (solid lines) in p–Pb collisions and to the ratio predicted by PYTHIA 8 4C simulations at  $\sqrt{s_{NN}} = 5.02$  TeV (dotted lines, showing spread for the used values of  $R$ ). The measured ratio in jets shows no visible enhancement at intermediate  $p_T$  and is far below the inclusive ratio. Within the systematic uncertainties, the ratio in jets is in agreement with the PYTHIA simulations. Furthermore there is no significant dependence on the  $p_T^{\text{jet}}$  interval or on the jet cone size  $R$  visible.

In chapter 4 we compare the results of the current work also to this measurement in p–Pb collisions.



## Chapter 2

# Experimental access

This second chapter gives an overview about the experimental set-up of ALICE (A Large Ion Collider Experiment) [124–126] situated at the [127], [128], [129], [130] (Large Hadron Collider).

### 2.1 The Large Hadron Collider

The LHC accelerator is part of the scientific research facility at CERN (Conseil Européen pour la Recherche Nucléaire) in Switzerland and is illustrated in Fig. 2.1. It is designed for high luminosities and high beam intensities at very high collision energy. Eight arcs and eight straight sections build the 26.7 km long LHC accelerator that is located in the underground tunnel of the former LEP [131] (Large Electron Positron Collider) accelerator. To achieve these high collision energies (for proton beams the top energy is  $\sqrt{s} = 14$  TeV, for lead ion beams it is  $\sqrt{s_{NN}} = 5.52$  TeV) and for the usage of proton beams, high magnetic fields ( $B \sim 8.33$  T) are required. This made the development of superconducting dipole magnets necessary that can guide two oppositely directed beams of either protons or ions on their way along the LHC beam-line and to the interaction points (IP) where the various experiments are located. The injection energy into the LHC is 450 GeV that is provided by the Super Proton Synchrotron (SPS). Several more pre-accelerators are used to feed the SPS with either protons ( $H^+$ ) or lead nuclei (ions). Protons are accelerated by the LINAC2 (that is a linear accelerator), then by a circular accelerator BOOSTER, the Proton Synchrotron (PS) and injected into the SPS. Lead nuclei are first accelerated by LINAC3, then by LEIR (Low Energy Ion Ring) followed by PS and SPS. The beams are distributed in a set of bunches that are spaced in length and distance to match the radio-frequency (RF) cavities of 400 MHz. For pp beams at top energy the LHC design values are luminosities of the order  $10^{34} \text{ cm}^{-2} \text{ s}^{-1}$ , the beam is divided into  $1.15 \cdot 10^{11}$  bunches separated by a bunch spacing of 25 ns. The bunches are organised in trains (each one containing a set of up to 72 bunches) for injection into the LHC. The lead nuclei are designed for luminosities of the order of  $10^{27}$  and distributed into  $7 \cdot 10^7$  bunches, each bunch separated by a spacing of 100 ns from the next one. The LHC has two separate RF systems which make it possible to inject protons in one beam-pipe and lead nuclei into the oppositely directed second beam-pipe. In the area around the IPs both

## CERN's Accelerator Complex

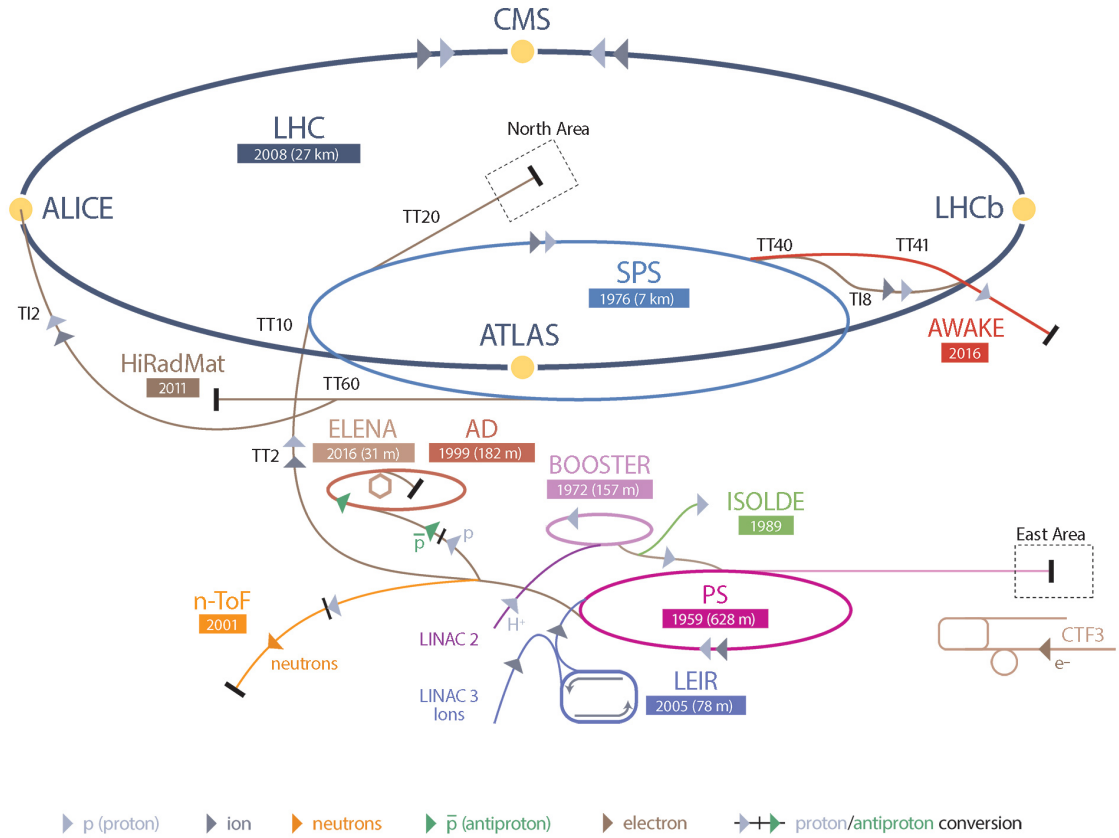


Figure 2.1: LHC complex with injector chain and interaction points (yellow points). Where the two oppositely directed beams intersect, the 4 largest experiments are ALICE, CMS, LHCb and ATLAS are located. Several pre-accelerators are required to reach the final LHC collisional energy [132].

separated beam-pipes are combined into one and the beams can be moved (in transverse direction) via magnetic fields and brought into collision. The four largest LHC experiments are ATLAS (A Toroidal LHC Apparatus for Spectroscopy) at IP1, CMS (Compact Muon Solenoid) at IP5, LHCb at IP8 and ALICE (A Large Ion Collider Experiment) at IP8.

ATLAS [133] was designed for the search of the Higgs boson and physics beyond the standard model (e.g. SUSY i.e. detection of supersymmetric particles, black holes, etc.). It consists of a solenoid magnet close to the collision point and a toroidal magnet positioned at larger distance to the beam-pipe. ATLAS is equipped with an inner tracking system close to the beam pipe, with silicon pixels and a transition radiation detector for tracking. Electromagnetic and hadronic calorimeters use liquid argon and scintillators for particle identification, particle momentum and energy measurement. A huge muon chamber system for tracking and triggering is installed as well.

CMS [134] has similar physics goals as ATLAS. It consists of a huge superconducting solenoid

oid that encloses the inner tracking system, the electromagnetic and hadronic calorimeters. The muon chambers are installed within the return yoke of the big solenoid magnet. LHCb [135] focuses on heavy-flavour physics. One of the main goals is the search for new physics in CP violation and rare decays of hadrons with beauty and charm quark content. LHCb is a single-arm spectrometer with a dipole magnet of 4 Tm. Close to the collision point a vertex locator is positioned that allows precise tracking and secondary vertex reconstruction. The spectrometer furthermore consists of Ring Imaging Cherenkov (RICH) detectors, electromagnetic and hadronic calorimeters and a set of muon chambers at a larger distance ( $\sim 15\text{--}20$  m) from the interaction point. ALICE is described in detail in the following section.

## 2.2 ALICE at the LHC

ALICE [136] is a general purpose experiment which has been designed to study the properties of strongly interacting matter and the Quark Gluon Plasma created in heavy-ion collisions. The high multiplicity of tracks present in central Pb–Pb collisions requires a detector setup that allows fast reconstruction of all tracks to enable event by event analyses. Furthermore detection of global event properties like the event centrality and the event plane is needed as input for physics analyses. Since most of the particles created in heavy-ion collisions are situated at low momentum, the tracking and particle identification abilities of the detector setup have to perform with good resolution down to very low transverse momentum (starting from around  $p_T \sim 150$  MeV/c). The detector is composed into a central barrel detector enclosing the collision point and surrounded by the L3 solenoidal magnet (that was inherited by the former L3 experiment at LEP) and a forward muon-spectrometer.

The right-handed orthogonal cartesian coordinate system used to indicate positions in the ALICE detector is shown in Fig. 2.2. The origin is placed at the interaction point (IP2). The  $z$  axis is parallel to the LHC mean beam direction and points along LHC beam 2. The  $x$  axis is perpendicular to the beam direction and pointing (approximately) to the LHC accelerator center and the  $y$  axis is perpendicular to the  $x$  axis and pointing (approximately) upwards. The azimuthal angle  $\phi$  increases from the  $x$  axis and is zero when pointing along the  $x$ -axis.  $\theta$  is the polar angle between the charged particle and the beam axis  $z$ .

An overview of the detector sub-systems is shown in Fig. 2.3. The central barrel detectors are the Inner Tracking System (ITS) [138], the Time Projection Chamber (TPC) [139, 140], the Transition Radiation Detector (TRD) [141], the Time-Of-Flight Detector (TOF) [142], the Photon Spectrometer (PHOS), the Electromagnetic Calorimeter (EMCal), the Di-jet Calorimeter (DCal) and the High Momentum Particle Identification Detector (HMPID). An event display recorded from a Pb–Pb collision event is shown in Fig. 2.4, it demonstrates the high particle multiplicity in central collisions that produce up to several thousand tracks.

The central barrel serves to determine particle observables like the transverse momentum

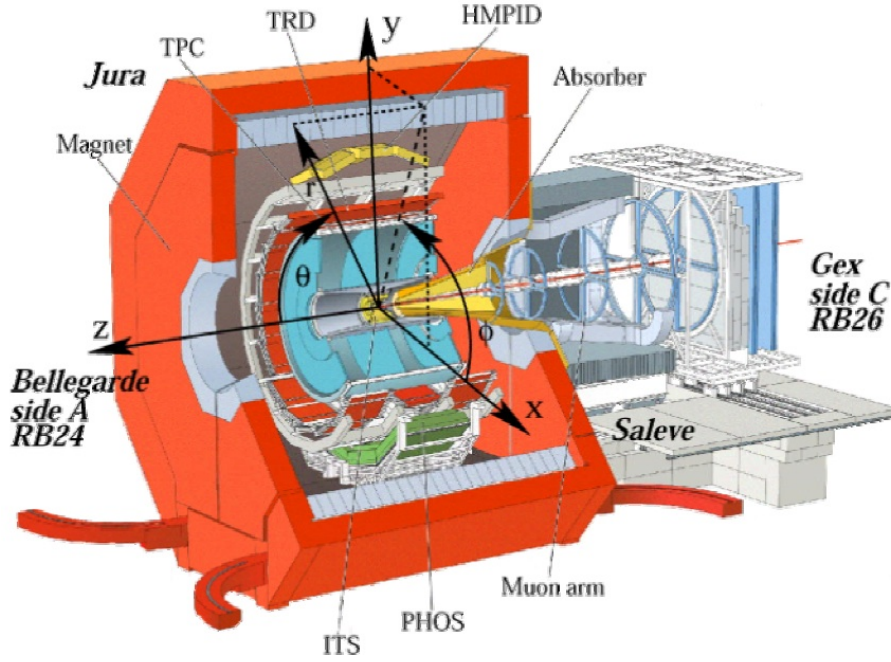


Figure 2.2: Definition of the coordinate system axis and the angles in ALICE [137].

( $p_T$ ) and pseudo-rapidity ( $\eta$ ) of the particles traversing it. The pseudo-rapidity is defined as:

$$\eta = -\ln\left(\tan\frac{\theta}{2}\right) \quad (2.1)$$

where  $\theta$  is the polar angle with the beam axis  $z$ .  $\eta$  can also be written in dependence of the longitudinal ( $p_L$ ) momentum and the total momentum  $p$  of the particle:

$$\eta = \frac{1}{2} \ln\left(\frac{p + p_L}{p - p_L}\right) \quad (2.2)$$

where  $p_T$  is the projection of the particle momentum  $p$  on the  $x$ - $y$  plane. In the following the sub-detectors are described which are relevant for the physics analysis presented in this thesis. More information about the ALICE sub-detectors and their performance can be found in [122].

### 2.3 Inner Tracking System (ITS)

The Inner Tracking System [138] (ITS) is located close to the beam-pipe and consists of six detector layers, grouped into 3 detectors: the Silicon Pixel Detector (SPD), the Silicon Drift Detector (SDD) and the Silicon-Strip Detector (SSD). Together with TPC and TRD it is one of the main detectors used for charged particle track reconstruction.

The acceptance of the ITS covers  $|\eta| < 0.9$  (for interaction vertices within  $|z| < 5.3$  cm) and the full azimuth, the first pixel layer covers an even larger window in pseudo-rapidity  $|\eta| < 1.98$  (for interaction vertices at  $z = 0$ ). The ITS allows to measure the primary event vertex and secondary vertices with high precision and contributes to the global tracking

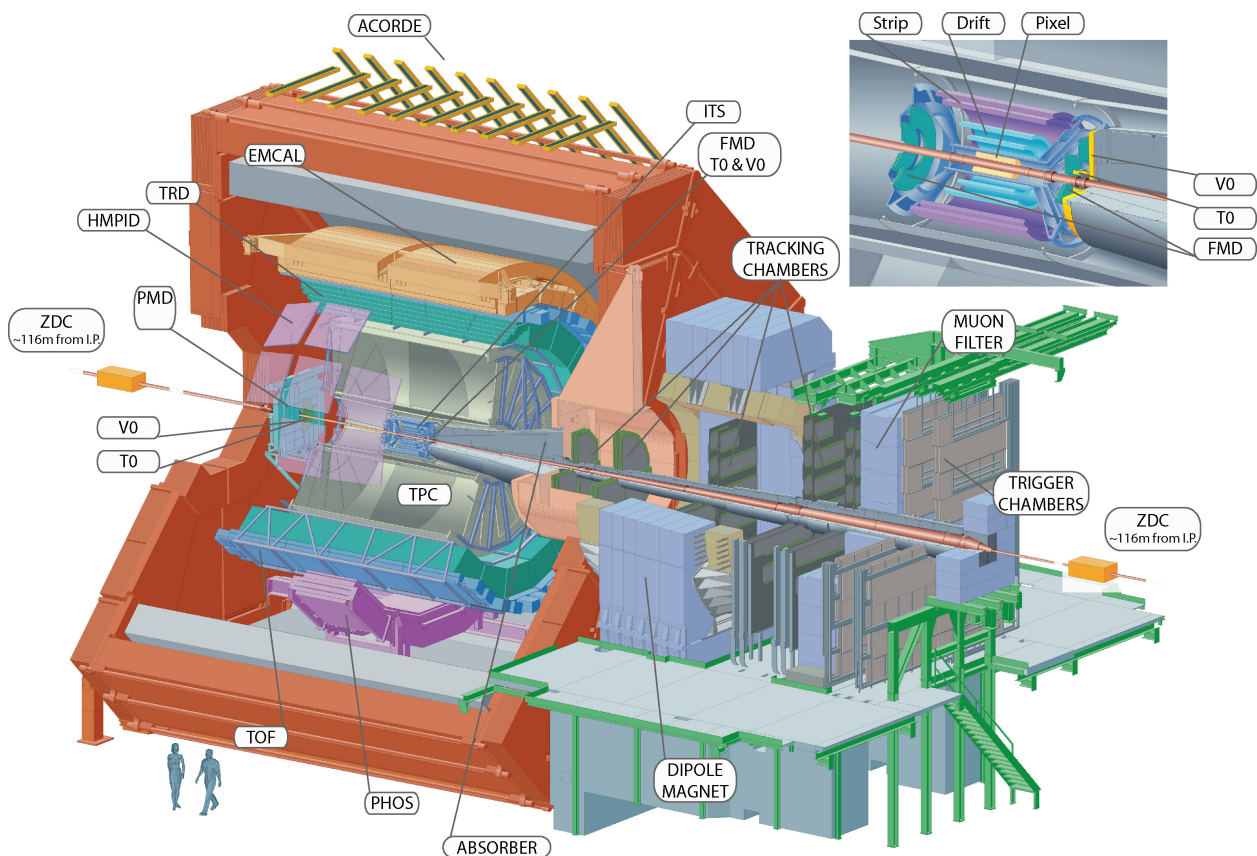
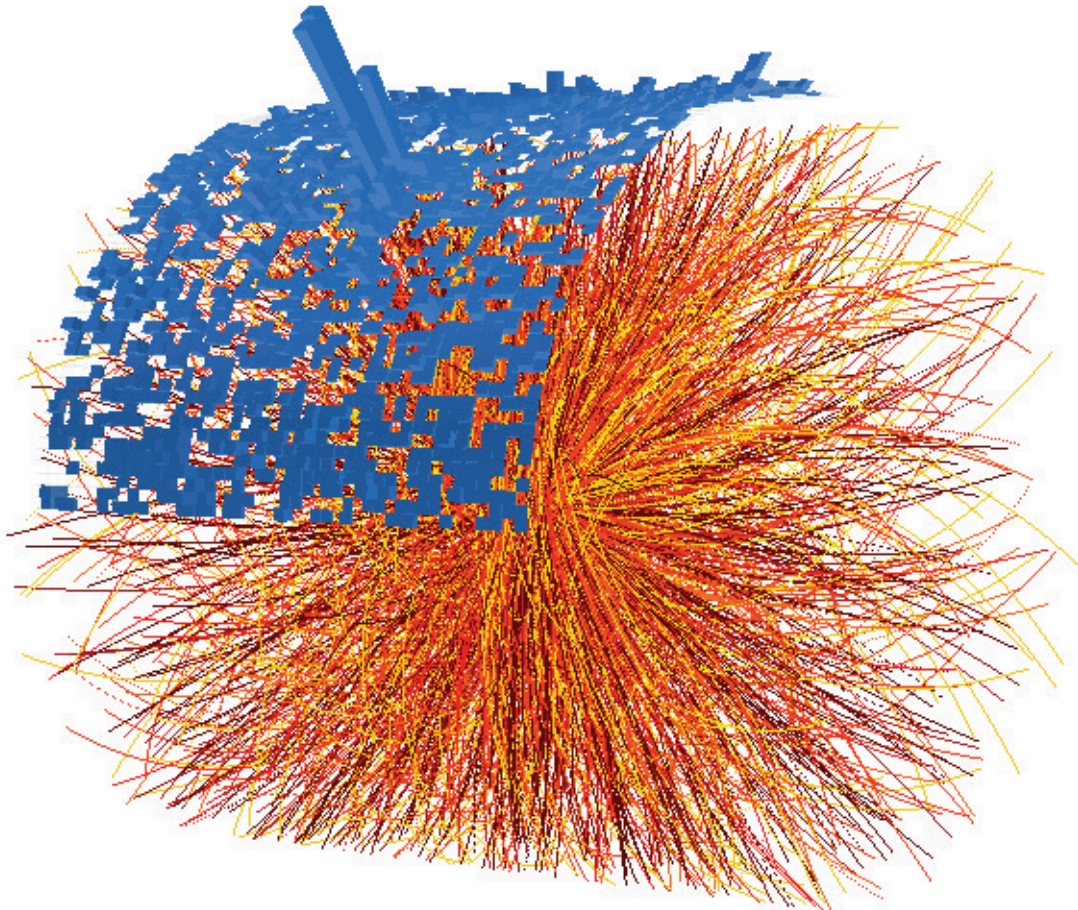


Figure 2.3: The ALICE detector at the CERN LHC. Shown are several sub-detectors of the central barrel at mid-rapidity (ITS, TPC, TRD, TOF, PHOS, EMCAL and HMPID) and in the forward-rapidity region (PMD, FMD, V0, T0 and ZDC). They are surrounded by a solenoid magnet providing a 0.5 T longitudinal magnetic field. The muon-spectrometer is located in forward direction.



ALI-PUB-72702

Figure 2.4: A Pb–Pb collision event recorded in ALICE at  $\sqrt{s_{\text{NN}}} = 2.76$  TeV. Several thousand charged particles are produced in one collision that are recorded by the various detector systems. Neutral particles are visible as (blue) calorimeter towers on top, where the Electromagnetic calorimeters are installed. The reconstructed charged particle tracks within the central barrel detector are visible as reddish-yellow trajectories.

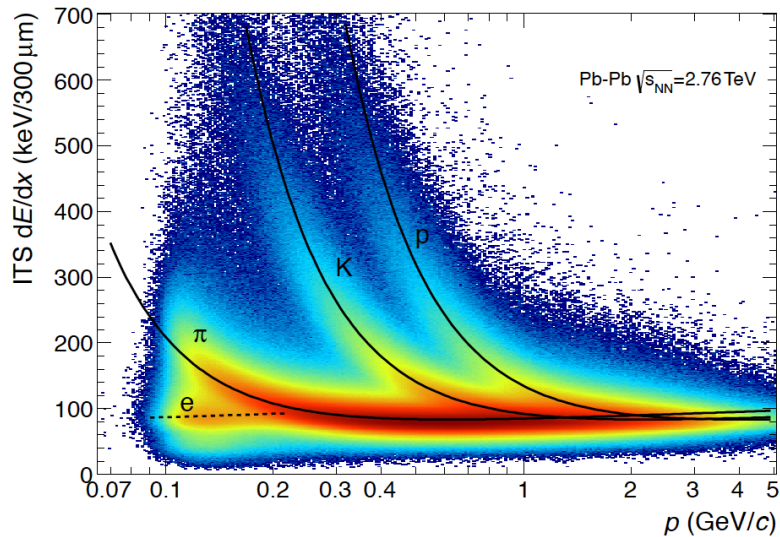


Figure 2.5: Energy loss distribution in the ITS as a function of the particle momentum [136].

and reconstruction of the event. The first two layers consist of silicon pixels with high granularity that are positioned in a distance w.r.t the beam-line of 3.9 and 7.6 cm. The SSD layers are double-sided micro-strip detectors that help to align the reconstructed tracks with the Time Projection Chamber (TPC). For tracks not reconstructed by the TPC (e.g. because the track falls into an insensitive region of the TPC support structure), the ITS tracking information enables the global tracking for these tracks that otherwise would have been lost for physics analysis like presented in this thesis.

The four inner layers provide 2-dimensional tracking, that enables to deal with track densities up to  $90 \text{ tracks}/\text{cm}^2$  (at the position of the two outermost layers the track density is lower and a 1-dimensional read-out is sufficient instead). The outer four layers (located at radii from 15.0, 23.9, 38.0 and 43.0 cm distant from the beam-line) provide an analog read-out to measure the energy loss  $dE/dx$  of particles traversing it [136]. The distribution of the particle energy loss as a function of the particle momentum  $p$  is shown in Fig. 2.5. The energy loss distribution in the ITS shows how particles of different types, especially with low particle momentum (down to  $\sim 100\text{-}200 \text{ MeV}/c$ ) can be identified and distinguished from each other using their  $dE/dx$  information<sup>11</sup>.

## 2.4 Time Projection Chamber

The TPC is the main tracking device in the central barrel detector. Its main goal is to provide charged track reconstruction in the transverse momentum range of  $0.1 < p_T < 100 \text{ GeV}/c$  and Particle Identification (PID) up to  $p_T \sim 20 \text{ GeV}/c$ . It covers  $|\eta| < 0.9$  for charged tracks traversing the full TPC, for tracks only partially reconstructed inside

<sup>11</sup>In this momentum range no TPC  $dE/dx$  information is available since the tracks don't reach the TPC because of their strong track curvature.

the TPC (i.e. that are not reaching the outer TPC radius) an acceptance of  $|\eta| < 1.5$  is covered, however with a reduced momentum resolution.

The TPC consists of a cylindrical barrel with a length of 5 meters (along the beam direction), an outer radius of 280 cm and an inner radius of about 80 cm w.r.t the beam-line. The inner radius of the active gas volume is at 84.1 cm, the outer radius is located at 246.6 cm. The inner radius is determined by the maximum acceptable hit density that can be processed, the outer radius by the minimum track length which is needed to get a good  $dE/dx$  resolution (the geometrical design of the TPC is shown in Fig. 2.6). It is furthermore divided into two half volumes by a central electrode (cathode) which have together a drift volume of about  $95 \text{ m}^3$ . Together with the anodes the central HV electrode (which is on 100 kV w.r.t. the endplates of the TPC barrel) provides the electrical drift field to guide the created ionization (which consists of electrons) to the read-out pads on both sides of the TPC. The end plates are equipped with multi-wire proportional (MWPC) chambers, in which the signal of the primary ionization is amplified and read out as a electrical current. A maximum of 159 pad-rows can be read-out to reconstruct one particle track. The endplates are, like all central barrel sub-detectors, divided into 18 trapezoidal sectors. In between the trapezoid sectors the TPC is insensitive to tracking which makes about 10% of the full azimuthal acceptance.

The inner volume is filled with a gas<sup>12</sup> mixtures of  $Ne-CO_2-N_2$  [90-10-5] (until the year 2011, from 2012 on it was a mixture of  $Ne-CO_2$ ). The maximum drift time in this mixture is about  $95 \mu\text{s}$ . The momentum resolution is about 7% (at 10 GeV/c) and the  $dE/dx$  resolution about 5%.

In between the MWPC and the drift volume another plane of wires is installed, this is the *TPC gate* which can be put under negative potential w.r.t. the central electrode. It serves as a barrier for all charges drifting out of the amplification region. Most of the time it is closed to avoid ions from the amplification region entering the drift region. In case of triggered interesting events the gate is opened to let electrons from ionisation from the drift volume enter into the amplification region. [139], [143].

A distribution of the TPC  $dE/dx$  signal as a function of the rigidity  $\frac{p}{z}$  is shown in Fig. 2.7. The different particle types are visible as bands that are well described by the ALEPH parametrization [140] of the Bethe-Bloch curve.

For the  $\Lambda$  and  $\bar{\Lambda}$  particles (in the range  $p_T < 2.0 \text{ GeV}/c$ ) studied in this analysis, the TPC PID information is used to identify the (anti-)proton daughter which are stemming from the  $\Lambda$  decay.

## 2.5 VZERO detector

The VZERO detector [144] consists of two segmented discs (V0A covering  $2.8 < \eta < 5.1$  and V0C covering  $-3.7 < \eta < -1.7$ ) of scintillator counters that are read-out by optical fibers and positioned close around the beam-pipe. The VZERO serves as an online

<sup>12</sup>The choice of using Neon instead of Argon (the latter is a rather common choice for a counting gas) is to reduce multiple scattering effects in the gas and to increase the ion mobility (since Argon is more heavy than Neon), and thereby reduce the (positive) space charge in the drift volume.

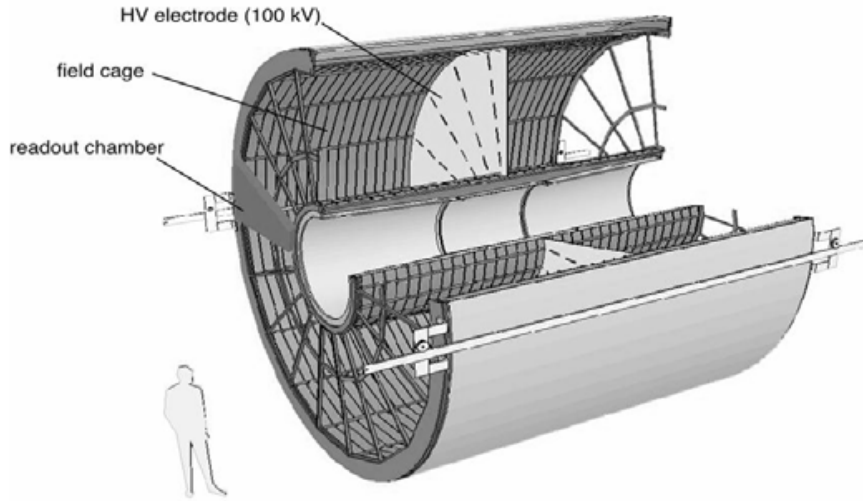


Figure 2.6: ALICE Time Projection Chamber. Together with the anodes on both sides of the TPC barrel, the central HV electrode (which is on 100 kV w.r.t. the endplates of the TPC barrel) provides the electrical drift field to guide the created ionization to the read-out pads on both sides of the TPC.

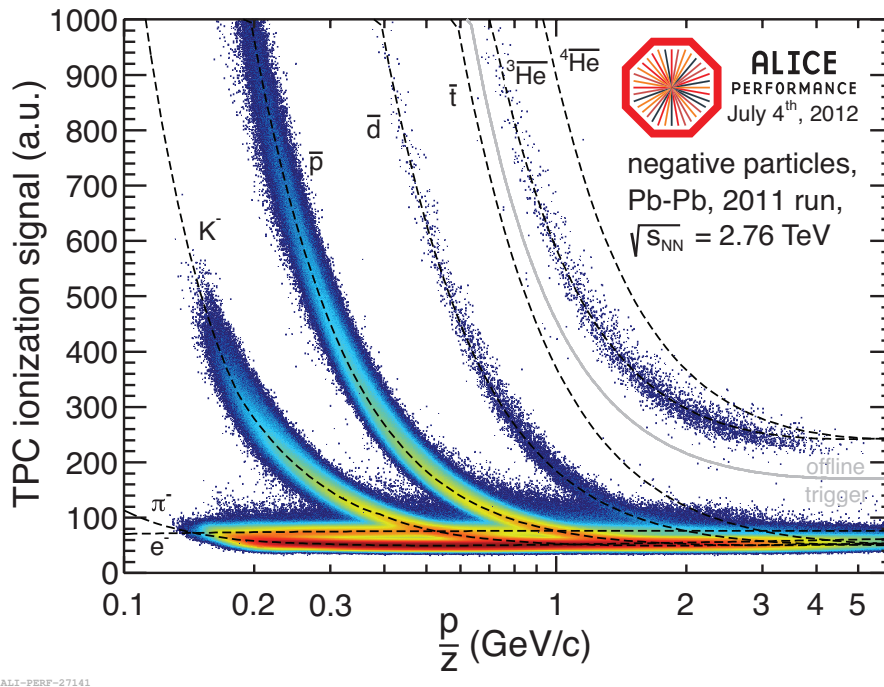


Figure 2.7: TPC specific energy loss  $dE/dx$  as a function of the rigidity  $\frac{p}{z}$ . The most probably value for the mean energy loss per particle type and momentum is derived with the ALEPH parametrisation [140] of the Bethe Bloch curve [136].

trigger whose trigger requirement is defined as an energy threshold of particles coming from the interaction point and passing through the scintillator paddles. It furthermore serves to reconstruct the event plane angle (see section 2.9 for more details on event plane reconstruction) in heavy-ion collisions and helps to determine the event centrality (see section 2.8 about centrality determination).

## 2.6 Zero Degree Calorimeters (ZDC)

The Zero Degree Calorimeters [145] (ZDC-A covering  $2.8 < \eta < 5.1$  and ZDC-C covering  $-3.7 < \eta < -1.7$ ) are located on the opposite sides of ALICE inside the LHC tunnel and in a distance of  $\pm 116$  m from the interaction point. Each ZDC consists of two modules: one neutron calorimeter and one detecting protons. The nucleons are called spectators since they did not interact during the collision (see also section 2.8). The protons are separated from the neutrons by magnetic elements inside the beam-line and are detected by a neutron calorimeter. The protons that are deflected via magnetic fields from their original trajectory reach the proton calorimeter. The ZDC detectors work with quartz fibre calorimetry. The centrality estimated with ZDC has a resolution of  $\sim 1\%$  in most central collisions and about  $3\%$  in mid-central events [146].

## 2.7 Detectors for Particle Identification

The central barrel detector system combines signals from several detectors in order to identify particles. They are the already described ITS and TPC, furthermore the Transition Radiation Detector (TRD) [141], the Time-Of-Flight detector (TOF) [142], the High-Multiplicity Particle Identification Detector (HMPID) [147], the Electromagnetic and Di-Jet Calorimeter (EMCAL and DCAL) [148]. The TOF provides particle identification (PID) in the range  $0.5 < p_T < 4.0$  GeV/c which overlaps with the PID  $p_T$  range of the TPC and extends it to larger  $p_T$  values. The HMPID provides PID for high- $p_T$  particles with  $3.0 < p_T < 5.0$  GeV/c. The Calorimeters EMCAL and DCAL identify electrons and neutral pions via two-photon decay and are also used for the full reconstruction of jets (via charged and neutral jet constituents) and as an online jet trigger. The TRD enables electron-pion separation for  $p_T > 1.0$  GeV/c and can also be used as a trigger for high- $p_T$  hadrons and electrons from heavy quarks.

## 2.8 Centrality determination

The centrality is directly related to the initial overlap of the two colliding nuclei via the impact parameter  $b$  (as shown on the left side in Fig. 2.8) i.e. via the fraction of the geometrical cross-sections that overlap  $\frac{\pi b^2}{\pi(2R)^2}$ , with  $R$  the nuclear radius.  $b$  is defined as the distance between the centers of the two colliding nuclei in the  $x$ - $y$  plane transverse to the beam axis  $z$ . The number of nucleons inside the nuclei which undergo one or more interactions during the nucleus-nucleus collision, are called the number of participants  $N_{part}$ , those which are not participating are called the spectators  $N_{spec} = 2A - N_{part}$  (see Fig. 2.8

right panel). The most central collisions are given when the nuclei perfectly overlap during the collision, which produces a maximum number of participants. For the most peripheral collisions the impact parameter is large and only few nucleons participate in the interaction.

Since it is not possible to measure  $b$  directly, it has to be determined e.g. via Glauber Monte Carlo simulations [149] that relates the impact parameter to experimental observables.

The Glauber model assumes that the colliding nucleons are not deflected and are moving on straight line trajectories during the entire collision process. It furthermore assumes that the nucleus is much larger than the nucleon-nucleon force and that the motion of the nucleons is independent from the nucleus, in order to describe the total cross-section in terms of the nucleon-nucleon cross-section. The input observables to the Glauber model is the inelastic nucleon-nucleon cross-section and the density profile of the nucleus. The latter can be described by the Wood-Saxon distribution  $\rho(r)$ :

$$\rho(r) = \frac{\rho_0(1 + wr^2/R^2)}{1 + \exp((r - R)/a)} \quad (2.3)$$

as a function of  $r$ , the distance from the nucleus center. The parameters  $a$  (represents the “skin thickness” that describes how quickly the nuclear density falls off near the edge of the nucleus) and the  $R = 1.25 \text{ fm} \cdot A^{1/3}$ .  $w$  is a parameter describing nuclei whose maximum density is at  $r > 0$ , for Pb  $w = 0$ . The parameters only depend on the charge distribution of the nucleus and can be determined via  $e^-$ -nucleus scattering [150]. For the Pb nucleus that has the mass number  $A = 208$ ,  $R$  is  $\sim 6.62 \text{ fm}$  and  $a$  is  $\sim 0.546 \text{ fm}$ .

The Monte Carlo implementation [151] of the Glauber Model simulates many collision processes, for each of them a random  $\mathbf{b}$  is selected from the geometrical distribution  $dP/db \sim b$  up to a maximum impact parameter (at almost the double radius of the Pb nucleus)  $b_{\max} \simeq 20 \text{ fm}$ . Two nuclei are assumed to undergo a collision if the relative transverse distance of the center of both nuclei is smaller than the distance corresponding to the inelastic nucleon-nucleon cross section  $d < \sqrt{\sigma_{\text{NN}}^{\text{inel}}/\pi}$ .  $N_{\text{part}}$  and  $N_{\text{coll}}$  are derived by counting the number of nucleons that participated at least once in a collision and accordingly the binary nucleon collisions  $N_{\text{coll}}$ .  $\sigma_{\text{NN}}^{\text{inel}} = (64 \pm 5) \text{ mb}$  for Pb–Pb at  $\sqrt{s_{\text{NN}}} = 2.76 \text{ TeV}$  is derived from an interpolation of pp data at different values of  $\sqrt{s}$  and from cosmic ray data [152].

The geometrical overlap function  $T_{\text{AA}}$  (that is needed e.g. for the estimation of the nuclear modification factor) is calculated by  $T_{\text{AA}} = N_{\text{coll}}$  and represents the effective nucleon luminosity in the collision process.

Experimental observables used to estimate the centrality are e.g. the charged-particle multiplicity  $N_{\text{ch}}$  (which increases monotonically with the impact parameter  $b$ ) as measured with VZERO, SPD and TPC, or the energy carried by the spectators close to the beam direction (which decreases for more central collisions) and can be measured in the ZDC detector.

For the centrality estimation in the current analysis the centrality estimation method by

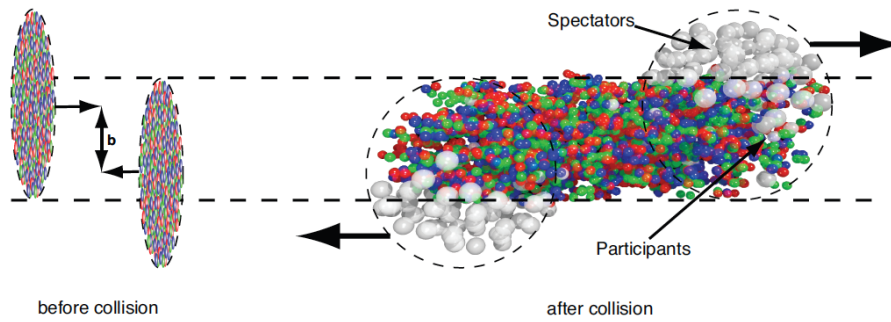


Figure 2.8: The left sketch illustrates two heavy-ion nuclei briefly before the collision that is characterised by their impact parameter  $b$ . On the right side the nuclei are colliding inelastically, all nucleons affected by the collisions are called “participants”, those continuing their trajectory bound in the remnant of the original nucleus are called “spectators”. They can serve to estimate the centrality of the event e.g. with help of the ZDC detector signal (Fig. adapted from [57]).

the VZERO detectors is used. The charged particles in forward direction and passing the VZERO scintillators induce a signal amplitude proportional to the multiplicity.

Figure 2.9 shows the VZERO signal amplitude distribution in which the different centrality classes are indicated by different areas.

The distribution peaks at small amplitudes corresponding to the most peripheral collisions (e.g. for the 80-90% centrality class), for increasing amplitude followed by a plateau and ending with an edge for the most central collisions (which are the 0-5% most central events). The “NBD Glauber” fit, shown in the graphic as a red line, is based on the Monte Carlo implementation of the Glauber model with the assumptions described above and together with a particle production model that is based on a negative binomial distribution (NBD). With this phenomenological approach charged-particle multiplicity distributions can be simulated and fitted to the experimental multiplicity in order to estimate the geometrical properties of the collision with a certain centrality. Furthermore the fit is needed to define a so-called “Anchor Point” (AP) (that is positioned at very small VZERO amplitude), where electromagnetic interactions contribute and the trigger efficiency is decreasing. The AP determines a certain centrality value until where the event selection is fully efficient and no contamination of background interactions (e.g. caused by electromagnetic processes) is present. The resolution of this centrality estimation from the VZERO detectors is  $\sim 0.5\%$  for the 20% most central collisions and smaller than 2% for the more peripheral collisions (within the 20-80% centrality class).

## 2.9 Event plane determination

Figure 2.10 shows the case of two nuclei that are colliding with a certain impact parameter  $b$ . The line connecting the centers of the nuclei and the beam axis (into the paper) defines the reaction plane  $\psi_{\text{RP}}$  and as introduced in section 1.4. The initial overlap of the nuclei

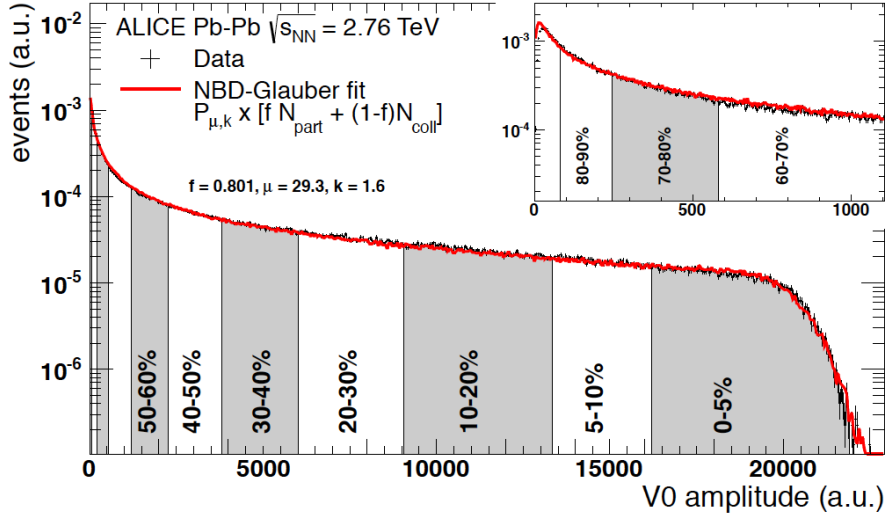


Figure 2.9: Distribution of the sum of the amplitudes in the VZERO scintillators in Pb–Pb collisions at  $\sqrt{s_{\text{NN}}} = 2.76$  TeV. By integration of the signal from the right to the left, the different centrality intervals can be defined. The VZERO signal amplitude (corresponding to the charged-particle multiplicity in forward direction) is fitted by a function from a NBD-Glauber model calculation [149]. Figure adapted from [149].

results in a spatial anisotropy of the interaction zone that translates into a momentum anisotropy of the produced particles in the final state.

$\psi_{\text{RP}}$  can be only reconstructed approximately (e.g. with the VZERO detectors) due to interactions within the produced matter. In practice  $\psi_{\text{RP}}$  is replaced by the so-called  $n$ -th harmonic “event plane”  $\psi_n$  that can be estimated e.g. from the anisotropic azimuthal distribution of particles that is expressed by a Fourier expansion:

$$\rho(\phi - \psi_n) = \frac{1}{2\pi} \left( 1 + 2 \sum_{n=1}^{\infty} \nu_n \cos[n(\phi - \psi_n)] \right) \quad (2.4)$$

in which  $\nu_n$  is the  $n$ -th order flow coefficient (see also section 1.4) and  $\phi$  is the azimuthal angle of the reconstructed particle momentum. Due to its fine granularity in azimuthal direction the VZERO detector is used to measure the azimuthal particle distribution  $\rho(\phi)$ . The resolution  $\mathcal{R}_{\psi_n}$  of the event plane estimation can be determined e.g. via sub-event correlation techniques [154] and is used for the resolution correction. The event plane resolution of the 2nd order harmonic event plane for the 10% most central Pb–Pb events at  $\sqrt{s_{\text{NN}}} = 2.76$  TeV is  $\mathcal{R}_{\psi_2} \sim 0.47$ . The event plane resolution is best for semi-central events ( $\sim 20$ -30% centrality) in which the anisotropic flow due to the initial overlap of the nuclei is largest and reaches a resolution of  $\sim 60$ -75%.

## 2.10 Track reconstruction

The charged track finding in the central barrel is done in several steps by the procedure shown in Fig. 2.11 and by using the “Kalman-filtering” method [155]. With this Kalman

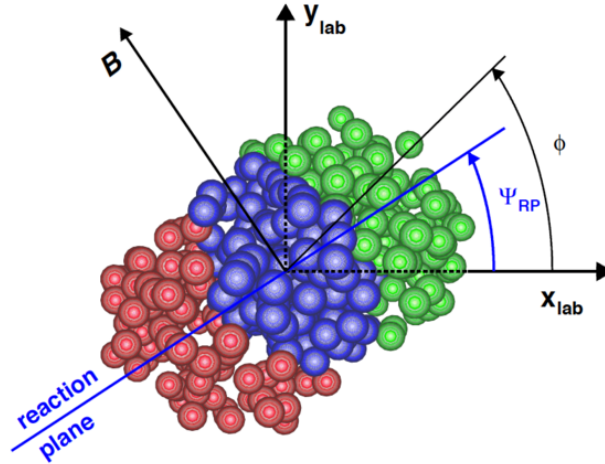


Figure 2.10: View of a semi-central nucleus-nucleus collision in beam direction. The line connecting the centers of the nuclei and the beam axis (into the paper) defines the reaction plane  $\psi_{RP}$ . Figure adapted from [153].

filter a track inside the TPC is reconstructed in a subsequent procedure in which incorrect clusters can be automatically rejected during the online tracking. For each reconstructed track a “state vector” is defined, which provides a “measurement matrix” in which all information of the fitting procedure is stored and updated after each step. The Kalman filter provides a local track estimate that contributes to the finding of a global track that is including information from several sub-detectors. Between the sub-detectors a matching is done to prolongate the track finding from one sub-detector into the adjacent one. The track finding and fitting is done in an inwards-outwards scheme [156, 157].

First the data measured by a sub-detector is converted into clusters. This is done separately for each sub-detector. Each cluster contains all specific information like the spatial information, signal amplitudes and the timing information and their associated errors. Then the preliminary primary interaction vertex is reconstructed by only using clusters in the two layers of the SPD. The preliminary vertex serves as the starting point of the following tracking procedure (and serves also as an important “anchor point” for the global track finding).

Only tracks with at minimum 20 TPC clusters out of 159 (corresponding to the maximum number of TPC pad-rows) are accepted. This tracking is proceeded to the ITS where the reconstructed track from the TPC starts as a seed for the fit of the ITS clusters. The fitting is proceeded into direction of the preliminary vertex until it is reached. Afterwards the tracks are refitted back in outwards direction (towards the TPC) using the already obtained tracking information. Then also TRD tracklets (which are track segments within a TRD layer) and TOF information can be used to prolongate the tracking to external detectors like the EMCAL, HMPID or the PHOS. The information at larger radii than

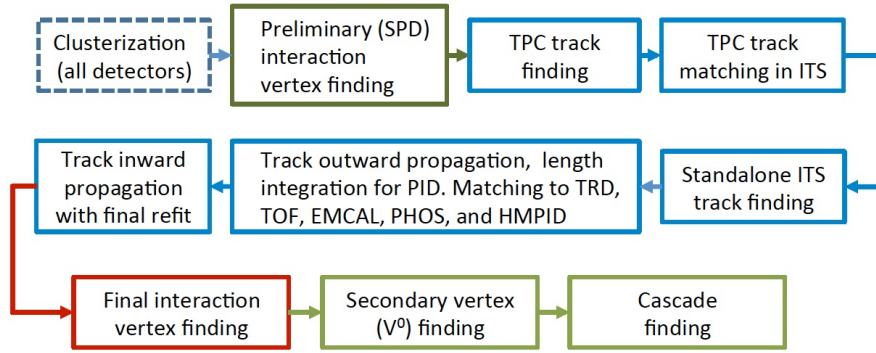


Figure 2.11: The event reconstruction in the central barrel detector system is done in several steps[136]

the TPC is not required for the track reconstruction of charged particles but stored for particle identification. A final refit of the global tracks in inwards direction is made (the so-called “TPCrefit” or “ITSrefit”) and the final primary interaction vertex is determined. More detailed information about this tracking method can be found in [155, 157].

## 2.11 Reconstruction of secondary vertices

Secondary vertices that stem from photon conversions ( $\gamma \rightarrow \pi^+ + \pi^-$ ) and particle decays are reconstructed as illustrated in Fig. 2.12. For this all tracks, that cannot be extrapolated to the primary vertex (i.e. all charged tracks with a minimum distance of closest approach (DCA) to the interaction vertex) are used. All pairs of opposite charge are combined to form a  $V^0$  particle candidate. Secondary vertices correspond e.g. to weak decays for which the decay vertex has a sizable distance from the primary vertex. The current analysis focuses on the  $V^0$  particles, more details about the  $V^0$  particle selection from the candidates are given in the following chapter 3 in section 3.1.

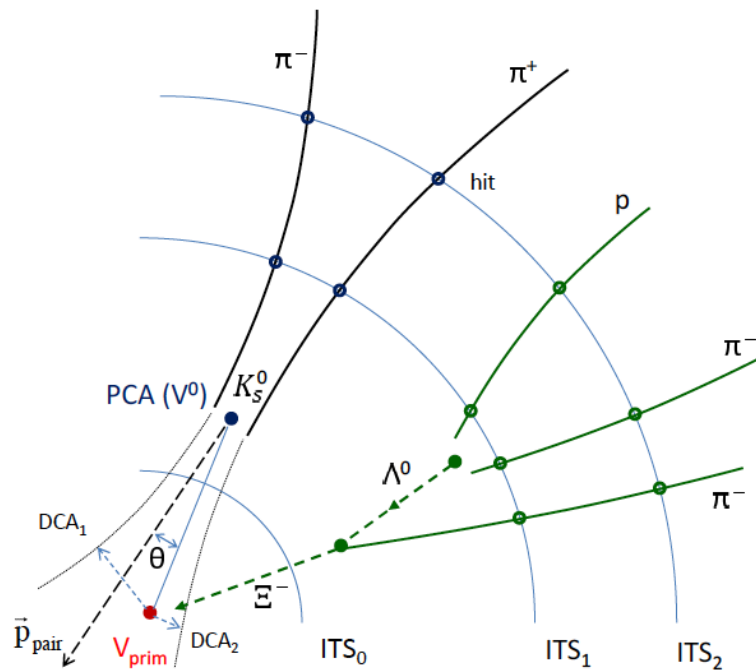


Figure 2.12: Secondary vertex reconstruction in the first two layers of the ITS. The reconstructed charged daughter tracks are drawn as solid lines, the dashed lines are extrapolations to the primary vertex and represent the  $V^0$  particles. Also shown is an example for a cascade particle decay ( $\Xi^-$ ) [136]. Figure adapted from [136].

## Chapter 3

# Analysis of strange particles in jets in Pb-Pb collisions

Having discussed the physics motivation for studying the characteristics of heavy-ion collisions, the special potential of hard probes to study the quark gluon plasma and after the brief overview of the experimental setup, this chapter presents in detail the analysis strategy. We start with the principle of  $V^0$  particle reconstruction to obtain the inclusive strange particle  $p_T$  spectra and continue with an excursion on the experimental reconstruction of particle jets and how jets are defined in the context of the current work. Afterwards we will come to the most important part of the analysis, the measurement of the strange particles inside the jet cones, and the corrections needed to separate hadrons originating from the hard scattering process from the soft background, the so-called "Underlying Event" (UE) (that makes the majority of all particles produced in a Pb-Pb collision). The following chapter 4 presents and discusses the results of this measurement and compares to the results in pp and p-Pb collisions by ALICE. The last chapter 5 gives a brief summary and concludes on the observations.

### 3.1 Reconstruction of the $V^0$ particles

Before the neutral  $K_S^0$ ,  $\Lambda$  and  $\bar{\Lambda}$  particles can be reconstructed and analysed, some more general requirements (described in section 3.1.1) have to be imposed on the collision events that are selected for this analysis. This data quality selection is described in this first section, before the analysis of the  $V^0$  particles is explained in more detail in section 3.1.4.

#### 3.1.1 Analysis software

The analysis is performed with software tools that are commonly used for the data analysis of the LHC experiments and adapted to the geometry and characteristics of the ALICE Experiment. The "ALICE Off-line framework" (AliRoot) is used for the simulation, reconstruction and the data analysis. The framework and all applications are based on the data analysis software ROOT and written in C++. Furthermore, GEANT3.21 is used to provide a realistic detector simulation which describes the full detector response

on the Monte-Carlo (MC) data that is the basis for all correction procedures applied to the uncorrected measurements. The jet reconstruction is done with the software package "FastJet" that contains a set of commonly used jet reconstruction algorithms, such as the anti- $k_t$  or the  $k_t$  algorithm (more details about the jet reconstruction are given in 3.2).

### 3.1.2 Data

The data used for this analysis have been recorded by the ALICE experiment in the year 2011. The numerous particles which are created in Pb–Pb collisions are stored event-by-event in the AOD (Analysis Object Data) format. The AOD is a compressed file which contains the most important physical observables on the collision event together with reconstructed  $V^0$  particles, charged jets, all charged tracks and, if needed, it contains more specialised branches carrying information according to the analysis purpose. The advantage of this file format is the smaller memory usage when compared to the larger file format ESD ("Event Summary Data") which is the extended version of the AODs. The ESD files are sometimes used in ALICE physics analyses in case of an even more detailed selection of events or particles.

Two data sets of measured and simulated minimum bias<sup>13</sup> data have been used, selecting only runs that have been checked for a good data quality (e.g. enough track hits in the ITS, minimum number of charge clusters in the TPC) to ensure a clean sample of collision events:

- Measured data: LHC11h\_2, AOD145, comprising 50 "good runs" with different numbers of events (according to the individual run duration)
- Simulated data: LHC12a17d\_fix (0-10% event centrality, adjusted to the detector characteristics during the data taking)

### 3.1.3 Event selection

The events were selected with the `AliPhysicsSelection` class in AliRoot that imposes several cuts on the data to avoid a selection of non-physical events<sup>14</sup>. This event selection is applied on the data and the Monte Carlo (MC) simulated events (even if they are per default simulated as good physical events) in order to treat them equally. The physics selection is followed by a cut selection on the primary event vertex (the list of cuts is given in table 3.1 and described more in detail in the following). All cuts are defined w.r.t. the ALICE coordinate system, as described in section 2.2. The primary vertex of each event is reconstructed, using information from several trigger detectors and in several steps of the event reconstruction. The preliminary determination of the interaction vertex uses the

<sup>13</sup>A "Minimum Bias" event in the context of the ALICE analyses means an event with at least one hit in the SPD and in the VZERO detector.

<sup>14</sup>It provides a user-transparent and efficient event selection before the physical analysis. It avoids the selection of non-physical data taking runs (i.e. calibration runs) or events without the interaction trigger, i.e. the trigger on bunch crossings, or events that are flagged as a beam-gas interaction by either the V0A or the V0C detector.

Table 3.1: The following event selection criteria were imposed to select only events with high data quality:

<b>Collision candidates are events which are:</b>
minimum bias events, triggered central (0-10%) or semi-central (10-50%) events
<b>Requirements on the primary (event) vertex:</b>
at least 2 contributors (tracks) (distribution before cut given in Fig. 3.1)
The longitudinal $z$ -position has to be within $ z  < 10$ cm w.r.t. the origin of co-ordinates
$\Delta z_{\text{SPD}} =  z_{\text{vertex}}^{\text{SPD}} - z_{\text{vertex}}^{\text{nominal}}  < 0.1$ cm
radial distance from $z$ axis: $r < 1$ cm, $r = \sqrt{x^2 + y^2}$
not reconstructed from TPC tracks only (but also from ITS reconstructed tracks)

SPD silicon pixels to estimate a point to which a maximum of reconstructed tracklets<sup>15</sup> contribute. In case a single convergent point is not directly found, an one-dimensional search along the  $z$  axis and for a minimum of the Points-of-Closest-Approach (PCA) (of all primary tracks) is carried out. The PCA is the point with the shortest distance between each track-let and the  $z$  (beam) axis. To determine the primary vertex with higher precision global tracks are reconstructed with the ITS and the TPC. The tracks are extrapolated into direction to the beam axis and the PCA. Outlying tracks are removed and a precise fitting of the vertex is performed using a track weighting procedure. Furthermore the longitudinal distance between the preliminary and the final primary vertex  $\Delta z_{\text{SPD}} = |z_{\text{vertex}}^{\text{SPD}} - z_{\text{vertex}}^{\text{nominal}}|$  is not allowed to be larger than 0.1 cm in the 2011 taken Pb–Pb data.

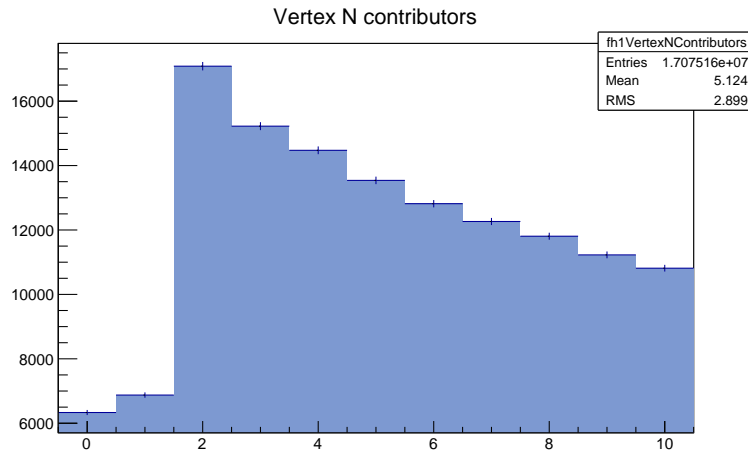


Figure 3.1: Number of vertex contributors (before the cut is applied) of the analysed events in the analysed data set in Pb–Pb collisions at  $\sqrt{s_{\text{NN}}} = 2.76$  TeV. All events with less contributing tracks than 2 are rejected.

<sup>15</sup>A SPD tracklet is defined as a line segment built by using clusters in the two layers of the SPD within a small azimuthal window (0.01 rad)

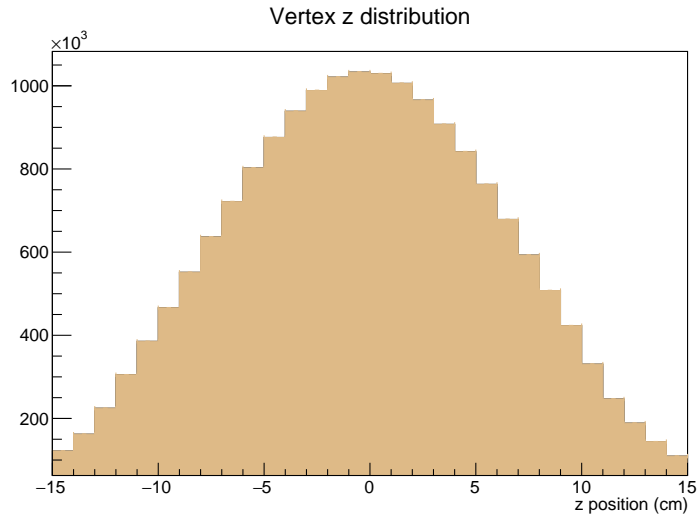


Figure 3.2: The nominal primary vertex  $z$  position (before cuts) of the analysed events in the analysed data set in Pb–Pb collisions at  $\sqrt{s_{\text{NN}}} = 2.76$  TeV. Only events with  $|z| < 10$  cm are accepted by the physics selection.

More than 2 contributing tracks were required for the reconstruction of the primary vertex (PV) in order to provide a good resolution of the SPD vertex reconstruction. As can be seen from Fig. 3.1 this criterion is fulfilled by the majority of the analysed events. The  $z$ -position of the primary vertex was selected to be within  $|z| < 10$  cm (w.r.t. the origin of the ALICE coordinate system) for what is fulfilled by most of the events (Fig. 3.2 shows the distribution before the cut is applied). This cut aims to ensure uniform tracking quality and high reconstruction efficiency within the selected pseudo-rapidity window  $|\eta| < 0.9$ . Primary vertices reconstructed solely with the TPC tracks were not accepted. The radial distance  $r = \sqrt{x^2 + y^2}$  of the primary vertex to the  $z$ -axis was restricted to be less than 1 cm.

For the centrality estimation the “V0M” estimator is used which relies on the combined evaluation of the signals measured by the “V0A” and “V0C” detectors. The event centrality distribution is shown in Fig. 3.3. The majority of events in the 2011 recorded data of Pb–Pb collisions at  $\sqrt{s_{\text{NN}}} = 2.76$  TeV are the most central events. For this analysis only events with a centrality smaller than 10% are considered.

### 3.1.4 $V^0$ particle reconstruction

The  $K_S^0$  meson and the  $\Lambda$  ( $\bar{\Lambda}$ ) baryon are neutral particles which decay via weak interaction into a pair of charged daughter particles. This decay topology is used for their reconstruction (see Figure 3.4) from their charged daughter tracks that are bent by the homogenous magnetic field of the 0.5 Tesla that is produced by the “L3” solenoid magnet. Both daughter tracks are associated with a displaced secondary vertex. The 3-dimensional

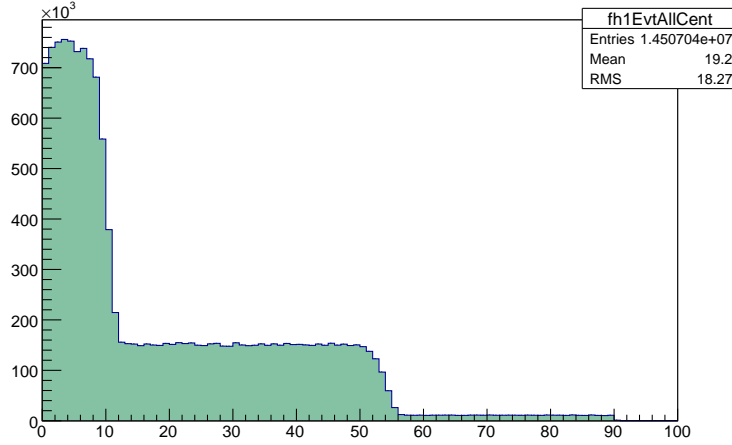


Figure 3.3: The centrality distribution of all events contained in the used 2011 Pb–Pb data set at  $\sqrt{s_{\text{NN}}} = 2.76$  TeV. Only events with an event centrality of 0-10% are selected for the analysis.

$V^0$  particle momentum  $\mathbf{p}$  can be determined by the Lorenz- and the centrifugal force to

$$q \cdot \mathbf{v} \cdot \mathbf{B} = m \cdot \frac{v^2}{R} \quad (3.1)$$

and the particle momentum then by  $\mathbf{p} = q \cdot \mathbf{B} \cdot R$ .

The 4-momentum of the  $V^0$  candidate that has decayed into the charged daughter particles (track+, track-) is given by

$$\begin{pmatrix} E_{V^0} \\ \mathbf{p}_{V^0} \end{pmatrix} = \begin{pmatrix} E_{\text{track}+} \\ \mathbf{p}_{\text{track}+} \end{pmatrix} + \begin{pmatrix} E_{\text{track}-} \\ \mathbf{p}_{\text{track}-} \end{pmatrix} \quad (3.2)$$

By using the energy-momentum relation

$$E^2 = \mathbf{p}^2 c^2 + m^2 \cdot c^4 \quad (3.3)$$

and with the momentum conservation for the  $V^0$  candidate and the (oppositely) charged daughter particles (and with  $c = 1$ ) the equation writes

$$m_{\text{invM},V^0}^2 = \mathbf{E}_{V^0}^2 - \mathbf{p}_{V^0}^2 = (E_{\pi^+} + E_{\pi^-})^2 - (\mathbf{p}_{\pi^+} + \mathbf{p}_{\pi^-})^2. \quad (3.4)$$

The  $V^0$  particles are reconstructed using their most frequent decay channels:

- $K_S^0 \rightarrow \pi^+ + \pi^-$  (with a branching ratio of 69%,  $\tau \approx 9 \times 10^{-11}$  s),
- $\Lambda \rightarrow p + \pi^-$ ,  $\bar{\Lambda} \rightarrow \bar{p} + \pi^+$  (with a branching ratio of 64%,  $\tau \approx 3 \times 10^{-10}$  s).

When imposing a mass hypothesis [22] for the charged daughters one derives the invariant

mass finally as

$$m_{inv,V^0} = \sqrt{\left(\sqrt{\mathbf{p}_{\pi^+}^2 + m_{\pi^+}^2} + \sqrt{\mathbf{p}_{\pi^-}^2 + m_{\pi^-}^2}\right)^2 - (\mathbf{p}_{\pi^+} + \mathbf{p}_{\pi^-})^2} \quad (3.5)$$

For the  $K_S^0$  the  $\pi$  mass was associated for both daughters, for the  $\Lambda$  the track with the higher momentum was associated with the proton, while for the track with the lower momentum the  $\pi$  mass was assigned (since for  $\Lambda$  particles with  $p_T > 0.3$  GeV/c the proton carries away most of the mother momentum).

The  $V^0$  candidates were selected using some topological and other cuts and from the charged secondary tracks (secondary tracks are tracks with a sufficiently large impact parameter to the primary event vertex). The complete list of criteria requested for selected  $V^0$  candidates is presented in the following table 3.2.

Quality selection on $V^0$ daughter tracks	Cut requirement
$ \eta $	$\leq 0.8$
DCA to primary vertex	$\geq 0.1$ cm
DCA between $V^0$ daughters	$\leq 1\sigma_{\text{TPC}}$
$ \Delta(dE/dx) $ (proton, $p_T < 1$ GeV/c)	$\leq 3\sigma_{dE/dx}$
TPC refit	required
Reconstruction vertex type: kKink	rejected
Cuts on $V^0$ candidate	
$ \eta $	$\leq 0.7$
$V^0$ reconstruction method	Offline
Radius of the decay vertex	$5 < R_{\text{decay}} < 100$ cm
Cosine of pointing angle (CPA)	$\leq 0.998$
Transverse proper lifetime	$\leq 5\tau$
Armenteros-Podolanski cut (only for $K_S^0$ )	$q_T^{\text{Arm.}} \geq 0.2  \alpha $

Table 3.2: The  $V^0$  particle selection is applied on the topology of the reconstructed  $V^0$  decay.

On the  $V^0$  daughter tracks a TPC refit is applied, and kink daughters (i.e. secondary vertices not describing the required decay topology which can be e.g.  $K^\pm$  decays) are rejected. A cut of  $1\sigma_{\text{TPC}}$  is applied on the Distance of the Closest Approach (DCA) between the daughter tracks (see Fig. 3.4) for a geometrical description of the  $V^0$  cuts. Another cut is imposed on the pseudo-rapidity of the daughter tracks  $|\eta| < 0.8$  and one of 0.1 cm on the DCA of the daughter tracks with respect to the primary vertex. The proton (antiproton) daughter candidates of the  $\Lambda$  ( $\bar{\Lambda}$ ) candidates, with  $p_T < 1$  GeV/c, have to be identified by the  $dE/dx$  signal in the TPC within  $3\sigma$ <sup>16</sup>.

<sup>16</sup> $\sigma$  is the standard deviation of the  $dE/dx$  signal in the TPC that is fitted with a gaussian fit function at a given momentum  $p_{\text{TPC}}$  for a particle of a given species

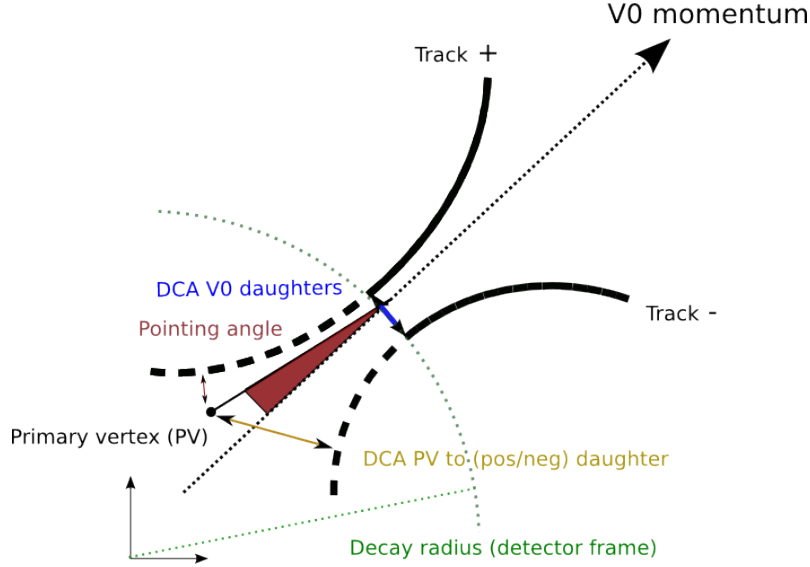


Figure 3.4: Topological properties of a  $V^0$  decay and the selection parameters used for  $V^0$  reconstruction.

For the  $V^0$  candidate, the cosine of the pointing angle<sup>17</sup> was required to be larger than 0.998. A cut of 5 cm on the minimum distance of the decay vertex from the  $z$ -axis was applied to reject the  $V^0$  vertices that were closer to the PV than the first layer of the Silicon Pixel Detector (SPD).

Furthermore, a cut on the “transverse proper lifetime”<sup>18</sup> is needed to further suppress the combinatorial background, for which the mean lifetime (expressed as  $c\tau$ ) of the  $K_S^0$ ,  $\Lambda$  and  $\bar{\Lambda}$  was taken as 2.6844 cm and 7.89 cm respectively [159]. A cut in the  $K_S^0$  Armenteros-Podolanski variables was used to suppress the contamination of the  $K_S^0$  candidates with  $\Lambda$  and  $\bar{\Lambda}$  particles. Figure 3.5 shows the  $V^0$  candidates separated into different particle types via the Armenteros-Podolanski variables  $q_T$  (which is the momentum component perpendicular to the momentum of the mother particle) and  $\alpha$  is the longitudinal projection asymmetry:

$$\alpha = \frac{p_L^+ - p_L^-}{p_L^+ + p_L^-} \quad (3.6)$$

where  $p_L$  is the longitudinal projection of the daughter track onto the mother ( $V^0$ ) particle. At low  $q_T$  one can see  $\gamma$  conversions into pairs of electrons. The left plot in a) shows the Armenteros-Podolanski plot for  $V^0$  candidates in pp events, in which a clear separation of the different particle species can be seen (in absence of the huge combinatorial background that is present in the Pb–Pb data). Since the  $K_S^0$  mesons decay into particles with equal mass they show a symmetric distribution. The  $\Lambda$  baryons decay into particles with the heavier daughter (the proton) carrying (on average) much more of the mother momentum than the lighter daughter (the pion) does, therefore the  $\Lambda$  and  $\bar{\Lambda}$  distribution is asymmetric.

<sup>17</sup>between the measured  $V^0$  momentum and the line that connects the reconstructed  $V^0$  decay vertex and the primary vertex.

<sup>18</sup>calculated as  $c\tau = \frac{Lm}{p_T}$  where  $L$  is the projection of the decay length on the transverse plane  $x$ - $y$  and connects the primary and  $V^0$  vertex,  $m$  and  $p_T$  are the particle mass and the transverse momentum.

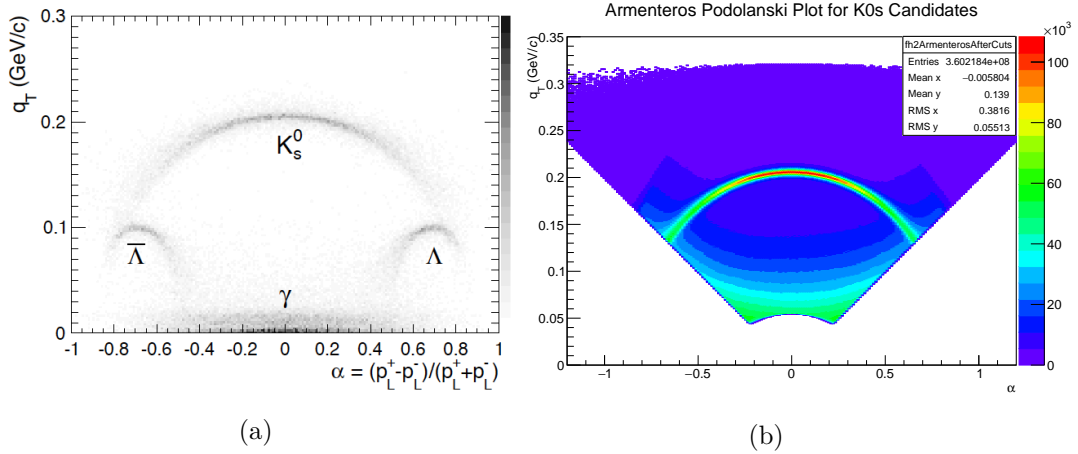


Figure 3.5: The  $V^0$  candidates separated into different particle types via the Armenteros-Podolanski variables  $q_T$  (momentum component perpendicular to mother particle momentum) and  $\alpha = \frac{p_L^+ - p_L^-}{p_L^+ + p_L^-}$ . At low  $q_T$  one can see  $\gamma$  conversions into pairs of electrons. a) The Armenteros-Podolanski plot for  $V^0$  candidates in pp events shows a clear separation of the different particle species. b) The  $K_S^0$  candidates are separated from a possible contamination of  $\Lambda(\bar{\Lambda})$  candidates by the requirement:  $q_T^{\text{Arm.}} \geq 0.2 |\alpha|$ . For the rejection of  $\gamma$  conversions, another cut is applied already during the  $V^0$  reconstruction. Left Fig. adapted from [158].

For the overlap of the different bands the different particle types are indistinguishable and present a contamination of the corresponding invariant mass distributions. Since the contamination leads to special shapes of the combinatorial background and is also situated in some cases below the signal peak, this contamination can be removed by the Armenteros cut.

The plot in b) shows the  $K_S^0$  candidates, separated from a possible contamination of  $\Lambda(\bar{\Lambda})$  candidates by the requirement  $q_T^{\text{Arm.}} \geq 0.2 |\alpha|$ . For the rejection of  $\gamma$  conversions, another cut is applied already during the  $V^0$  reconstruction which can be seen at very low  $q_T$ .

### 3.1.5 Signal extraction

The following section describes the method that is used to extract the particle signal for inclusive  $V^0$  and  $V^0$  in jet and in the UE estimation methods. The particle signal is extracted from invariant-mass distributions for different intervals in particle  $p_T$  and in  $p_T^{\text{jet}}$ .

#### Signal extraction via bin counting and fit of combinatorial background

The  $V^0$  particle signal is extracted from the invariant mass distributions separately for each  $V^0$   $p_T$  interval. A complete set of the invariant mass distributions used for the signals extracted in inclusive events, in the jet cone and in the Underlying Event are given in the appendix B, C and D.

Figures 3.6 and 3.7 shows examples for the signal extraction method for inclusive  $K_S^0$  candidates in  $3 \text{ GeV}/c < V^0 p_T < 4 \text{ GeV}/c$  (and  $7 \text{ GeV}/c < V^0 p_T < 10 \text{ GeV}/c$ ), the signal region is selected as fixed ranges with the limits that are listed in table 3.3 and

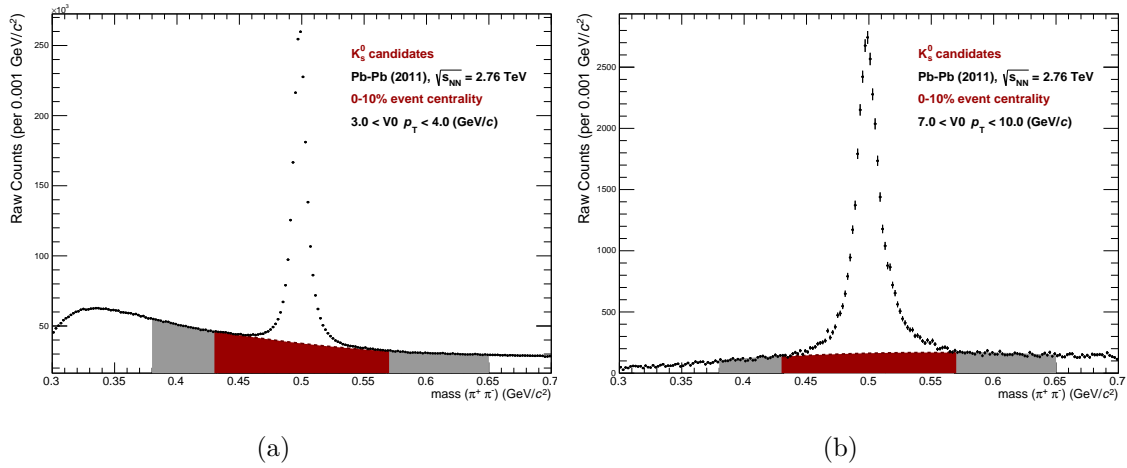


Figure 3.6: a) Invariant mass distribution for inclusive  $K_S^0$  candidates in  $3 \text{ GeV}/c < V^0 p_T < 4 \text{ GeV}/c$ , the signal region is indicated in red. The regions for the background fit are indicated in grey. b) Invariant mass distribution for inclusive  $K_S^0$  candidates in  $7 \text{ GeV}/c < V^0 p_T < 10 \text{ GeV}/c$ .

indicated as a red area. The two sideband regions for the background fit are indicated by grey areas. These regions are chosen carefully to consider the signal peak that shows small non-gaussian tails to both sides and provide a good shape description of the combinatorial background on both sides of the peak.

The method with fixed regions allows to select the three regions independently from each other which is important especially for the  $\Lambda$  candidates that have a steeply falling background shape at low  $p_T$  in the limit, where the sum of the rest masses of  $\pi$  and proton is located ( $\sim 1077.84 \text{ MeV}/c$ ). A disadvantage of the fixed regions is the position of the sideband regions in case of low  $V^0 p_T$  intervals. In this particular case the fixed sideband regions are more distant from the peak region than for the case of higher  $V^0 p_T$  intervals in which they are closer to the peak (and thus provide a better estimate for the background shape in the peak region). This can be seen e.g. in Fig. 3.6, where the edges of the signal region (red area) are more distant to the signal peak for a) than they are for b).

Alternatively, regions for the signal extraction and background estimation defined by multiples of the signal peak  $\sigma$  (estimated via a global fit with a polynomial of 3rd order plus a gaussian fit function) have been tried instead of the fixed regions which enables to keep the side-band regions closer to the particle peak. However this method turned out to be very sensitive on statistical fluctuations of the peak shape, lead to a partial overlap of the sideband (grey) regions with the (non-gaussian) tails of signal peak and failed more often to converge in the sideband fits. Therefore this method was firstly tried but then not used anymore for the current analysis.

The applied signal extraction method has the following strategy. As a first step, 3 intervals on the invariant mass axis are defined by the fixed regions listed in table 3.3.

The (grey) background regions on both sides of the invariant mass peak are fitted with a polynomial function of second order in case of  $K_S^0$  candidates and of third order for the  $\Lambda$  (and  $\bar{\Lambda}$ ) candidates. This choice of the polynomial fit function aims to provide an optimal

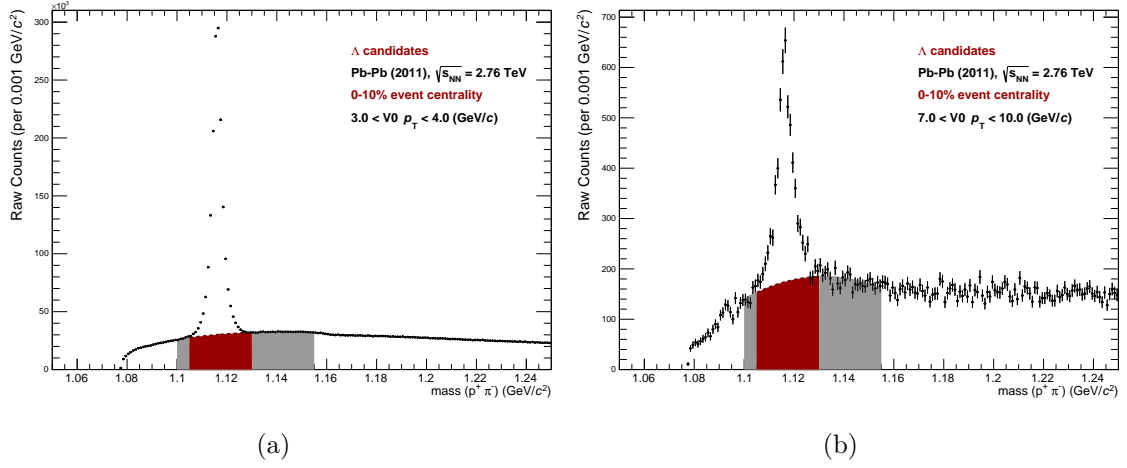


Figure 3.7: a) Invariant mass distribution for inclusive  $\Lambda$  candidates from  $3 \text{ GeV}/c < V^0 p_T < 4 \text{ GeV}/c$ , the signal region (defined according to table 3.3) is indicated in red. b) Example of an invariant mass distribution for inclusive  $\Lambda$  candidates from  $7 \text{ GeV}/c < V^0 p_T < 10 \text{ GeV}/c$ , the two regions for the background fit are indicated in grey.

Table 3.3: Signal and background regions for fixed intervals and dependent on  $\sigma$  of the mass peak (gaussian) fit

Regions:	left sideband	peak region	right sideband
Particle type	Fixed regions:		
$K_S^0$	[0.38, 0.43] GeV/c	[0.43, 0.57] GeV/c	[0.57, 0.65] GeV/c
$\Lambda(\bar{\Lambda})$	[1.1, 1.105] GeV/c	[1.105, 1.13] GeV/c	[1.13, 1.155] GeV/c

description of the shape of the combinatorial background that changes for the different particle types and also differs for the various selected  $p_T$  intervals (as can be seen e.g. in Fig. 3.6 and 3.7). In case the mean number of entries in one or both of the sideband regions is less than 20, a polynomial fit function of 1st order is used (which is mostly the case for the highest  $V^0$   $p_T$  bin).

If the fit converges in both sideband regions, with the derived fit parameters a background-fit function is interpolated over the already specified mass range that includes signal and background regions, and is then used to estimate the combinatorial background below the particle peak, where no direct fit is possible. In case the sideband fit does not converge or the mean number of entries is less than 1, a constant function is fitted to the whole mass range in order to estimate the combinatorial background.

The particle signal ( $S$ ) is finally derived as the integral ( $B$ ) of the background fit function ( $\text{fit}_{\text{bgr}}$ ) (below the particle peak and divided by the bin width) and subtracted from all entries sampled via "bin counting" in the peak region ( $S + B$ ):

$$S = (S + B) - \int_{\text{signal region}} (\text{fit}_{\text{bgr}}/\text{bin width}) \quad (3.7)$$

The corresponding statistical error is calculated by the square-root of the sum of squares of the entries for the signal plus background ( $S + B$ ) and the error of the fit ( $\delta\text{fit}_{\text{bgr}}$ ) of the integrated background ( $B$ ) below the peak. The error of the fit function is given by the covariance matrix of  $\text{fit}_{\text{bgr}}$ . These errors follow a Gaussian error propagation to

$$\text{err}_{(\text{sig})} = \sqrt{(S + B) + (\delta\text{fit}_{\text{bgr}})^2} \quad (3.8)$$

For the  $V^0$  candidates in the jet cone (and in the methods used to estimate the  $V^0$  contribution from the UE) the same signal extraction strategy is used. Fig. 3.8 shows an example for the invariant mass distributions for  $K_S^0$  and  $\Lambda$  in the jet cones which have lower  $V^0$  candidate statistics (due to the in-cone criterion) but provide a well pronounced signal peak.

Along with the signal extraction also the signal purity in the peak region is measured for each  $V^0$   $p_T$  interval separately and plotted versus  $p_T$ . The signal purity is defined as the ratio of the signal yield (in the peak region) over the signal+background yield in the same region. Two examples for the signal purity as function of the  $V^0$   $p_T$  can be seen in Fig. 3.9 for inclusive  $K_S^0$  (left panel) and the  $K_S^0$  particle in jet cones (right panel). They indicate that the best signal purity for  $V^0$  candidates is situated around  $p_T \sim 1-2$  (GeV/c) and for higher  $p_T \sim 8-10$  (GeV/c) reaches around 80%. At intermediate  $p_T$  ( $2 < V^0 p_T < 5$  GeV/c) the purity is lower with around 40-50%. However for the candidates in jet cones the purity seems to be slightly better (around 10% higher for  $p_T \geq 3$  GeV/c) compared to the case of inclusive particles. The purity is furthermore used to correct the  $V^0$  yields in the Monte-Carlo simulation used for the  $V^0$  reconstruction efficiency correction (see section 3.4.2). The  $\text{err}_{(\text{sig})}$  for the signal extraction in the jet cones is calculated in the same way as described already for the case of the inclusive particles. In the MC simulations, by requiring additional information (e.g. the correct particle identities, etc.) the combinatorial

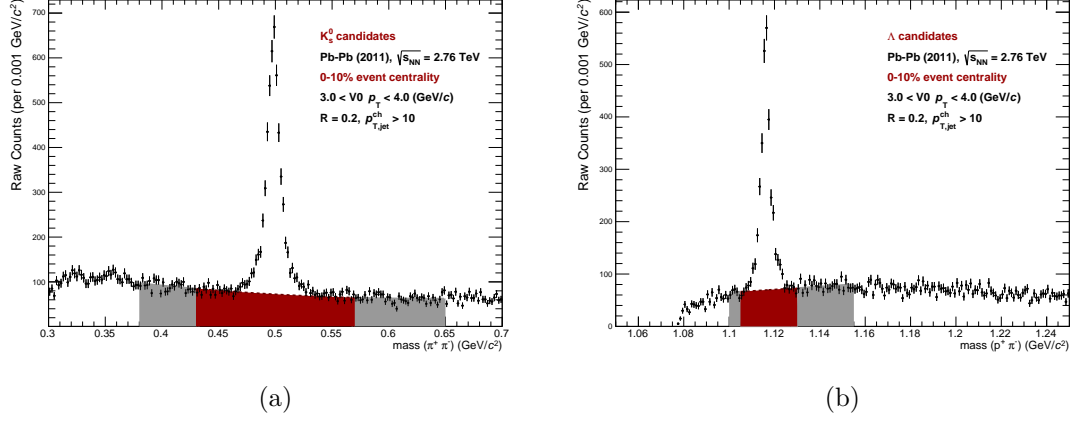


Figure 3.8: Invariant mass distribution for  $K_S^0$  (left) and  $\Lambda$  (right) candidates in the jet cone (with  $R = 0.2$ ) and for  $p_T^{\text{jet}} > 10$  GeV/c and  $3.0 \text{ GeV}/c < V^0 p_T < 4.0 \text{ GeV}/c$ .

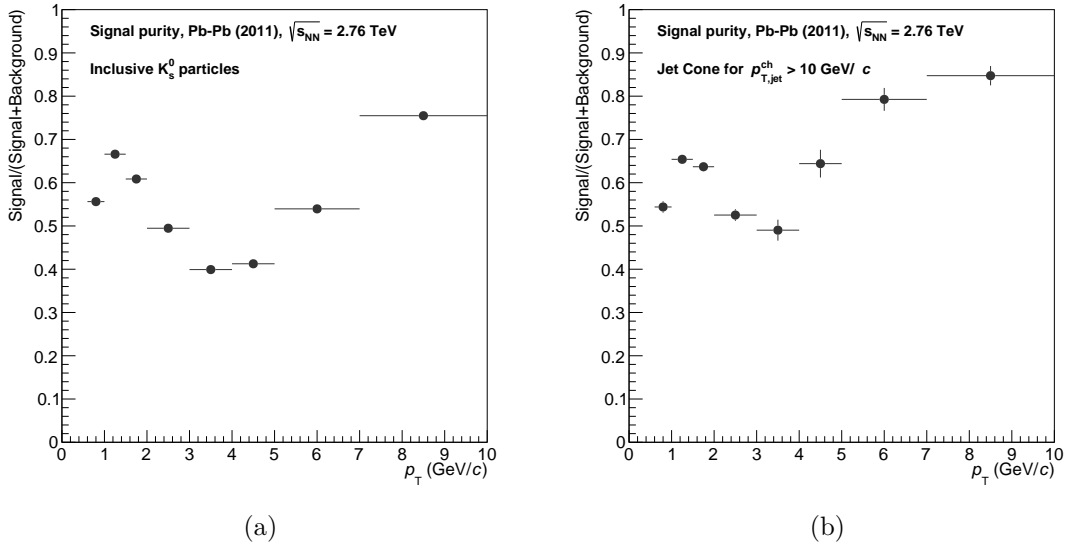


Figure 3.9: Two examples for the signal purity as function of the  $V^0 p_T$  obtained with the signal extraction for inclusive  $K_S^0$  (left panel) and the  $K_S^0$  particle in jet cones (right panel). The signal purity is defined as the ratio of the signal yield (in the peak region) over the signal+background sample in the same region.

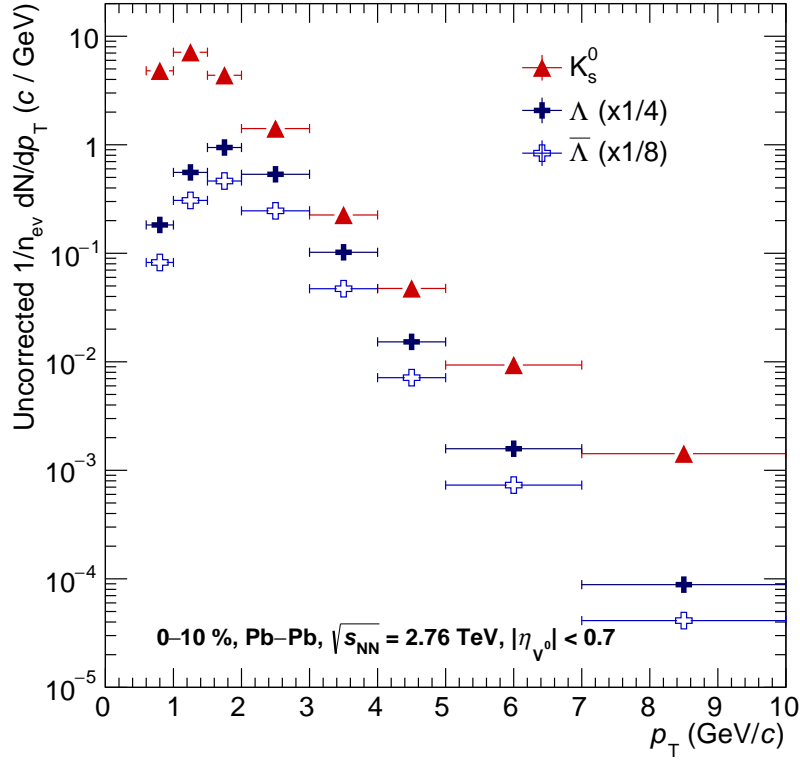


Figure 3.10: Raw  $p_T$  spectrum of inclusive  $K_s^0$ ,  $\Lambda$  and  $\bar{\Lambda}$  for 0-10% most central events of the 2011 Pb–Pb data at  $\sqrt{s_{NN}} = 2.76$  TeV.

background of these “associated” particles is much reduced compared to the measured distributions and therefore the signal extracted from the (fixed) signal regions is gained by integration of the bin entries (without applying a background subtraction).

### 3.1.6 Uncorrected $p_T$ spectra

As a next step in the analysis procedure, the uncorrected inclusive  $V^0$   $p_T$  spectra are obtained and shown in Fig. 3.10. Furthermore the raw yields in the jet cone and in the UE estimation method (more details about this methods is given in the following sections) are shown in Fig. 3.11. Already in the uncorrected spectra it is clearly visible how different the spectral shape for the particles inside and outside the jet cone are and that much more high- $p_T$   $V^0$  particles can be found inside. At low  $V^0$   $p_T$  (around 0.5 - 3 GeV/c) the spectra show very similar yields (compare red markers to the different other methods which describe the spectrum of the UE  $V^0$ s) which is due to the huge contribution of the UE  $V^0$  particles that still needs to be subtracted accurately in order to get a clean sample of  $V^0$  particles that stem from a hard scattering process of initial state partons.

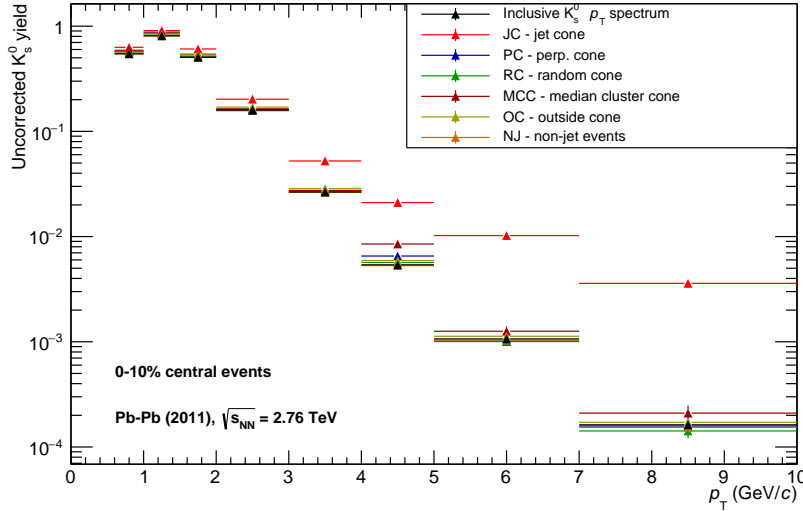


Figure 3.11: Comparison of raw  $V^0$   $p_T$  spectra in different selections and event regions (inclusive - black markers, JC - red markers, PC - blue markers, RC - green markers, MCC - brown markers, OC - beige markers, NJ - orange markers). From the shape of the  $V^0$   $p_T$  spectra, already before the subtraction of the  $V^0$  contribution from the Underlying Event (UE), a clear different slope of the intra-jet  $V^0$  particles w.r.t. the inclusive particles or those from the UE can be seen (compare red markers to the others).

### 3.1.7 Analysis workflow

Before the discussion of the jet analysis and the combined  $V^0$ -jet association a general overview of the analysis strategy is sketched in the following. Figure 3.12 shows the workflow of the analysis of inclusive  $V^0$  particles or those inside of charged jets. It starts with the event selection, in which only events with 0-10% event centrality are accepted and the cut selection on the primary event vertex is applied (see details in section 3.1.3). Then follow two analysis branches, one for the  $V^0$  particle reconstruction in the entire event and one for the reconstruction of jets from charged tracks that are selected via the "hybrid track" selection cuts (as listed in the appendix E.1). Afterwards both information ( $V^0$   $p_T$ ,  $\eta$  and  $\phi$  and the  $p_T^{\text{jet}}$ , jet  $\eta$  and  $\phi$ ) is combined and the invariant mass distributions for different intervals of  $V^0$   $p_T$  (or  $V^0$   $\eta$ ) are produced for jets (in either  $p_T^{\text{jet}} > 10$  GeV/c or  $p_T^{\text{jet}} > 20$  GeV/c). The next step is the correction for the  $V^0$  reconstruction efficiency that is estimated separately for the different kind of particle spectra. Afterwards the spectra are normalized by either the number of events (for the inclusive particle spectra and the UE estimation method), or the number of jets, times the active area (the jet area or the area of the  $\eta$ - $\phi$  acceptance to sample the  $V^0$  particles). Then the contribution of  $V^0$  particles from the UE to the yields in the jet cone is subtracted. For the  $\Lambda(\bar{\Lambda})$  particles the contribution from feed-down (from decays of heavier particles into  $\Lambda$  baryons) is subtracted. From the so derived fully corrected spectra in Pb–Pb collisions the particle ratio is calculated (the results are described in section 4).

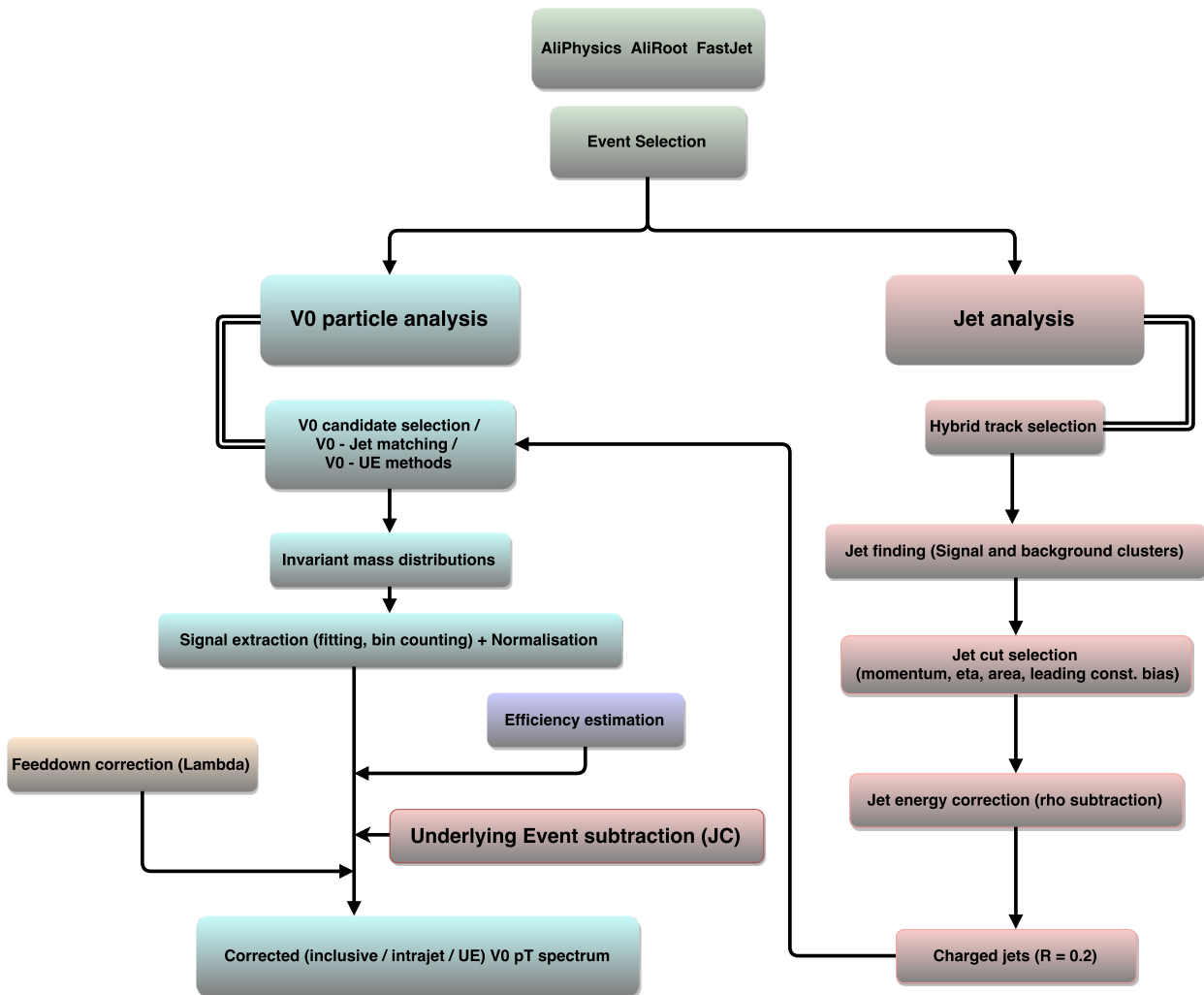


Figure 3.12: Analysis workflow

## 3.2 Reconstruction of jets from charged particle tracks

This section gives some information about jet finding procedures in general and specifies the strategy for the charged jet reconstruction that is used for the current analysis.

### 3.2.1 Some aspects of the jet reconstruction

For this analysis the anti- $k_t$  and the  $k_t$  jet algorithms are used to reconstruct particle jets from primary charged tracks. The anti- $k_t$  jet finding algorithm is part of the FastJet [160] package and belongs to the class of sequential recombination algorithms that cluster particle tracks into jets.

#### The Jet reconstruction algorithms

As a standard algorithm for jet reconstruction at the LHC experiments the anti- $k_t$  jet algorithm is used. Its working principle to reconstruct charged jets is the following:

As an input to the jet finder, all reconstructed tracks (that also passed a track cut selection as described later in this chapter) from charged particles of a collision event are used. For each pair of particles  $i, j$  (which can be particles or pseudo-jets) a symmetric distance  $d_{ij}$  is defined as

$$d_{i,j} = d_{j,i} = \min(p_{T,i}^{2p}, p_{T,j}^{2p}) \Delta R_{i,j}^2 / R^2$$

with

$$\Delta R_{i,j}^2 = (y_i - y_j)^2 + (\phi_i - \phi_j)^2$$

and in which  $p_{T,i}$  is the transverse momentum,  $y_i$  the rapidity  $y_i = \frac{1}{2} \ln \frac{E_i + p_{z,i}}{E_i - p_{z,i}}$  and  $\phi_i$  the azimuthal angle of entity “ $i$ ”.  $R$  is the jet resolution parameter which is a constant<sup>19</sup> and determines the angular reach (in rapidity  $y$  and azimuthal  $\phi$  direction) of the jet cone. The parameter  $p$  sets the relative power of energy versus the geometrical measure  $d_{ij}$ .

$$d_{i,B} = p_{T,i}^{2p}$$

is a special distance measure of the squared transverse momentum of entity “ $i$ ”.

The algorithm starts by calculating the distances between all entities  $i$  and  $j$ :  $d_{i,j}$  and the respective  $d_{i,B}$ . The smallest of these distances is taken and compared to  $d_{i,B}$ . If  $d_{i,j}$  is found as the minimum, the two entities are combined to form a new entity and also respectively their  $p_T$  values. If  $d_{i,B}$  gives the minimum, the jet candidate is declared as a jet and removed from the list of entities. This procedure is repeated until no entities are left on the list of candidates.

If the power is set to  $p = -1$ , one gets the anti- $k_t$  jet algorithm which is suitable especially for events with few high- $p_T$  particles together with many soft particles. This is typically the case for heavy-ion collision events and therefore used for the signal jets that are studied

<sup>19</sup>For  $R$  typical values are 0.2(0.3) for the jet reconstruction in heavy-ion collisions, in pp collisions larger values up to 0.8 are usually used.

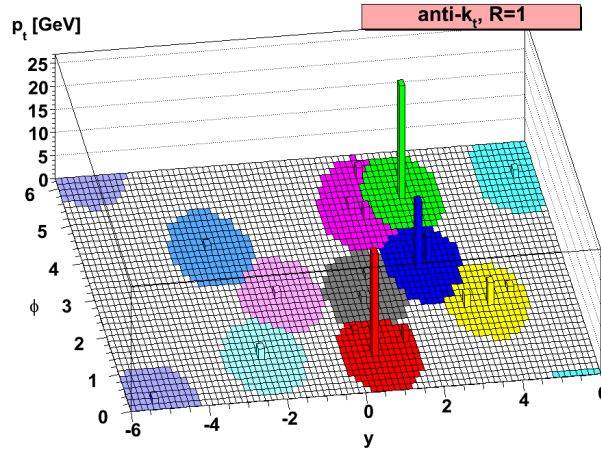


Figure 3.13: Herwig8 generated event together with many randomly placed soft particles is clustered up by the anti- $k_t$  jet algorithm. The resulting areas of this jet finder have circular shapes [161].

in this analysis. The distance

$$d_{h,i} = \min(p_{T,i}^2, p_{T,h}^2) \Delta R_{h,i}^2 / R^2$$

between a high- $p_T$  particle  $h$  and another particle  $i$  (with a lower  $p_T$ ) is basically given by  $p_{T,h}$  and their geometrical distance by  $\Delta R_{h,i}^2$ . On the other hand, the distances  $d_{i,j}$  between soft particles that have similar separation from each other, are much larger. Therefore soft particles try to cluster first with high- $p_T$  particles. This is a characteristic feature of the anti- $k_t$  jet algorithm, to cluster firstly hard particles and finish the clustering with the softer particles. If there are no other hard particles within a distance of  $2R$  around the single hard particle with  $p_{T,h}$ , the resulting anti- $k_t$  reconstructed jet will just cluster up soft particles and end up with a perfectly conical shape, as can be seen in Fig. 3.13. A key feature of this algorithm is that soft particles do not modify the jet area, whereas hard particles do have an impact on the final form of the jet.

For setting the power to  $p = 1$ , we obtain the inclusive  $k_t$  algorithm which starts to cluster up soft particles first. The resulting jet shapes are non-conical, as can be seen in Fig. 3.14.

All these jet algorithms are infrared and collinear safe which is important for a description by perturbative calculations. Infrared safety is important to ensure that soft gluon radiation does not influence the jet finding procedure. On the other hand high- $p_T$  particles that are close to the energy and direction of the initial hard parton (from which the shower evolution started) have a probability to do a parton splitting under a very small angle and might end up with two partons, carrying each half of the initial parton energy and having almost the same direction. This collinear splitting process must also not have an influence on the jet finding.

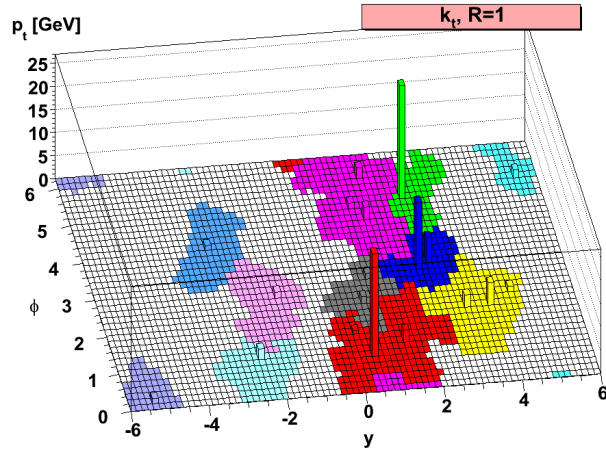


Figure 3.14: Resulting areas of the  $k_t$  jet algorithm have non-regular shapes [161].

### 3.2.2 Contribution from the Underlying Event and background fluctuations

Since jets in heavy-ion collisions suffer from a large contribution of charged tracks stemming from the UE, one has to correct for all resulting effects. This UE contribution has an impact on both the  $p_T^{\text{jet}}$  and the charged track  $p_T$  distribution inside a jet cone.

In the general case of an event in which a hard parton scattering takes place, its final state particles can be clustered into a set of jets  $\{J_i\}$ . When many soft particles, like a pile-up of events or the Underlying Event (UE) present in heavy-ion collisions are added on top of that, the resulting list of reconstructed jets  $\{J_{i,UE}\}$  differ in several aspects. First the total jet energy is increased by the additional contribution of many low-energy tracks from the UE which also depends on the jet area. Secondly, the track distribution inside the jet changes and affects the jet constituent  $p_T$  spectrum.

The contribution to the jet energy can be huge in heavy-ion events with large event multiplicity and can be split in an average contribution that fluctuates around its mean value. The total change of the  $p_T^{\text{jet}}$  is then given by [162]:

$$\Delta p_T = A \cdot \rho \pm \sigma \sqrt{A} \quad (3.9)$$

Here  $\rho$  is the average level of noise contributing to the event per unit area.  $A$  is the jet area and  $\sigma \sqrt{A}$  is the uncertainty of the first term, as described later. Jet areas can be measured by embedding numerous (non-physical) low  $p_T$  particles uniformly into the event which are clustered up by the jet finder. By the number of these “ghost” tracks that are clustered into one jet, the jet area can be measured.  $\rho$  is carefully estimated for the charged jets in Pb–Pb collisions and a corresponding correction of  $p_T^{\text{jet}}$  is applied event by event [163]. This average  $p_T$  density  $\rho$  of the UE background is estimated using the  $k_t$  algorithm. It clusters up all charged hybrid tracks of one event and sorts the list of found  $k_t$  jets by the cluster size. Afterwards the first two largest clusters are removed, with the assumption

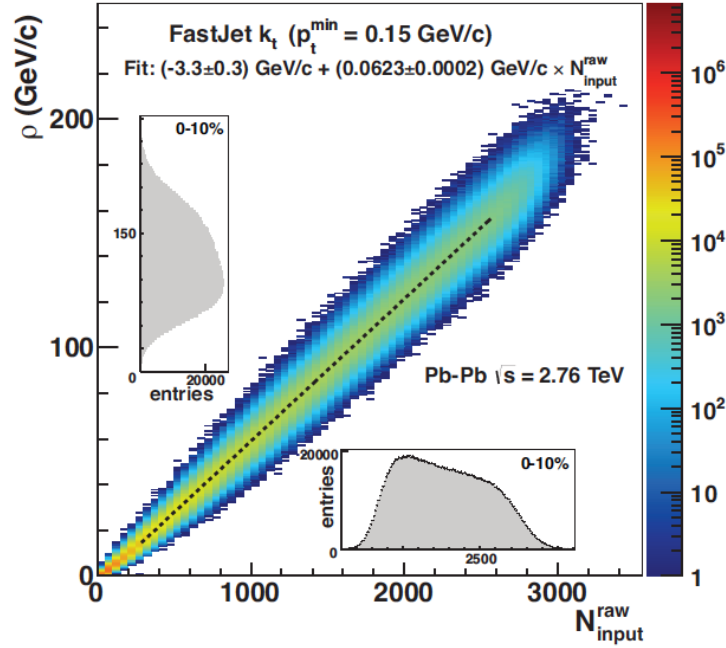


Figure 3.15: Dependence of the average background  $p_T$  density  $\rho$  on the uncorrected multiplicity of tracks used for jet finding ( $|\eta| < 0.9$ ) in Pb–Pb collisions at  $\sqrt{s_{NN}} = 2.76$  TeV. The dotted line is a linear fit to the centroids in each multiplicity bin. The insets show the projected distributions of  $\rho$  and raw multiplicity for the 10% most central events. Figure and caption adapted from [163].

they might be real jets. From the remaining list, the median cluster

$$\rho = \text{median} \left( \frac{p_T^{\text{rec}}}{A^{\text{rec}}} \right)$$

is taken and applied as the following jet  $p_T^{\text{jet}}$  correction:

$$p_T^{\text{jet}} = p_T^{\text{jet,rec.}} - \rho \cdot A^{\text{jet,rec.}} \quad (3.10)$$

Figure 3.15 shows the linear dependence of the average background  $p_T$  density  $\rho$  on the (uncorrected) multiplicity of tracks that are used for the jet finding (in  $|\eta| < 0.9$ ) in Pb–Pb collisions at  $\sqrt{s_{NN}} = 2.76$  TeV. For a used cut value<sup>20</sup> of  $p_T^{\text{min}} = 0.15$  GeV/c and for the 10% most central events the average value for the  $p_T$  density per unit area ( $\rho$ ) was estimated (in the study by [163]) to  $(138.32 \pm 0.02)$  GeV/c with a standard deviation of  $\sigma_\rho = (18.51 \pm 0.01)$  GeV/c. From this estimate it becomes clear that the UE contribution might have a sizeable impact on all measurements of modifications like e.g. the baryon-meson ratio in jets, jet quenching effects, etc. Therefore it has to be subtracted carefully on an event-by-event basis [163].

The second term in equation 3.9 is the uncertainty  $\delta p_T = \sigma\sqrt{A}$  of the first term and

<sup>20</sup>The median cluster also depends on the settings used for the  $k_t$  algorithm, such as the  $p_T^{\text{min}}$  cut on the charged tracks that go into the jet finder. It is usually chosen to be consistent with the same minimum  $p_T$  cut for the signal jet reconstruction

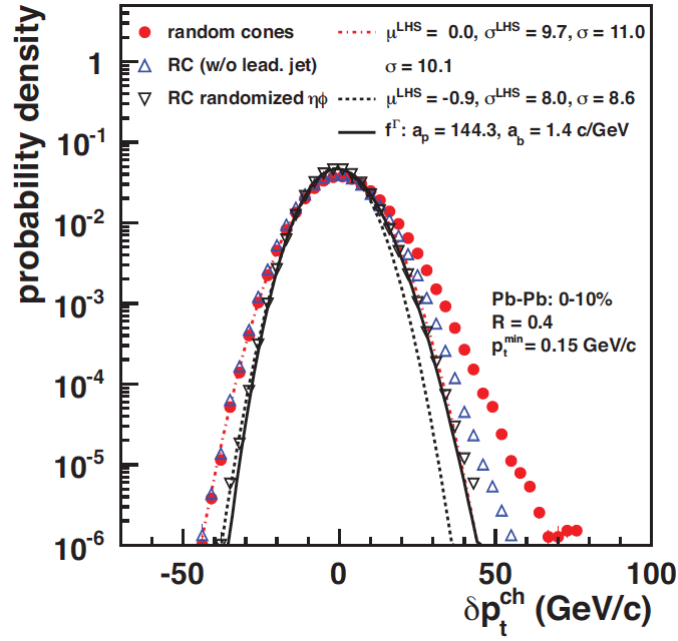


Figure 3.16:  $\delta p_T$  distribution of random cones in the 10% most central Pb–Pb events for three different kind of random cone probes with  $p_T^{\min}=0.15$  GeV/c cut. A Gaussian fit to the left-hand-side and its extrapolation to positive  $\delta p_T$  are shown for measured Pb–Pb events ( $\mu^{\text{LHS}}$  and  $\sigma^{\text{LHS}}$  in GeV/c). The solid line is a fit according to a probability distribution of  $\delta p_T$  which is shifted to zero (see reference for more details). Figure and caption adapted from [163].

corresponds to the statistical fluctuations of this noise. The fluctuations are caused by several effects that are firstly uncorrelated fluctuations of particle numbers and momenta, but also region-dependent correlations of particle momenta and the asymmetric impact of the event eccentricity (determined by the nuclear overlap during the collision). Last but not least also a non-uniform detector response can influence these region-to-region fluctuations and introduce asymmetries in track reconstruction and jet finding. To correct for these effects in jet analyses usually an "Unfolding" correction procedure is made.

A study of the UE fluctuations that was done for previous jet analyses in ALICE, is shown in Fig. 3.16. The  $\delta p_T$  distribution is derived from random cones that are placed with a random  $\phi$  and  $\eta$  value into measured events (with 0-10% event centrality). The cone size is chosen as  $R = 0.4$  which corresponds to a typical measured jet area size. All tracks inside the random cone have at minimum  $p_T^{\min}=0.15$  GeV/c. The  $\delta p_T$  is calculated as the comparison from the tracks inside the random cone and corrected with the “expected” background (calculated as  $\rho$  multiplied with the cone area  $A = \pi R^2$ ,  $R = 0.4$ ):

$$\delta p_T = \sum_i p_{T,i} - A \cdot \rho \quad (3.11)$$

As a measure of the size of the fluctuations, the  $\sigma^{\text{LHS}}$ , derived with a gaussian fit to the negative  $\delta p_T$  values, gives a value of  $\sigma^{\text{LHS}} = 8.0$  GeV/c. When using smaller jet cones (e.g.  $R = 0.2$  as used in this analysis) this  $\sigma$  is expected to decrease and the impact of the

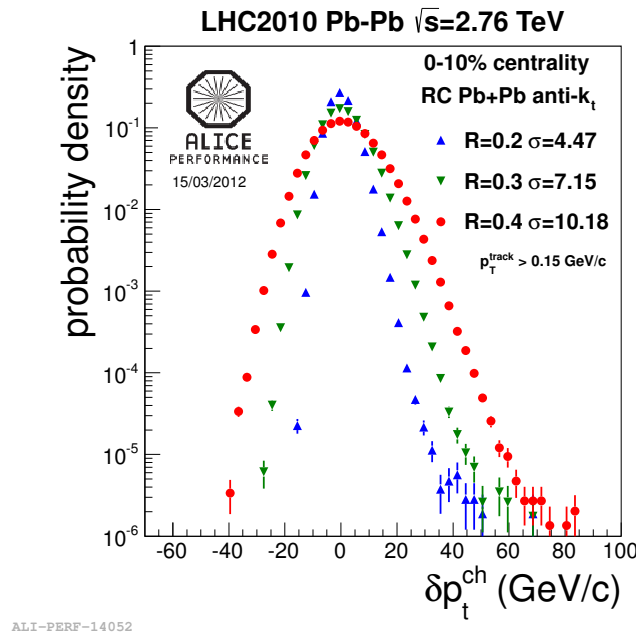


Figure 3.17:  $\delta p_T$  distribution obtained from random cones in Pb–Pb events and for different size of the jet cone ( $R = 0.4, 0.3, 0.2$ ). The  $\sigma$  of the  $\delta p_T$  decreases for smaller cone size. Figure adapted from [164].

UE fluctuations on the jet becomes smaller. That is confirmed by an ALICE performance study (see Fig. 3.17) that shows how the  $\sigma$  values of the  $\delta p_T^{\text{ch}}$  distribution decreases for a smaller jet cone size.

The following part describes the settings for the jet reconstruction used for this analysis.

### 3.2.3 Track selection

The charged tracks that go into the jet finding algorithm have to fulfill the “hybrid track” selection [165] which is a commonly used cut selection in the ALICE charged jet analyses. The cut selection cleans the track sample for the usage of only primary tracks and ensures good track reconstruction quality. In particular it avoids the selection of tracks from regions with lower tracking quality<sup>21</sup>. The hybrid tracks are selected to have uniform distribution in the  $\eta$ - $\phi$  plane. A minimum  $p_T$  cut of 150 MeV/c is applied to all jet tracks and the track acceptance is restricted to the range of  $|\eta^{\text{track}}| < 0.9$ , i.e. adjusted to the TPC acceptance.

### 3.2.4 Combinatorial jets

Since by far not all tracks found in a heavy-ion event stem from hard processes and the jet finding algorithm clusters up all tracks into jets, some of the jets are only combinatorial clustered tracks from the UE. To suppress these type of clusters from the jet sample used for the analysis, one can e.g. impose a cut on the jet area, since the jet area for combinatorial jets is normally smaller than those from signal jets. The signal jets are

<sup>21</sup>These are inefficient regions in which parts of the SPD have been switched off or had only rather poor track reconstruction efficiency during the data taking in 2011.

required to have an area of at minimum  $A_{\text{jet}} > 0.6\pi R^2$ . Furthermore combinatorial jets are more probable to have a small  $p_T^{\text{jet}}$ . By requiring that at least one jet constituent has a minimum  $p_T$  (leading constituent criterion:  $p_T^{\text{track}} > 5 \text{ GeV}/c$ ) we aim to reduce the fake jet contamination. The impact of this cut at low  $p_T^{\text{jet}}$  is clearly visible in Fig. 3.18 where the  $p_T^{\text{jet}}$  spectrum with and without this leading constituent criterion is shown.

How this leading jet track biases the jet selection e.g. in pp (i.e. without the impact of the huge charged UE in Pb–Pb) is shown in Fig. 3.19. From the ratio of the  $p_T^{\text{jet}}$  spectrum with and without this leading jet track requirement one can see that 95% of all jets above 50 GeV/c have at least one track higher than 5 GeV/c.

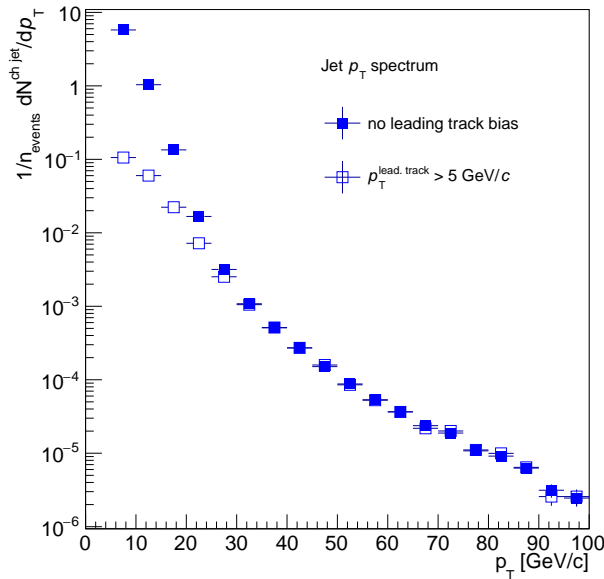


Figure 3.18: Charged jet  $p_T$  spectrum from PbPb events at  $\sqrt{s_{\text{NN}}} = 2.76 \text{ TeV}$ , with (open markers) and without (filled markers) leading track  $p_T$  bias. This cuts aim to suppress combinatorial jets at low  $p_T^{\text{jet}}$ .

However one needs to keep in mind that this value is estimated for pp collisions in the study and can change for jets in Pb–Pb events due to jet quenching effects. For the  $p_T^{\text{jet}}$  interval, relevant for the current analysis, for which the majority of all charged jets stems from the interval  $10 \text{ GeV}/c < p_T^{\text{jet}} < 20 \text{ GeV}/c$ , a sizable amount of signal jets are suppressed by this leading constituent bias, because they consist of entirely soft constituent particles. This leading track cut might also introduce a fragmentation bias by rejecting the softest signal jets (which are probably also more numerous produced due to jet quenching effects) however it is a necessary compromise to reject the huge amount of fake jets at low  $p_T^{\text{jet}}$ .

The leading constituent criterion is also used in this analysis to select all events which do not contain jets with  $p_T^{\text{lead, const}} > 5 \text{ GeV}/c$  and therefore represent a cleaner sample for particle produced by soft processes in Pb–Pb collisions. These are the so-called "non-jet" events which serve in a later analysis step to estimate the Underlying Event (UE)

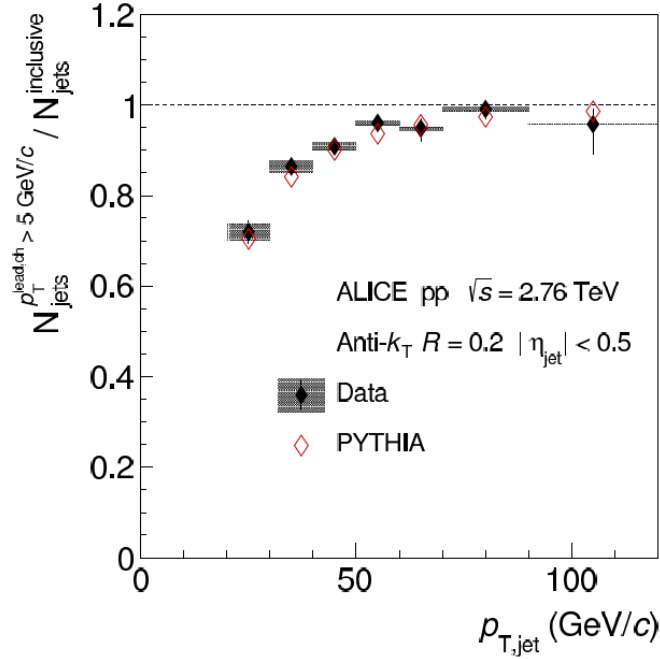


Figure 3.19: Ratio of the full jet spectra in pp at  $\sqrt{s} = 2.76$  TeV with and without leading constituent  $p_T$  requirement. The ratios are obtained from data (full markers) and MC PYTHIA simulation (open markers). Figure adapted from [84].

contribution of  $V^0$  particles (see section 3.3).

### 3.2.5 Statistics after jet selection

Apart from the "hybrid track" cut selection, the cut on the jet area and the leading constituent criterion, further requirements are imposed on the signal jets before they are finally selected for the analysis. An acceptance cut  $|\eta^{\text{jet}}| < 0.5$  on the jet pseudo-rapidity is applied in order to make sure that the jet cones of radius  $R$  cover the acceptance region of  $V^0$  particles but do not exceed it. The jet analysis only considers jets having a minimum total transverse momentum of  $p_T^{\text{jet}} > 10$  GeV/c or  $p_T^{\text{jet}} > 20$  GeV/c.

The jet spectrum measured from the around 7 million Pb–Pb events, at  $\sqrt{s_{\text{NN}}} = 2.76$  TeV and in the 2011 dataset, is shown in Fig. 3.18 and consists of around 1.5 million selected jets after all cuts (see open markers). Several observations can be made in this  $p_T^{\text{jet}}$  spectrum. Most of the statistics is contained in the lowest  $p_T^{\text{jet}}$  intervals (e.g.  $p_T^{\text{jet}} < 10$  GeV/c) which is reduced for the number of combinatorial jets, as discussed before, when requiring the leading constituent bias (compare open to full markers in the interval  $p_T^{\text{jet}} \geq 30$  GeV/c). Furthermore almost all jets from  $p_T^{\text{jet}} > 30$  GeV/c seem not to be sizably affected by this leading constituent requirement. This is indicated by the agreement of the two jet  $p_T$  spectra with (open markers) and without this leading constituent cut (full markers) for this higher  $p_T^{\text{jet}}$  values. The number of jets with higher energies (from 50 GeV/c on) are very rare in this selected sample, so that only every 10.000th event contains a selected jet of such high energy, while a jet with a  $p_T^{\text{jet}}$  around 10-20 GeV/c can be found in almost every 10th-20th event.

The focus of this analysis of strange particles in jets lies on the low energy range of the jet  $p_T$  spectrum in contrary to most of the jet analyses that measure e.g. unidentified particle fragmentation functions and which are focusing on jets with typical momenta larger than 30-50 GeV/c. This has several reasons and is motivated by the expectation that modifications of jet constituents can be seen rather at lower than at larger energies e.g. as seen by the CMS measurement of medium modified fragmentation functions for (unidentified) jet constituents (see publication by CMS collaboration [9] or in Fig. 1.22 in first chapter). In the context of this analysis it is of advantage to study these very low energetic jets, since most of the statistics are available in the  $p_T^{\text{jet}}$  range of around 5-30 GeV/c. However, only jets with  $p_T^{\text{jet}} > 10$  GeV/c are used for the analysis, that aims to decrease an possible impact of the UE fluctuations on the jets. In addition to this choice of  $p_T^{\text{jet}}$  a correction of the impact of the UE on the  $V^0$   $p_T$  spectra in jets is applied and described later in section 3.5.

The need for large statistics is mainly caused by the signal extraction that is used in this analysis. It starts to work in a satisfying way once a minimum number of found  $V^0$  candidates for the invariant mass distributions and in the different intervals in  $V^0$  and jet  $p_T$  is available in order to form a visible signal peak on top of the combinatorial background<sup>22</sup>. In this analysis this requires (together with all selection cuts for jets and the  $V^0$  particles) at least around 1 million selected jets from the data set. Almost 47% of them are jets with  $p_T^{\text{jet}} > 10$  GeV/c, that can be used for the analysis.

### 3.3 Identification of $V^0$ particles in jet cones

In this section some general information about this analysis is given, then all correction procedures on the uncorrected particle yields are described in detail.

Both the inclusive  $V^0$  hadrons and the reconstructed jets can be combined for this analysis of identified strange hadrons in charged jets. To obtain the  $V^0$   $p_T$  spectra inside the jet cone, a  $V^0$ -jet matching is done, based on the geometrical condition in Eq. 3.12 and as illustrated in Fig. 3.20. This matching requires that the angular distance between the momentum vector of the strange hadron and the jet axis is smaller than the (constant) cone size  $R$ :

$$\sqrt{(\phi_{V^0} - \phi_{\text{jet}})^2 + (\eta_{V^0} - \eta_{\text{jet}})^2} < R \quad (3.12)$$

For the analysis  $R = 0.2$  is chosen.

In the context of this analysis the Underlying event (UE) is defined as the sum of all particles which were not produced via hard parton fragmentation. The resulting  $V^0$  yield inside the jet cone (JC) is composed by the following hadrons (h) which are stemming from different origins:

---

<sup>22</sup>In cases where no combinatorial  $V^0$  background was visible in the sideband regions, all entries in the peak region were collected by integration. That ensures that in the ideal case of 100% signal purity the signal extraction works in a correct way.

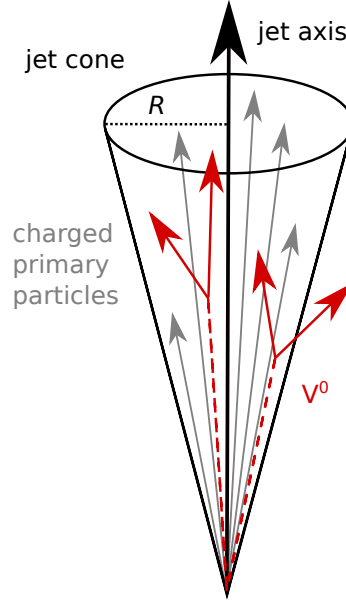


Figure 3.20: Jet- $V^0$  particle matching via a geometrical requirement (see definition in Eq. 3.12).

- $N_h^{\text{jet,true prim. FF}}$ : these are hadrons produced via jet fragmentation, they consist of charged and neutral hadrons. The charged particles are used for the jet reconstruction. Once they decay into charged daughter tracks, they could in principle contribute to the jet constituents. However, the special cut selection (“hybrid cut selection”) used for the charged track sample that is used for the jet finding, suppresses these secondary tracks with a cut on their distance of closest approach (DCA) to the primary vertex of the event (see “hybrid track cut selection” E.1).
- $N_h^{\text{jet,sec.}}$ : are jet constituents which are not primary particles but stemming from decays of heavier hadrons (their contribution is suppressed with a DCA cut imposed on the charged track w.r.t the primary vertex of the event, as well).
- $N_h^{\text{UE,true prim.}}$ : are primary hadrons (i.e. not coming from particle decays) stemming from the UE.
- $N_h^{\text{UE,sec.}}$ : are hadrons from decays of UE particles. For the  $K_S^0$  and  $\Lambda(\bar{\Lambda})$  particles, the most relevant source of secondary particle contribution are decays from the  $\Xi$  into  $\Lambda$  and a  $\pi$ . The relevant decay channels for the strange hadrons are the following:
  - $\Xi^{0,-} \rightarrow \Lambda + \pi^{0,-}$  (via weak decay,  $\tau \approx 2 \times 10^{-10}$  s), this contribution is estimated as the “feed-down” fraction  $f^{\text{FD}}$  and serves as a correction for the  $\Lambda$  particles (see following section 3.4)
  - $\Omega^- \rightarrow \Lambda + K^-$  (weak decay,  $\tau \approx 8 \times 10^{-11}$  s), this is assumed to be negligible since it contributes to the feed-down with a factor of 6-10 times smaller than the  $\Xi^{0,-}$  decays

- $\Sigma^0 \rightarrow \Lambda + \gamma$  (electromagnetic decay,  $\tau \approx 7 \times 10^{-20}$  s), since it has a very short decay length, its decay vertex cannot be separated from the  $\Lambda$  primary vertex and is therefore considered as a primary particle
- $\Sigma^{*+,*0,*-} \rightarrow \Lambda + \pi^{+,0,-}$  (strong decay,  $\tau \approx 2 \times 10^{-23}$  s), considered as a primary particle since the decay vertex also cannot be resolved due to its very short decay length
- $\varphi(1020) \rightarrow K_S^0 + K_L^0$  (strong decay,  $\tau \approx 2 \times 10^{-22}$  s), included in primary particles as well (also due to very short decay length)

In total all these mentioned contributions add up to the total uncorrected yield of  $V^0$  particles inside the jet cone:

$$N_h^{\text{JC}} = N_h^{\text{jet,true prim. FF}} + N_h^{\text{jet,sec.}} + N_h^{\text{UE,true prim.}} + N_h^{\text{UE,sec.}} \quad (3.13)$$

Although there is no feed-down to be considered for the  $K_S^0$  particles, for the  $\Lambda(\bar{\Lambda})$  particles however the following sources of feed-down have to be regarded:

$$N_\Lambda^{\text{jet,sec.}} = N_\Lambda^{\text{jet,\Xi} \rightarrow \Lambda} + N_\Lambda^{\text{jet,\Omega} \rightarrow \Lambda}$$

$$N_\Lambda^{\text{UE,prim.}} = N_\Lambda^{\text{UE,prim.}} + N_\Lambda^{\text{UE,\Sigma} \rightarrow \Lambda}$$

$$N_\Lambda^{\text{UE,sec.}} = N_\Lambda^{\text{UE,\Xi} \rightarrow \Lambda} + N_\Lambda^{\text{UE,\Omega} \rightarrow \Lambda}$$

### 3.4 Corrections on inclusive and intra-jet $V^0$ particles

Starting from the uncorrected  $V^0$   $p_T$  spectra (inclusive, in jet cone or in bulk of the event), several corrections need to be applied in order to obtain the fully corrected  $p_T$  spectra. These different corrections are described in this section. The following section 3.5 describes one correction (called the ‘‘PYTHIA Embedding study’’) to the UE  $V^0$   $p_T$  spectrum, that aims to correct for the impact of the UE fluctuations on the  $V^0$  yields.

The fully corrected  $V^0$  yields for the inclusive  $p_T$  spectrum is obtained as:

$$N_{V^0}^{\text{incl.}}(p_T) = \frac{1}{N_{\text{ev}}} \cdot \frac{N_{V^0}^{\text{uncorr.,incl.}}(p_T)}{\epsilon_{V^0}(p_T)} (1 - f^{\text{FD, incl.}}(p_T)) \quad (3.14)$$

Where  $N_{V^0}^{\text{uncorr.,incl.}}(p_T)$  is the inclusive, uncorrected  $V^0$  yield (per 1 GeV/c) of a certain  $p_T$  interval (inside the  $\eta$  acceptance and from events out of the 10% centrality interval).  $N_{\text{ev}}$  is the the number of events to which the spectrum is normalized and  $\epsilon_{V^0}(p_T)$  denotes the correction for the  $V^0$  reconstruction inefficiency. The correction for the feed-down fraction  $f^{\text{FD, incl.}}$  for the  $\Lambda(\bar{\Lambda})$  baryons is then done as the last correction step by the factor  $(1 - f^{\text{FD, incl.}}(p_T))$ .

<sup>22</sup>To express the hadron yield per GeV/c the yield per  $p_T$  interval is divided by its bin width.

For the analysis of the hadrons in jets, this calculation needs to be modified. Firstly the  $V^0$  yield is measured in the different hadron  $p_T$  and  $p_T^{\text{jet}}$  intervals. To provide the highest possible measurement accuracy in terms of the  $V^0$   $p_T$  binning and because of the limited particle statistics in the jet cone measurements, the  $p_T^{\text{jet}}$  intervals have been chosen to

$$p_T^{\text{jet}} \in \{(10.0 - 100.0), (20.0 - 100.0)\} \text{ (GeV/c)}$$

The content inside the jet cone, corrected for the limited reconstruction efficiency for the hadrons inside the jet cone (in intervals of the  $V^0$   $p_T$ ), is then given by

$$N_{V^0}^{\text{jet,FF}}(p_T, p_T^{\text{jet}}) = (N_{V^0}^{\text{JC}}(p_T) - N_{V^0}^{\text{UE}}(p_T) \cdot \text{CF})(1 - f^{\text{FD, Incl.}}(p_T)) \quad (3.15)$$

where  $N_{V^0}^{\text{JC}}(p_T)$  is the (efficiency-)corrected  $V^0$  yield in the jet cone, normalised to the number of jets times the cone area ( $N_{\text{jets}} \cdot \pi R^2$ ) and corrected for the  $V^0$  reconstruction efficiency in the jet cones (which is different compared to the inclusive  $V^0$  efficiency and described in more detail in section 3.4.2).

$N_{V^0}^{\text{UE}}(p_T)$  is the (efficiency-)corrected  $V^0$  yield in the UE, measured in “no-jet” events, corrected for the efficiency in this selected class of events and normalised<sup>23</sup> to the number of “no-jet” events times the event area  $N_{ev,NJ} \cdot A_{ev}$ .

$A_{ev}$  is given by the  $V^0$ -acceptance  $\Delta\phi \cdot \Delta\eta = 2\pi \cdot 1.4$ .

“CF” is a correction factor which is obtained by embedding of PYTHIA jets into real Pb–Pb events to study the UE fluctuations. This correction procedure is described in detail in the following section 3.5.

As the final step of this correction the  $\Lambda(\bar{\Lambda})$  feed-down is subtracted by the term  $(1 - f^{\text{FD, Incl.}}(p_T))$ . For the  $K_S^0$  mesons the same strategy as in Eq. 3.15 is used, however there is no feed-down contribution that needs to be subtracted.

In the following more information is given on the individual correction steps, such as the reconstruction efficiency, the subtraction of the UE  $V^0$  contribution, the feed-down fraction and some more detailed analysis checks.

### 3.4.1 $V^0$ reconstruction efficiency

In real life, any particle detector is not a fully efficient apparatus and one has to correct the measured raw particle spectrum for the limited efficiency, with which the tracks have been reconstructed. The reason for this inefficiency can be e.g. detector elements which were switched-off or that have performed with a lower quality during the data taking. In addition to that, dead regions in particle detectors (like e.g. mechanical support structures in between the detector segments) cannot contribute to the data taking and decrease the overall reconstruction efficiency of the detector. Furthermore all tracks with lower reconstruction quality that have been rejected for the analysis are missing in the analysed data and therefore lower the particle detection efficiency.

The calculation of this correction starts with the inclusive  $V^0$  spectra. The inclusive  $K_S^0$  and  $\Lambda(\bar{\Lambda})$  yields are corrected for the reconstruction efficiency with HIJING Monte Carlo [166]

<sup>23</sup>This normalisation is needed because of the different active areas that the  $V^0$  measurement in the jet cones compared to the UE  $V^0$  estimation method have.

generated Pb–Pb events, using a realistic GEANT3 [167] simulation of all detector features and geometries that also affected the real data during data taking. The MC generated events undergo the full detector simulation and are reconstructed with the same procedure and the same reconstruction cuts that are also used for the real data. The reconstruction efficiency is defined as the ratio of all  $K_S^0$  and  $\Lambda$  ( $\bar{\Lambda}$ ) hadrons that are reconstructed in the MC data (i.e. after undergoing the detector simulation) and the particles generated for the MC true distributions, as expressed in Eq. 3.16. It furthermore considers only  $V^0$  particles decaying via the  $V^0$  topology with which the invariant mass is calculated<sup>24</sup>.

$$\epsilon(p_{T,\text{gen.}}^h, p_{T,\text{gen.}}^{\text{jet}}, (\eta_{T,\text{gen.}}^h, \eta_{T,\text{gen.}}^{\text{jet}})) = \frac{N_h^{\text{associated}}(p_{T,\text{gen.}}^h, p_{T,\text{gen.}}^{\text{jet}}, (\eta_{T,\text{gen.}}^h, \eta_{T,\text{gen.}}^{\text{jet}}))}{N_h^{\text{generated}}(p_{T,\text{gen.}}^h, p_{T,\text{gen.}}^{\text{jet}}, (\eta_{T,\text{gen.}}^h, \eta_{T,\text{gen.}}^{\text{jet}}))} \quad (3.16)$$

The reconstructed particles (“detector level” hadrons) that are “associated” (ass.) to the MC generated truth (“particle level” hadrons), have to fulfill the following requirements:

- The reconstructed particles pass the  $V^0$  cut selection (see chapter 3.1, table 3.2)
- The two MC daughter particles originate both from the same MC mother particle
- All MC particles that are considered in this reconstruction belong to the correct hadron species
- The MC particle have the correct reconstructed invariant mass (i.e. they contribute to the mass window used for the signal extraction on the detector level)
- The MC mother particle ( $K_S^0$  or  $\Lambda$  ( $\bar{\Lambda}$ ) particle) are primary particles (i.e. they are originating from the primary event vertex)
- Only MC mother particles within the  $V^0$   $\eta$  acceptance are accepted ( $\eta_{V^0, \text{MC ass.}} < 0.7$ )

The MC generated particles which are contributing to the denominator of equation 3.16 have to pass these requirements:

- All MC particles involved in the  $V^0$  decay topology belong to the correct hadron species
- They fall inside the  $\eta$  acceptance (the corresponding cut is applied on the "particle level":  $\eta_{V^0, \text{MC gen.}} < 0.7$ )
- The  $V^0$  particle is primary-like (there is no mother particle for the  $V^0$  hadron existing on the MC stack, carrying the MC true particle information)

<sup>24</sup>In the case the branching ratios are included in the estimation of the  $V^0$  reconstruction efficiency the maximum reachable efficiency is determined by the branching ratio. Furthermore the  $\eta$  acceptance is included into the efficiency definition, as done here for  $V^0$  particle with  $|\eta(V^0)| < 0.7$ .

The  $V^0$  reconstruction efficiency obtained for the inclusive  $V^0$   $p_T$  distribution is shown in Fig. 3.21 for the three different particle types.

It reaches small values at low hadron  $p_T$  which is mainly caused by the fact that these slow  $V^0$  particles decay into daughters that are partially located outside<sup>25</sup> the track acceptance of  $|\eta| < 0.8$  and therefore their  $V^0$  mother particle does not contribute to the selected amount of  $V^0$  particles. Many of these candidates are removed by the analysis cut selection that uses a minimum (transverse) decay length of 5 cm. The efficiency quickly rises with increasing  $p_T$  and reaches its maximum value around 3-4 GeV/c. For very high  $p_T$  values it is slightly decreasing again, since these  $V^0$  particles decay rather late inside the TPC active volume and cannot produce enough TPC clusters to be reconstructed, furthermore  $V^0$  candidates with a decay length longer than 100 cm are rejected. The main difference between the  $\Lambda(\bar{\Lambda})$  and the  $K_S^0$  reconstruction efficiency at higher transverse momentum ( $\sim 3$ -10 GeV/c) are the different average decay lengths (the  $K_S^0$   $c\tau$  is  $\sim 2.68$  cm, the  $\Lambda(\bar{\Lambda})$   $c\tau$  is  $\sim 7.89$  cm) which makes it more probable for the  $\Lambda$  hadrons to decay deeper inside the TPC active volume than most of the  $K_S^0$  do. That causes the  $\Lambda$  efficiency to be about 10% smaller for  $p_T > 3$  GeV/c compared to the  $K_S^0$  efficiency. At very low  $V^0$   $p_T$ , the  $\Lambda$  and  $\bar{\Lambda}$  particles show a small difference, due to the absorption of the  $\Lambda$  daughters ( $p^+$ ) in the detector material.

### 3.4.2 Acceptance correction

In the following, a correction procedure on the reconstruction efficiency for  $V^0$  hadrons in the jet cone and in "no-jet" events is presented. It is needed, in order to take the  $\eta$  dependence of the different  $V^0$  distributions into account (whose statistics do not allow to estimate the dedicated efficiencies directly as a function of  $\eta$  and  $p_T$ ), and correct for the MC simulated distributions which do not reproduce the real shapes. For this correction the binning in  $V^0$   $\eta$  in the region close to mid-rapidity is done in steps of 0.1 in  $\eta$ :

$$\eta(V^0) \in \{-0.7, -0.65, -0.6, \dots, -0.1, 0.0, 0.1, \dots, 0.6, 0.65, 0.7\}.$$

At larger  $\eta$  and on both sides of the  $\eta$  acceptance, one smaller interval of 0.05 is chosen, to take better into account the decreasing of the efficiency at the edges.

It has been seen, when comparing the efficiency for several  $\eta$ - $p_T$  intervals, that the single- $V^0$  particle efficiency  $\epsilon(\eta_{V^0}, p_T^{V^0})$  in jet cones (JC) is the same as for inclusive  $V^0$ s and also for that in the UE estimation methods:

$$\epsilon_h^{\text{JC}}(p_T^h, \eta^h, p_T^{\text{jet}}) = \epsilon_h^{\text{UE}}(p_T^h, \eta^h) = \epsilon_h^{\text{inclusive}}(p_T^h, \eta^h). \quad (3.17)$$

An increase of the local track density inside a jet cone might be expected, since tracks originating from hard parton scattering are strongly collimated close to the jet axis. In presence of many collimated tracks (and also considering the  $V^0$  daughter tracks as part of such a region) the reconstruction efficiency of the  $V^0$  particles in jet cones could be

<sup>25</sup>This is due to the decay kinematics, since the  $V^0$  opening angle (which is defined by the two daughter tracks) increases for decreasing  $V^0$   $p_T$ .

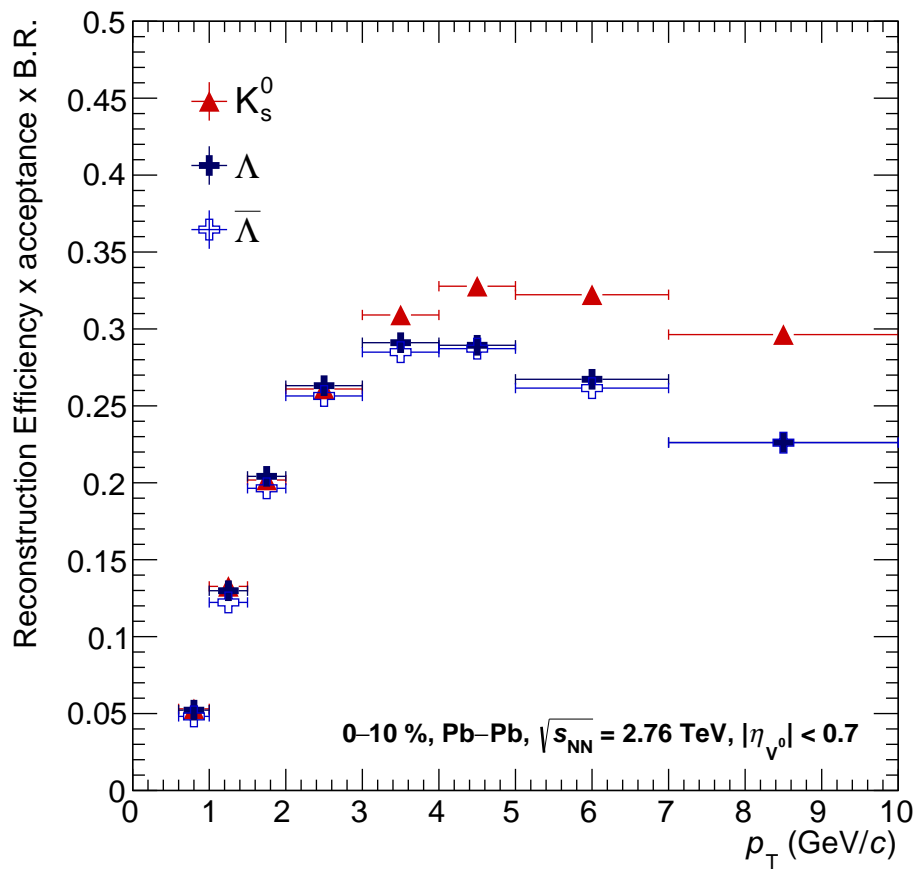


Figure 3.21: Reconstruction Efficiency of inclusive  $V^0$  particles in  $|\eta_{V^0}| < 0.7$ .

expected to be slightly smaller. However, no hint on such local track density dependence of the efficiency is found.

The right plot in Fig. 3.22 shows the probability density for the  $K_S^0$  production (as obtained from the MC simulation) as a function of  $\eta$  and for different  $p_T$  intervals. The left plot shows the MC true  $K_S^0$  probability density as a function of the  $V^0$   $\eta$ . The different  $\eta$  shape of the distribution (when compared to the left plot) corresponds to a convolution of the inclusive  $V^0$   $\eta$  distribution with the one of the selected (reconstructed) jets.

Because the reconstruction efficiency is calculated as a function of  $p_T$  and integrated over  $\eta$ , the MC generated  $V^0$  distributions have to reproduce this particular shape in  $\eta$  properly. Unfortunately this is not the case as can be seen in Fig. 3.22. In order to avoid a possible bias, a “MC reweighting” method is developed and used for the efficiency calculation in the jet cones, taking into account the correct  $\eta$  dependence of the measured spectra in the jet cones. This method works as follows.

A two-dimensional efficiency estimation is done for the inclusive particles as a first step which is shown in Fig. 3.23.

As a second step the (uncorrected) measured  $V^0$  (candidate) distributions inside the jet cone and in intervals of  $(p_T^{\text{jet}}, \eta_{V^0}, p_T^{V^0})$  are calculated. The  $V^0$  particle yield in each interval  $m(p_T^{V^0}, \eta_{V^0}, p_T^{\text{jet}})$  inside the jet cone (or in the UE method), is derived by using information from the signal extraction of the inclusive distributions.

In this way the yields  $m^{\text{JC,UE}}(p_T^{V^0}, \eta_{V^0}, p_T^{\text{jet}})$  in the corresponding invariant mass distribution (in the JC or UE) are sampled in the signal region (see Eq. 3.19) and multiplied by the signal purity  $P_{\text{incl.}}$  from the inclusive  $V^0$  distributions:

$$P_{\text{incl.}} = \frac{\text{Signal}}{\text{Signal} + \text{Background}} \quad (3.18)$$

as shown in Fig. 3.24.

For the signal purity we make the assumption to be the same for the inclusive  $V^0$  candidates as inside the jet cone or in the UE.

$$m^{\text{JC,UE}}(p_T^{V^0}, \eta_{V^0}, p_T^{\text{jet}}) = m_{\text{cand.}}(p_T^{V^0}, \eta_{V^0}, p_T^{\text{jet}}) \Big|_{\text{signal region}} \cdot P_{\text{incl.}}(p_T^{V^0}, \eta_{V^0}) \Big|_{\text{signal region}} \quad (3.19)$$

These measured distributions  $m^{\text{JC,UE}}(p_T^{V^0}, \eta_{V^0}, p_T^{\text{jet}})$  serve to reproduce the correct  $\eta$  shapes in the MC distributions.

From that point on, their distribution is considered as the one of the "associated"  $V^0$  particle distributions ("detector level" MC particles):

$$m^{\text{JC,UE}}(p_T^{V^0}, \eta_{V^0}, p_T^{\text{jet}}) = a_{\text{MC,rew.}}^{\text{JC,UE}}$$

and without statistical errors  $\sigma_m = 0$ .

As a next step, they are divided by the inclusive efficiency (in the corresponding  $\eta - p_T$

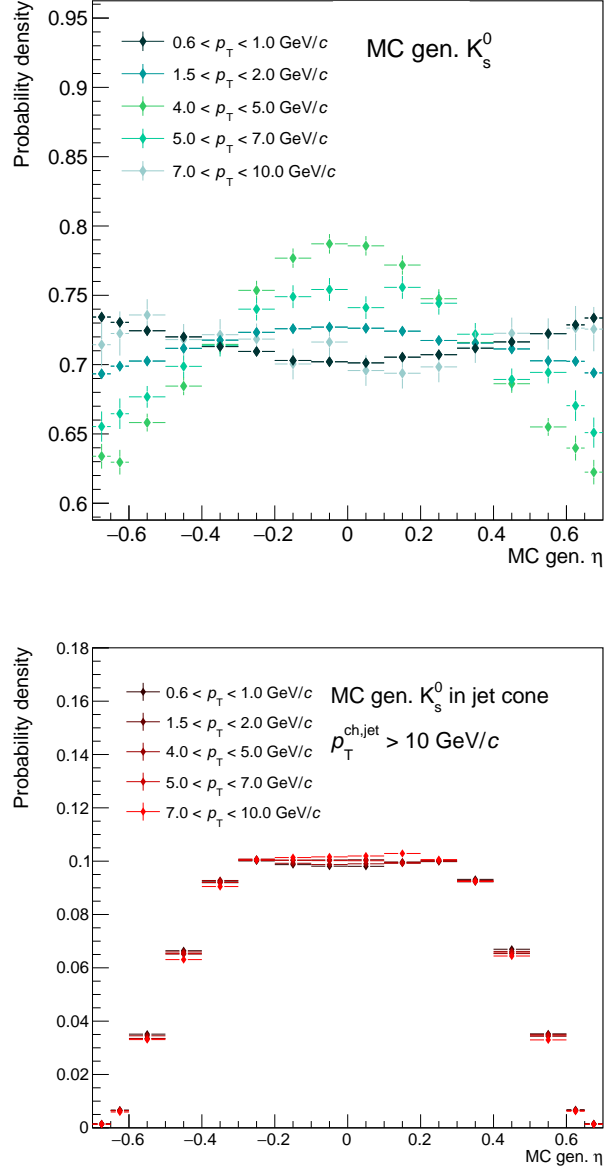


Figure 3.22: (Upper plot) MC true  $K_S^0$   $\eta$  probability density for different  $V^0$   $p_T$  intervals. The shape of this distribution in  $\eta$  is varying for the different  $p_T$  intervals. (Lower plot) MC generated  $K_S^0$   $\eta$  probability distribution inside a jet cone ( $R = 0.2$ ), for different intervals of the  $V^0$   $p_T$  and for  $p_T^{\text{jet}} > 10$  GeV/c.

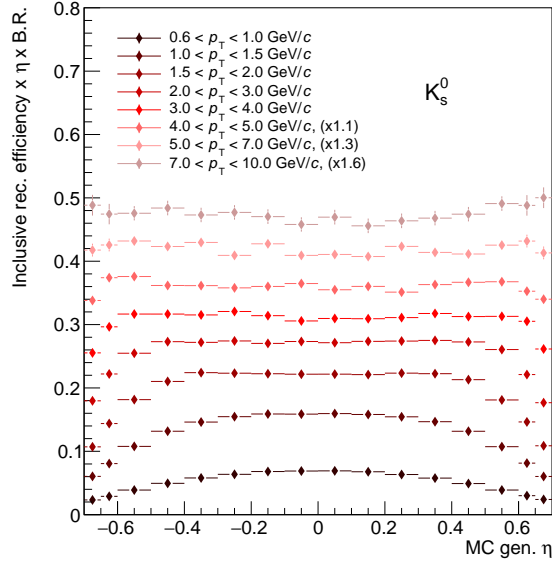


Figure 3.23: Inclusive  $V^0$  reconstruction efficiency as a function of MC true  $V^0$   $\eta$  for different  $V^0$   $p_T$  intervals. These efficiency distributions are the starting point of the MC "re-weighting" procedure.

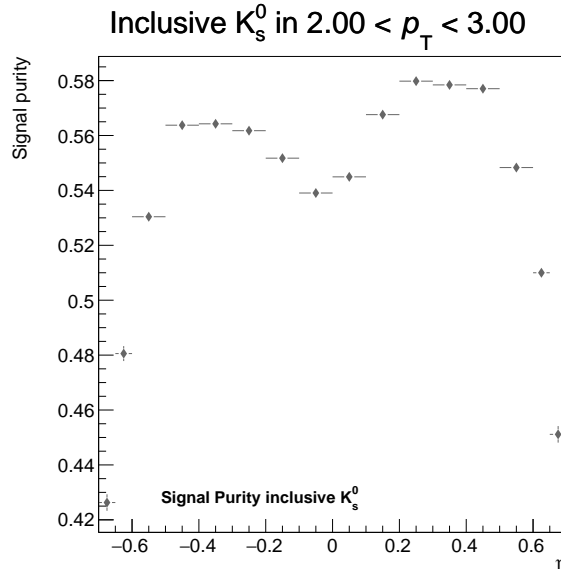


Figure 3.24: Example for signal purity (Signal/Signal+Background) from the inclusive  $V^0$  signal extraction as a function of  $V^0$   $\eta$  (and for the  $V^0$   $p_T$  interval 2-3 GeV/c).

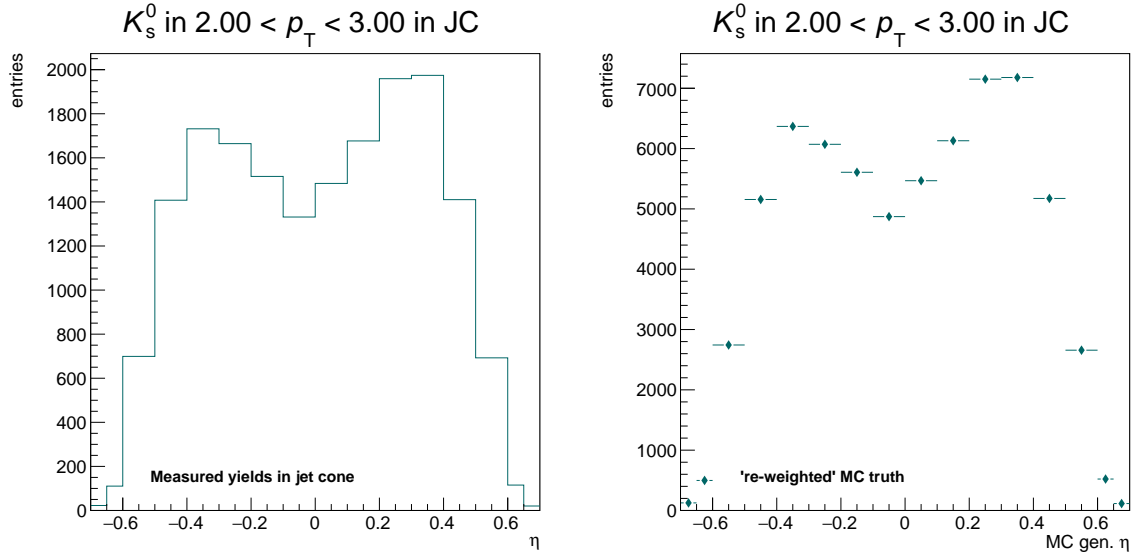


Figure 3.25: Two examples are shown for the measured  $K_S^0$   $\eta$  distribution inside the jet cone (left plot) and the MC generated  $K_S^0$   $\eta$  distribution (right plot) obtained from the "reweighting" with the shape of the measured distribution. The thus obtained MC truth is used to estimate finally the ("reweighted")  $K_S^0$  reconstruction efficiency in the jet cone.

interval)  $\epsilon(\eta_{V^0}, p_T^{V^0})$  to serve as the "re-weighted" MC truth

$$g^{\text{JC,UE}_{MC,rew.}}$$

(i.e. the denominator of the efficiency in jet cones  $\epsilon^{\text{JC,UE}}(p_T^{V^0})$ ) (for the corresponding distribution see right plot in Fig. 3.25) which now correctly describes the  $\eta$ -shapes (which have been measured in the data).

Afterwards the yields are integrated over  $\eta$ , separately for each  $p_T$  bin:

$$g_{\text{MC,rew.}}^{\text{JC,UE}}(p_T^{V^0}, \eta_{V^0}, p_T^{\text{jet}}) = \sum_{\eta_{V^0}} \frac{m^{\text{JC,UE}}(p_T^{V^0}, \eta_{V^0}, p_T^{\text{jet}})}{\epsilon^{\text{incl.}}(\eta_{V^0}, p_T^{V^0})} \quad (3.20)$$

Finally the "reweighted" efficiency in the jet cone is obtained:

$$\epsilon^{\text{JC,UE}}(p_T^{V^0}) = \frac{a_{\text{MC,rew.}}(p_T^{V^0}, \eta_{V^0}, p_T^{\text{jet}})}{g_{\text{MC,rew.}}(p_T^{V^0}, \eta_{V^0}, p_T^{\text{jet}})} \quad (3.21)$$

Figure 3.26 shows the so estimated reconstruction efficiencies for  $K_S^0$ ,  $\Lambda$  and  $\bar{\Lambda}$  particles in jet cones (JC) and for jets with  $p_T^{\text{jet}} > 10$  GeV/c.

Figure 3.27 shows the "reweighted" efficiency in "no-jet" events. These efficiencies are calculated for each particle type and interval in  $p_T^{\text{jet}}$  and applied to the corresponding measured  $V^0$   $p_T$  spectrum.

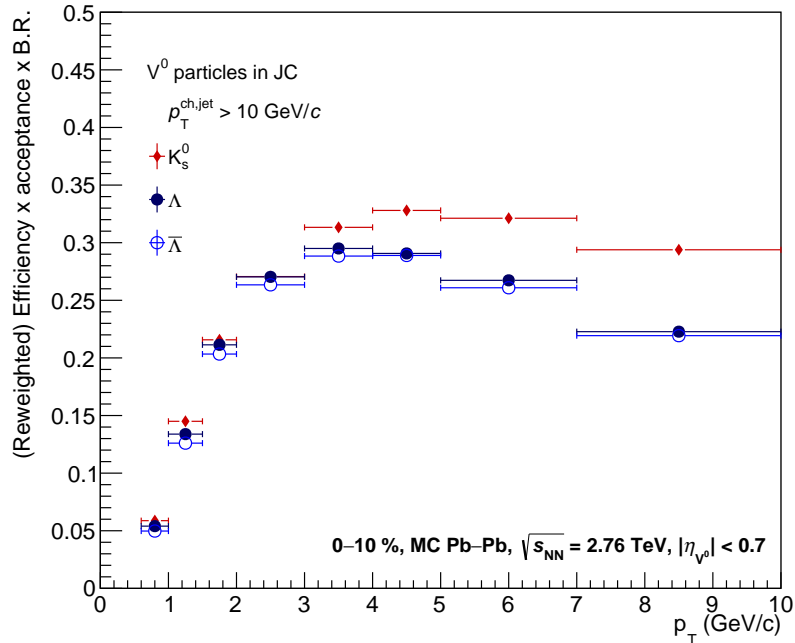


Figure 3.26: The "reweighted" reconstruction efficiency for the  $V^0$  particles inside the jet cone (within  $|\eta^{V^0}| < 0.7$ ) is calculated as a function of  $V^0$   $p_T$ . The efficiency includes furthermore the branching ratios of the  $V^0$  types.

### 3.4.3 Subtraction of particles from the Underlying Event

As a method to subtract the  $V^0$  contribution from the Underlying Event (UE), events with no selected jets are analysed. These "no-jet" events make about 80% of all analysed events in the 0–10% central events and therefore provide large statistics. The number of these events  $N_{ev,NJ}$  depends on the jet selection as already described in section 3.2.4.

Furthermore several different estimation methods (which are commonly used in jet analyses) for the  $V^0$  contribution from the UE have been developed and tested and are presented in the appendix F. Since they seem to agree within 5% at low hadron momentum we focus on the "no-jet" events as the method with the largest statistics from now on. In the following section 3.5 a correction (based on PYTHIA generated jets that are embedded into real events) to this default method is described. It is needed to correct for the effect of UE fluctuations on the UE  $V^0$   $p_T$  spectrum.

Studies based on Monte Carlo simulated jets that are embedded into real Pb–Pb events showed that for smaller jet cone sizes (as e.g.  $R = 0.2$ ) the impact of the UE to the particles in the reconstructed jets is smaller and easier to correct for (after the jet energy correction (the " $\rho$ "-subtraction) as described in the previous section 3.2.2, has been carried out) than for larger  $R$  (e.g.  $R = 0.3, 0.4$ , etc.). Therefore the choice  $R = 0.2$  has been made as a compromise between sampling the majority of particles, produced by the jet fragmentation and keeping the impact of the UE (after "average"  $\rho$  background subtraction) as small as possible.

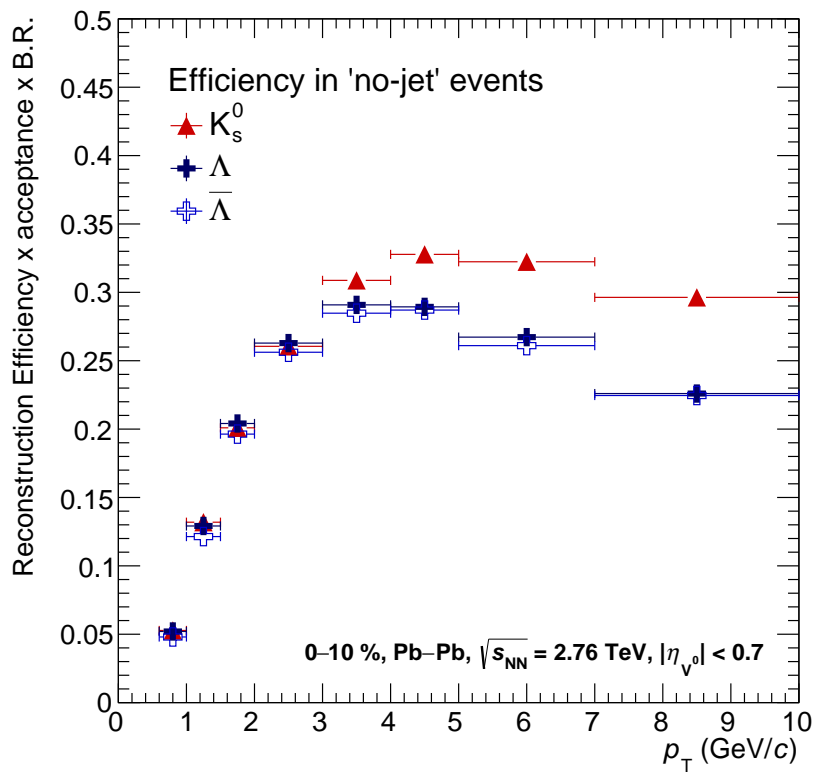


Figure 3.27: The "reweighted" reconstruction efficiency for the  $V^0$  particles in "no-jet" events and as a function of  $V^0$   $p_T$ . The efficiency considers the branching ratios as well as the  $\eta$  acceptance of the  $V^0$  particles.

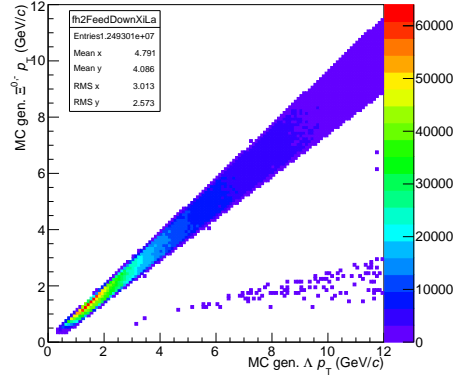


Figure 3.28: Correlation of the mother ( $\Xi$ )  $p_T$  with the daughter ( $\Lambda$ )  $p_T$  obtained from a Monte Carlo simulation of Pb–Pb collisions at  $\sqrt{s_{NN}} = 2.76$  TeV and for reconstructed inclusive MC particles.

### 3.4.4 Subtraction of decay products (“feed-down”)

#### Inclusive particles

Not all  $\Lambda$  particles populating the measured (inclusive)  $\Lambda$   $p_T$  spectrum are primary particles but they originate from a decay of heavier hadrons like e.g.  $\Xi$  baryons. This contribution has to be determined and subtracted from the inclusive  $\Lambda$  particle yields. For the  $\Lambda(\bar{\Lambda})$  particles most of the feed-down is coming from weak decays of  $\Xi^{0,-}$  ( $\bar{\Xi}^+$ ) baryons, as already described at the beginning of section 3.3. The estimation method used in this analysis is identical with the one chosen by the authors of the published ALICE paper [3, 168] that reports the inclusive analysis of  $K_S^0$  and  $\Lambda$  in Pb–Pb at  $\sqrt{s_{NN}} = 2.76$  TeV. Since we are interested in the primary  $\Lambda(\bar{\Lambda})$  particles that are produced during the collision process, the following subtraction of the  $\Lambda$  fraction (assumed to be the same for  $\bar{\Lambda}$ ) that stem from feed-down, needs to be done:

$$N_{\Lambda\text{prim.}} = N_{\Lambda\text{prim.}+\text{decay}} - N_{\Lambda\text{FD}}. \quad (3.22)$$

In order to obtain  $N_{\Lambda\text{FD}}$ , a two-dimensional histogram, the “feed-down matrix” is constructed. It combines MC simulated  $\Xi$  and  $\Lambda$  (“particle level”) yields with measured  $\Xi$  yields in order to calculate the fraction of  $\Lambda$ s that stem from  $\Xi^{0,-}$  particle decays.

For all reconstructed  $\Lambda$  particles in the MC events (which are also passing the selection cuts) it is checked, whether they are stemming from a decay<sup>26</sup> (and if yes, only the ones from  $\Xi^{0,-}$  decays are considered as feed-down  $\Lambda$ ). Then these feed-down  $\Lambda$  particles  $N_{\Lambda}^{\text{jet},\Xi \rightarrow \Lambda}$  are filled into the “feed-down matrix” (see Fig. 3.28) that correlates the (MC true)  $\Lambda$   $p_T$  with the one of the mother (MC true)  $\Xi$   $p_T$ .

The rows of this histogram are then divided by the  $p_T$  yields of the MC generated  $\Xi^-$   $p_T$  spectrum and multiplied by the  $p_T$  yields of the measured  $\Xi^-$   $p_T$  spectrum. For the

<sup>26</sup>As already mentioned in section 3.3,  $\Lambda$ s coming from  $\Omega$  and  $\Sigma$  decays are considered as primary, since their contributions are either very small (negligible compared to the one of  $\Xi$ ) or their decay vertex is indistinguishable close to the primary event vertex.

measured  $\Xi^-$   $p_T$  spectrum, it was assumed that the yields for  $p_T > 7$  GeV/c (the upper limit of the measurement) do not change significantly until  $p_T < 10$  GeV/c. Finally the columns (carrying the  $\Xi$  mother  $p_T$  information) are integrated over  $p_T$ .

The estimated amount of uncorrected (i.e. not corrected for efficiency) FD  $\Lambda$  particles for the inclusive (i.e. all particles in the acceptance)  $V^0$  particles calculates then as

$$N_{\Xi^0, - \rightarrow \Lambda}^{\text{real, incl.}}(p_T^\Lambda) = \sum_{p_T^\Xi} N_{\Xi^0, - \rightarrow \Lambda}^{\text{MC, incl.}}(p_T^\Lambda, p_T^\Xi) \frac{N_{\Xi^-}^{\text{real, incl.}}(p_T^\Xi)}{N_{\Xi^-}^{\text{MC, incl.}}(p_T^\Xi)} \quad (3.23)$$

where

- $N_{\Xi^-}^{\text{real, incl.}}$  is the measured spectrum of inclusive  $\Xi^-$  in  $|y| < 0.5$  which is normalized to the number of analysed data events [169].
- $N_{\Xi^0, - \rightarrow \Lambda}^{\text{MC, incl.}}$  is the distribution of reconstructed inclusive  $\Lambda$  particle  $p_T$  and the  $p_T$  of their  $\Xi^{0, -}$  mother particles, normalized per number of MC events.
- $N_{\Xi^-}^{\text{MC, incl.}}$  is the spectrum of inclusive  $\Xi^-$  in  $|y| < 0.5$  generated in the MC production (which is used for this feed-down estimation) and normalized per number of MC events.

The feed-down fraction is defined as the ratio of the estimated  $N_{\Xi^0, - \rightarrow \Lambda}^{\text{real, incl.}}(p_T^\Lambda)$  spectrum divided by the uncorrected  $\Lambda$   $p_T$  spectrum  $N_{\Lambda}^{\text{real, incl., raw}}(p_T^\Lambda)$  in the data (normalized per number of real events):

$$f_{\Lambda}^{\text{FD, incl.}}(p_T^\Lambda) = \frac{N_{\Xi^0, - \rightarrow \Lambda}^{\text{real, incl.}}(p_T^\Lambda)}{N_{\Lambda}^{\text{real, incl., raw}}(p_T^\Lambda)} \quad (3.24)$$

The FD fractions obtained from this calculation and for each  $\Lambda$   $p_T$  bin are shown as the black markers in Fig. 3.29. The next paragraph shows a second approach for the FD calculation for the particles inside the jet cones.

### Feed-down from PYTHIA jets

In order to evaluate which fraction of measured  $\Lambda(\bar{\Lambda})$  particles in jets are originating from decays of  $\Xi^{0, -}$  particles in jets, one would need ideally the measured  $p_T$  spectra of  $\Xi$  hadrons inside jets. Since no such measurement is available and also not feasible with the current dataset due to statistical limitations, the feed-down fractions are estimated using (PYTHIA8 tune 4C) simulated pp jets.

For this PYTHIA FD estimate, the pp simulated events are analysed by running the *anti* –  $k_t$ -jet finder (with  $R = 0.2$ ) and collecting all MC true  $\Lambda(\bar{\Lambda})$  inside the jet cone which are also stemming from decays of  $\Xi^{0, -}$  hadrons. This FD  $\Lambda$   $p_T$  spectrum is taken and divided by the spectrum of all MC true  $\Lambda(\bar{\Lambda})$  particles (which can be both, primary and feed-down particles). Figure 3.29 shows the resulting FD fraction from PYTHIA jets for two different jet resolution parameters ( $R = 0.2$  in red markers,  $R = 0.3$  in blue markers) and for jets with  $p_T^{\text{jet}} > 10$  GeV/c. This  $\Lambda$  FD from PYTHIA jets indicates no strong

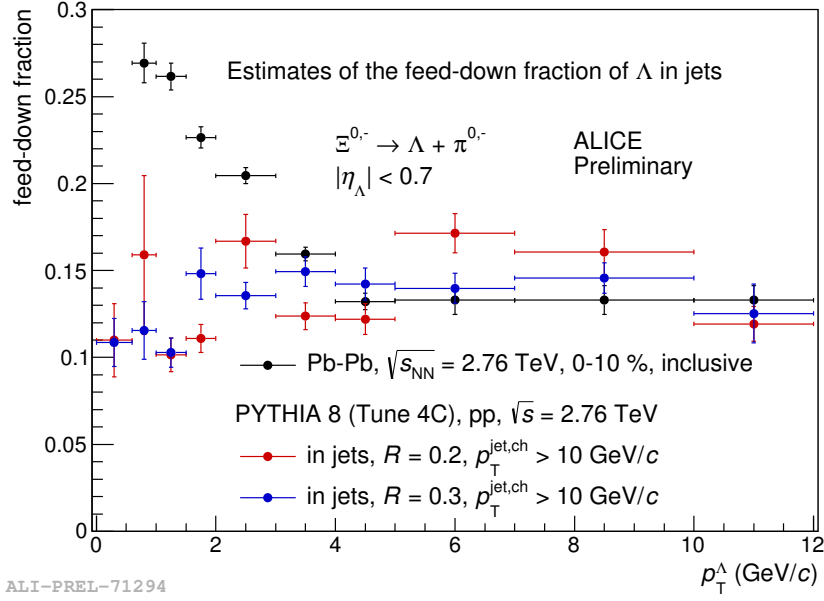


Figure 3.29: The calculated feed-down (FD) fractions obtained by the FD matrix from inclusive particles (black markers) with simulated in pp (PYTHIA8) jets (for  $R = 0.2$  in red markers, for  $R = 0.3$  in blue markers).

dependence on the  $\Lambda$   $p_T$ , therefore a constant fit (not shown in graphic) on the estimated FD in  $R = 0.2$  PYTHIA jets is used:

$$f^{\text{FD, jet}} = 0.142$$

As the default method for this FD correction however the FD fractions obtained from the inclusive particle estimate are chosen. The PYTHIA simulation of FD in pp jets serves to evaluate the systematic uncertainty of this subtraction. These two approaches represent two "extreme" scenarios, since the  $\Lambda$  FD from the inclusive analysis is expected to overestimate the real  $\Lambda$  FD in jets in Pb–Pb collisions while the simulated FD from pp jets only subtracts a small FD fraction inside the jets in Pb–Pb collisions.

### 3.4.5 Correction of the jet transverse momenta

As already described in section 3.2.2, the total transverse momentum of a measured jet is affected by several effects. On one hand the detector response (affected by the efficiency of the single-track (i.e. also the  $V^0$ ) reconstruction and the jet momentum resolution) modifies the "true" value of the  $p_T^{\text{jet}}$ . On the other hand there exists the huge contamination of the jet content by soft  $p_T$  particles from the UE (commonly up to one order of magnitude more tracks, than those stemming from the fragmentation itself). The total jet transverse momentum is mostly corrected by the subtraction of the average background density on an event-by-event basis. However the background density in a given event is not completely

isotropic<sup>27</sup> and shows local fluctuations (which determines the measured  $p_T^{\text{jet}}$  resolution). This effect is usually accumulated in a  $\delta p_T$  distribution which is used for the unfolding of the jet spectra which however requires sufficient statistics of all the entangled observables. In addition also the calculation of the jet area, and therefore the calculation of the average  $p_T$  density from the UE  $\rho$  suffers from numerical fluctuations.

In this analysis the relevant observables are  $p_T^{\text{jet}}$  and  $p_T^{\text{h}}$  of associated particles (in jets). In order to correct such a distribution  $f^{\text{measured}}$  for the effects of the detector response (via a response matrix  $RM_{\text{det}}$ ) and the UE fluctuations ( $RM_{\text{bkg}}$ ) one would need to perform a two-dimensional unfolding:

$$f^{\text{measured}} = RM_{\text{bkg}} \times RM_{\text{det}} \times f^{\text{true}} \quad (3.25)$$

which requires a measurement of the  $V^0 p_T$  distributions in jets down to very low jet momenta ( $p_T^{\text{jet}} \leq 5 \text{ GeV}/c$ ) in order to enable the unfolding to work properly. However no such measurement is feasible for the current analysis.

The approach used for this analysis is firstly to use open  $p_T^{\text{jet}}$  bins in order to select a hard scattering process by imposing a cut on the minimum reconstructed  $p_T^{\text{jet}}$  and to maximise statistics in terms of the jets. Secondly since the results of this analysis cannot be corrected for the  $p_T^{\text{jet}}$  smearing by the fluctuations of the charged UE, the reference result is “smeared”. The reference is provided by PYTHIA simulations or a measurement in p–Pb collisions and presented in the following chapter 4. It is smeared according to the  $\sigma$  value of the corrected (“true”)  $\delta(p_T^{\text{jet}})$  distribution that was studied for the charged jet suppression analysis in ALICE (for more details see [171]).

### 3.5 Impact of Underlying Event fluctuations on the measurements

To estimate a possible impact of the background fluctuations in Pb–Pb collisions the following “PYTHIA jet embedding” study is done. This provides a valuable alternative to estimate these effects of the UE on the final results. The origin of these rather complex effects on the jet constituent spectrum lies in the steeply falling  $p_T^{\text{jet}}$  spectrum, in which each jet is smeared by the UE fluctuations, following a gaussian function. In this way, softer jets (with a steeper falling constituent  $p_T$  spectrum) are systematically pushed into bins of higher  $p_T^{\text{jet}}$  which affects the analysed jet  $p_T$  spectrum (with a certain  $p_T^{\text{jet}}$  value) as well as the selection of jets falling into the selected  $p_T^{\text{jet}}$  intervals in a systematic way. The net effect is that the fluctuations soften these jet constituent spectra.

---

<sup>27</sup>Although in the 10% most central events there is no strong dependence on the (2nd or 3rd harmonic) event plane angle expected (the charged particle elliptic flow e.g. has a maximum  $v_2$  of around 2-4% in the relevant range of this analysis and for the same centrality interval which indicates a rather small event asymmetry [170])

### 3.5.1 Embedding of PYTHIA jets into PbPb events

The method of the jet embedding is done in the following way. First a real Pb–Pb event is taken from a “AOD”<sup>28</sup> and the charged tracks as well as the  $V^0$  particles of a PYTHIA simulated event, which is containing selected jets, are added to this AOD file on a event-by-event basis. This results in "hybrid" events containing both real and MC simulated particles. The embedded jets are selected from a minimum-bias PYTHIA production at  $\sqrt{s_{NN}} = 2.76$  TeV. We also use a  $p_T$ -hard bin PYTHIA production<sup>29</sup> as a systematic check to study a possible impact of the shape of the jet  $p_T$  spectrum (described in more detail in the following discussion).

For the pre-selection of the PYTHIA events, the event is picked randomly from the full PYTHIA production and has to fulfill the same jet selection criteria like the signal jets in this analysis. In case the PYTHIA event contains such a selected jet, all corresponding charged tracks and  $V^0$  particles are taken and added into an "extra" branch of the Pb–Pb AOD file which also makes it possible to analyse real and simulated tracks together or separately. In case the PYTHIA event does not fulfill the jet selection criteria, a next randomly chosen event is picked until a suitable one is found for the embedding. After the embedding procedure is finished, the *anti* –  $k_t$  jet finder is run again on this new created "hybrid" events. Figure 3.30 illustrates the composition of such a “hybrid” event that consists of the huge amount of charged UE tracks from the real event (grey arrows) but also of the embedded PYTHIA jets (red arrows). On top of that, also signal jets from the real event are populating these “hybrid” events and may in few cases overlap with the embedded PYTHIA jets. To minimise and estimate the size of this effect, the PYTHIA jets can be embedded into the "no-jet" events, i.e. real events, in which no jet is selected (more about that procedure can be found later in this section).

In the following these PYTHIA embedded tracks are referred to as

- "extraonly" tracks, if they are not mixed with the "signal" tracks from the real event (in which they are embedded).
- In the case, both type of tracks are mixed i.e. for the “hybrid” events, all these tracks together are labeled as “extra tracks”.
- The signal tracks from the real event alone are labeled as "standard" tracks.

### 3.5.2 Datasets

The following data sets are used for the jet embedding study. For the PYTHIA simulation the minimum bias production "LHC12f1a" (pp at  $\sqrt{s} = 2.76$  TeV, Pythia-8 minimum-bias production) at the same energy is taken. The signal events are taken from the same run selection that was used for this analysis of the 2011 Pb–Pb data.

<sup>28</sup>The “AOD” is a compressed data file format which contains the relevant information for the analysis.

<sup>29</sup>The  $p_T$ -hard bin PYTHIA production provides an strongly enhanced production of jets from a certain  $p_T^{\text{jet}}$  interval that helps to estimate corrections and carry out studies in the Monte-Carlo simulated data with higher statistical precision.

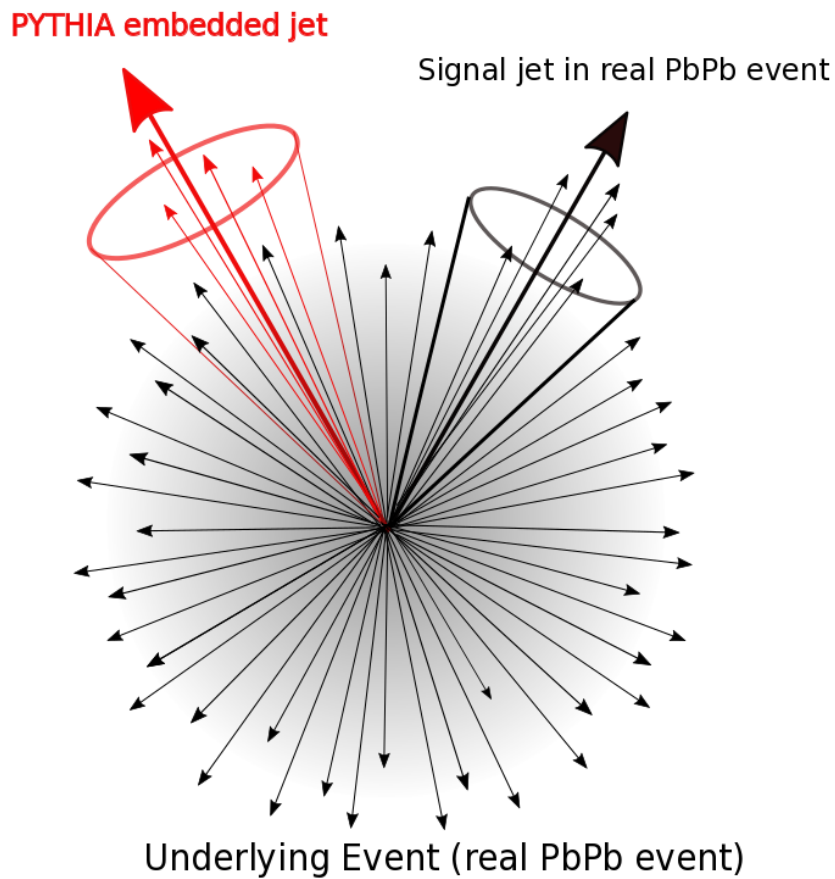


Figure 3.30: A PYTHIA simulated jet is embedded into a real Pb–Pb event. The jet finding algorithm reconstructs the embedded PYTHIA jet as well as real jets stemming of the Pb–Pb collision.

The statistical limit of this Embedding study is given by the number of PYTHIA events which provide a jet that fulfills the jet selection criteria (leading jet constituent bias  $p_T^{\text{jet, lead. const.}} > 5 \text{ GeV}/c$ , jet area  $A^{\text{jet}} > 0.6\pi R^2$ ). This leads to the multiple selection of MB PYTHIA events which is around 20-30 times (see comparison in Fig. 3.31) for each PYTHIA jet that is selected.

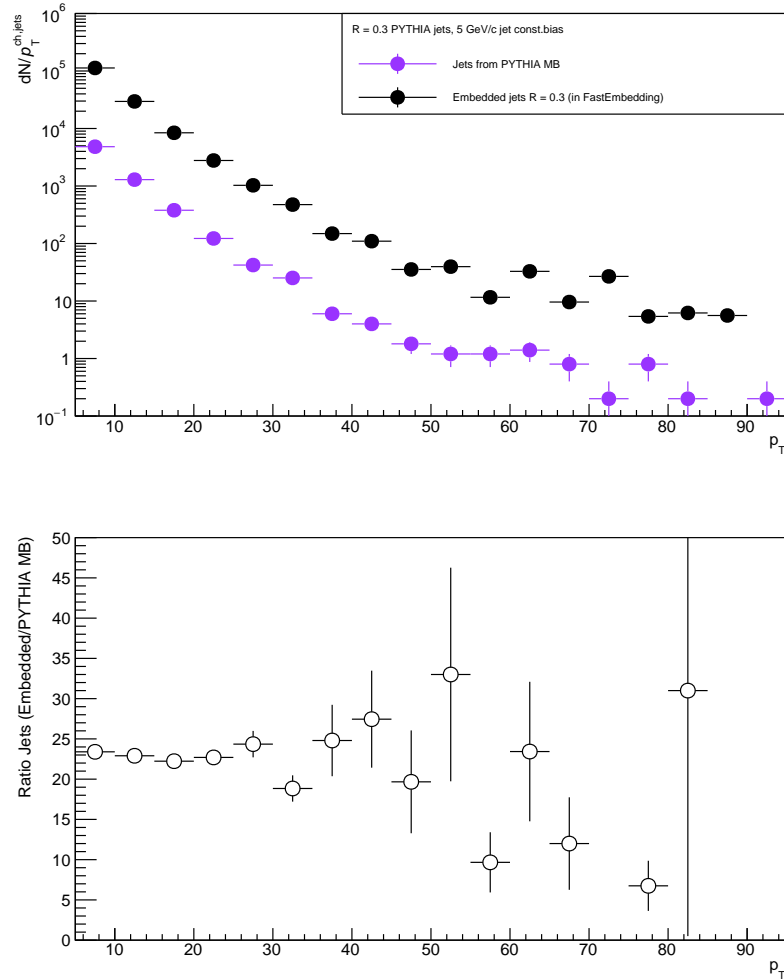


Figure 3.31: Comparison of the minimum-bias PYTHIA spectrum (“Jets from PYTHIA MB”), used for the embedding and the embedded reference  $p_T^{\text{jet}}$  spectrum (“Embedded jets R = 0.3 in FastEmbedding” with multiple event selection).

### 3.5.3 Jet matching

To select only those jets from the "signal+embedded" events which were embedded, and whose properties are therefore known, a jet matching to the PYTHIA embedded jets is done.

The matching method (using the AliRoot methods “AliAnalysisHelperJetTasks::FindClosestJets()” and “AliAnalysisHelperJetTasks::GetFractionOfJet()”) compares two lists of jets:

- The true jets from the embedded PYTHIA jets, reconstructed from “extraonly tracks” and on the "particle level")
- and the reconstructed jets from the "hybrid" events (reconstructed from the “extra tracks”, also referred to as "signal+embedded" tracks)

in order to match the two most similar jets.

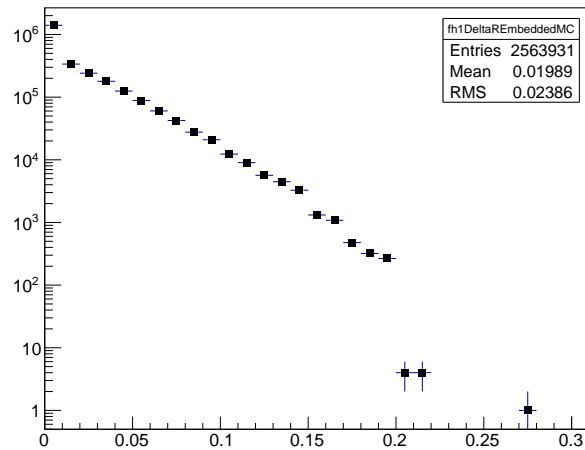


Figure 3.32: Distribution of the radial distance between the jet axis from matched ( $R = 0.2$ ) jets to embedded ("particle level") jets. A loose cut of 0.3 is imposed (per default for the method) on the  $\Delta R$  distribution of the matched jet (pairs) candidates to minimize the combinations of jet pairs that are the input of the next matching check, the shared  $p_T$  fraction (see figure 3.33) of commonly used jet-tracks.

The two matched jets are allowed to have a certain maximal radial distance  $\Delta R$  (see  $\Delta R$  distribution of jet pairs with  $\Delta R < 0.3$  in Fig. 3.32) and a minimum shared  $p_T$  fraction of the jet-tracks which they have in common (and which is contained within the overlapping region of the two jet cones). Figure 3.33 shows the second step of the matching procedure, the fraction of total  $p_T$  of the reconstructed ( $R = 0.2$ ) jets in the "hybrid" events that is shared with the embedded ("particle level") PYTHIA jets in the overlapping region of both jet cones. On this distribution of shared total  $p_T$  a cut of 50% is applied to select good candidates for the "matched" jets in the "hybrid" events. In principal one can "match" the reconstructed ("detector level") jets in the "hybrid" events with the PYTHIA jets on the "detector level" or on "particle level" (i.e. to the MC true information). As a default the matching to the "particle level" is used, if otherwise the matching is done to the "detector level" it is indicated in the following.

This similarity is finally ensured then by a  $\Delta R < 75\% \cdot R$  (which is for  $R = 0.2$  jets  $\Delta R < 0.15$ ) and the shared  $p_T$  fraction of the jet constituents (detector level tracks) of at minimum 50%.

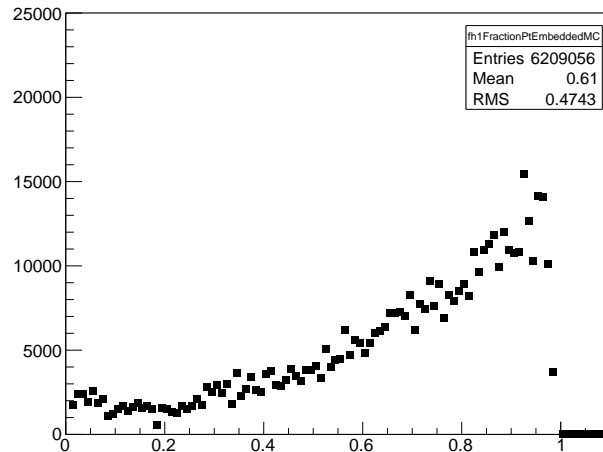


Figure 3.33: Fraction of total  $p_T$  of matched ( $R = 0.2$ ) jets that is shared with the embedded ("particle level") PYTHIA jets in the overlapping region of both jet cones. Already a loose  $\Delta R < 0.3$  is applied for these jet pairs (matched & embedded jet). On this distribution of shared total  $p_T$  a cut of 50% is applied to select good candidates for the "matched" jets in the "hybrid" events.

### 3.5.4 PYTHIA embedded jet spectrum

The embedded jet  $p_T$  spectrum using PYTHIA events can be seen in Fig. 3.34. The reference (embedded) jets, that are the embedded PYTHIA tracks, are shown in brown markers, while the reconstructed hybrid (event) jets (those which are reconstructed from "signal+embedded" tracks) are shown in green markers (referred to as "Jets from extra tracks") before the jet matching procedure. The jets that passed the jet matching are shown in pink markers, while the reconstructed jets from the standard tracks are shown in purple markers. At high  $p_T^{\text{jet}}$  (around 55-85 GeV/c) a bump can be seen in all PYTHIA related jet spectra which is due to the original PYTHIA minimum-bias spectrum, from which all (selected) jets are taken multiple times. This leads to the shape that is caused by the originally large statistical fluctuations whose statistical errors are then decreased by the embedding procedure. However, since we focus mainly on jets in the interval  $10 < p_T^{\text{jet}} < 30$  GeV/c and (later in this section) it is shown that the shape of the embedded PYTHIA  $p_T^{\text{jet}}$  spectrum has no impact on the UE  $V^0$  estimation in the "hybrid" events, we expect that this effect has no impact on the results of the Embedding study. At lowest  $p_T^{\text{jet}}$  the reference jets (brown markers) show the largest yields, whereas the reconstructed jets are affected by the impact of the UE fluctuations and therefore are "smeared" in their reconstructed  $p_T^{\text{jet}}$  value. Together with the steeply falling slope of the jet spectrum this leads to an effective shift of low  $p_T^{\text{jet}}$  jets to higher values and causes the lowest  $p_T^{\text{jet}}$  yield to decrease for the reconstructed jets in the "hybrid" events.

The jet matching efficiency for jets with  $R = 0.2$  is presented in the lower panel of Fig. 3.35. It is finite at very low  $p_T^{\text{jet}}$  (up to around 10 - 20 GeV/c) but increases rapidly for jets from 10 GeV/c on and reaches 100% matching efficiency from 20 GeV/c on. The matching

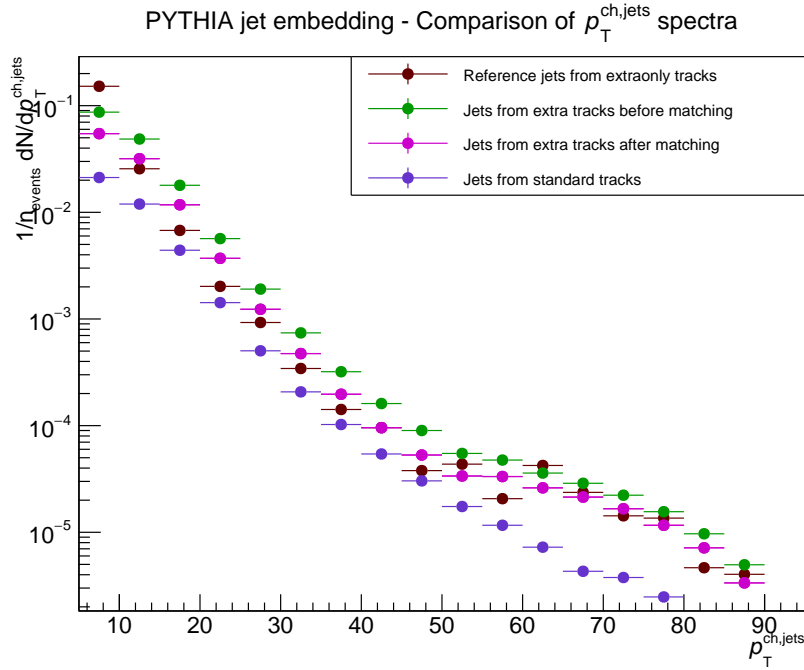


Figure 3.34: PYTHIA jets that are reconstructed from all embedded PYTHIA simulated events at  $\sqrt{s_{NN}} = 2.76$  TeV

efficiency describes the amount of jets in the "hybrid" event ("signal+embedded" tracks), shown in blue markers that have been correctly identified as PYTHIA embedded jets which are drawn with red open markers. These "matched" jets are therefore not signal jets from the Pb–Pb event, although they might coincidentally overlap to some extent with signal jets from the Pb–Pb event.

### 3.5.5 Results for the charged tracks as a crosscheck

Figure 3.36 shows the results obtained by using the charged (jet constituent) tracks that were used for the jet finding to get a first impression of the impact of the UE fluctuations. For the subtraction of the UE contribution from charged tracks to the jet cone, perpendicular cones<sup>30</sup> are used.

When comparing the obtained signal ("Measured signal") to the embedded ("Reference") charged track distribution, one can see several effects:

- At low track  $p_T$  one can see a rise of the signal over the reference, this is due to the impact of the UE fluctuations, pushing more charged particles upwards in  $p_T$  than the UE subtraction method could correct for.
- Furthermore the reference at high  $p_T$  is seen above the measured signal. This is due to the fact that we compare the PYTHIA jet energy with the matched jet energy,

<sup>30</sup>Using perpendicular cones provide enough statistics for the numerous charged tracks, however for the  $V^0$  hadrons enough statistics can only be achieved by using the "no-jet" events instead of perpendicular cones.

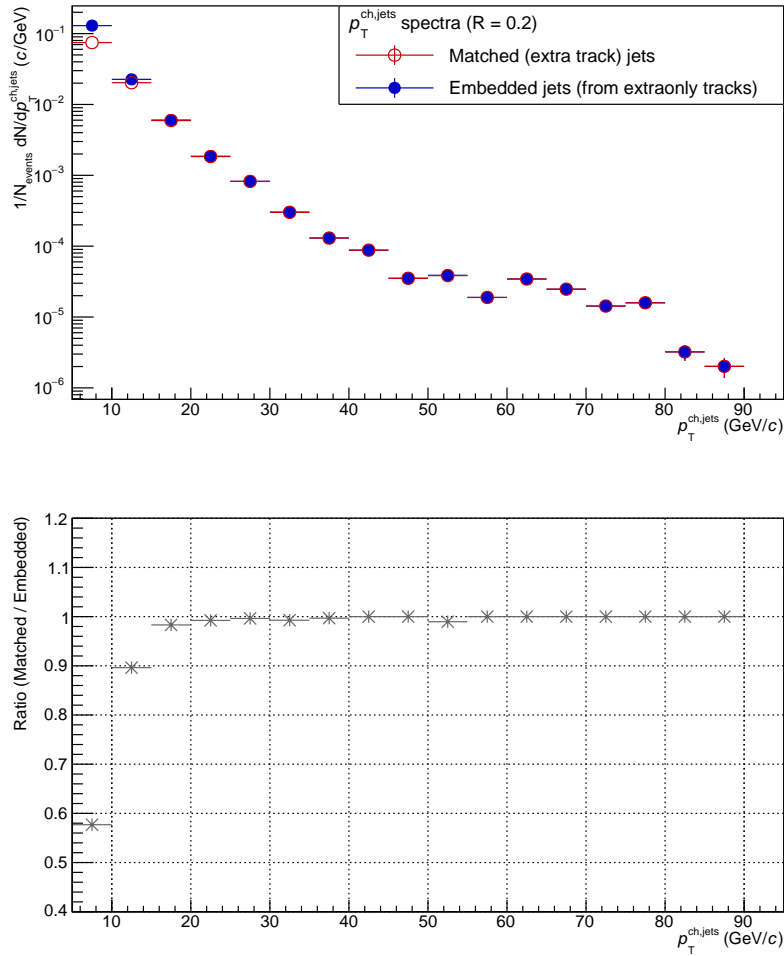


Figure 3.35: The jet matching efficiency (ratio from matched to embedded jets) is finite at very low  $p_T^{\text{jet}}$  (up to around 10 - 20 GeV/c) but increases rapidly for jets from 10 GeV/c on and reaches 100 % matching efficiency from around 20 GeV/c on. For a better comparability the matched jet spectrum is plotted versus the corresponding  $p_T^{\text{jet}}$  before the embedding (which avoids the  $p_T^{\text{jet}}$  "smearing").

both on detector level. The matched jets are smeared in  $p_T^{\text{jet}}$  in consequence of the UE fluctuations and in this way the jet particle spectrum gets a bit softer after smearing.

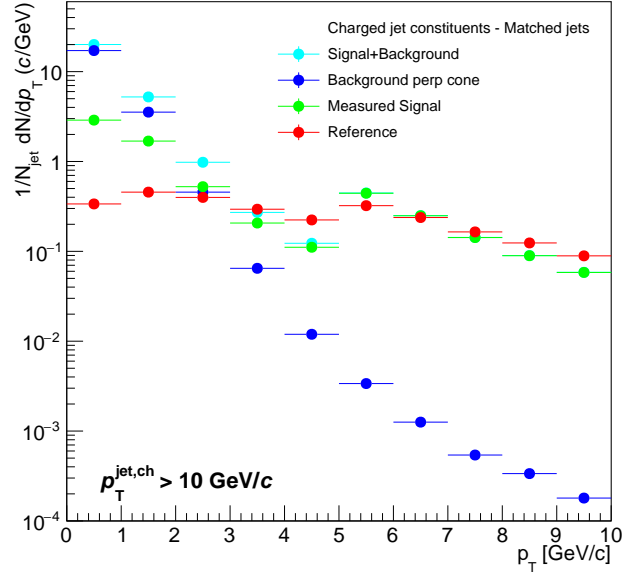


Figure 3.36: Charged track  $p_T$  spectrum in "signal+embedded" jet cones (light blue markers) for  $p_T^{\text{jet}} > 10$  GeV/c and jet resolution parameter  $R = 0.2$ , charged track spectrum in perpendicular cones (dark blue), after subtraction of UE (perp. cones) and compared to embedded PYTHIA jet constituents (red markers)

### 3.5.6 Development of a precise $V^0$ background estimation derived from PYTHIA embedding

In the following, the UE  $V^0$  environment inside the jet cone is studied in detail and a correction for the default method, the  $V^0$   $p_T$  spectrum from "no-jet" events, is developed. Besides its higher accuracy (a better modeling of the real jet  $V^0$  background) the new UE  $V^0$  subtraction method from Embedding also helps to reduce the systematic error on its subtraction<sup>31</sup>. The embedded and reconstructed PYTHIA jets serve, in the following, to study the UE  $V^0$   $p_T$  spectrum below the jet cone. Since UE fluctuations are of statistical nature and therefore show upward and downward fluctuations with equal probability one would assume that the event-averaged background of charged tracks and  $V^0$  particles is an accurate measure and therefore sufficient for the UE subtraction. However this is not the case, in the following it becomes clear why:

The main motivation for this background study inside the jet is the expectation that the local particle background in the environment of a reconstructed jet differs measurable from

<sup>31</sup>..when compared to the agreement (5% deviation for  $2 \lesssim V^0 p_T \lesssim 4$  (GeV/c), much worse for  $V^0 p_T \gtrsim 4$  GeV/c) of the 5 different UE  $V^0$  estimation methods that served in the first approach to estimate an systematic uncertainty on the  $V^0$  background subtraction in jet cones.

the "event-area" averaged particle background. There are two effects that can lead to this difference:

- In nucleon-nucleon (or nucleus-nucleus) collisions low  $p_T$  partons are produced more abundant than high  $p_T$  partons. This expresses itself in the steeply falling shape of the jet  $p_T$  spectrum.
- As described in chapter 3.2, the UE fluctuations of the charged tracks cause a “smearing” of the jet  $p_T$  and can also change the particle multiplicity inside the jet as well as the shape of  $p_T$  spectrum of the jet constituents (see also embedding study for charged tracks in Fig. 3.36).

In the end, these effects lead to the observation that upward fluctuations of the charged background inside a jet cone are more probable to be found than downward fluctuations, for which the UE subtraction has to correct for. In order to study the effect on the  $V^0$  particles, matched jets are selected and their  $V^0$  content is studied. Inside the jet cone, it is easily possible to distinguish between the PYTHIA tracks (that are marked with a special flag in their MC track information) and all background  $V^0$  tracks that stem from the data event (into which the PYTHIA jet has been embedded before). With the identification of the origin of the  $V^0$  particles (either from PYTHIA or from the Pb–Pb data) it is possible to separate the different  $V^0$  spectra and entirely focus on the study of the background particles. This is illustrated for the  $K_S^0$  and the  $\Lambda$  particles in Fig. 3.37. Figures a) and b) show the full  $V^0$  particle content for all  $K_S^0$  and  $\Lambda$  particles in the jet cone ("PYTHIA signal + data bckg" - cyan markers). All  $V^0$ s that are generated by PYTHIA ("PYTHIA signal") are plotted with red markers. The focus of this study lies entirely on the  $V^0$  particle background inside the jet cone (blue markers), coming from the PbPb real event. The background derived from this embedding study serves to estimate correction factors ("CF") for the default method ("no-jet" events) used to subtract the UE  $V^0$  contribution to the jet cone. The raw  $V^0$  spectra from this embedding study are corrected with the reconstruction efficiency estimated for the  $V^0$  hadrons in the jet cones, since they should follow the same  $\eta$  distribution.

A comparison of this "Embedding background" to the  $V^0$   $p_T$  spectrum from “no-jet” events is shown in Fig. 3.38a for the  $K_S^0$  particles (in Figure 3.38b for the  $\Lambda$  particles).

On the bottom of each histogram the ratio between the background  $V^0$  particles from the embedding study (referred to as "Emb") and the  $V^0$  particles collected in the "no-jet" events is drawn. The ratio calculated for the first  $p_T$  bin is chosen as a correction factor (CF) for the default method. The reason to choose only the first point of the ratio (in the Fig. referred to as "Emb/NJ") as CF is on one hand the small statistical uncertainty for  $p_T \gtrsim 3$  GeV/c and on the other hand the linear rise of the ratio. From a previous embedding study of PYTHIA jets into a background of charged tracks which are generated by a MC simulation according to a thermal distribution, this ratio was found to be flat [172]. The reason for this linear increase of the ratio is assumed to be due to a possible contamination<sup>32</sup> of signal jets. This slope of the ratio therefore needs to be considered later in the

<sup>32</sup>It might be due to some remaining overlap of embedded PYTHIA jets with signal jets from the data events that are selected for the embedding.

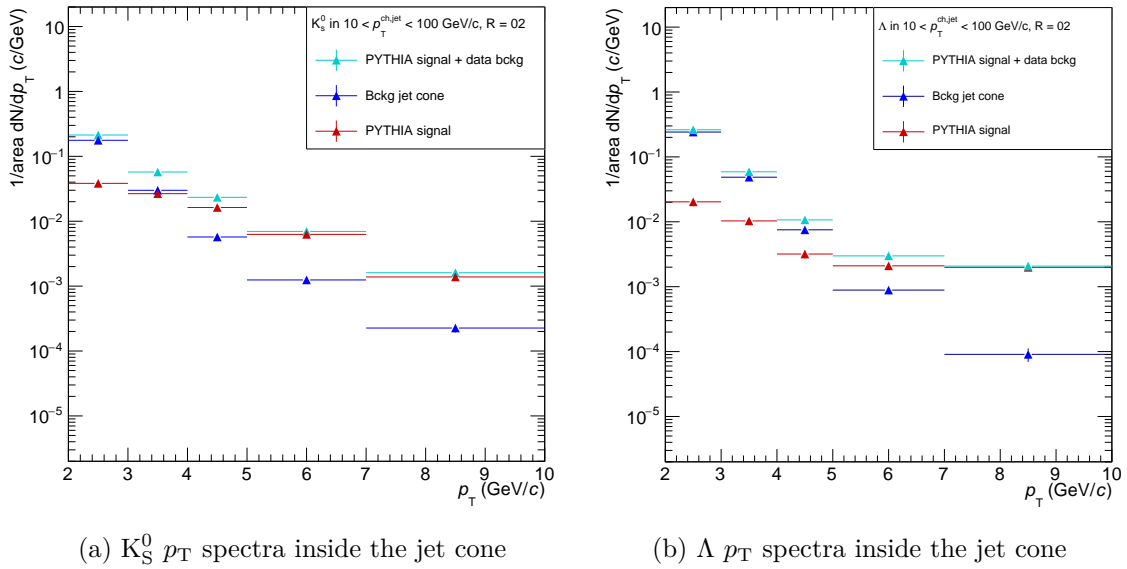


Figure 3.37: The  $V^0$  particle  $p_T$  spectra inside the jet cone. Figures a) and b) show the full  $V^0$  particle content (“PYTHIA signal + data bckg” - cyan markers), only the PYTHIA (embedded signal) in red markers. The main interest of this study is the  $V^0$  particle background inside the jet cone (blue markers), coming from the PbPb event (in which the PYTHIA jets have been embedded). The background derived from this embedding study serves to estimate correction factors for the default method (“no-jet” events) that was used so far to subtract the UE  $V^0$  contribution to the jet cone.

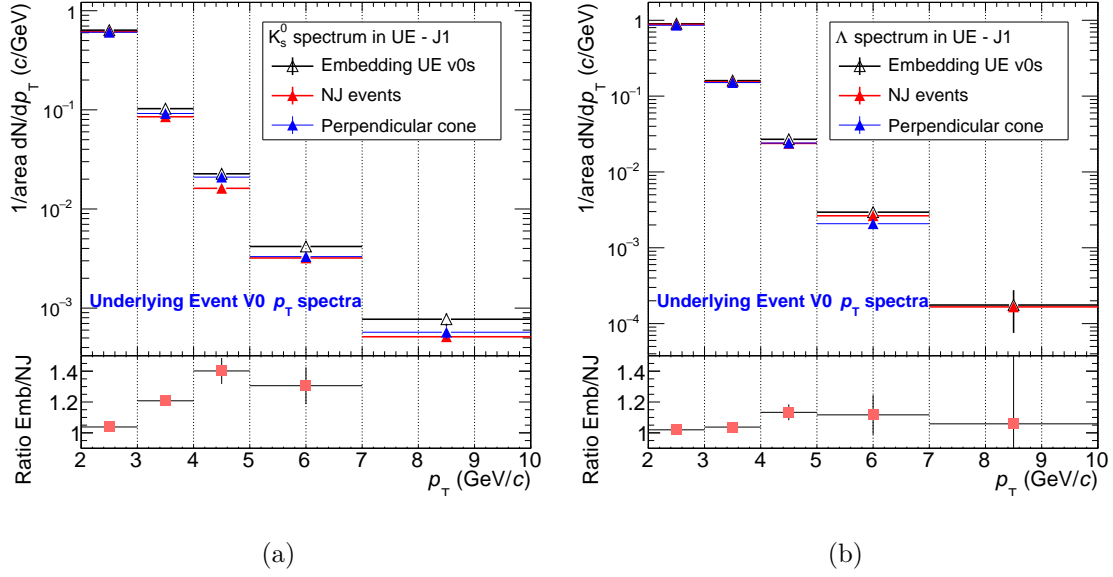


Figure 3.38:  $\Lambda$   $p_T$  spectrum in “no-jet” (NJ) events and from perpendicular cones, compared to the spectrum from the UE in embedded PYTHIA jet cones. The ratio (lower panel) is used to calculate a correction factor (CF) for the impact of the UE fluctuations on the  $V^0$  particles inside the jet cone (for  $p_T^{\text{jet}} > 10$  GeV/c (J1) and  $R = 0.2$ ). Used as CF is finally only the first  $p_T$  bin (centered at 2.5 GeV/c) of the ratio shown below the spectra. a) UE  $K_s^0$   $p_T$  spectra and ratio from comparison of UE  $V^0$  Embedding  $p_T$  spectrum to “no-jet”  $V^0$   $p_T$  spectrum. b) UE  $\Lambda$   $p_T$  spectra and ratio.

calculation of the systematical uncertainty for this correction.

Therefore PYTHIA jet embedding into (preselected) “no-jet” (data) events is done (however it provides around 20% less statistics for this study). Figure 3.40 shows the corresponding result, the UE  $V^0$   $p_T$  spectra from PYTHIA Embedding into all events (default method) compared to the one which is obtained from Embedding into “no-jet” events. The difference gives a hint on the jet contamination of the sampled UE  $V^0$  particles. Especially for high particle  $p_T$  (from around 5 GeV/c on) the spectra from Embedding into all events show a slightly harder shape than the spectrum from Embedding into “no-jet” events. This can be interpreted as a contribution to the jet cone from  $V^0$  particles that stem from jet fragmentation (by signal jets in the real Pb–Pb event). The impact of this comparison on the correction factor of the first  $V^0$   $p_T$  bin is shown in Fig. 3.41.

In order to assign a systematic uncertainty for this correction procedure a linear fit is applied to the ratio and compared to a constant that is adjusted to the first data point (at  $p_T = 2.5$  GeV/c) that is used for the correction (see Fig. 3.39). The impact of the deviation of the fit values from the constant fit and the linear fit (the value of the fit function at each  $p_T$  bin center) is applied as a correction factor to the “no-jet” spectrum and the UE  $V^0$  subtraction is carried out. From the deviation of the final result for both different corrections (linear + constant correction values) an relative systematic uncertainty is calculated for the final fully corrected  $V^0$   $p_T$  spectrum in jets.

For the correction factor, obtained from the first bin (see Fig. 3.39) and estimated for

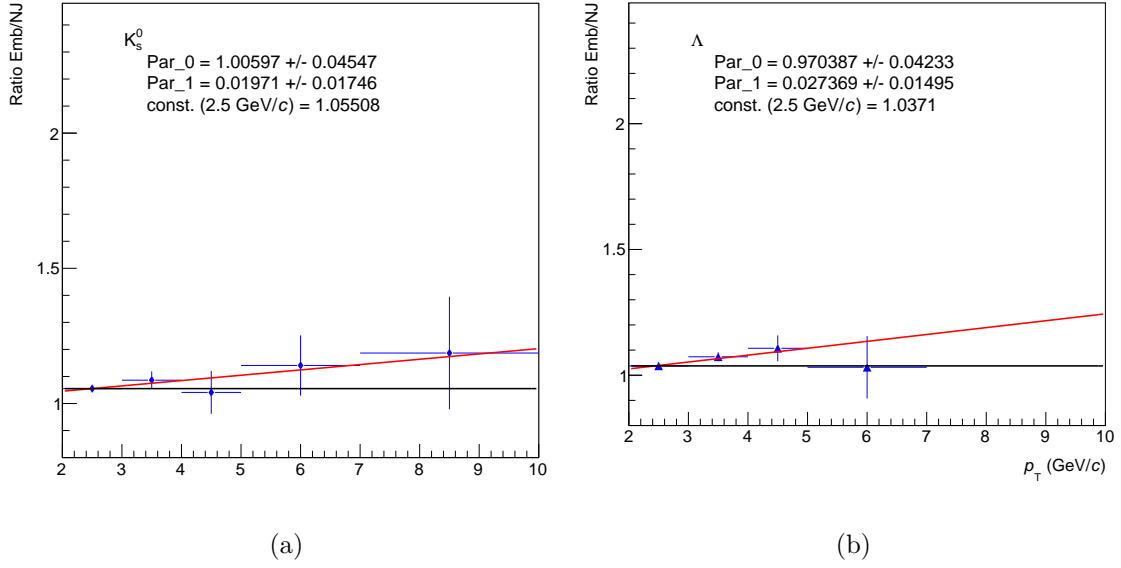


Figure 3.39: Ratio of  $V^0$  background from Embedding to the "event-averaged" UE  $V^0$  estimation from sampling  $V^0$  particles in "no-jet" events. a) shows the correction factors for the  $K_S^0$ , b) for the  $\Lambda$  particles. A linear fit together with a constant (through the first data point) serves to estimate a systematic uncertainty to the ratio value in the first  $p_T$  bin that is used as a correction factor (CF) for the default method ("no-jet" events).

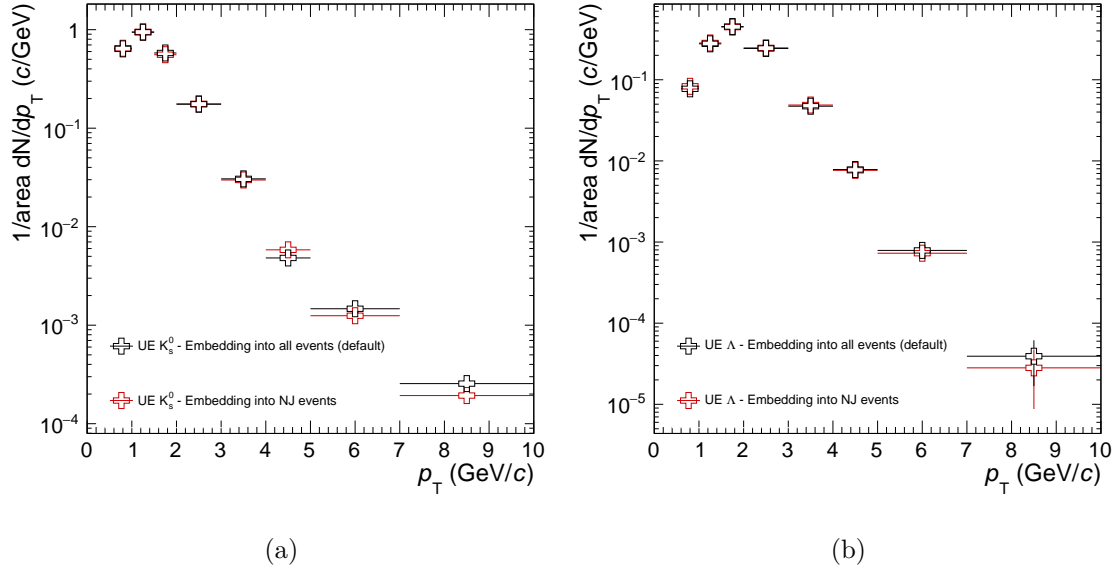


Figure 3.40: UE  $V^0$   $p_T$  spectra from PYTHIA Embedding into all events (default method) compared to the one obtained from Embedding into "no-jet" events. The difference (visible at high  $p_T$ ) gives a hint on the jet contamination of the sampled UE  $V^0$  particles. a) Results for  $K_S^0$  particles. b) Results for  $\Lambda$  particles.

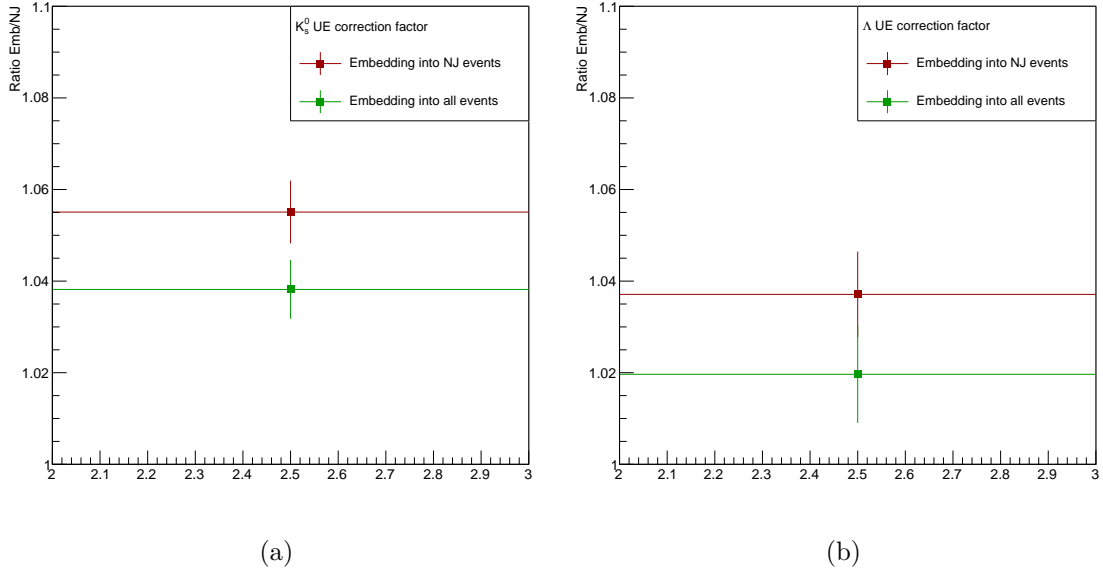


Figure 3.41: Correction factor (CF = Ratio of Embedding UE  $V^0$   $p_T$  spectrum divided by the UE  $V^0$   $p_T$  spectrum measured in “no-jet” events) from the first  $p_T$  bin obtained by Embedding into all events (default method) compared to the one which is obtained from Embedding into “no-jet” events. The difference serves to estimate a systematic uncertainty for a remaining jet contamination of the CF of this first bin.

the  $K_S^0$  and  $\Lambda$  particles separately, a possible remaining jet contamination needs to be considered as a second systematic uncertainty on this correction procedure. This is done by comparing the CF from Embedding into all events to the one obtained from Embedding into only “no-jet” events. This difference for the CF is shown in Fig. 3.41. Once the UE  $V^0$   $p_T$  spectrum is corrected for this UE fluctuation effect, it can be subtracted from the (reconstruction efficiency corrected)  $V^0$   $p_T$  spectrum inside the jet cone. The impact of this correction on the final (fully corrected)  $V^0$   $p_T$  spectrum in the jet depends on the CF as well as on the background-to-signal (B/S) ratio of the  $V^0$ s inside the jet cone. It can therefore result in a sizable correction for the lowest particle  $p_T$  bins where the (B/S) ratio is large, but be negligible for the higher  $V^0$   $p_T$  intervals. In Fig. 3.42 this difference is visible, when comparing the  $K_S^0$   $p_T$  spectrum in jets (green markers) with the correction factor CF (derived from the Embedding method) to the one (blue markers) obtained without applying the CF.

### 3.5.7 Impact of PYTHIA $p_T^{\text{jet}}$ spectral shape on $V^0$ background estimation

In order to exclude a possible impact of the PYTHIA  $p_T^{\text{jet}}$  spectral shape on the resulting estimated  $V^0$  background  $p_T$  spectrum, the embedding study is repeated with a  $p_T$  hard bin PYTHIA production at the same energy. The first PYTHIA  $p_T$  hard bin sample contains MC generated jets with  $5 \lesssim p_T \lesssim 25$  (GeV/c).

In Fig. 3.43 a comparison of two different PYTHIA jet  $p_T$  spectra is shown. Compared

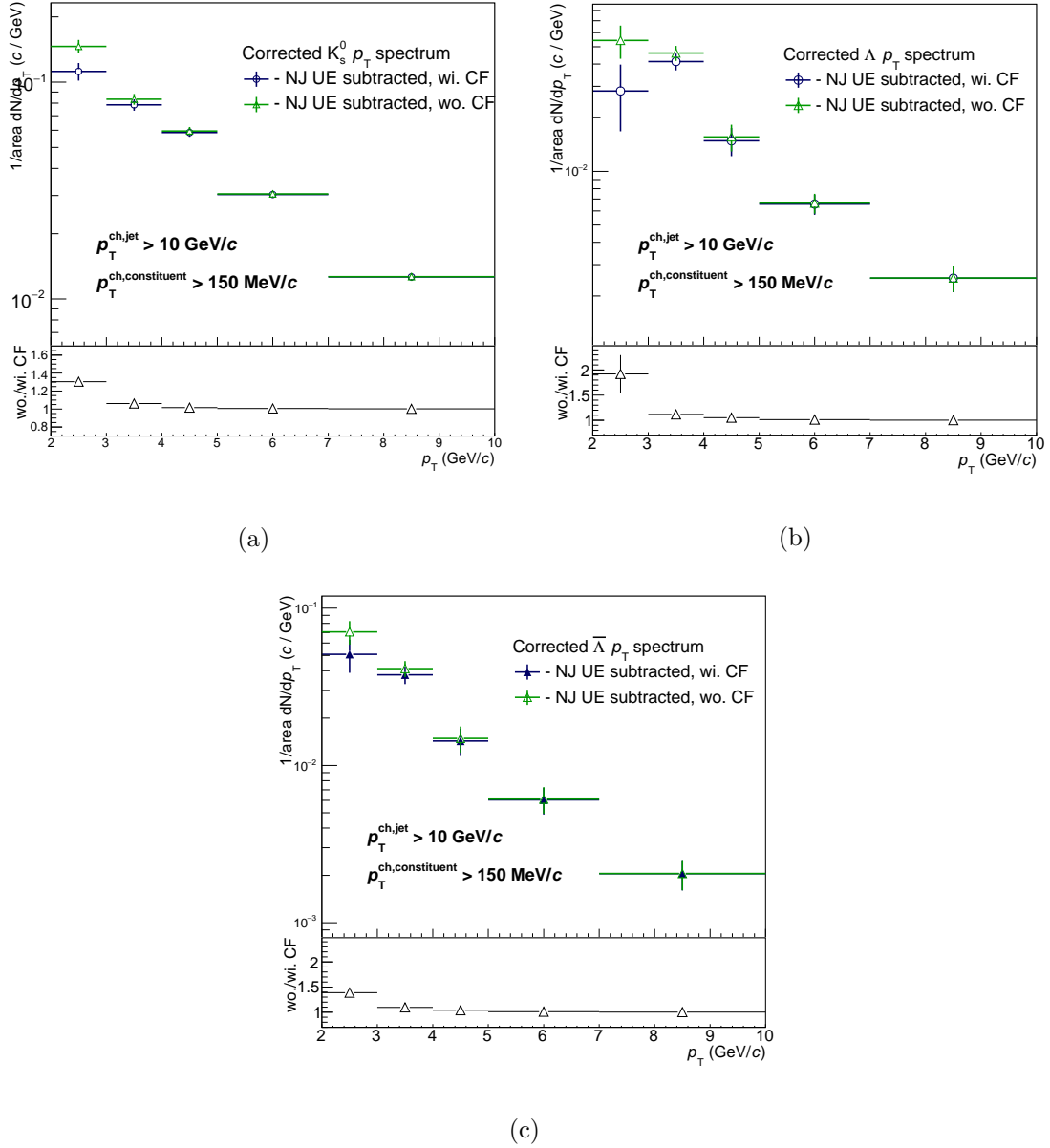


Figure 3.42: Corrected  $V^0$   $p_T$  spectra in jets. The  $V^0$  UE contribution is subtracted with the “no-jet” event estimation method (green markers). Compared is the  $K_S^0$   $p_T$  spectrum in jets with the one corrected with the correction factor (CF) derived from the Embedding method (blue markers). a) Results for  $K_S^0$  particles. b)+c) Results for  $\Lambda$  and for  $\bar{\Lambda}$  particles.

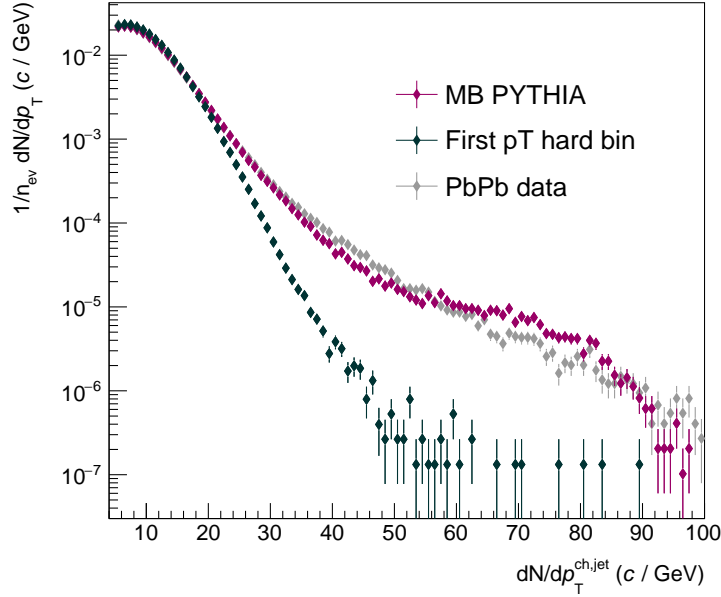


Figure 3.43: Jet  $p_T$  spectrum ( $R = 0.2$ ) for a PYTHIA minimum bias spectrum (magenta markers) and a PYTHIA  $p_T$  hard bin (first  $p_T$  hard bin containing generated jets from 5 GeV/c up to 25 GeV/c, black markers) jet  $p_T$  spectrum. For comparison also the measured  $p_T^{\text{jet}}$  spectrum from the Pb–Pb data is drawn (grey markers).

are the PYTHIA MB spectrum (magenta markers) to the PYTHIA  $p_T$  hard bin spectrum (black markers), also the measured  $p_T^{\text{jet}}$  spectrum in Pb–Pb (gray markers) is shown for this comparison of the spectral shapes.

The  $K_S^0$  and  $\Lambda$   $p_T$  spectra, obtained from the embedding study by using these two different PYTHIA jet spectra, are compared to each other (see Fig. 3.44 for both particle types) and are consistent with unity for the two different  $p_T^{\text{jet}}$  intervals. This means that an impact of the shape of the embedded jet  $p_T$  spectrum can be excluded from the search for sources of systematic uncertainty.

### 3.5.8 Event-plane dependence of the $V^0$ background

This analysis considers the 10% most central collisions only, in which the azimuthal asymmetry of the momentum distribution of the produced hadrons caused by elliptic flow is rather small (see e.g. charged particle elliptic flow  $v_2 \sim 2\text{--}4\%$  for 10% event centrality and integrated over  $0.2 < p_T < 5.0$  (GeV/c), from [170]).

For this study of the UE, the embedding of PYTHIA jets into data events is done isotropic in azimuthal direction and the studied jets therefore have random values in  $\eta$  and  $\phi$  (but are located within the jet axis acceptance of  $-0.5 < \eta^{\text{ch jet}} < 0.5$ ). However a remaining impact of the measured elliptic flow  $v_2^{\text{ch jet}}$  [173, 174] of the reconstructed signal jets on the  $V^0$  background estimation inside the jet cone has to be considered as a systematic uncertainty to the correction procedure (that is described in the previous section 3.5.6).

The  $v_2^{\text{ch jet}}$  is the second coefficient ( $n = 2$ ) of a Fourier expansion of the angular dependence

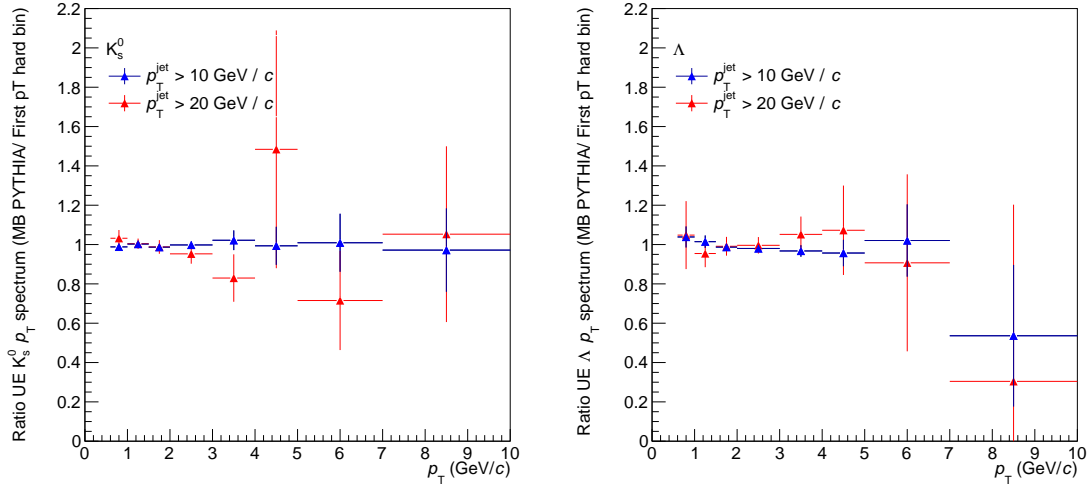


Figure 3.44: Ratio of the  $V^0$  background as measured in matched PYTHIA jets by using the PYTHIA MB  $p_T^{\text{jet}}$  spectrum and by using the first  $p_T$ -hard bin PYTHIA simulation. Left side shows the ratio for  $K_S^0$ , right side shows the ratio for  $\Lambda$  particles.

of the reconstructed jets on the  $n^{\text{th}}$  harmonic order symmetry plane  $\psi_n$ :

$$\frac{dN}{d(\phi_{\text{jet}} - \psi_n)} \propto 1 + \sum_{n=1}^{\infty} 2v_n^{\text{ch jet}} \cos[n(\phi_{\text{jet}} - \psi_n)]. \quad (3.26)$$

These  $n$  symmetry planes define the symmetry axes of the initial nucleon distributions before the nucleon-nucleon collision and translate into the asymmetry of the final state particle momentum distributions. They are measured by the  $n_{\text{th}}$  harmonic order event-plane.

Figure 3.45 shows the elliptic flow coefficient  $v_2^{\text{part}}$  for charged particles [175], [176] (in orange, green markers), for charged jets in ALICE (black markers) and for full (charged+neutral fragments) jets  $v_2^{\text{part}}$  with  $R = 0.2$  in ATLAS (blue markers), measured in  $\eta < 2.1$  [173]. The centrality intervals used for the different measurements are not the same, but consider all the most central Pb–Pb collisions. However when comparing the  $v_2$  measurements one has to keep in mind that the same parton  $p_T$  (initiating the fragmentation process) corresponds to different single particle  $p_T$  or  $p_T^{\text{jet}}$ .

It can be concluded from this plot that the measured  $v_2^{\text{ch jet}}$  for a  $p_T^{\text{jet}} = 30$  GeV/c is around 0.02 - 0.05. From the trend of the ALICE measurement (black markers) for the smallest  $p_T^{\text{jet}}$  intervals, one expects a very similar value for even smaller  $p_T^{\text{jet}}$  (corresponding to the jet energy intervals used for this analysis). In the following calculations a conservative estimate of  $v_2^{\text{ch jet}} = 10\%$  is used. Another difference which is assumed to be negligible for the following estimate is the fact that  $v_2^{\text{ch jet}}$  is measured with fully corrected (unfolded) jets which is not done for the reconstructed jets in this analysis due to statistical limitations. The first step in this approach to determine the event-plane dependence of the UE  $V^0$   $p_T$  spectrum, is to embed all PYTHIA jets firstly in-plane (IP) and secondly out-of-plane (OP) (w.r.t. the  $V^0$  detector determined event-plane angle in azimuthal direction). For

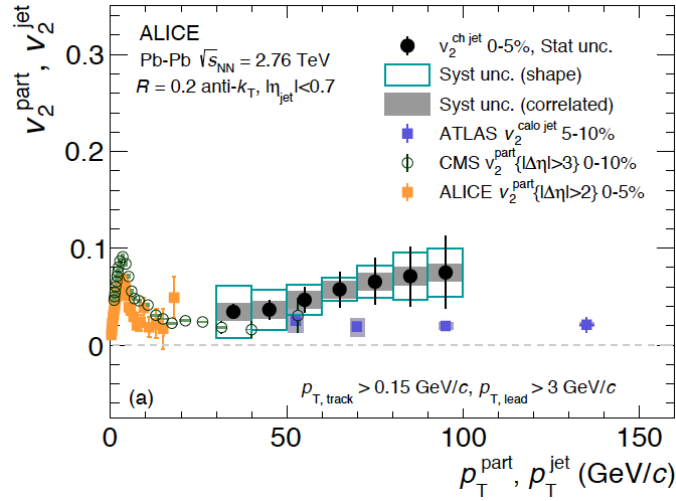


Figure 3.45: The elliptic flow coefficient  $v_2^{\text{part}}$  for charged particles [175], [176] (in orange, green markers), for charged jets in ALICE (black markers) and for full (charged+neutral fragments) jets  $v_2^{\text{ch jet}}$  with  $R = 0.2$  in ATLAS (blue markers), measured in  $\eta < 2.1$  [173]. Note that the centrality intervals used for the different measurements are not the same. Furthermore the same parton  $p_T$  corresponds to different single particle  $p_T$  or  $p_T^{\text{jet}}$ .

the definition of in-plane and out-of-plane see also section 1.4.

From the absolute difference of the two spectra obtained from Embedding IP compared to OP:

$$\Delta(\text{IP} - \text{OP}) = \frac{1}{\text{area}} \frac{dN^{\text{IP, emb}}}{dp_T} - \frac{1}{\text{area}} \frac{dN^{\text{OP, emb}}}{dp_T} \quad (3.27)$$

we calculate the impact of the event-plane and the  $v_2^{\text{ch jet}}$  on the  $V^0$  background in the jet as follows (the following description is adapted from [172]):

The number of jets as a function of  $\phi$  is given by

$$N^{\text{jet}}(\phi) = \frac{\bar{N}}{2\pi} (1 + 2v_2^{\text{ch jet}} \cos(2\phi)) \quad (3.28)$$

and follows from the 2nd harmonic coefficient of the Fourier expansion in Eq. 3.26 and for the case that the reaction-plane angle  $\psi_2 = 0$ .  $\bar{N}$  is the average number of jets.

The  $V^0$  background  $B_{V^0}$  which is affected by elliptic flow, is given by

$$B_{V^0}(\phi) = \bar{B}_{V^0} (1 + 2v_2^{B_{V^0}} \cos(2\phi)) \quad (3.29)$$

with the average background  $\bar{B}_{V^0}$ .

The average background inside the jets  $\langle B \rangle$  can be derived by an integration of the product of the two expressions (3.28 and 3.29) over  $\phi$  and by dividing by the average number of jets  $\bar{N}$ :

$$\langle B_{V^0} \rangle = \frac{1}{N} \int_0^{2\pi} N^{\text{jet}}(\phi) \cdot B_{V^0}(\phi) d\phi \quad (3.30)$$

$$= \bar{B}_{V^0} + \frac{\bar{B}_{V^0}}{2\pi} 4v_2^{\text{ch jet}} v_2^{B_{V^0}} \int_0^{2\pi} \cos^2(2\phi) d\phi \quad (3.31)$$

$$= \bar{B}_{V^0} + 2\bar{B}_{V^0} v_2^{\text{ch jet}} v_2^{B_{V^0}} \quad (3.32)$$

This last form has two unknown observables, the average  $V^0$  background  $\bar{B}_{V^0}$  and the elliptic  $V^0$  background flow  $v_2^{B_{V^0}}$ . They can be determined by embedding the PYTHIA jets (exactly) in-plane ( $\phi = 0$ ) and afterwards out-of-plane ( $\phi = 2\pi$ ) and using the resulting UE  $V^0$  spectra for these two embedding scenarios.

For  $\phi = 0$  and  $\phi = 2\pi$  Eq. 3.29 then returns

$$B_{V^0}(0) = \bar{B}_{V^0}(1 + 2v_2^{B_{V^0}}) \quad (3.33)$$

$$B_{V^0}\left(\frac{\pi}{2}\right) = \bar{B}_{V^0}(1 - 2v_2^{B_{V^0}}) \quad (3.34)$$

$$(3.35)$$

The averaged background calculated from those two extreme cases follows as

$$\bar{B}_{V^0} = \frac{B_{V^0}(0) + B_{V^0}\left(\frac{\pi}{2}\right)}{2} \quad (3.36)$$

And with the difference of  $B_{V^0}(0)$  and  $B_{V^0}\left(\frac{\pi}{2}\right)$  the second unknown  $v_2^{B_{V^0}}$  can be determined

$$\frac{B_{V^0}(0) - B_{V^0}\left(\frac{\pi}{2}\right)}{2} = 4 \cdot \bar{B}_{V^0} \cdot v_2^{B_{V^0}} \quad (3.37)$$

what finally leads to a measurable expression for the average  $V^0$  background inside the jet cone:

$$\langle B \rangle = \frac{B(0) + B\left(\frac{\pi}{2}\right)}{2} + v_2^{\text{ch jet}} \cdot \frac{B(0) - B\left(\frac{\pi}{2}\right)}{2}. \quad (3.38)$$

The first term of Eq. 3.38 represents the  $\phi$ -averaged  $V^0$  background which should correspond to the UE  $V^0$   $p_T$  spectra, obtained with an isotropic PYTHIA jet embedding in azimuth and that is also the standard method for the embedding-based UE correction.

In the context of this analysis a PYTHIA jet is defined as "in-plane", when its  $\phi$  angle of the jet axis has the same value as the experimentally determined  $\phi$  value of the event plane from the Pb–Pb event. In case the  $\phi^{\text{ch jet}}$  has a  $\Delta\phi = \pm \frac{\pi}{2}$  w.r.t. the event plane  $\phi$ , it is "out-of-plane". The 2nd order harmonic event plane angle  $\phi_{\text{EP},2}$  is reconstructed using the VZERO detector information. Some more information of how this is done is given in the chapter about the experimental setup of ALICE in section 2.9.

The second term of Eq. 3.38 gives the deviation of the UE  $V^0$  yield from the standard (isotropic PYTHIA jet embedding) UE  $V^0$   $p_T$  spectrum (referred to in the following equation as " $N_{\text{UE},v^0}$ ").

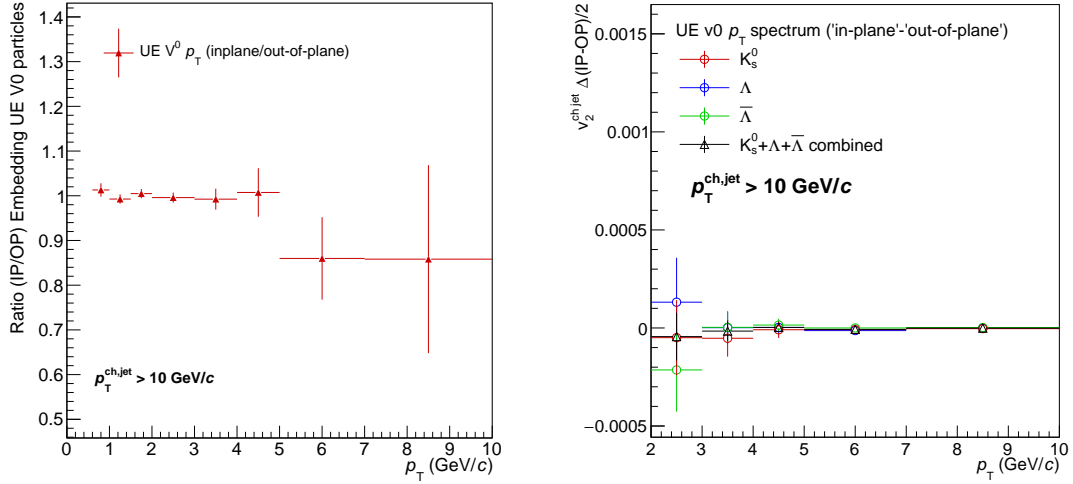


Figure 3.46: Left side: Ratio of UE V<sup>0</sup> p<sub>T</sub> spectra from PYTHIA jet embedding in-plane and embedding out-of-plane. Right side: Second term of Eq. 3.38 (the impact of event asymmetry) calculated for all V<sup>0</sup> hadron species. The black markers show the combined result for all particle species which gives a negligible deviation ( $\lesssim 4.4 \cdot 10^{-6}$ ). Instead a relative difference of the spectra of 1% is assumed as a conservative estimate.

The ratio of the UE V<sup>0</sup> p<sub>T</sub> spectra obtained with PYTHIA jet embedding in-plane and out-of-plane can be seen on the left side in Fig. 3.46 considering the statistical errors it seems to agree with unity. Therefore a sizable impact of the event asymmetry due to elliptic flow and a jet-eventplane correlation does not show a sizable effect for the V<sup>0</sup> statistics available in this study.

However we make a conservative assumption for this deviation and assign this difference of the spectra to be a 1% effect, since there might be a small discrepancy expected from the event asymmetry of events of around 8–10% centrality (and which is probably not visible for the V<sup>0</sup> particles, because of the limited statistics from the Embedding procedure). The calculated values of this second term is shown on the right side in Fig. 3.46. For low hadron p<sub>T</sub> the obtained difference of the UE V<sup>0</sup> p<sub>T</sub> spectra from Embedding "in-plane" compared to Embedding "out-of-plane" is very small ( $v_2^{\text{ch,jet}} \cdot \frac{B(0)-B(\frac{\pi}{2})}{2} \lesssim 0.000044$ ) and it seems to be negligible (see combined K<sub>S</sub><sup>0</sup>+Λ+Λ̄ as black markers). With the conservative estimate of 1% difference in the spectra we obtain for the second term  $v_2^{\text{ch,jet}} \cdot \frac{B(0)-B(\frac{\pi}{2})}{2} = 0.0005$ . From this a relative systematic uncertainty "ΔN<sub>EP</sub>" of the UE V<sup>0</sup> yields obtained by the embedding study due to elliptic flow  $v_2^{\text{ch,jet}}$  is calculated as:

$$\Delta N_{\text{EP}} = \frac{v_2^{\text{ch,jet}}}{N_{\text{UE},v0}} \cdot \frac{1}{\mathfrak{R}_2} \cdot \frac{B(0) - B(\frac{\pi}{2})}{2}$$

where  $\mathfrak{R}_2$  is the event plane resolution (from the VZERO detector estimation) that was estimated to be  $\mathfrak{R}_2 = 0.47$  [174].

The results for the second term and the relative systematic uncertainty for K<sub>S</sub><sup>0</sup> and Λ hadrons are listed in table 3.4 and provide a measure to assign a relative systematic uncertainty.

Table 3.4: Estimation of the averaged  $V^0$  background in jet cone with isotropic PYTHIA jet embedding ( $= \overline{B}_{V^0}$ ) and the deviation term due to  $v_2^{\text{ch jet}}$  ( $\sim 10\%$ ).

Calculated values (according to Eq. 3.38):	$K_S^0$	$\Lambda$
$v_2^{\text{ch jet}} \cdot \frac{B(0)-B(\frac{\pi}{2})}{2}$	$5 \cdot 10^{-3}$	$0.5 \cdot 10^{-3}$
<b>Relative syst. uncertainty <math>\Delta N_{EP}</math></b>	<b>0.60%</b>	<b>0.44%</b>

More details about all sources of relative systematic uncertainties on the particle spectra and ratios are given in the next two sections.

Table 3.5: Estimation of relative systematic uncertainties

Source	Method to estimate related systematic uncertainty
Efficiency	$V^0$ cut variations (for details see 3.8)
Signal extraction	Variation of range of signal extraction and side-band region (background)
Underlying Event	Uncertainties on UE estimation from Embedding study
$\Lambda$ feed-down (FD)	FD from inclusive analysis compared to FD from PYTHIA jets
Material Budget	Estimated values taken from published inclusive analysis

### 3.5.9 Estimation of the systematic uncertainties

The total systematic uncertainty of each data point of the final results consists of several contributions, each of them associated with a certain source of uncertainty. In order to estimate these contributions to the total error, different methods (like e.g. cut variations or small variations of the estimation method) have to be used and the variation of the result serves as an estimate for the systematic uncertainty associated with the certain source of uncertainty.

The following section describes all methods which are used to calculate the relative systematic uncertainties on the final results. First some general considerations on the error calculation are made. Then all different error sources relevant for this analysis are discussed. First for the  $V^0$  hadron  $p_T$  spectra in jets and then for the  $V^0$  hadron ratio in jets. Finally the total relative systematic uncertainties for the spectra and the ratio in jets are shown and discussed.

An overview of the different systematic error sources which are considered to have a sizable impact for this analysis, and the corresponding estimation methods are shown in Tab. 3.5. For all the following error calculations considering  $V^0$  particles in jets, the sample of jets from  $p_T^{\text{jet}} > 10 \text{ GeV}/c^2$  are used and these total relative systematic uncertainties are taken to also calculate the absolute systematic uncertainty for the results for jets from  $p_T^{\text{jet}} > 20 \text{ GeV}/c^2$  (whose statistics are rather limited and therefore are not used for the systematic uncertainty estimation).

The relative systematic uncertainty of the reconstruction efficiency corrections e.g. can be calculated by varying the cut parameters that act on the topology of the  $V^0$  particle decay. The standard cut values and their variation are shown in Tab. 3.8. They are chosen in the way that the uncorrected yield of the inclusive  $V^0$  particles, when integrated in the transverse momentum range  $2 < p_T < 10 \text{ (GeV}/c)$ , is decreasing by 10%. While for most of the varied cuts, the same variation was used for all particle types, the Cosine of Pointing Angle (CPA) cut was varied slightly differently for  $K_S^0$  and  $\Lambda$  particles, since the amount of selected candidates shows a different dependence for  $K_S^0$  and  $\Lambda(\bar{\Lambda})$ .

The variations are done for each cut independently. Five of the  $V^0$  selection cuts that have been found (in the inclusive particle analysis of the published  $V^0$  spectra) to have the largest contribution to the total systematic uncertainty, are varied and the final results (like  $p_T$  spectra and particle ratios) are recalculated. The difference of the final data points determine the systematic uncertainty.

These deviating data points  $x_i$  are expected to follow a symmetric distribution around the default value  $a$  and their deviation can be described by the root-mean-square (RMS) of the results obtained with the varied cuts (or different estimation methods).

$$\text{RMS} = \sqrt{\frac{1}{N_{var}} \sum_{i=1}^{N_{var}} (x_i - a)^2} \quad (3.39)$$

However since these cut variations  $N_{var}$  and different methods of estimation are not equal in terms of statistics, the individual statistical errors of the  $x_i$  have to be considered in this calculation as well, since only differences which are significant in terms of the statistical error should be considered as a systematic deviation from the default value. They can be included by imposing weights  $w_i$  on the RMS summands:

$$\text{wRMS} = \sqrt{\frac{1}{N_{var}} \sum_{i=1}^{N_{var}} (x_i - a)^2 w_i} \quad (3.40)$$

in which the weighting factors are given by

$$w_i = 1 - \exp(-d^2/2) \quad (3.41)$$

and the dissimilarity ( $d$ ) of the data points  $x_i$  and the constant factor  $f$  by

$$d = \frac{a - x_i}{\sqrt{(\sigma_a^2 + \sigma_{x_i}^2)/f}} \quad (3.42)$$

where the factor  $f$  is chosen to be 2, in case the deviations  $x_i$  are stemming from very similar samples (e.g. subsamples of the same data set) and as 1, if the samples are totally independent from each other. Since the cut variations are based on the same data set, and reduce - one by one varied - or enhance the amount of  $V^0$  candidates,  $f$  is chosen as 2 for the calculation of the uncertainty for the reconstruction efficiency correction.

The situation is similar for the uncertainty of the signal extraction method (SE) (see Tab. 3.6 for the default settings), where the range of the signal extraction (of the invariant mass distribution) and also the background estimation interval are varied (see Tab. 3.7 for details). The fit function on the other hand, was not varied, since it turned out from the quality of the fit results that the optimal choice is a polynomial of 2nd order to fit the  $K_S^0$  invariant mass distributions (for the various intervals of  $V^0$   $p_T$ ) and a polynomial of 3rd order respectively for the  $\Lambda$  (and  $\bar{\Lambda}$ ) particles. Any variation of the degree of the polynomial results in a worse performance. Because the invariant mass distributions in these variations, are based all on the same set of  $V^0$  candidates, the factor  $f = 2$  is used also for the systematic uncertainty calculation of the SE.

For the uncertainty estimation of the signal extraction for the  $V^0$   $p_T$  spectra, the signal region intervals (describing the area below the particle peak, in which the  $V^0$  particles are sampled) are varied, using the inclusive particle yields. It is assumed that the variation study represents the same situation as for the particles in the jets and in the Underlying Event (in "no-jet" events). The variations for the different  $V^0$  particle types are listed in

Table 3.6: Signal extraction settings for the different particle types (for inclusive, intra-jet and UE mass distributions)

Particle type	Signal and background estimation regions (invariant mass (GeV/ $c^2$ ))
$K_S^0$ polynomial 2 <sup>nd</sup> order	signal in (0.43, 0.57) (= inner background edges), background in (0.38, 0.65)
$\Lambda$ polynomial 3 <sup>rd</sup> order	signal in (1.105, 1.13) (= inner background edges), background in (1.1, 1.155)
$\bar{\Lambda}$ polynomial 3 <sup>rd</sup> order	signal in (1.105, 1.13) (= inner background edges), background in (1.1, 1.155)

Table 3.7: Signal extraction variations

Variation type	
Variation $K_S^0$	signal in 0.44, 0.56 (= inner background edges)
Variation $\Lambda$	signal in (1.107, 1.127) (= inner background edges)
Variation $\bar{\Lambda}$	signal in (1.107, 1.127) (= inner background edges)
Type 1 for particle ratio	Variation for $K_S^0$ , default settings for $\Lambda+\bar{\Lambda}$
Type 2 for particle ratio	Variation for $\Lambda+\bar{\Lambda}$ , default settings for $K_S^0$
Type 3 for particle ratio	Variation for $K_S^0$ and $\Lambda+\bar{\Lambda}$

table 3.7 and the resulting variation of the  $V^0$   $p_T$  spectra is shown as the ratio of variation w.r.t. the default settings in Fig. 3.47a. The variation of the signal extraction is small for low  $p_T$  intervals (about 1-2%) and increases for the higher  $p_T$  intervals up to about 5% deviation.

For the  $(\Lambda+\bar{\Lambda})/2K_S^0$  ratio on the other hand, three different combinations of the variation are used. They are listed in Tab. 3.7 as "Type 1", "Type2" and "Type 3". The resulting variation of the uncorrected  $(\Lambda+\bar{\Lambda})/2K_S^0$  ratio is then shown in Fig. 3.47b.

For all ratios derived with a certain variation (Type 1-3) and the ratio obtained with the default settings for the signal extraction the weighted RMS value is calculated. It is furthermore calculated for each  $V^0$   $p_T$  interval separately and is small for the lowest  $V^0$   $p_T$  intervals (in which the smooth shape of the combinatorial  $V^0$  background can be well described by a polynomial fit) and increases slightly for higher  $p_T$  bins. In both cases, for the spectra and ratio, a maximum relative systematic uncertainty of around 4-5% is reached for the highest  $V^0$   $p_T$  interval in case of the  $V^0$  spectra (see also Fig. 3.55a and 3.55b that are described later). For the particle ratio this uncertainty reduces to slightly smaller values (around 2.5-3%) in the highest  $V^0$   $p_T$  interval (see Fig. 3.56).

The systematic uncertainty of the FD subtraction is estimated by comparing the results (see Fig. 3.52) which are obtained when using either the FD fractions from the inclusive particle analysis or the one obtained from a simulation in PYTHIA8 [48] jets (both FD fractions are shown in Fig. 3.51).

The systematic error calculation for the UE subtraction (which is done by using "no-jet"  $V^0$   $p_T$  spectra that are corrected for the impact of the UE fluctuations via embedding of PYTHIA jets into data events) was already presented in the previous section, but the error calculation strategy is briefly repeated at this point in the context of this uncertainty discussion. The uncertainty of the Embedding correction factor (CF) considers contributions

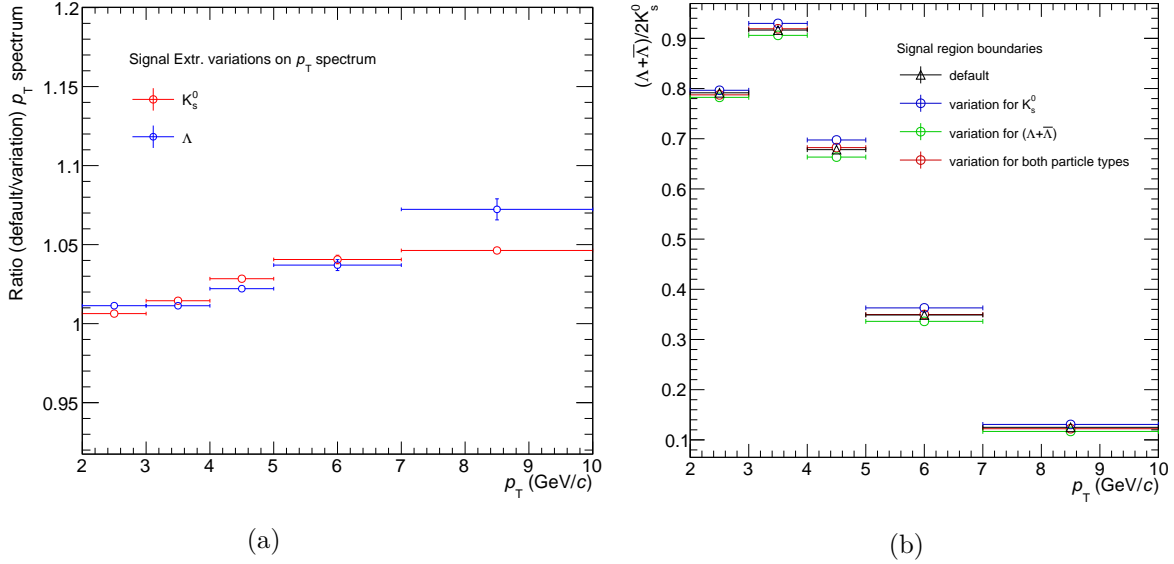


Figure 3.47: a) Variations of the signal extraction for the  $V^0$   $p_T$  spectra. b) Impact on the (uncorrected) inclusive  $(\Lambda + \bar{\Lambda})/2K_S^0$  particle ratio for 3 different variations.

Table 3.8: Cut variations for the estimation of the systematic uncertainty of reconstruction efficiency correction.

$V^0$ decay observable	default value	variation $K_S^0(\Lambda)$
CosPointAngle	0.998	0.9996 (0.9994)
DCA $V^0$ daughters	$1.0 \sigma$	$0.45 \sigma$
$V^0$ transverse proper lifetime (mL(in 2D)/ $p_T$ )	$5 c\tau$	$2.8 c\tau$
DCA IP daughters	0.1	0.2
Max. decay radius	100 cm	40 cm
Min. decay radius	5 cm	7.3 cm

from three sources:

- Slope of the CFs due to a possible jet contamination at higher  $p_T$  intervals (one has to keep in mind that however only the first CF is used to correct all  $p_T$  intervals of the measured "no-jet" event  $p_T$  spectrum).
- Jet contamination of CF in first  $p_T$  bin (used for the corrections)
- Impact of charged jet  $v_2$  and 2nd order harmonic event plane on UE  $V^0$   $p_T$  spectrum in jet cone

These effects are estimated with the following strategies:

- Constant fit (through first  $p_T$  bin) versus linear fit through all CFs (as function of  $V^0$   $p_T$ )
- Embedding of PYTHIA jets into all events versus into "no-jet" events
- PYTHIA jets are embedded in-plane and out-of-plane (w.r.t. the 2nd order harmonic event-plane) and weighted with measured charged jet  $v_2$  (assumed to be at maximum 10 % at  $p_T^{\text{jet}} \sim 10$  GeV/c)

With each of these variations of the CF, the "no-jet"  $V^0$   $p_T$  spectrum is corrected (i.e. the first  $p_T$  bin content or all  $p_T$  bin contents are multiplied with the CF(varied)). Afterwards this CF-corrected "no-jet"  $V^0$   $p_T$  spectrum is subtracted from the efficiency-corrected  $V^0$   $p_T$  spectrum in the jet cone. The resulting UE subtracted spectra are compared (i.e. varied result is compared to result obtained from default method) and from the deviation the relative systematic uncertainty is obtained. These estimates lead to a maximum contribution to the total relative systematic error for the  $K_S^0$  spectrum of around 3-4% and for the  $\Lambda + \bar{\Lambda}$   $p_T$  spectrum of around 2-3% (see Fig. 3.55a and Fig. 3.55b) and have therefore rather small fractions of the total systematic uncertainty. This contribution is similar when calculated for the ratio. The previously calculated relative uncertainties on the different particle  $p_T$  spectra are added up quadratically for each of the sources of the CF uncertainty. Together, they result in a error fraction of the particle ratio systematic uncertainty of at maximum 2-3% (see Fig. 3.56).

### Systematic uncertainties for the $V^0$ spectra in jets

For all  $K_S^0$  and  $\Lambda(\bar{\Lambda})$  particles the systematic uncertainties on the spectra are calculated individually. The sources of uncertainty for the fully corrected  $V^0$   $p_T$  spectra in jets are briefly listed in Tab. 3.5. The first source of systematic uncertainty concerning the reconstruction efficiency correction of the  $V^0$  particle  $p_T$  raw spectra is addressed by the  $V^0$  cut variations that have been already described in the previous paragraph. The impact of this cut variations on the  $V^0$   $p_T$  spectra are shown in Fig. 3.48. From the differences of the varied spectra the relative systematic uncertainty is calculated.

The  $\Lambda$  FD fractions are calculated as described above. The impact of the two approaches on the efficiency corrected  $V^0$   $p_T$  spectrum in jets with  $p_T^{\text{jet}} > 10$  GeV/c can be seen

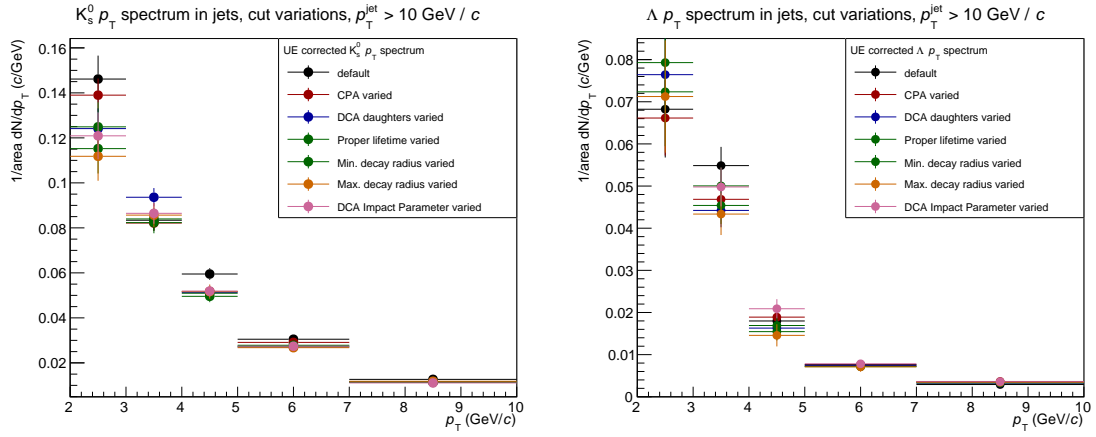


Figure 3.48: Cut variations for the estimation of a relative systematic uncertainty on the efficiency correction of the  $V^0$   $p_T$  spectra in jets ( $R = 0.2$ ) and estimated with jets of  $p_T^{\text{jet}} > 10 \text{ GeV}/c^2$ . Left plot shows the results for  $K_S^0$  mesons, the right plot the results for  $\Lambda$  baryons.

in Fig. 3.49. The default method to correct the efficiency corrected  $\Lambda$  yields for the FD fraction is chosen to be the FD calculated from the inclusive particle estimate. For the FD from PYTHIA8 jets a constant line fit was applied and assumed to be constant with  $p_T$ , the fit result gave a constant PYTHIA FD fraction of

$$f_{\Lambda, \bar{\Lambda}}^{\text{FD, PYTHIA}} = 0.142$$

for both,  $\Lambda$  and  $\bar{\Lambda}$  particles.

For the systematic uncertainty coming from the determination of the material budget (that causes particle absorption effects inside the detector system) was already studied for the inclusive particle analysis in pp at  $\sqrt{s} = 0.9 \text{ TeV}$  [158]. For the  $V^0$  particles analysed in [158] an uncertainty of the efficiency correction caused by the uncertainty on the estimated material budget for each particle type was estimated by varying the material budget in a MC simulation and studying the impact on the estimated  $V^0$  reconstruction efficiency. This uncertainty was estimated to be 1.1% for  $K_S^0$ , 1.6 % for  $\Lambda$  and 4.5 % for  $\bar{\Lambda}$  and is assumed to contribute in such way also to the current analysis. This uncertainty is considered constant for all  $p_T$  intervals.

### Systematic uncertainties for the $(\Lambda + \bar{\Lambda})/2K_S^0$ ratio in jets

For the  $(\Lambda + \bar{\Lambda})/2K_S^0$  ratio in jets the calculation of the total systematic uncertainty is slightly modified, since the error sources might partially cancel out. The same strategy of variations was applied, but the error estimation is based on their impact on the final particle ratio.

The variation of the  $(\Lambda + \bar{\Lambda})/2K_S^0$  particle ratio, when varying the  $V^0$  cuts separately can be seen in Fig. 3.50 (no FD subtraction is applied on these ratios).

It shows that the relative variation of the Cosine Pointing Angle (CPA), the Distant-of-

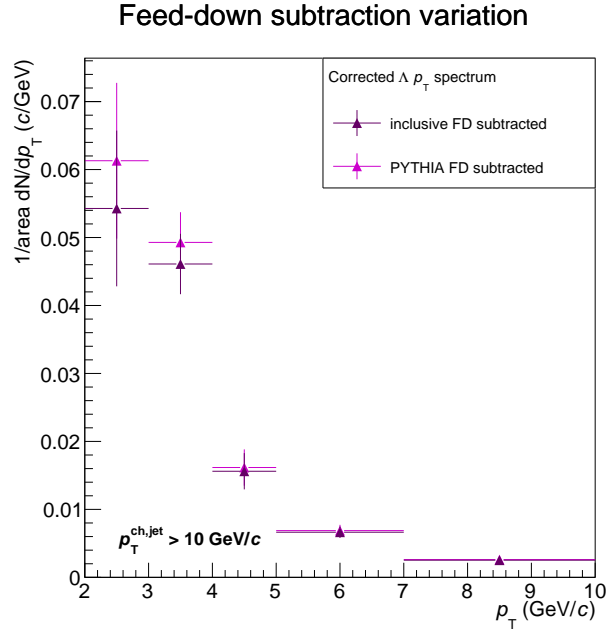


Figure 3.49: Two feed-down (FD) estimation approaches allow to calculate a systematic uncertainty for the FD subtraction. The default method is the FD fraction calculated for  $\Lambda$  particles as in the inclusive  $\Lambda$  analysis [177]. The second approach is the FD fraction derived from a PYTHIA8 simulation. Shown are the FD corrected  $\Lambda$   $p_T$  spectra with  $p_T^{\text{jet}} > 10$  GeV/c obtained from both approaches.

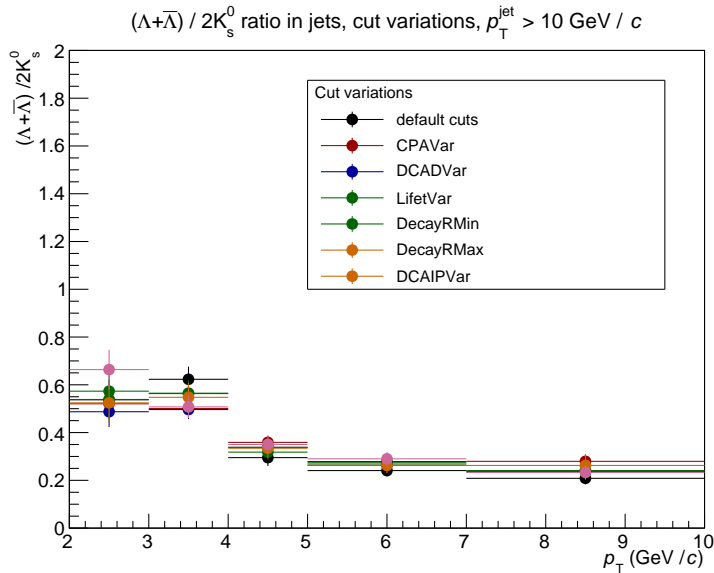


Figure 3.50: Cut variations for the estimation of a relative systematic uncertainty of the  $V^0$  reconstruction efficiency on the  $(\Lambda + \bar{\Lambda}) / 2K_s^0$  ratio in charged jets ( $R = 0.2$ ).

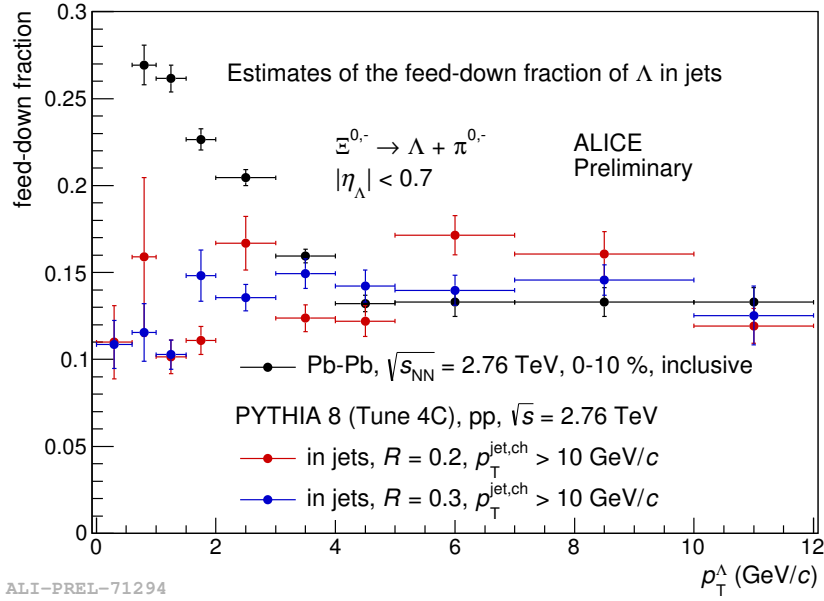


Figure 3.51: The feed-down fractions from inclusive particle analysis (black markers) and from simulation in PYTHIA8 jets (red markers -  $R = 0.2$ , blue markers -  $R = 0.3$ ) that have been calculated for the current analysis.

Closest Approach (CPA) and the  $V^0$  (transverse) Proper Lifetime (which is calculated as  $\frac{m_{\text{PDG}, V^0} \cdot L}{p_T}$  with "L" being the two-dimensional transverse decay length of the  $V^0$  particle) cut have a small, but sizable, impact on the final result. For this systematic error calculation also the MC  $V^0$  data, used for estimation of the efficiency, is analysed by applying the cut-by-cut variation accordingly.

The systematic uncertainty on the material budget (that was already mentioned in the previous section for the error calculation of the  $V^0$  spectra in jets) was calculated as the sum in quadrature of the three different uncertainties (under the assumption that the  $p_T$  spectra of  $\Lambda$  and  $\bar{\Lambda}$  particles are equal) to 2.6% and considered to be constant throughout the entire  $p_T$  range of the measurement.

The two different feed-down (FD) estimation methods (see Fig. 3.51) are applied on the efficiency corrected  $\Lambda$   $p_T$  spectrum and the resulting difference of the FD-corrected  $\Lambda(\bar{\Lambda})$   $p_T$  spectra (see Fig. 3.52) serves as an estimate of the relative systematic uncertainty.

### $\bar{\Lambda}$ - $\Lambda$ difference

At the LHC energies and in the heavy-ion collisions with vanishing baryonic chemical potential, the ratio of particles to antiparticles is expected to be unity. However in the analysed 2011 dataset a discrepancy of the inclusive  $\Lambda$  and  $\bar{\Lambda}$   $p_T$  spectra is seen. The cause of this discrepancy is not completely understood but it is probable that a not entirely proper calibration of the TPC data might cause a shift of the charge over  $V^0$   $p_T$  that causes the  $\Lambda$  and  $\bar{\Lambda}$   $p_T$  spectra to be different from the already published spectra (obtained

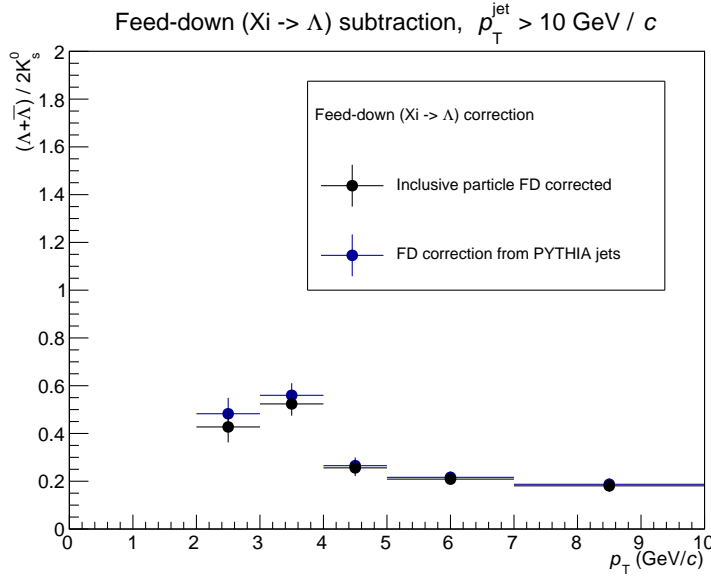


Figure 3.52:  $(\Lambda + \bar{\Lambda})/2K_S^0$  ratio in jets ( $p_{T,\text{jet}}^{\text{ch}} > 10 \text{ GeV}/c$  and  $R = 0.2$ ), corrected with FD fractions from inclusive particle analysis and from simulation in PYTHIA8 jets ( $R = 0.2$ ).

from the 2010 data-set). The effect is much smaller when only taking  $\Lambda(\bar{\Lambda})$  particles from positive  $\eta^{V^0}$  (what corresponds to the "A-side" of the detector) as can be seen in the left panel of Fig. 3.53 as the open markers that are closer to unity for the entire  $V^0 p_T$  range. The  $\Lambda/\bar{\Lambda}$  ratio as a function of  $p_T$  in jet cones and for uncorrected particle yields is shown in the right panel in Fig. 3.53. It indicates that the ratio on the  $\Lambda$  and  $\bar{\Lambda}$  in the jet cones is different than the one for the inclusive particles and might be closer to unity (considering the large statistical errors at higher  $p_T$ ).

It was studied for this analysis whether considering only  $\Lambda(\bar{\Lambda})$  reconstructed within the "A-side" of the TPC can be used to obtain the final results. However it became clear that the required statistics are not sufficient in that case for the analysis method to work properly. Therefore instead all available  $\Lambda(\bar{\Lambda})$  baryons are considered and a constant uncertainty on this ratio of 6% is used for all  $V^0 p_T$  intervals.

### Difference between corrected inclusive $V^0 p_T$ spectra from 2011 and 2010

A deviation of the (inclusive corrected) results from the data sets of the Pb–Pb data recorded in 2010 (which were used for the published analysis that calculated the inclusive  $\Lambda$  and  $K_S^0 p_T$  spectra as well as the  $\Lambda/K_S^0$  ratio) to the current (inclusive corrected) results (using the 2011 data set) is found.

The uncertainty that reflects this discrepancy is assumed to be constant over the entire measured  $V^0 p_T$  range (see Fig. 3.54). Since the origin of this (at maximum) 10% deviation is not yet completely understood, it is included as a systematic uncertainty into all results of the current analysis.

This uncertainty contributes the largest systematic uncertainty fraction to the results and makes it necessary for a publication of the results to trace back the reason and apply an

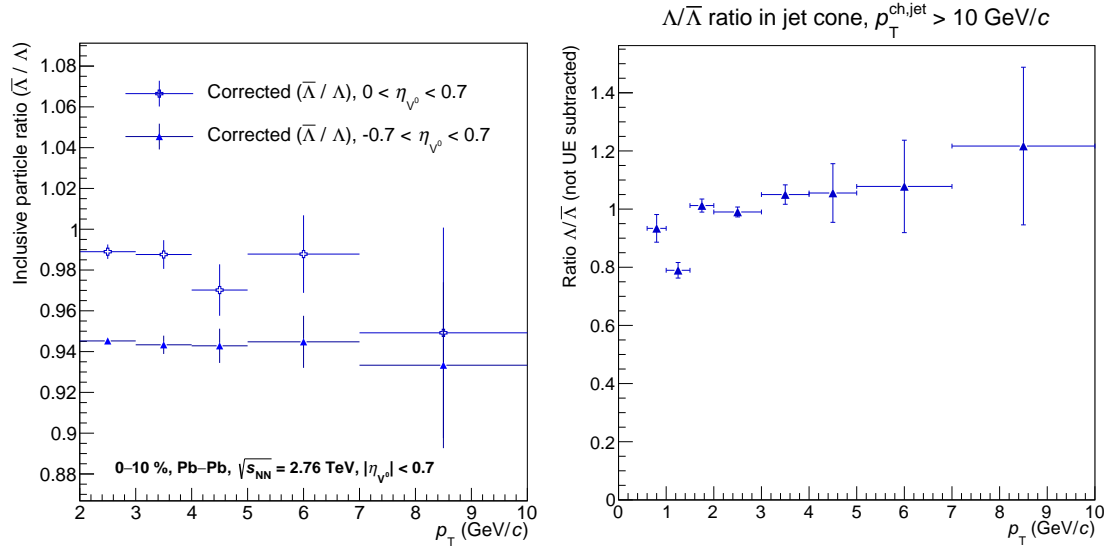


Figure 3.53: Left side: Ratio of the inclusive  $\Lambda$  and  $\bar{\Lambda}$   $p_T$  spectrum measured in the 2011 dataset (for the entire  $\eta^{V_0}$  acceptance) shows a deviation from unity. The effect is about 5-10% smaller when only taking  $\Lambda(\bar{\Lambda})$  particles with positive  $\eta^{V_0}$  (what corresponds to the "A-side" of the detector) shown as open markers. Right side:  $\Lambda/\bar{\Lambda}$  ratio as function of  $p_T$  in jet cones (uncorrected yields).

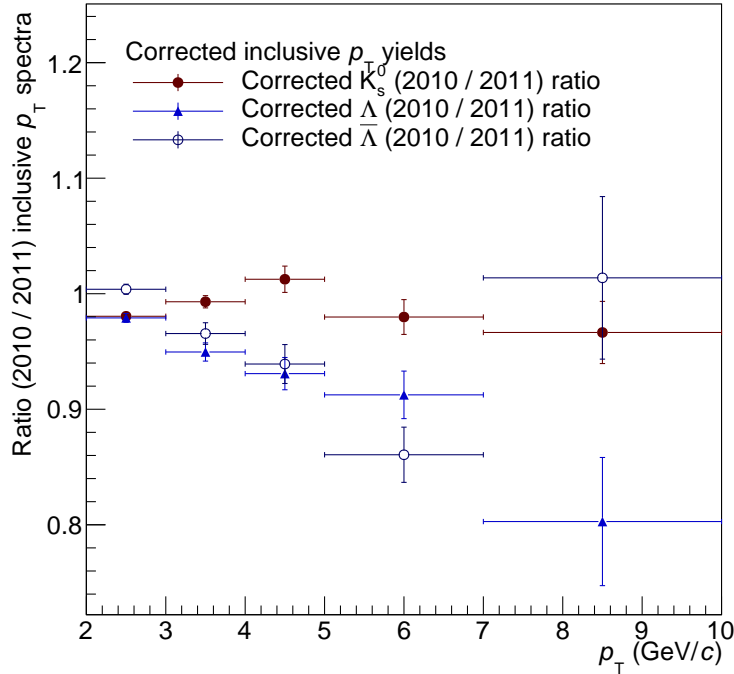


Figure 3.54: Ratio of inclusive particle  $p_T$  spectrum from 2010 data (and respective MC) to those recorded in 2011 (used for this work). Since the ratio of  $p_T$  spectra deviates from unity a systematic uncertainty of 10% on this effect is assigned to all data points in the final results.

Table 3.9: The minimal and maximal fractions of the relative systematic uncertainty on the final results

Systematic effects (all in %)	$K_S^0$ $p_T$ spec.	$(\Lambda + \bar{\Lambda})$ $p_T$ spec.	$(\Lambda + \bar{\Lambda})/2K_S^0$
2010-2011 data discrepancy	10	10	10
$\Lambda/\bar{\Lambda}$ discrepancy	–	6	6
Efficiency (cut variations)	[2.4 - 0.1]	[0.80-0.041]	[9.0-2.71]
Feed-down (incl. vs PYTHIA)	–	[12.9-3.6]	[12.9-3.6]
Underlying Event (Embedding CF):			
CF slope ( $p_T$ dependence)	[0.0-0.17]	[0.0-0.42]	[0.0-0.4]
CF jet contamination (all ev./NJ ev.)	0.95	[1.85-0.0]	[1.8-0.0]
CF event plane dependence	0.6	0.44	0.74
Material Budget			
	1.1	4.6	2.6
Signal extraction			
	[0.6-4.4]	[1.1-6.7]	[0.8-4.7]
Total systematic uncertainty:			
	[10.4-10.0]	[18.1-13.2]	[18.2-13.0]

appropriate correction or re-do the MC simulation.

What was seen so far, is that the ratio of the uncorrected spectra from 2011 w.r.t. 2010 is in agreement with unity but the corrected ratios deviate from unity by about 10%. This was seen for the currently used  $V^0$  finding method and is still under investigation for all analysis that include identified  $K_S^0$ ,  $\Lambda$  or  $\bar{\Lambda}$  particles.

### Total relative systematic uncertainty

As a final step of the systematical error calculation, the contributions (from different sources) of the relative systematic uncertainty are combined to the final total systematic uncertainty by a sum in quadrature as shown in Eq. 3.43.

$$\sigma_{\text{tot.,sys.}} = \sqrt{\sum_{i=1}^N (\sigma_{\text{rel.,sys.}}^{\text{source},i})^2} \quad (3.43)$$

with the different sources as listed in Tab. 3.9.

Since some of the effects show a dependence on the particle  $p_T$ , most of the uncertainties are calculated for each  $p_T$  bin separately.

The total systematic uncertainties for the  $(\Lambda + \bar{\Lambda})/2K_S^0$  ratio in jets in  $R = 0.2$  and for  $p_T^{\text{jet}} > 10$  GeV/c are shown in Tab. 3.10 (those for the results for jets from  $p_T^{\text{jet}} > 20$  GeV/c in Tab. 3.11). The various contributions of the different sources of uncertainty to the total systematic uncertainty are shown for the  $K_S^0$  and  $\Lambda$   $p_T$  spectrum in Fig. 3.55a and in Fig. 3.55b. The uncertainties for the  $(\Lambda + \bar{\Lambda})/2K_S^0$  ratio in jets are shown in Fig. 3.56. The source of contributions are indicated by different colours and add up linear on top of each other for a better comparability of the size of the certain contribution. The total systematic error is shown as a dotted line superimposed with the various contributions.

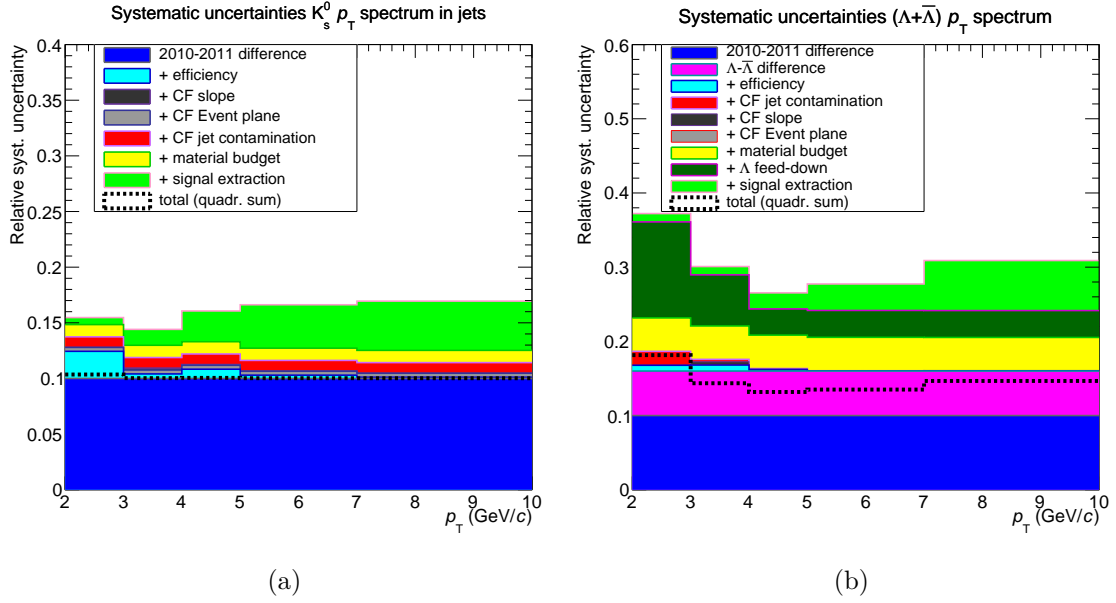


Figure 3.55: Contributions to the total relative systematic uncertainty (black dashed line) for the  $K_S^0 p_T$  spectra in jets ( $R = 0.2$ ). The various contributions are added linearly, while the total relative systematic uncertainty is calculated according to Eq. 3.43. a) Uncertainty contributions for the  $K_S^0 p_T$  spectrum. b) Uncertainty contributions for the  $\Lambda + \bar{\Lambda} p_T$  spectrum.

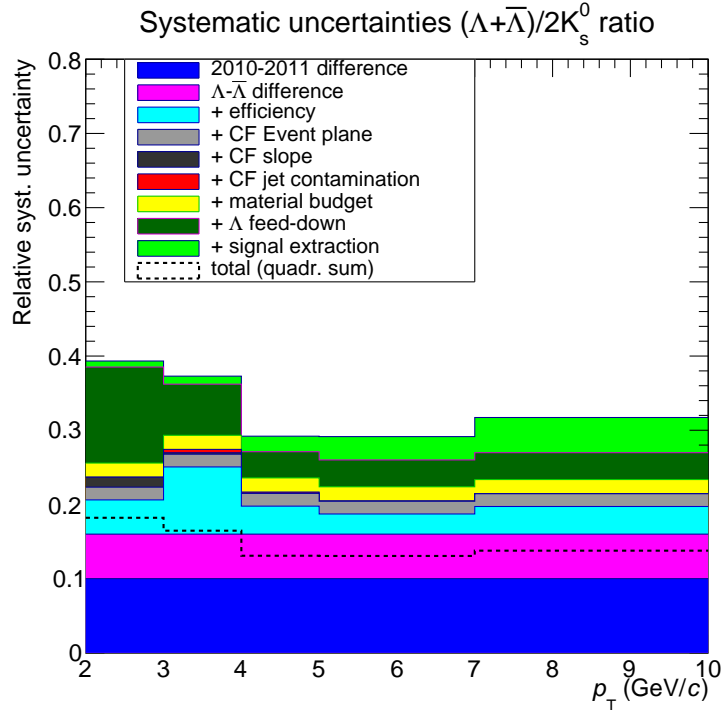


Figure 3.56: Contributions to the total relative systematic uncertainty (black dashed line) for the  $(\Lambda+\bar{\Lambda})/2K_S^0$  in jets (of  $R = 0.2$ ). The various contributions are added linearly, while the total relative systematic uncertainty is calculated according to Eq. 3.43.

$p_T$ interval (GeV/c)	Data point	Relative syst. error	Absolute syst. error
2.0-3.0	0.372854	0.182689	0.0681165
3.0-4.0	0.507227	0.165364	0.0838772
4.0-5.0	0.250714	0.131786	0.0330405
5.0-7.0	0.207972	0.131512	0.0273507
7.0-10.0	0.180750	0.138588	0.0250498

Table 3.10: Data points and total systematic uncertainty for the  $(\Lambda+\bar{\Lambda})/2K_S^0$  ratio in jets ( $R = 0.2$ ) and in  $p_{T,\text{jet}}^{\text{ch}} > 10$  GeV/c

$p_T$ interval (GeV/c)	Data point	Relative syst. error	Absolute syst. error
2.0-3.0	0.138142	0.182689	0.0252371
3.0-4.0	0.408729	0.165364	0.0675891
4.0-5.0	0.189009	0.131786	0.0249087
5.0-7.0	0.214187	0.131512	0.0281681
7.0-10.0	0.18466	0.138588	0.0255916

Table 3.11: Data points and total systematic uncertainty for the  $(\Lambda+\bar{\Lambda})/2K_S^0$  ratio in jets ( $R = 0.2$ ) and in  $p_T^{\text{jet}} > 20$  GeV/c

In order to calculate the absolute symmetric error for each data point, the relative total systematic uncertainty of each source is multiplied by the corresponding data point and drawn symmetrically as a box around the data point.

The largest contribution is given by the discrepancy of the 2011 to 2010 dataset, followed by the uncertainty due to the signal extraction (which is slightly increasing with increasing  $p_T$  value) and the efficiency correction. For the  $\Lambda$  related results (as shown in Fig. 3.55b and in Fig. 3.56), the uncertainty from the  $\Lambda$ -to- $\bar{\Lambda}$  discrepancy, contributes with 6% the second-largest fraction of the total systematic uncertainty. The third-largest error fraction is contributed by the feed-down subtraction, with the largest values at small  $p_T$  and gets smaller for the higher  $V^0$   $p_T$  intervals. The resulting total relative and absolute systematic errors are at maximum around 11% for the  $K_S^0$   $p_T$  spectrum and around 20% for the  $(\Lambda+\bar{\Lambda})$   $p_T$  spectrum. For the  $(\Lambda+\bar{\Lambda})/K_S^0$  ratio they are also listed as numbers in Tab. 3.10 and Tab. 3.11.

In the following chapter 4, the final results of this analysis are presented and discussed.



# Chapter 4

## Results and discussion

In this chapter, the results of the  $K_S^0$ ,  $\Lambda$  and  $\bar{\Lambda}$  analysis in the inclusive event, inside the jets and in the Underlying Event (in “no-jet” events) are presented.

The corrected inclusive spectra for the current analysis are shown and compared to the already published results [92]. Then the  $(\Lambda + \bar{\Lambda})/2K_S^0$  ratio and the  $V^0$   $p_T$  spectra inside the jets and in “no-jet” events are presented. The particle ratio in jets is compared to the inclusive measurement, to a PYTHIA simulation of jets in pp collisions and to the particle ratio measured in jets in p–Pb collisions at  $\sqrt{s_{NN}} = 5.02$  TeV.

### 4.1 Inclusive particles

In Fig. 4.1 (upper panel) the results are presented of the inclusive  $K_S^0$ ,  $\Lambda$  and  $\bar{\Lambda}$   $p_T$  spectra in Pb–Pb collisions at  $\sqrt{s_{NN}} = 2.76$  TeV, as obtained with the in 2011 recorded data set from this analysis. Figure 4.1 (lower panel) shows the derived inclusive  $(\Lambda + \bar{\Lambda})/2K_S^0$  ratio from our analysis (open markers) together with the  $\Lambda/K_S^0$  ratio which was published in [92]. The published results have been obtained with a previous analysis that used a slightly different  $V^0$  cut selection and also a different binning for the  $V^0$   $p_T$  and the event centrality (0-5%, 5-10%, etc.). Although the inclusive ratio in this analysis is measured in a larger interval of the  $V^0$  pseudo-rapidity  $|\eta^{V^0}| < 0.7$  than the published spectra (which have been measured in the rapidity acceptance  $|y^{V^0}| < 0.5$ ), the resulting ratios show good agreement.

In this ratio of the inclusive  $\Lambda(\bar{\Lambda})$  baryons and  $K_S^0$  mesons in Pb–Pb collisions, the characteristic baryon enhancement around intermediate particle  $p_T$  (around 2-4 GeV/c) becomes visible. It will serve as a comparison to the particle ratio inside jets which is presented in the following.

### 4.2 $(\Lambda + \bar{\Lambda})/2K_S^0$ ratio in jets in Pb–Pb collisions

The  $(\Lambda + \bar{\Lambda})/2K_S^0$  ratio in jets for the two different  $p_T^{\text{jet}}$  intervals (for  $p_T^{\text{jet}} > 10$  GeV/c in red markers and for  $p_T^{\text{jet}} > 20$  GeV/c in blue markers) are shown in Fig. 4.2. The jets are selected with a leading track requirement of  $p_T^{\text{track}} > 5$  GeV/c. They are compared to the ratio obtained from the inclusive  $V^0$  particles (open markers, only statistical errors

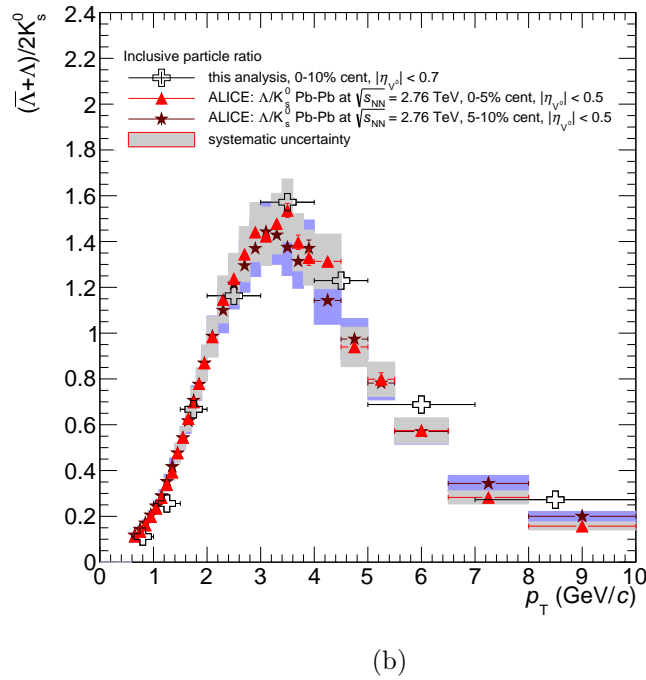
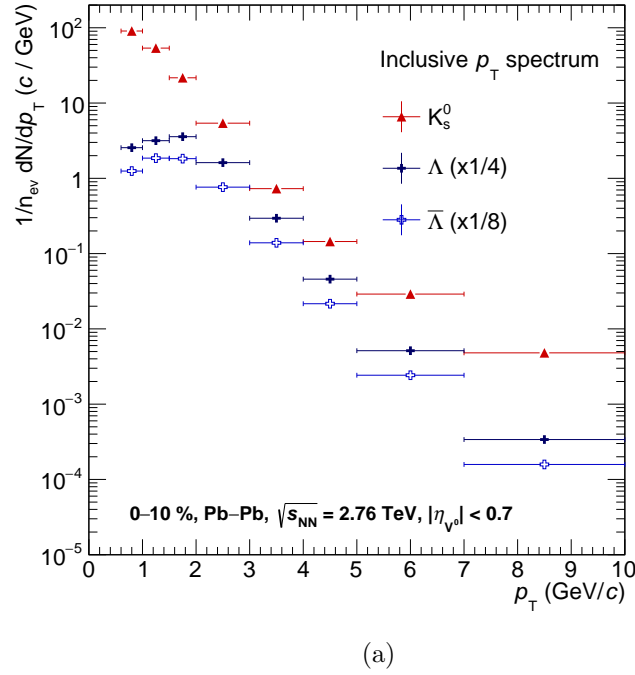


Figure 4.1: a) Corrected inclusive  $K_S^0$  and  $\Lambda(\bar{\Lambda})$   $p_T$  spectra of the 10% most central events in Pb–Pb collisions. The  $\Lambda$  and  $\bar{\Lambda}$   $p_T$  spectra are scaled for better visibility and only statistical errors are shown. b)  $(\Lambda + \bar{\Lambda})/2K_S^0$  ratio of the 10% most central events in Pb–Pb collisions (only statistical errors are shown) compared to the published [92] inclusive  $\Lambda/K_S^0$  ratio from events of the centrality intervals 0-5% (red markers) and 5-10% (black markers).

are shown). As already expected from the particle ratio [123] in jets in p–Pb collisions we observe the particle ratio in jets in Pb–Pb collisions as far below the huge enhancement seen for the inclusive particle ratio in Pb–Pb data.

The upper panel in Fig. 4.2 shows the  $(\Lambda+\bar{\Lambda})/2K_S^0$  ratio in jets for the two different  $p_T^{\text{jet}}$  intervals ( $p_T^{\text{jet}} > 10$  GeV/c in red markers and  $p_T^{\text{jet}} > 20$  GeV/c in blue markers). Furthermore they are compared to the  $(\Lambda+\bar{\Lambda})/2K_S^0$  ratio obtained from PYTHIA8 (tune 4C) jets (with the same jet resolution parameter of  $R = 0.2$ ). The measured particle ratio shows a slight enhancement for the  $V^0$  hadrons with  $2 < p_T < 4$  GeV/c, compared to the ratio at higher particle  $p_T$  ( $\gtrsim 4$  GeV/c). The comparison of the ratio in jets to the one from a PYTHIA simulation in jets (simulated with “smeared”<sup>33</sup>  $p_T^{\text{jet}}$ ) in pp collisions however does not exhibit the same shape of the ratio at intermediate transverse momentum ( $2 < p_T < 4$  (GeV/c)) but instead predicts a larger ratio for the higher  $p_T$  values ( $\gtrsim 4$  GeV/c). PYTHIA furthermore shows a slightly higher increase of the  $(\Lambda+\bar{\Lambda})/2K_S^0$  ratio in the interval with jets of a higher  $p_T^{\text{jet}}$  threshold (i.e.  $p_T^{\text{jet}} > 20$  GeV/c) compared to the ratio with the lower jet  $p_T$  limit ( $p_T^{\text{jet}} > 10$  GeV/c).

The lower panel in Fig. 4.2 shows the comparison from the  $(\Lambda+\bar{\Lambda})/2K_S^0$  ratio in jets to the one obtained from inclusive particles (i.e. all  $V^0$  particles in the Pb–Pb event). It indicates that the baryon-to-meson ratio inside the jet environment is much less enhanced than in the inclusive particles in Pb–Pb collisions. This might indicate that the huge baryon enhancement in heavy-ion collisions is mainly a bulk effect (attributed to the soft component of the collision) and due to an hadronisation mechanism which is not dominating the hadron production inside jets.

### 4.3 $K_S^0$ , $\Lambda$ and $\bar{\Lambda}$ hadrons in “no-jet” events in Pb–Pb collisions

The  $V^0$  particles from “no-jet” events, that are events in which no reconstructed jet was selected, are considered to have only a very small to negligible contribution of  $V^0$  particles stemming from jet fragmentation. It is therefore expected that the  $V^0$   $p_T$  spectra which are shown in Fig. 4.3 (left panel) in these events represent a measurement of bulk particle production. Although the “bulk”<sup>34</sup> represents a measure of the Underlying Event in the Pb–Pb event the “no-jet”  $V^0$   $p_T$  spectrum still might contain few particles with  $p_T \gtrsim 5$  GeV/c. This is mainly due to the selection criteria for the selected jets (minimum  $A_{\text{jet}} > 0.6 \pi R^2$  with  $R = 0.2$ , leading constituent track  $p_T > 5$  GeV/c) which are optimised to distinguish between signal and background jets but still let a minor fraction of (very soft) signal jets (with  $p_T^{\text{jet}} < 5$  GeV/c) pass the “no-jet” event selection. Therefore few  $V^0$  hadrons that originate from these soft jets might populate the  $V^0$   $p_T$  spectrum for “no-jet” events. The resulting measured  $(\Lambda+\bar{\Lambda})/2K_S^0$  ratio is therefore very close to the one seen in the inclusive particle analysis, since the majority of particles are produced in

<sup>33</sup>The  $p_T^{\text{jet}}$  of the PYTHIA jets is smeared using the published [171] (corrected)  $\sigma(\delta p_T) = 5.10$  GeV/c in order to account for the impact of the Underlying Event fluctuations on the jet reconstruction in Pb–Pb collisions.

<sup>34</sup>The term “bulk” is commonly attributed to the soft particle production in heavy-ion events that produces the majority of particles and is also considered as the “Underlying Event” (UE) in this analysis.

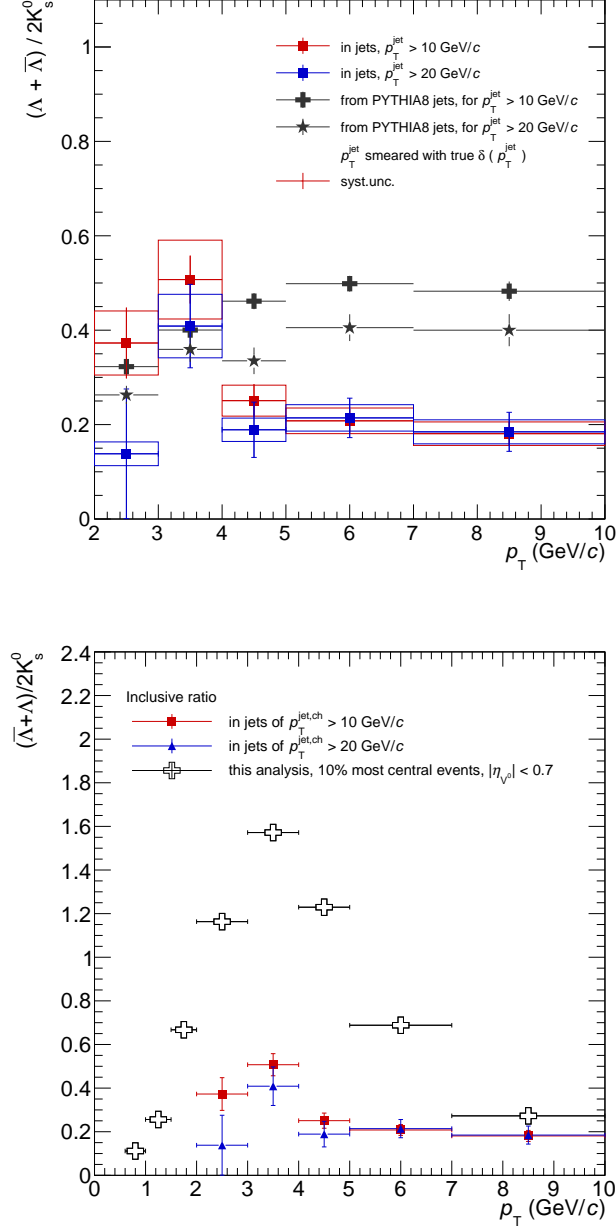


Figure 4.2: Upper panel:  $(\Lambda + \bar{\Lambda}) / 2K_S^0$  ratio in jets ( $R = 0.2$ ) for  $p_T^{\text{jet}} > 10$  GeV/c and  $p_T^{\text{jet}} > 20$  GeV/c. Furthermore the  $(\Lambda + \bar{\Lambda}) / 2K_S^0$  ratio obtained from PYTHIA jets ( $R = 0.2$ ) is shown. Lower panel: The  $(\Lambda + \bar{\Lambda}) / 2K_S^0$  ratio in jets ( $R = 0.2$ ) for  $p_T^{\text{jet}} > 10$  GeV/c (red markers) and  $p_T^{\text{jet}} > 20$  GeV/c (blue markers) and in the inclusive (i.e. all  $V^0$  particles) event (open black markers) obtained from this analysis. Shown are only statistical errors.

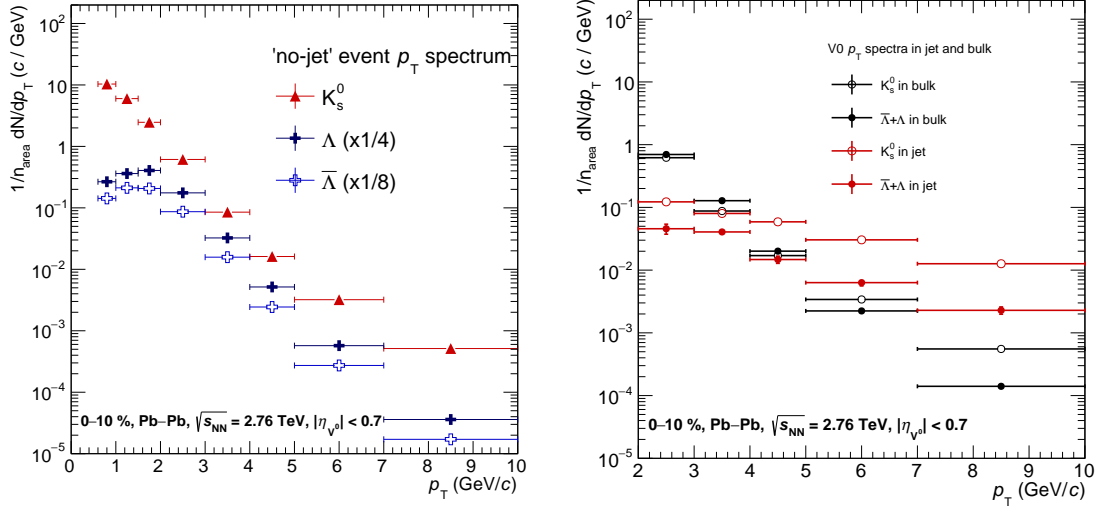


Figure 4.3: Corrected  $\Lambda$ ,  $\bar{\Lambda}$  and  $K_S^0$   $p_T$  spectra in ("no-jet") events from Pb–Pb data (left panel). Right panel: Spectra outside (black markers) and inside ( $R = 0.2$ ) jets (red markers) together. Open markers are  $K_S^0$ , full markers are  $\Lambda$  hadrons.

the soft regime of the heavy-ion collision. The label " $\Lambda+\bar{\Lambda}$ " is standing here and in the following for the hadron  $p_T$  spectrum of  $\Lambda$  and  $\bar{\Lambda}$  baryons, both added up and divided by 2. Figure 4.3 shows the  $\Lambda+\bar{\Lambda}$  (full markers) and  $K_S^0$  (open markers)  $p_T$  spectra in the bulk (black markers) together with the spectra in jets (red markers). As expected one finds the  $p_T$  spectra inside the jets to be much harder compared to the bulk spectra, the latter contain therefore much more soft particles (higher yields at low  $V^0$   $p_T$ ) and less particles at higher  $V^0$   $p_T$  (from around  $p_T > 5$  GeV/c).

A comparison for the  $(\Lambda+\bar{\Lambda})/2K_S^0$  ratio in the bulk (in green markers) to the inclusive, published spectra in Pb–Pb collisions at  $\sqrt{s_{NN}} = 2.76$  TeV and to the inclusive ratio measured in pp collisions at  $\sqrt{s} = 7$  TeV and  $\sqrt{s} = 0.9$  TeV is shown in Fig. 4.4. Furthermore the ratio in jets is also shown for the two  $p_T^{\text{jet}}$  intervals (red markers for  $p_T^{\text{jet}} > 10$  GeV/c, blue markers for  $p_T^{\text{jet}} > 20$  GeV/c). The particle ratio in both jet  $p_T$  intervals is far below the one measured in the inclusive (grey markers) particle analysis (at the same center-of-mass energy and from the data recorded in 2010) as well as the ratio measured outside the jet cones, in the "no-jet" events (green markers). On one hand this points to a scenario in which the hadronisation of soft particles is disentangled from the hard fragmentation processes. On the other hand, the baryon enhancement at intermediate  $p_T$  could also stem (entirely or partially) from collective effects like particle flow that modify the spectra shape and therefore lead to the enhancement in the baryon-to-meson ratio. Therefore the baryon enhancement seen in inclusive production at intermediate particle  $p_T$  in Pb–Pb collisions seems to be a feature of the UE and not due to hard parton fragmentation. At high  $V^0$   $p_T$  (from around  $p_T \geq 7$  GeV/c) the inclusive ratio and the ratio in jets in Pb–Pb collisions are in agreement. This can be expected, since the dominating hadron production mechanism at these higher  $p_T$  values is considered to be fragmentation and not to be affected by

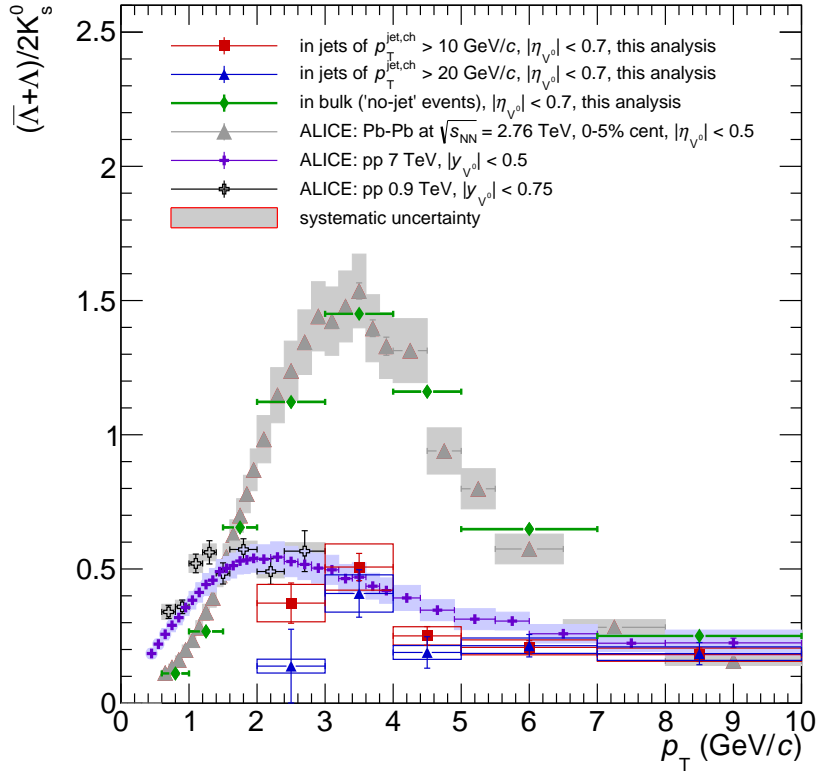


Figure 4.4:  $(\bar{\Lambda} + \Lambda)/2K_S^0$  ratio in jets ( $R = 0.2$ ) for  $p_T^{\text{jet}} > 10$  GeV/c (red markers) and  $p_T^{\text{jet}} > 20$  GeV/c (blue markers) and in the bulk of the Pb–Pb collision event (green markers) via “no-jet” events. The measured ratios from this analysis are compared to the inclusive, published  $\Lambda/K_S^0$  ratio (grey markers) and the inclusive ratio measured in pp collisions at  $\sqrt{s} = 7$  TeV and  $\sqrt{s} = 0.9$  TeV.

soft particle production mechanisms anymore. Furthermore the impact of collective effects (direct flow, elliptic flow,..) in the bulk on the jet  $V^0$  constituents seems to be negligible in this  $p_T$  range and in this centrality interval (0-10%).

Within the statistical uncertainties of both  $p_T^{\text{jet}}$  intervals, there is no clear evidence for a dependence on the  $p_T^{\text{jet}}$  threshold. The ratios in jets furthermore seem to agree with the inclusive  $\Lambda/K_S^0$  ratios measured in pp collisions at  $\sqrt{s} = 7$  TeV and at  $\sqrt{s} = 0.9$  TeV.

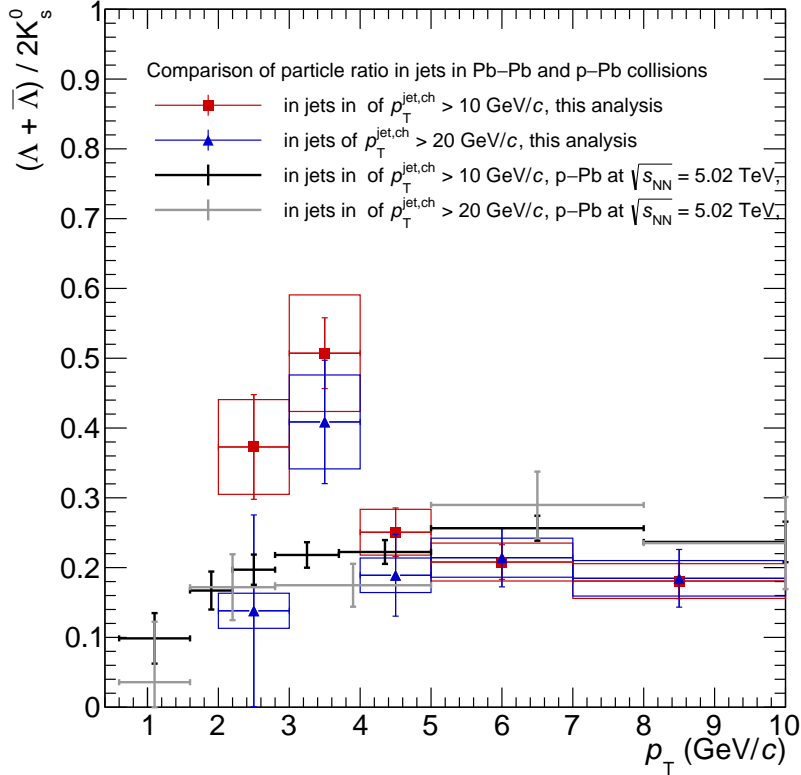


Figure 4.5:  $(\bar{\Lambda} + \Lambda) / 2K_S^0$  ratio in jets in p–Pb collisions compared to the ratio measured in this analysis in Pb–Pb collisions. Results in p–Pb collisions adapted from [123].

#### 4.4 Comparison of $\Lambda + \bar{\Lambda} / 2K_S^0$ ratio to other measurements

In the following, comparisons to other measurements in ALICE and the results of other experiments are discussed.

Fig. 4.5 shows the  $(\Lambda + \bar{\Lambda}) / 2K_S^0$  ratio in jets from this analysis to the one measured in p–Pb collisions. Both analyses follow the same strategy but use slightly different settings and selections (e.g. it is not necessary to require a leading track with  $p_T > 5$  GeV/c in the p–Pb analysis to suppress the numerous combinatorial jets as present in Pb–Pb events). This implies that there is no  $p_T^{\text{jet}}$  "smearing" present, like in the Pb–Pb data. The main difference, when analysing p–Pb and Pb–Pb data, is the huge UE contribution to the jet energy and the spectra in jets. The observed particle ratio in Pb–Pb events might hint on a possible modification of hadron production in jets in Pb–Pb collisions compared to the result in p–Pb collisions, seen as the peak-like structure around  $p_T \sim 2\text{--}4$  GeV/c. Later in this chapter we will have a more differential look on this possible modification at intermediate  $p_T$  when looking at the  $V^0$   $p_T$  spectra in jets.

The question of a possible modification of the baryon-to-meson ratio in a jet-like environment compared to the one from the bulk of the event can be also addressed by particle correlation techniques which do not require jet reconstruction but only single selected

high- $p_T$  tracks, so-called "trigger" particles. A "trigger" particle is expected to be one of the leading jet constituents that is pointing approximately into the direction of the initial hard scattered parton. The jet reconstruction is expected as a better approach since it considers (almost) all jet constituents in order to calculate a jet axis that should be much closer to the "true" parton direction.

Since the high- $p_T$  trigger particles are selected from a certain momentum interval (e.g.  $p_T^{\text{hadron}} > 5 \text{ GeV}/c$ ) they are more likely produced at the surface of the evolving medium (which is created in the heavy-ion collision) than deeply inside the volume of the fireball. From this consideration it could be expected that the associated  $V^0$  particles close to this trigger hadron (which could be e.g. the leading particle of a jet shower) also do not have a sizable path-length within the medium and therefore may only show a tiny medium-modification. However such a possible surface bias [178] is reduced in an intra-jet analysis but also requires to correct for all effects that the charged Underlying Event can have on a reconstructed jet. That makes jet analyses in general more sophisticated and require an accurate correction procedure, like presented in this thesis, which is not required when only selecting high- $p_T$  trigger hadrons. To which extent this surface bias can modify the results compared to those from a jet analysis is not completely clear and not straightforward to be predicted by specific Monte Carlo (MC)<sup>35</sup> simulations.

On the other hand, jet analysis requiring a minimum leading track  $p_T$  ( $p_{T,\text{track}}^{\text{leading}} > 5 \text{ GeV}/c$  that is intended to suppress combinatorial (background) jets) also might impose a certain small fragmentation bias on the jet sample which could lead to a similar effect like the surface bias. Therefore any difference on high- $p_T$  trigger hadron correlation studies and the results of analyses employing jets could be due to a bias in either one or the other way.

Fig. 4.6 shows a comparison of the particle ratio obtained from this analysis (red and blue markers) and in an analysis employing such a hadron- $V^0$  correlation technique (that was also briefly discussed in the Introduction section 1.9). The graphic shows the  $\Lambda/K_S^0$  ratio (green markers) in a jet-like environment (w.r.t. a high- $p_T$  trigger hadron in  $|\eta_{\text{trig}}| > 0.2$ ) obtained from the so-called “ $\eta$ -reflection method” as presented in [117]. Considering the size of the systematic uncertainties one can not see a significant difference between both results and therefore no surface bias could be found. Furthermore one can conclude the same physics message from both results that the baryon-to-meson enhancement in a jet-like environment does not exhibit the characteristic peak shape that is seen in the inclusive  $\Lambda$  and  $K_S^0$  analysis, but might hint on a possible small enhancement when compared to the particle ratio obtained in jets in p–Pb collisions (see Fig. 4.5). The next section dedicates a closer look on the  $V^0$   $p_T$  spectra and investigates how they might exhibit some modifications w.r.t. the measurement of the  $V^0$   $p_T$  spectra in jets in p–Pb collisions and the prediction of a PYTHIA simulation.

---

<sup>35</sup>There are MC event generators existing which can in general describe the  $\Lambda/K_S^0$  enhancement with good agreement in heavy-ion collisions like e.g. EPOS [179].

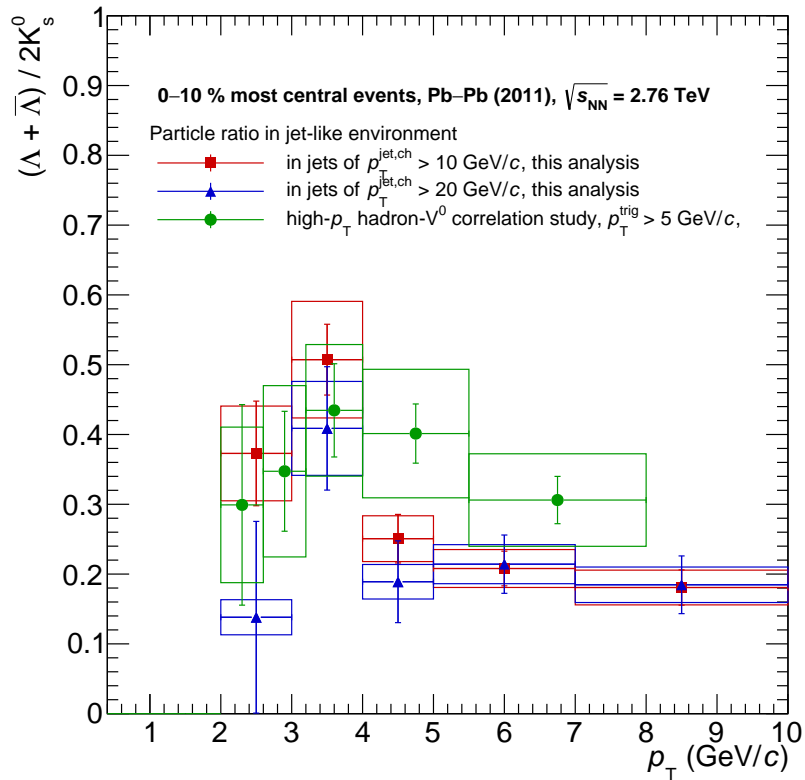


Figure 4.6: Comparison of results obtained in the current jet analysis and in the high- $p_T$  hadron- $V^0$  correlation study (data adapted from T. Richert, thesis at Lund University [117]).

## 4.5 $K_S^0$ and $\Lambda + \bar{\Lambda}$ $p_T$ spectra in jets in Pb–Pb collisions

The particle ratio measurements can give a first hint on possible medium-modifications of the baryon and meson production in jets from Pb–Pb data compared to PYTHIA simulations or to the results obtained from p–Pb events. The form of the related  $V^0$   $p_T$  spectra presented in this section however can give us even more detailed information.

The fully corrected  $K_S^0$ ,  $\Lambda$  and  $\bar{\Lambda}$   $p_T$  spectra in jets are shown in Fig. 4.7 (both in logarithmic and linear scale of the y-axis and for the two  $p_T^{\text{jet}}$  intervals (red and blue markers)). It is visible that the  $K_S^0$  particle  $p_T$  spectra have higher yields than the heavier  $\Lambda(\bar{\Lambda})$  baryons, as it is also the case for the inclusive particle spectra. Also the shape of the spectra differ from each other. While the  $K_S^0$  follow an exponential distribution, the  $\Lambda$   $p_T$  spectrum show slightly smaller relative yields at the lower  $p_T$  intervals (around  $p_T \sim 2\text{--}4$  GeV/c) which might indicate a peak-like structure.

Figure 4.8 shows a comparison of these measured spectra to a simulation of PYTHIA jets<sup>36</sup> in pp events, using three different PYTHIA tunes (PYTHIA6 [23] tunes “Perugia 2011” and “NoCR” (i.e. no colour-reconnection) and PYTHIA8 [180] tune “Monash”). The left panel shows the  $K_S^0$  and  $(\Lambda + \bar{\Lambda})$   $p_T$  spectrum in jets with  $p_T^{\text{jet}} > 10$  GeV/c. On the right panel the spectra are shown for jets with  $p_T^{\text{jet}} > 20$  GeV/c. The four panels below show the ratios for the data divided by the MC simulation (different PYTHIA tunes in different marker colour) for  $K_S^0$  and  $(\Lambda + \bar{\Lambda})$  separately. The ratios (data/MC) are shown separately for the two  $p_T^{\text{jet}}$  intervals and below the corresponding measurement.

Due to the limited  $V^0$  particle statistics it is not possible to correct the reconstructed  $p_T^{\text{jet}}$  value for the jet  $p_T$  smearing that is caused by the fluctuations of the charged tracks from the UE. Therefore the PYTHIA jets are smeared in  $p_T^{\text{jet}}$  according to the particle level  $\sigma(\delta p_T^{\text{ch}})$  value (i.e. using the true Monte Carlo simulated values of the observables) that is the width of the  $\delta p_T^{\text{ch}}$  distribution<sup>37</sup>. For this the  $\delta p_T^{\text{ch}}$  has been studied in the 10% most central events and for a  $p_T^{\text{ch track}} > 150$  MeV/c (as used in this analysis) and as published in [84].

The measured  $K_S^0$   $p_T$  spectrum in jets from the PYTHIA simulation (see Fig. 4.8) shows a slope similar to the one from the spectra in jets in Pb–Pb events. The various PYTHIA tunes, when compared to each other, show small or no deviation which depends on the  $V^0$   $p_T$  interval.

The  $K_S^0$   $p_T$  spectrum seems to agree or exceed the PYTHIA predicted yields depending on the PYTHIA tunes. Agreement is seen for the tune “Monash” while an excess of the

<sup>36</sup>The Pythia program is a standard tool for the generation of events in high-energy collisions, comprising a coherent set of physics models for the evolution from a few-body hardprocess to a complex multiparticle final state. It contains a library of hard processes, models for initial- and final-state parton showers, matching and merging methods between hard processes and parton showers, multiparton interactions, beam remnants, string fragmentation and particle decays. It also has a set of utilities and several interfaces to external programs. Pythia8.2 is the second main release after the complete rewrite from Fortran to C++, and now has reached such a maturity that it offers a complete replacement for most applications, notably for LHC physics studies. The many new features should allow an improved description of data." As cited from PYTHIA manual [180].

<sup>37</sup>Which is a distribution describing the deviation of the reconstructed  $p_T^{\text{jet}}$  value, that is corrected for the “average”  $p_T$  density contribution from the charged UE tracks with respect to the “true”  $p_T^{\text{jet}}$  value (i.e. without UE fluctuations) “true”  $p_T^{\text{jet}}$  value.

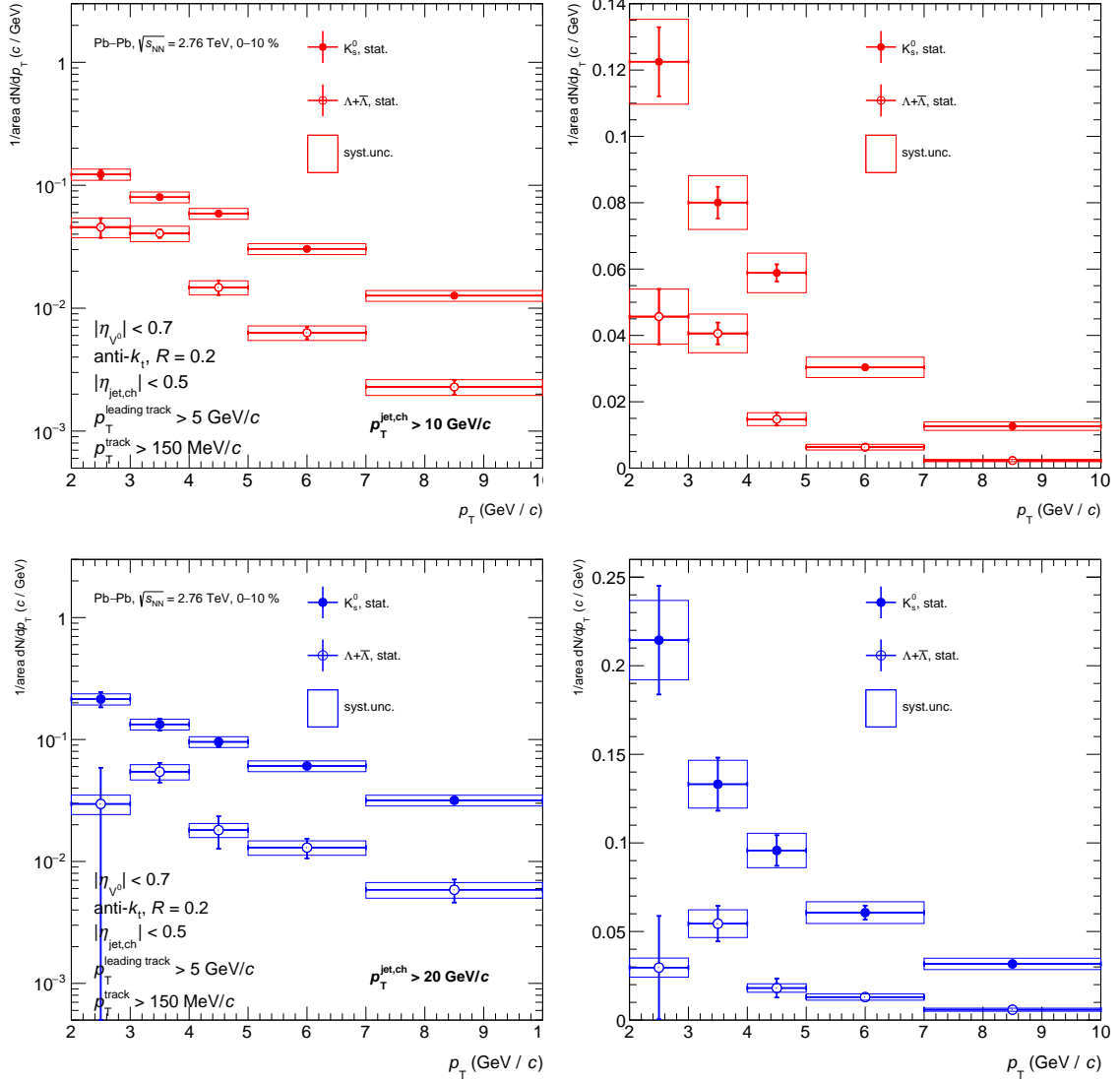


Figure 4.7: Corrected  $K_S^0$  and  $\Lambda$  spectrum in jets ( $R = 0.2$ ) for  $p_T^{\text{jet}} > 10$  GeV/c (upper panels)  $p_T^{\text{jet}} > 20$  GeV/c (lower panels), in logarithmic and linear y-axis scale. Jets are selected with a leading track bias  $p_T^{\text{leading track}} > 5$  GeV/c.

mesons in the data is seen when compared to PYTHIA6 tune "Perugia2011". The  $\Lambda$   $p_T$  spectrum from Pb–Pb and the PYTHIA simulation exhibits a systematical deviation in the spectral shape. For low  $\Lambda$  particle  $p_T$  (in the interval  $2 \text{ GeV}/c < p_T < 4 \text{ GeV}/c$ ) the measured yields are slightly higher than predicted by PYTHIA jets, but for higher  $\Lambda$   $p_T$ , the measured yields are lower compared to the predictions from the different PYTHIA tunes. In summary from this PYTHIA comparison an interpretation of the observed effects is not clearly possible (because different tunes result partially in different effects), but another comparison to a reference measured in p–Pb collisions can be made as well:

Figure 4.9 contains all these spectra for the different hadron species and for the two different  $p_T^{\text{jet}}$  intervals. The left panel shows the spectra in jets for  $p_T^{\text{jet}} > 10 \text{ GeV}/c$  and the right panel those for jets with  $p_T^{\text{jet}} > 20 \text{ GeV}/c$ . The results from the p–Pb data are scaled according to a PYTHIA simulation to take into account the effect of the UE fluctuations (present in Pb–Pb events), the leading constituent cut  $p_T^{\text{leading track}} > 5 \text{ GeV}/c$  and the different collision energy. This scaling procedure [172] of the measured spectra from [123] and at  $\sqrt{s_{\text{NN}}} = 5.02 \text{ TeV}$  is done by using  $V^0$   $p_T$  spectra simulated by PYTHIA (of a certain tune) at the same energy and then dividing it by the PYTHIA spectrum simulated at  $\sqrt{s_{\text{NN}}} = 2.76 \text{ TeV}$  and with the same analysis settings ( $p_T^{\text{leading track}} > 5 \text{ GeV}/c$ ) as used in the current work. The so obtained  $p_T$ -dependent ratio from PYTHIA is applied as a scaling to the measured spectrum in p–Pb collisions and returns the  $K_S^0$  and  $(\Lambda + \bar{\Lambda})$  spectra (shown in black markers) as shown in Fig. 4.9. More information about this scaling procedure is given in the appendix G. Three different tunes of PYTHIA8 are used for comparison (used are the tunes “Monash”, “Perugia 2011” and the tune “NoCR” (no colour reconnection)) which seem to be consistent within statistics.

The following observations can be made:

The measured  $K_S^0$   $p_T$  spectra in Pb–Pb collisions show significantly enhanced yields for all  $p_T$  intervals compared to the scaled reference spectrum from the p–Pb data. For the  $\Lambda$  baryons a similar trend as for the comparison in 4.8 is seen: The yields of the measurement in Pb–Pb hint at an enhancement at lower  $\Lambda$   $p_T$  and at a slight suppression compared to the reference from p–Pb collisions. This observation can be made for both  $p_T^{\text{jet}}$  thresholds.

These observations could point to a scenario, in which the baryons in jets in Pb–Pb collisions are quenched and therefore shifted from higher (e.g. stemming from the interval  $4 \text{ GeV}/c < p_T < 10 \text{ GeV}/c$ ) to lower  $V^0$  particle  $p_T$  (into the  $p_T$  interval of  $2 \text{ GeV}/c < p_T < 4 \text{ GeV}/c$ ). This could be similar to the observation made by CMS [87] and by ATLAS [10] and as discussed in the first chapter (see Fig. 1.22): The CMS measurement of the medium-modified jet fragmentation functions (FFs) in Pb–Pb compared to the reference in pp showed that low  $p_T$  particles (what is corresponding to large values of  $\xi \sim \frac{1}{p_T^{\text{jet constituent}}}$  in the FFs) in jets are more abundant than in pp events and at intermediate  $\xi$  a depletion w.r.t. pp data was seen.

In summary, we saw from these comparisons that  $K_S^0$   $p_T$  yields in Pb–Pb collisions seem to be enhanced w.r.t. the spectrum from the (scaled)  $K_S^0$   $p_T$  yields in jets in p–Pb collisions. The  $p_T$  yields for  $(\Lambda + \bar{\Lambda})$  baryons in Pb–Pb collisions hint at an enhancement at low  $p_T$  ( $2 \lesssim p_T \lesssim 4 \text{ GeV}/c$ ) but show a slight suppression from  $p_T \gtrsim 4 \text{ GeV}/c$  on.

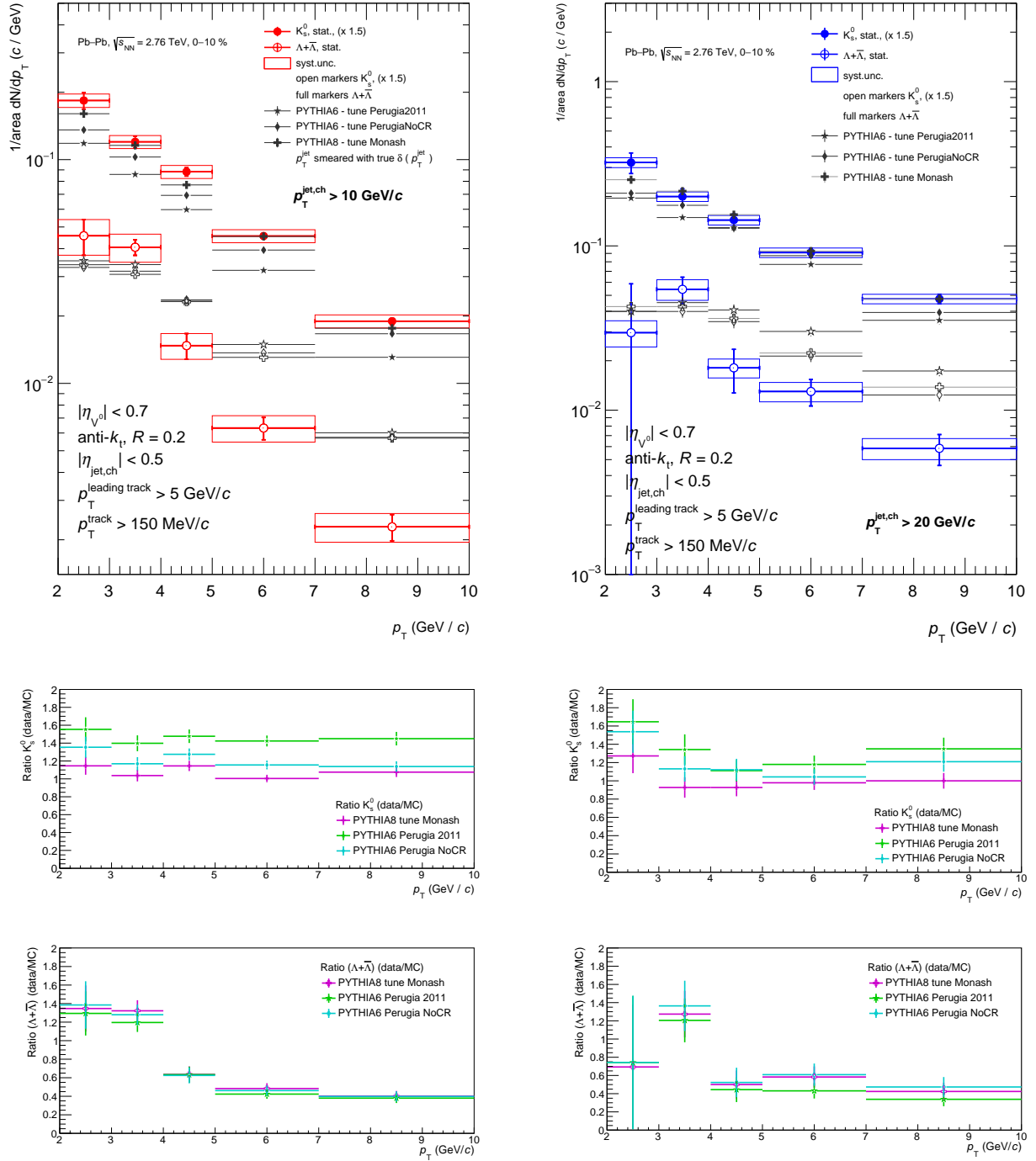


Figure 4.8: Comparison of the  $V^0$   $p_T$  spectra in jets in Pb–Pb collisions to the prediction of PYTHIA jets (simulating pp events at  $\sqrt{s} = 2.76$  TeV) is made. The left panel shows the  $K_S^0$  and  $\Lambda$   $p_T$  spectrum in jets with  $p_T^{\text{jet}} > 10$  GeV/c. The right panel shows the spectra for jets with  $p_T^{\text{jet}} > 20$  GeV/c. The results from PYTHIA jets (for three different tunes) are smeared in  $p_T^{\text{jet}}$  according to the particle level  $\sigma(\delta p_T^{\text{ch}})$  values [84]. The four panels below show the ratios for data divided by MC simulation (different PYTHIA tunes in different marker colours), for  $K_S^0$  and  $(\Lambda + \bar{\Lambda})$  separately. The ratios (data/MC) are shown separately for the two  $p_T^{\text{jet}}$  intervals and below the corresponding measurement. The PYTHIA simulations are adapted from [172].

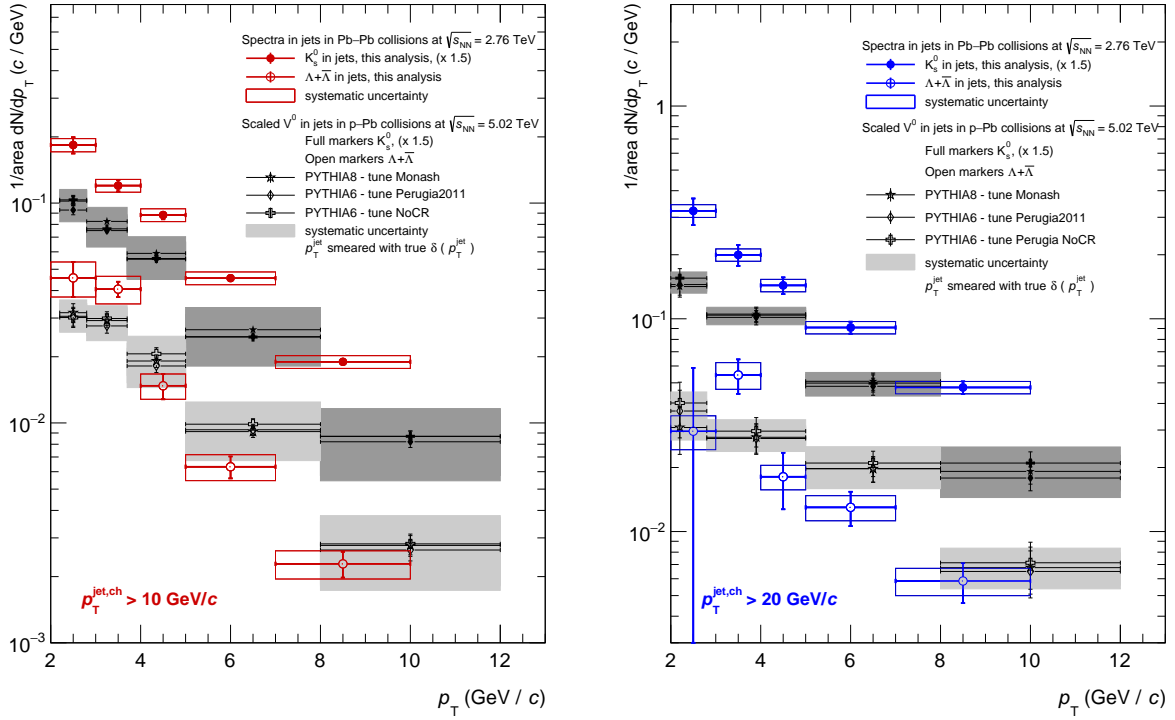


Figure 4.9: Comparison of the  $K_S^0$  and  $(\Lambda + \bar{\Lambda})$   $p_T$  spectra from this analysis to the spectra measured in p–Pb events at  $\sqrt{s_{NN}} = 5.02$  TeV. The left panel shows the spectra in jets for  $p_T^{\text{jet}} > 10$  GeV/c. On the right panel the spectra are shown for jets with  $p_T^{\text{jet}} > 20$  GeV/c. The results from the p–Pb data are scaled according to a PYTHIA8 simulation to take into account the effect of the UE fluctuations on  $p_T^{\text{jet}}$  that are present in Pb–Pb events, the leading constituent cut  $p_T^{\text{leading track}} > 5$  GeV/c and the different collision energy. Used are three different tunes of PYTHIA8 (tune "Monash", "Perugia 2011" and "NoCR"). The systematic uncertainties of the PYTHIA tunes are superimposed, they are lightgrey for the  $\Lambda$  baryons and darkgrey for the  $K_S^0$  mesons. Scaled reference is adapted from [172] and based on the measurement from [123].

# Chapter 5

## Conclusions

In this last chapter, the physics conclusions of this measurement and the analysis strategy are briefly summarised.

### 5.1 Physics conclusions

In this work the  $\Lambda(\bar{\Lambda})$  and  $K_S^0$   $p_T$  spectra in jets in Pb–Pb collisions and for two different  $p_T^{\text{jet}}$  thresholds ( $p_T^{\text{jet}} > 10$  GeV/c and  $p_T^{\text{jet}} > 20$  GeV/c) are reported.

Based on the measured spectra the  $(\Lambda+\bar{\Lambda})/2K_S^0$  ratio in jets in Pb–Pb collisions is derived which provides the first measurement of strange particles in charged jets in heavy-ion collisions.

The results are compared to the measurements in p–Pb collisions from ALICE and to the results obtained from a high- $p_T$  hadron- $V^0$  correlations in Pb–Pb collisions.

The following observations have been made

- At intermediate  $V^0$   $p_T$  (around 2-5 GeV/c) the observed  $(\Lambda+\bar{\Lambda})/2K_S^0$  ratio in jets in Pb–Pb collisions (see Fig. 4.4) is significantly smaller than the inclusive measurement in Pb–Pb collisions and the particle ratio from “no-jet” events. Within uncertainties it is compatible with the inclusive particle pp analysis (see in Fig. 4.4) at  $\sqrt{s} = 7$  TeV as published in [92] and at  $\sqrt{s} = 0.9$  TeV from [158].
- A comparison to the particle ratio in jets in p–Pb collisions (see Fig. 4.5) showed a hint at a small enhancement in Pb–Pb collisions w.r.t. the measured ratio in p–Pb collisions. A more differential observation can be made in the  $V^0$   $p_T$  spectra in jets.
- At high  $V^0$   $p_T$  (from  $p_T \geq 7$  GeV/c) the inclusive ratio and the ratio in jets in Pb–Pb collisions are in agreement. This can be expected, since the dominant hadron production mechanism at these higher  $p_T$  values is fragmentation and therefore not affected by soft particle production mechanisms. A modification would rather be expected at low particle momentum as seen by CMS (in terms of the modified fragmentation functions that exhibit an excess for soft particles in jets in the 10% most central Pb–Pb collisions [9]).

- A comparison of the  $\Lambda/K_S^0$  particle ratio from a high- $p_T$  trigger hadron correlation study [117] (comparison shown in Fig. 4.6) to the particle ratio of this analysis showed no significant deviation. From this comparison a sizable effect of a possible surface bias [178] of the correlation analysis technique could not be observed.
- In the particle ratio no dependence on the  $p_T^{\text{jet}}$  threshold was visible.
- The  $(\Lambda+\bar{\Lambda})/2K_S^0$  particle ratio (see Fig. 4.2) shows a modification compared to the one obtained from the PYTHIA8 simulation of jets in pp collisions. At intermediate  $V^0$   $p_T$  the measured ratio is higher than PYTHIA, whereas at high  $p_T$  the opposite behaviour was seen. This could point to a scenario in which low- $p_T$  hadrons are produced according to a thermal distribution while high- $p_T$  hadrons are following a power-law spectrum, as predicted by a hadronisation model in [103]. This furthermore goes along with the observation in the ALICE  $R_{AA}$  measurements for different centrality intervals [70] in which a particle-type independent suppression at high- $p_T$  is attributed to a particle energy loss in the medium. One could imagine that in more central events a longer average path-length is traversed by partons and this can lead to a stronger suppression of final state hadrons with high  $p_T$ . Furthermore this scenario does not show a mass ordering [110] for hadrons  $\geq 5$  GeV/c. At intermediate hadron  $p_T$ , a mass ordering in the identified light flavour  $R_{AA}$  [110] was seen (see Fig. 1.28).
- In the  $V^0$   $p_T$  spectra in jets more hints on possible modifications are visible. At low  $p_T$  for  $\Lambda$  baryons a sizable enhancement w.r.t. the prediction from PYTHIA was seen (Fig. 4.8). At high- $p_T$  the measured  $\Lambda$  yields are significantly lower compared to the PYTHIA simulations.
- The comparison to the scaled  $V^0$   $p_T$  spectra in p–Pb collisions also indicates modifications of the spectra in Pb–Pb collisions. The  $K_S^0$  yields seem to be significantly enhanced in Pb–Pb over the entire hadron  $p_T$  range w.r.t. the reference. The  $\Lambda$  yields at low hadron  $p_T$  indicate an enhancement while for higher hadron  $p_T$  they seem to be slightly lower (which is however no significant effect due to large uncertainties of the scaled reference measurement). These observations point to a scenario in which the jet fragmentation could be modified by the surrounding medium i.e. via shower parton and medium parton interaction in which colour, momentum or baryon number is exchanged as discussed in the model by Sapeta and Wiedemann [88]. This modification would act with different strength on the mesons and the baryons.

## 5.2 Conclusions on the analysis strategy

The advantage of  $V^0$  reconstruction via their decay topology lies in the wide  $p_T$  range down to low hadron  $p_T$ , in which the particles can be identified with very good accuracy.  $\Lambda$  and  $K_S^0$  hadrons have a sizable difference in mass and therefore allow to study possible mass-dependencies of the results.

The jet reconstruction technique with the *anti* –  $k_t$ -finder is commonly used in jet analyses

at current high-energy colliders and therefore allow comparisons among different measurements.

The main difficulty of the identified particle analysis in the jets is the accurate subtraction of the huge background of the  $V^0$  particles, contributing to the particle yield inside the jet cone. How this is done in the presented analysis is described in detail in section 3.4.

For future analyses in this field, data with larger statistics can enable to use more sophisticated correction procedures, as e.g. unfolding of the  $V^0$   $p_T$  -  $V^0$   $\eta$  -  $p_T^{\text{jet}}$  entanglement. Also the need to use open  $p_T^{\text{jet}}$  intervals ( $p_T^{\text{jet}} > 10$  GeV/c,  $> 20$  GeV/c) would drop when using larger data sets or (jet-)triggered data (compared to the currently available 7 million minimum-bias Pb–Pb collisions at  $\sqrt{s_{\text{NN}}} = 2.76$  TeV) and enable to use a fine binning of the  $p_T^{\text{jet}}$  in order to measure the identified fragmentation functions and trace back medium modifications in an even more precise way.

Other analysis techniques for particle identification like e.g. the  $dE/dx$  TPC signal of charged tracks inside jets could enable to measure at a lower jet  $p_T$  threshold than the one used in this analysis (e.g. measure down to  $p_T^{\text{jet}} \sim 5$  GeV/c) and pinpoint possible modifications for charged kaons, protons etc.. at lower  $p_T^{\text{jet}}$ . In this way a possible dependence of the modifications on the particle mass or on the particle species (i.e. baryons or mesons) could be studied.

Since for the current work, only charged particles are combined to jet clusters, a next step would be to include also calorimeter information by studying fully reconstructed jets (that cluster charged and neutral particles into jets).

When compared to high- $p_T$  trigger (hadrons), jets have the advantage to be “closer” to the initial parton physics by tracing back the final state hadrons that stem from the initial parton shower.

The analysis strategy using identified hadrons in jets allows to access especially soft particles originating from the initial hard parton scattering. There were several observations made which are motivating this type of analysis. Two of them are e.g.

- The light-flavour high- $p_T$   $R_{\text{AA}}$  measurement by ALICE [110] showed a hadron type dependence on the jet quenching (for  $p_T$  up to  $\sim 6$ -12 (GeV/c)) as shown in the first chapter in Fig. 1.28.
- The CMS and ATLAS observations of medium-modified fragmentation functions (FFs) in the 10% most central Pb–Pb events motivates to study identified (low- $p_T$ ) hadron FFs down to very low  $p_T^{\text{jet}}$ .

In this way a separation of the hadrons that stem from initial hard parton scattering and from the soft bulk of the event becomes possible. In the corresponding light flavour  $R_{\text{AA}}$  measurements however this soft  $p_T$  range of the initial hard parton scattering cannot be accessed in a direct way due to the huge bulk of soft particles stemming from the Underlying Event.

A theoretical model description of these jet observables is not easily achievable with the main difficulty being the modeling of the hadronisation scenario. It comes with difficulties because it is not clear how to translate partonic information into the hadronic observables.

There are already several models existing which were able to describe numerous experimental observations with good or less good success (e.g. hydrodynamical models as [93], models which describes recombination [95] and the EPOS model [96]). This motivates further development of theoretical models and simulations on this field and makes it necessary to provide more experimental data, like from the current work, in order to confine model parameters and also provide new ideas for their description.

# Bibliography

- [1] Agakishiev G *et al.* (STAR Collaboration) 2012 *Phys. Rev. Lett.* **108** 072301 (*Preprint* [arXiv:nucl-ex/1107.2955](https://arxiv.org/abs/nucl-ex/1107.2955))
- [2] Adams J *et al.* (STAR Collaboration) 2006 (*Preprint* [arXiv:nucl-ex/0601042v1](https://arxiv.org/abs/nucl-ex/0601042v1))
- [3] 2013 *Phys. Rev. Lett.* **111** 222301 (*Preprint* [arXiv:1307.5530](https://arxiv.org/abs/1307.5530)[nucl-ex])
- [4] Abelev B *et al.* (ALICE Collaboration) 2014 *Phys. Lett.* 196–207 (*Preprint* [arXiv:1401.1250v4](https://arxiv.org/abs/1401.1250v4)[nucl-ex])
- [5] Werner K 2012 *Phys. Rev. Lett.* (*Preprint* [PhysRevLett.109.102301](https://arxiv.org/abs/PhysRevLett.109.102301))
- [6] Aamodt K *et al.* (ALICE Collaboration) 2010 *Phys. Rev. Lett.* **105** (*Preprint* [arXiv:nucl-ex/1405.4632](https://arxiv.org/abs/nucl-ex/1405.4632))
- [7] Salur S and the CMS Collaboration 2012 *Journal of Physics: Conference Series* **389** 012003 URL <http://stacks.iop.org/1742-6596/389/i=1/a=012003>
- [8] Milhano J G 2013 *Nucl. Phys.* **A904-905** 122c–129c (*Preprint* [arxiv:hep-ex/1211.2657v1](https://arxiv.org/abs/hep-ex/1211.2657v1))
- [9] Chatrchyan S *et al.* (CMS Collaboration) 2014 *Phys. Rev. C* **90**(2) 024908 URL <http://link.aps.org/doi/10.1103/PhysRevC.90.024908>
- [10] Aad G *et al.* (ATLAS Collaboration) 2014 *Phys. Lett.* **B739** 320–342 (*Preprint* [1406.2979](https://arxiv.org/abs/1406.2979))
- [11] Fries R, Müller B, Nonaka C and Bass S 2003 *Phys. Rev. Lett.* **90** 202303 (*Preprint* [arxiv:nucl-th/0301087](https://arxiv.org/abs/nucl-th/0301087))
- [12] Sarkar S, Satz H and Sinha B 2009 *The Physics of the Quark-Gluon Plasma: Introductory Lectures* Lecture Notes in Physics (Springer Berlin Heidelberg) ISBN 9783642022852 URL <https://books.google.de/books?id=1WPVONSenZ4C>
- [13] ALTARELLI G 2005 (*Preprint* [hep-ph/0510281](https://arxiv.org/abs/hep-ph/0510281))
- [14] Glzman L Ya 2012 [Acta Phys. Polon. Supp.6,245(2013)] (*Preprint* [1211.7267](https://arxiv.org/abs/1211.7267))
- [15] MissMJ Standard model of elementary particles, svg. file, wikipedia

- 
- [16] Fukuda Y *et al.* (Super-Kamiokande) 1998 *Phys. Rev. Lett.* **81**(8) 1562–1567 URL <http://link.aps.org/doi/10.1103/PhysRevLett.81.1562>
- [17] McGregor G A (SNO) 2002 First results from the Sudbury Neutrino Observatory *Proceedings, 37th Rencontres de Moriond on Electroweak Interactions and Unified Theories* pp 249–256 (Preprint [nucl-ex/0205006](https://arxiv.org/abs/nucl-ex/0205006)) URL <http://alice.cern.ch/format/showfull?sysnb=2308970>
- [18] Perkins D H 1947 *Nature* **159** 126–127
- [19] Povh B, Rith K, Scholz C and Zetsche F 2004 *Povh, B: Teilchen und Kerne.: Eine Einführung in die physikalischen Konzepte*. Physics and astronomy online library (Springer) ISBN 9783540210658 URL <https://books.google.de/books?id=PIw0leNupPoC>
- [20] Aad G *et al.* (ATLAS Collaboration) 2012 *Phys. Lett.* **B716** 1–29 (Preprint [1207.7214](https://arxiv.org/abs/1207.7214))
- [21] Chatrchyan S *et al.* (CMS Collaboration) 2012 *Phys. Lett.* **B716** 30–61 (Preprint [1207.7235](https://arxiv.org/abs/1207.7235))
- [22] Olive K A *et al.* (Particle Data Group) 2014 *Chin. Phys.* **C38** 090001
- [23] Sjostrand T, Mrenna S and Skands P Z 2006 *JHEP* **05** 026 (Preprint [hep-ph/0603175](https://arxiv.org/abs/hep-ph/0603175))
- [24] Gyulassy M and Wang X N 1994 *Comput. Phys. Commun.* **83** 307 (Preprint [nucl-th/9502021](https://arxiv.org/abs/nucl-th/9502021))
- [25] Boya L J and Rivera C 2011 *Physics of Particles and Nuclei* **42** 800–811 ISSN 1531-8559 URL <http://dx.doi.org/10.1134/S1063779611050030>
- [26] Dissertori G 2015 (Preprint [1506.05407](https://arxiv.org/abs/1506.05407))
- [27] Wilczek F 2005 *Proc. Nat. Acad. Sci.* **102** 8403–8413 [Rev. Mod. Phys.77,857(2005)] (Preprint [hep-ph/0502113](https://arxiv.org/abs/hep-ph/0502113))
- [28] Hagedorn R 1968 *Il Nuovo Cimento A (1965-1970)* **56** 1027–1057 ISSN 1826-9869 URL <http://dx.doi.org/10.1007/BF02751614>
- [29] Ding H T, Karsch F and Mukherjee S 2015 *Int. J. Mod. Phys.* **E24** 1530007 (Preprint [1504.05274](https://arxiv.org/abs/1504.05274))
- [30] Philipsen O 2007 *Eur. Phys. J. ST* **152** 29–60 (Preprint [0708.1293](https://arxiv.org/abs/0708.1293))
- [31] Wilson K G 1974 *Phys. Rev. D* **10**(8) 2445–2459 URL <http://link.aps.org/doi/10.1103/PhysRevD.10.2445>
- [32] Papantonopoulos E 2011 *From Gravity to Thermal Gauge Theories: The AdS/CFT Correspondence* Lecture Notes in Physics (Springer Berlin Heidelberg) ISBN 9783642048647 URL <https://books.google.de/books?id=sGMOBwAAQBAJ>
-

- [33] Edelstein J D and Salgado C A 2008 *AIP Conf. Proc.* **1031** 207–220 (*Preprint* [0805.4515](#))
- [34] Salgado C A and Wiedemann U A 2003 *Phys. Rev. D* **68**(1) 014008 URL <http://link.aps.org/doi/10.1103/PhysRevD.68.014008>
- [35] Fodor Z and Katz S D 2004 *JHEP* **04** 050 (*Preprint* [hep-lat/0402006](#))
- [36] Borsanyi S, Endrodi G, Fodor Z, Jakovac A, Katz S D, Krieg S, Ratti C and Szabo K K 2010 *JHEP* **11** 077 (*Preprint* [1007.2580](#))
- [37] Bhalerao R S 2014 Relativistic heavy-ion collisions *Proceedings, 1st Asia-Europe-Pacific School of High-Energy Physics (AEPSHEP)* pp 219–239 (*Preprint* [1404.3294](#)) URL <https://inspirehep.net/record/1290394/files/arXiv:1404.3294.pdf>
- [38] Harrison M, Ludlam T and Ozaki S 2003 *Nuclear Instruments and Methods in Physics Research Section A: Accelerators, Spectrometers, Detectors and Associated Equipment* **499** 235 – 244 ISSN 0168-9002 the Relativistic Heavy Ion Collider Project: {RHIC} and its Detectors URL <http://www.sciencedirect.com/science/article/pii/S016890020201937X>
- [39] Satz H 2004 *Phys. Rept.* **403-404** 33–50 (*Preprint* [hep-ph/0405051](#))
- [40] GSI History of gsi, gsi webpage
- [41] CERN Cern timelines - the large hadron collider, lhc webpage
- [42] Shen C and Heinz U 2015 **25** 6–11 (*Preprint* [1507.01558](#))
- [43] Placakyte R 2011 Parton Distribution Functions *Proceedings, 31st International Conference on Physics in collisions (PIC 2011)* (*Preprint* [1111.5452](#)) URL <https://inspirehep.net/record/954990/files/arXiv:1111.5452.pdf>
- [44] Desy The hera accelerator at desy (germany), webpage
- [45] Gelis F, Iancu E, Jalilian-Marian J and Venugopalan R 2010 *Ann. Rev. Nucl. Part. Sci.* **60** 463–489 (*Preprint* [1002.0333](#))
- [46] Kolb P F, Heinz U W, Huovinen P, Eskola K J and Tuominen K 2001 *Nucl. Phys.* **A696** 197–215 (*Preprint* [hep-ph/0103234](#))
- [47] Kolb P F and Heinz U W 2003 (*Preprint* [nucl-th/0305084](#))
- [48] Sjostrand T, Mrenna S and Skands P Z 2008 *Comput. Phys. Commun.* **178** 852–867 (*Preprint* [0710.3820](#))
- [49] Andronic A, Braun-Munzinger P and Stachel J 2009 *Acta Phys. Polon.* **B40** 1005–1012 (*Preprint* [0901.2909](#))
- [50] Braun-Munzinger P, Redlich K and Stachel J 2003 (*Preprint* [nucl-th/0304013](#))

- 
- [51] Kraus I, Cleymans J, Oeschler H, Redlich K and Wheaton S 2009 [Prog. Part. Nucl. Phys.62,538(2009)] (*Preprint* [0902.0873](#))
- [52] Stachel J, Andronic A, Braun-Munzinger P and Redlich K 2014 *Journal of Physics: Conference Series* **509** 012019 URL <http://stacks.iop.org/1742-6596/509/i=1/a=012019>
- [53] Abelev B B *et al.* (ALICE Collaboration) 2015 *JHEP* **06** 190 (*Preprint* [1405.4632](#))
- [54] Akiba Y *et al.* 2006 *Nuclear Physics A* **774** 403 – 408 ISSN 0375-9474 URL <http://www.sciencedirect.com/science/article/pii/S0375947406002806>
- [55] d’Enterria D G 2007 *Nucl. Phys.* **A782** 215–223 (*Preprint* [nucl-ex/0608049](#))
- [56] Voloshin S and Zhang Y 1996 *Z. Phys.* **C70** 665–672 (*Preprint* [hep-ph/9407282](#))
- [57] Snellings R 2011 *New J. Phys.* **13** 055008 (*Preprint* [1102.3010](#))
- [58] Yan T M and Drell S D 2014 *Int. J. Mod. Phys.* **A29** 0071 (*Preprint* [1409.0051](#))
- [59] Altarelli G 1995 *The Development of perturbative QCD*
- [60] d’Enterria D 2010 *Landolt-Bornstein* **23** 471 (*Preprint* [0902.2011](#))
- [61] Collins J C, Soper D E and Stermann G F 1989 *Adv. Ser. Direct. High Energy Phys.* **5** 1–91 (*Preprint* [hep-ph/0409313](#))
- [62] Miller M L, Reygers K, Sanders S J and Steinberg P 2007 *Ann. Rev. Nucl. Part. Sci.* **57** 205–243 (*Preprint* [nucl-ex/0701025](#))
- [63] Bjorken J D 1982 *FERMILAB-PUB-82-059-THY, FERMILAB-PUB-82-059-T*
- [64] Chatrchyan S *et al.* (CMS Collaboration) 2012 *Phys. Lett.* **B710** 256–277 (*Preprint* [1201.3093](#))
- [65] Chatrchyan S *et al.* (CMS Collaboration) 2012 *Phys. Lett.* **B715** 66–87 (*Preprint* [1205.6334](#))
- [66] Chatrchyan S *et al.* (CMS Collaboration) 2011 *Phys. Rev. Lett.* **106** 212301 (*Preprint* [1102.5435](#))
- [67] Horowitz W A and Gyulassy M 2011 *Nucl. Phys.* **A872** 265–285 (*Preprint* [1104.4958](#))
- [68] Chen X F, Hirano T, Wang E, Wang X N and Zhang H 2011 *Phys. Rev.* **C84** 034902 (*Preprint* [1102.5614](#))
- [69] Renk T, Holopainen H, Paatelainen R and Eskola K J 2011 *Phys. Rev.* **C84** 014906 (*Preprint* [1103.5308](#))
- [70] Abelev B *et al.* (ALICE Collaboration) 2013 *Phys. Lett.* **B720** 52–62 (*Preprint* [1208.2711](#))

- [71] Gyulassy M and Pluemer M 1990 *Physics Letters B* **243** 432 – 438 ISSN 0370-2693 URL <http://www.sciencedirect.com/science/article/pii/0370269390914095>
- [72] Baier R, Dokshitzer Y L, Mueller A H, Peigne S and Schiff D 1997 *Nucl. Phys.* **B484** 265–282 (*Preprint* [hep-ph/9608322](#))
- [73] Wiedemann U A 2000 *Nucl. Phys.* **B588** 303–344 (*Preprint* [hep-ph/0005129](#))
- [74] Thomas R, Kampf B and Soff G 2005 *Acta Phys. Hung.* **A22** 83–91 (*Preprint* [hep-ph/0405189](#))
- [75] Aad G *et al.* (ATLAS Collaboration) 2010 *Phys. Rev. Lett.* **105** 252303 (*Preprint* [1011.6182](#))
- [76] Burke K M *et al.* (JET) 2014 *Phys. Rev.* **C90** 014909 (*Preprint* [1312.5003](#))
- [77] Wang X N 2005 *Nucl. Phys.* **A750** 98–120 (*Preprint* [nucl-th/0405017](#))
- [78] Majumder A and Van Leeuwen M 2011 *Prog. Part. Nucl. Phys.* **66** 41–92 (*Preprint* [1002.2206](#))
- [79] Kovner A and Wiedemann U A 2003 (*Preprint* [hep-ph/0304151](#))
- [80] Armesto N *et al.* 2012 *Phys. Rev.* **C86** 064904 (*Preprint* [1106.1106](#))
- [81] Soyez G 2011 *Phys. Lett.* **B698** 59–62 (*Preprint* [1101.2665](#))
- [82] Frixione S, Kunszt Z and Signer A 1996 *Nucl. Phys.* **B467** 399–442 (*Preprint* [hep-ph/9512328](#))
- [83] Abelev B *et al.* (ALICE Collaboration) 2013 *Phys. Lett.* **B722** 262–272 (*Preprint* [1301.3475](#))
- [84] Adam J *et al.* (ALICE Collaboration) 2015 *Phys. Lett.* **B746** 1–14 (*Preprint* [1502.01689](#))
- [85] Zapp K C 2014 *Eur. Phys. J.* **C74** 2762 (*Preprint* [1311.0048](#))
- [86] Renk T 2011 *Int. J. Mod. Phys.* **E20** 1594–1599 (*Preprint* [1009.3740](#))
- [87] Chatrchyan S *et al.* (CMS Collaboration) 2014 *Phys. Rev.* **C90** 024908 (*Preprint* [1406.0932](#))
- [88] Sapeta S and Wiedemann U 2008 *The European Physical Journal C* **55** 293–302 ISSN 1434-6052 URL <http://dx.doi.org/10.1140/epjc/s10052-008-0592-8>
- [89] Sapeta S and Wiedemann U A 2009 *JHEP* **05** 023 (*Preprint* [0809.4251](#))
- [90] Dokshitzer Y L, Khoze V A and Troyan S I 1991 *Journal of Physics G: Nuclear and Particle Physics* **17** 1585 URL <http://stacks.iop.org/0954-3899/17/i=10/a=017>

- 
- [91] Abelev B I *et al.* (STAR Collaboration) 2007 *Phys. Rev.* **C75** 064901 (*Preprint* [nucl-ex/0607033](#))
- [92] Abelev B B *et al.* (ALICE Collaboration) 2013 *Phys. Rev. Lett.* **111** 222301 (*Preprint* [1307.5530](#))
- [93] Song H and Heinz U W 2008 *Phys. Lett.* **B658** 279–283 (*Preprint* [0709.0742](#))
- [94] Song H and Heinz U W 2008 *Phys. Rev.* **C77** 064901 (*Preprint* [0712.3715](#))
- [95] Song H, Bass S A and Heinz U 2011 *Phys. Rev.* **C83** 054912 [Erratum: *Phys. Rev.* C87,no.1,019902(2013)] (*Preprint* [1103.2380](#))
- [96] Werner K 2012 *Phys. Rev. Lett.* **109**(10) 102301 URL <http://link.aps.org/doi/10.1103/PhysRevLett.109.102301>
- [97] Werner K, Karpenko I, Bleicher M, Pierog T and Porteboeuf-Houssais S 2012 *Phys. Rev. C* **85**(6) 064907 URL <http://link.aps.org/doi/10.1103/PhysRevC.85.064907>
- [98] Werner K 2012 *Phys. Rev. Lett.* **109** 102301 (*Preprint* [1204.1394](#))
- [99] Adams J *et al.* 2005 *Physics Letters B* **616** 8 – 16 ISSN 0370-2693 URL <http://www.sciencedirect.com/science/article/pii/S0370269305005381>
- [100] Adams J *et al.* 2006 *Physics Letters B* **637** 161 – 169 ISSN 0370-2693 URL <http://www.sciencedirect.com/science/article/pii/S0370269306004928>
- [101] DELPHI collaboration P A e a 1998 *Eur. Phy. J.* **C** 585
- [102] Hwa R C and Yang C B 2004 *Phys. Rev.* **C70** 024905 (*Preprint* [nucl-th/0401001](#))
- [103] Fries R J, Müller B, Nonaka C and Bass S A 2003 *Phys. Rev. C* **68**(4) 044902 URL <http://link.aps.org/doi/10.1103/PhysRevC.68.044902>
- [104] Kniehl B A, Kramer G and Potter B 2000 *Nucl. Phys.* **B582** 514–536 (*Preprint* [hep-ph/0010289](#))
- [105] 2016 URL <https://home.cern/about/experiments/aleph>
- [106] 2016 URL <https://home.cern/about/experiments/delphi>
- [107] 2016 URL <https://home.cern/about/experiments/opal>
- [108] 2016 URL <http://www-sld.slac.stanford.edu/sldwww/sld.html>
- [109] Fries R J, Muller B, Nonaka C and Bass S A 2004 *J. Phys.* **G30** S223–S228 (*Preprint* [nucl-th/0305079](#))
- [110] Abelev B B *et al.* (ALICE Collaboration) 2014 *Phys. Lett.* **B736** 196–207 (*Preprint* [1401.1250](#))
-

- 
- [111] Adam J *et al.* (ALICE Collaboration) 2015 *Phys. Rev.* **C91** 064905 (*Preprint* [1412.6828](#))
- [112] Song H 2015 *Pramana* **84** 703–715 (*Preprint* [1401.0079](#))
- [113] Schuchmann S and Appelshaeuser H 2015 *Modification of  $K_s^0$  and  $\Lambda(\bar{\Lambda})$  transverse momentum spectra in Pb-Pb collisions at  $\sqrt{s_{NN}} = 2.76$  TeV with ALICE* Ph.D. thesis Frankfurt U. presented 22 Jul 2015 URL <https://cds.cern.ch/record/2102194>
- [114] Abelev B *et al.* (ALICE Collaboration) 2013 *Phys. Rev. C* **88**(4) 044910 URL <http://link.aps.org/doi/10.1103/PhysRevC.88.044910>
- [115] Abelev B *et al.* (ALICE Collaboration) 2015 *Phys. Rev.* **C91** 024609 (*Preprint* [1404.0495](#))
- [116] 2016 URL <http://cerncourier.com/cws/article/cern/60148>
- [117] Richert T O H, Christiansen P, Oskarsson A and Stenlund E 2016  *$\Lambda/K_s^0$  associated with a jet in central Pb-Pb collisions at  $\sqrt{s_{NN}} = 2.76$  TeV measured with the ALICE detector* Ph.D. thesis Lund University presented 09 Jun 2016 URL <http://cds.cern.ch/record/2160945>
- [118] Abelev B *et al.* (STAR Collaboration) 2016 (*Preprint* [1603.05477](#))
- [119] Lu X 2014 *Nuclear Physics A* **931** 428 – 432 ISSN 0375-9474 URL <http://www.sciencedirect.com/science/article/pii/S0375947414002528>
- [120] Lu X 2013-08-13 *Exploring the performance limits of the ALICE Time Projection Chamber and Transition Radiation Detector for measuring identified hadron production at the LHC* Ph.D. thesis Heidelberg U. URL [http://inspirehep.net/record/1296397/files/76039449\\_CERN-THESIS-2013-179.pdf](http://inspirehep.net/record/1296397/files/76039449_CERN-THESIS-2013-179.pdf)
- [121] Aamodt K *et al.* (ALICE Collaboration) 2008 *JINST* **3** S08002 (*Preprint* [doi:10.1088/1748-0221/3/08/S08002](https://doi.org/10.1088/1748-0221/3/08/S08002))
- [122] Abelev B *et al.* (ALICE Collaboration) 2014 *Int. J. Mod. Phys. A* 1430044 (*Preprint* [arxiv:nucl-ex/1402.4476](https://arxiv.org/abs/nucl-ex/1402.4476))
- [123] Zhang X 2014 *Nuclear Physics A* **931** 444 – 448 ISSN 0375-9474 URL <http://www.sciencedirect.com/science/article/pii/S0375947414003625>
- [124] Aamodt K *et al.* (ALICE Collaboration) 2008 *JINST* **3** (*Preprint* [doi:10.1088/1748-0221/3/08/S08002](https://doi.org/10.1088/1748-0221/3/08/S08002))
- [125] Alessandro B *et al.* (ALICE Collaboration) 2006 *J. Phys.* **II** (*Preprint* [doi:10.1088/0954-3899/32/10/001](https://doi.org/10.1088/0954-3899/32/10/001))
- [126] Carminati F *et al.* (ALICE Collaboration) 2004 *J. Phys.* **I** (*Preprint* [doi:10.1088/0954-3899/30/11/001](https://doi.org/10.1088/0954-3899/30/11/001))
-

- [127] Pettersson T S and Lefèvre P (LHC Study Group) 1995 The Large Hadron Collider: conceptual design Tech. Rep. CERN-AC-95-05-LHC URL <https://cds.cern.ch/record/291782>
- [128] Bruning O S, Collier P, Lebrun P, Myers S, Ostojic R, Poole J and Proudlock P 2004 *LHC Design Report* (Geneva: CERN) URL <https://cds.cern.ch/record/782076>
- [129] Bruning O S, Collier P, Lebrun P, Myers S, Ostojic R, Poole J and Proudlock P 2004 *LHC Design Report* (Geneva: CERN) URL <https://cds.cern.ch/record/815187>
- [130] Benedikt M, Collier P, Mertens V, Poole J and Schindl K 2004 *LHC Design Report* (Geneva: CERN) URL <https://cds.cern.ch/record/823808>
- [131] 2016 URL <https://home.cern/about/accelerators/large-electron-positron-collider>
- [132] 2016 URL <http://www.stfc.ac.uk/research/particle-physics-and-particle-astrophysics/large-hadron-collider/cern-accelerator-complex/>
- [133] Collaboration T A 2008 *Journal of Instrumentation* **3** S08003 URL <http://stacks.iop.org/1748-0221/3/i=08/a=S08003>
- [134] Collaboration T C 2008 *Journal of Instrumentation* **3** S08004 URL <http://stacks.iop.org/1748-0221/3/i=08/a=S08004>
- [135] Collaboration T L 2008 *Journal of Instrumentation* **3** S08005 URL <http://stacks.iop.org/1748-0221/3/i=08/a=S08005>
- [136] Abelev B *et al.* (ALICE Collaboration) 2014 *Int. J. Mod. Phys. A* **1430044** (Preprint [arxiv:nucl-ex/1402.4476](https://arxiv.org/abs/nucl-ex/1402.4476))
- [137] Collaboration A (ALICE Collaboration) 2003 *ALICE-INT-2003-038* **1.0**
- [138] Dellacasa G *et al.* (ALICE Collaboration) 1999 *CERN-LHCC-99-12*
- [139] Dellacasa *et al.* (ALICE Collaboration) 2000 *ALICE time projection chamber: Technical Design Report* Technical Design Report ALICE (Geneva: CERN) URL <https://cds.cern.ch/record/451098>
- [140] Alme J *et al.* 2010 *Nuclear Instruments and Methods in Physics Research A* **622** 316–367 (Preprint [1001.1950](https://arxiv.org/abs/1001.1950))
- [141] Cortese P (ALICE Collaboration) 2001 *ALICE transition-radiation detector: Technical Design Report* Technical Design Report ALICE (Geneva: CERN) URL <https://cds.cern.ch/record/519145>
- [142] 2000 *ALICE Time-Of-Flight system (TOF): Technical Design Report* Technical Design Report ALICE (Geneva: CERN) URL <https://cds.cern.ch/record/430132>

- [143] Grupen C 1993 *Teilchendetektoren* (BI Wissenschaftsverlag)
- [144] Cortese P *et al.* (ALICE Collaboration) 2004 *CERN-LHCC-2004-025*
- [145] Dellacasa G *et al.* (ALICE Collaboration) 1999 *CERN-LHCC-99-05*
- [146] Aamodt K *et al.* (ALICE Collaboration) 2011 *Phys. Rev. Lett.* **106** 032301 (*Preprint 1012.1657*)
- [147] Piuz F, Klempt W, Leistam L, De Groot J and Schukraft J (ALICE Collaboration) 1998 *ALICE high-momentum particle identification: Technical Design Report* Technical Design Report ALICE (Geneva: CERN) URL <http://cds.cern.ch/record/381431>
- [148] Fantoni A and the ALICE collaboration 2011 *Journal of Physics: Conference Series* **293** 012043 URL <http://stacks.iop.org/1742-6596/293/i=1/a=012043>
- [149] Abelev B *et al.* (ALICE Collaboration) 2013 *Phys. Rev.* **C88** 044909 (*Preprint 1301.4361*)
- [150] Vries H D, Jager C D and Vries C D 1987 *Atomic Data and Nuclear Data Tables* **36** 495 – 536 ISSN 0092-640X URL <http://www.sciencedirect.com/science/article/pii/0092640X87900131>
- [151] Alver B, Baker M, Loizides C and Steinberg P 2008 (*Preprint 0805.4411*)
- [152] Nakamura K and Group P D 2010 *Journal of Physics G: Nuclear and Particle Physics* **37** 075021 URL <http://stacks.iop.org/0954-3899/37/i=7A/a=075021>
- [153] Kharzeev D E 2015 *Ann. Rev. Nucl. Part. Sci.* **65** 193–214 (*Preprint 1501.01336*)
- [154] Poskanzer A M and Voloshin S A 1998 *Phys. Rev.* **C58** 1671–1678 (*Preprint nucl-ex/9805001*)
- [155] Belikov Y, Safarik K and Batyunya B (ALICE Collaboration) 1997 Kalman Filtering Application for Track Recognition and Reconstruction in ALICE Tracking System Tech. Rep. ALICE-INT-1997-24. CERN-ALICE-INT-1997-24 CERN Geneva URL <http://cds.cern.ch/record/689414>
- [156] Belikov I, Hristov P, Ivanov M, Kuhr T and Safarik K 2005 Track reconstruction in high density environment *Computing in high energy physics and nuclear physics. Proceedings, Conference, CHEP'04, Interlaken, Switzerland, September 27-October 1, 2004* pp 399–402 URL <http://doc.cern.ch/yellowrep/2005/2005-002/p399.pdf>
- [157] Ivanov M, Safarik K, Belikov Y and Bracinik J 2003 *ArXiv Physics e-prints* (*Preprint physics/0306108*)
- [158] Aamodt K *et al.* (ALICE Collaboration) 2011 *Eur. Phys. J.* **C71** 1594 (*Preprint 1012.3257*)

- 
- [159] et al (Particle Data Group) J B (Particle Data Group) 2012 *Phys. Rev. D* **86** 010001 URL <http://pdg.lbl.gov>
- [160] Cacciari M, Salam G P and Soyez G 2012 *Eur. Phys. J. C* **72** 1896 (*Preprint arXiv:1111.6097[hep-ph]*)
- [161] Cacciari M, Salam G P and Soyez G 2008 *JHEP* **04** 063 (*Preprint 0802.1189*)
- [162] Cacciari M and Salam G P 2008 *Phys. Lett.* **B659** 119–126 (*Preprint 0707.1378*)
- [163] Abelev B *et al.* (ALICE Collaboration) 2012 *JHEP* **03** 053 (*Preprint 1201.2423*)
- [164] Collaboration A Alice internal figure repository, ali-der-111701 preliminary result
- [165] Hybrid tracks twiki page URL <https://twiki.cern.ch/twiki/bin/viewauth/ALICE/HybridTracks>
- [166] Gyulassy M and Wang X N 1994 *Computer Physics Communications* **83** 307 – 331 ISSN 0010-4655 URL <http://www.sciencedirect.com/science/article/pii/0010465594900574>
- [167] CERN 1993 URL <http://hep.fi.infn.it/geant.pdf>
- [168] Barnby L S, Belikov I, Chinellato D D, Hanratty L D, Kalinak P and Putis M Measurement of  $K_S^0$  and  $\Lambda$  spectra and yields in Pb–Pb collisions at 2.76 TeV with the ALICE experiment analysis note URL <https://aliceinfo.cern.ch/Notes/node/88>
- [169] Elia D Measurement of multi-strange baryons in Pb–Pb collisions at  $\sqrt{s_{NN}}$  analysis note URL <https://aliceinfo.cern.ch/Notes/node/48>
- [170] Aamodt K *e a* (ALICE Collaboration) 2010 *Phys. Rev. Lett.* **105**(25) 252302 URL <http://link.aps.org/doi/10.1103/PhysRevLett.105.252302>
- [171] Abelev B *et al.* (ALICE Collaboration) 2014 *JHEP* **03** 013 (*Preprint 1311.0633*)
- [172] Busch O Private communication, university heidelberg (2016)
- [173] Aad G *et al.* (ATLAS Collaboration) 2013 *Phys. Rev. Lett.* **111** 152301 (*Preprint 1306.6469*)
- [174] Adam J *et al.* (ALICE Collaboration) 2016 *Phys. Lett.* **B753** 511–525 (*Preprint 1509.07334*)
- [175] Abelev B *et al.* (ALICE Collaboration) 2013 *Phys. Lett.* **B719** 18–28 (*Preprint 1205.5761*)
- [176] Chatrchyan S *et al.* (CMS Collaboration) 2012 *Phys. Rev. Lett.* **109** 022301 (*Preprint 1204.1850*)

- 
- [177] Abelev B *et al.* (ALICE Collaboration) 2013 *Phys. Rev. Lett.* **111**(22) 222301 URL <http://link.aps.org/doi/10.1103/PhysRevLett.111.222301>
- [178] Renk T 2013 *Phys. Rev.* **C87** 024905 (*Preprint* [1210.1330](#))
- [179] Pierog T, Karpenko I, Katzy J M, Yatsenko E and Werner K 2015 *Phys. Rev.* **C92** 034906 (*Preprint* [1306.0121](#))
- [180] Sjostrand T, Ask S, Christiansen J R, Corke R, Desai N, Ilten P, Mrenna S, Prestel S, Rasmussen C O and Skands P Z 2015 *Comput. Phys. Commun.* **191** 159–177 (*Preprint* [1410.3012](#))
- [181] Fries R J, Muller B, Nonaka C and Bass S A 2003 *Phys. Rev. Lett.* **90** 202303 (*Preprint* [nucl-th/0301087](#))
- [182] 2014 Git repository for AliRoot Source codes of the AliRoot software, official repository URL <http://git.cern.ch/pubweb/AliRoot.git>



# List of Tables

3.1	The following event selection criteria were imposed to select only events with high data quality: . . . . .	71
3.2	The $V^0$ particle selection is applied on the topology of the reconstructed $V^0$ decay. . . . .	74
3.3	Signal and background regions for fixed intervals and dependent on $\sigma$ of the mass peak (gaussian) fit . . . . .	78
3.4	Estimation of the averaged $V^0$ background in jet cone with isotropic PYTHIA jet embedding ( $= \bar{B}_{V^0}$ ) and the deviation term due to $v_2^{\text{ch jet}}$ ( $\sim 10\%$ ). . . . .	128
3.5	Estimation of relative systematic uncertainties . . . . .	129
3.6	Signal extraction settings for the different particle types (for inclusive, intra-jet and UE mass distributions) . . . . .	131
3.7	Signal extraction variations . . . . .	131
3.8	Cut variations for the estimation of the systematic uncertainty of reconstruction efficiency correction. . . . .	132
3.9	The minimal and maximal fractions of the relative systematic uncertainty on the final results . . . . .	139
3.10	Data points and total systematic uncertainty for the $(\Lambda + \bar{\Lambda})/2K_S^0$ ratio in jets ( $R = 0.2$ ) and in $p_{T,\text{jet}}^{\text{ch}} > 10$ GeV/c . . . . .	141
3.11	Data points and total systematic uncertainty for the $(\Lambda + \bar{\Lambda})/2K_S^0$ ratio in jets ( $R = 0.2$ ) and in $p_T^{\text{jet}} > 20$ GeV/c . . . . .	141
F.1	The 5 different methods to estimate the $V^0$ contribution to the jet cone from the UE. . . . .	216



# List of Figures

1.1	The standard model of elementary particles. (Figure adapted from [15]). . . . .	14
1.2	Interactions of the standard model. Figure adapted from [15]. . . . .	15
1.3	The proton structure function $F_2$ as a function of $x$ and for $Q^2$ between 2 $(\text{GeV}/c)^2$ and 18 $(\text{GeV}/c)^2$ . No dependence on $Q^2$ is found, which indicates a scattering off point-like targets and thus leads to the understanding that the proton consists of point-like constituents (Fig. adapted from [19]). . . . .	16
1.4	Fundamental types of the strong interaction. a) shows a quark emitting a gluon, in b) a gluon splits into a quark-antiquark pair and c),d) demonstrate the self-coupling of gluons. (Figure adapted from [19]). . . . .	17
1.5	(Upper figure) Fluctuations of gluons into a pair of quark anti-quark leads to screening of strong charge (colour screening). Electron-positron pair production in QED causes screening of electric charges. The gluon self-coupling however leads to anti-screening effect. (Lower figure) Comparison of the electromagnetic and the strong coupling. (Figure adapted from [19]). . . . .	19
1.6	Experimental measurements of $\alpha_s$ by different experiments and at different scales $Q = \sqrt{Q^2}$ [22]. . . . .	20
1.7	QCD calculations [36] on a discretised (hypercubic) lattice (of the euclidean spacetime of temperature $T$ and three-volume $V$ ) predict a rapid rise of the pressure and energy density of hadronic matter for rising temperature on $N_t = 4,6$ and 10 lattices. $N_t$ is the number of time points on the lattice grid. The Stefan-Boltzmann (SB) limits are marked with arrows. . . . .	21
1.8	QCD phase diagram of hadronic matter as a function of temperature and baryo-chemical potential. The current LHC experiments measure at very low net baryon densities and very high energy. At these values the phase transition from normal hadronic matter to the quark gluon plasma is a continuous crossover, at higher baryo-chemical potential a transition of 1st order is expected to take place. Figure from [37]. . . . .	22
1.9	Different stages of the Quark Gluon Plasma formation. Figure adapted from [42]. . . . .	23
1.10	Parton distribution functions (PDFs) [43] as measured at HERA. At small Bjorken $x$ (at high momentum transfer $Q^2$ ) the gluon PDF contributes the largest fraction of the proton momentum and dominates over the valence quark PDFs. . . . .	24

1.11	Comparison of prediction by the thermal model and the SPS data for central Pb–Pb collisions at $\sqrt{s_{\text{NN}}} = 7.6$ GeV. Figure adapted from [49]. . . . .	26
1.12	Statistical hadronisation model fitted to hadron yields measured by ALICE. The fit yields $T_c = 156$ MeV while also fit results for slightly higher $T = 164$ MeV are shown (blue dotted lines). Figure adapted from [52]. . . . .	26
1.13	Left panel: Spatial asymmetry in the reaction plane of the collisions in a peripheral heavy ion collision. Right panel: Measured elliptic flow parameter $v_2(p_T)$ for soft particles ( $p_T < 2$ GeV/c) measured by PHENIX [54], the comparison to hydrodynamical predictions show good agreement. Figures adapted from [55]. . . . .	27
1.14	Sketch of dijet production and pQCD collinear factorisation in hadronic collisions: $f_{a/A}(x_1, Q^2)$ are the PDFs. $\mathcal{D}_{c \rightarrow h}(z, Q^2)$ are the fragmentation functions (FFs) and ISR (FSR) represents initial (final-) state radiation. Figure and caption adapted from [55]. . . . .	29
1.15	Two quarks suffer a hard scattering: one goes out directly into the vacuum, radiates a few gluons and hadronises, the other goes through the dense plasma created (characterised by the transport coefficient $\hat{q}$ , the gluon density $dN^g/dy$ and temperature $T$ ), suffers energy loss due to medium-induced gluonstrahlung and finally fragments outside in a (quenched) jet. Figure and caption adapted from [60]. . . . .	30
1.16	Nuclear modification factor $R_{\text{AA}}$ measured at the LHC for the 5% most central events compared to theoretical model predictions [67–69]. Figure adapted from [70]. . . . .	31
1.17	Left side: Quark energy loss in the medium via elastic collisions, Right side: Inelastic scatterings with the medium results in radiative energy loss. Figure adapted from [60]. . . . .	33
1.18	Inclusive jet production cross sections ( $R = 0.2$ ) measured. NLO pQCD predictions [81, 81, 82] are superimposed with the data and show good agreement when hadronisation effects are included. The ratio of the simulation and the results are shown in the lower panel. Figure adapted from [83].	36
1.19	$R_{\text{AA}}$ of jets [84] reconstructed from charged and neutral particles indicates a strong suppression in Pb–Pb collisions. The left plot shows the jet suppression for the 10% most central events, the right plot for 10-30% event centrality. . . . .	37
1.20	Event display by CMS experiment showing a dijet event (left panel). The right panels show the calorimeter towers that measure the total jet energy and the distribution of charged tracks over the acceptance $\eta \times \phi$ both are indicating one high- $p_T$ jet and an almost vanished ("quenched") back-to-back jet appearing on the opposite side in azimuthal direction. Figure adapted from [75]. . . . .	38

1.21	Dijet asymmetry measurement [7] by CMS collaboration as a function of event centrality (from left upper side to right lower side with increasing event centrality). $p_{T,1}$ and $p_{T,2}$ are the transverse momentum from leading and sub-leading jets with an azimuthal distance $\Delta\phi_{1,2} > \frac{2}{3}\pi$ . The measurement (as black points) are compared to PYTHIA dijets, that are embedded into HYDJET simulated (Pb–Pb) events (red histogram). The different panels correspond to different centrality intervals. . . . .	39
1.22	Modification of the jet fragmentation pattern for different event centrality intervals as measured by the CMS experiment. The fragmentation functions (FF) for jets, for the interval $100 < p_T^{\text{jet}} < 120$ GeV/ $c$ and for a fragmentation radius of $R = 0.3$ , are shown in the panels above while the ratio to the FFs in pp collisions at the same energy are shown below [87]. . . . .	40
1.23	In the large $N_c$ approximation, gluons are represented as pairs of $q\bar{q}$ fermion lines. This sketch shows a gluonic parton shower, taking place in vacuum (left) and in the medium (right). Partons that interact with a medium parton via momentum, flavour or colour exchange (e.g. by hadronising with a medium parton via recombination) modify the shower pattern and can lead to an increased particle multiplicity, a shower softening and widening and may furthermore change the particle composition of the jet in the final state (after hadronisation) [88]. . . . .	41
1.24	Shown are the results of a perturbative parton shower calculation in the MLLA formalism and using the model of Sapeta, Wiedemann [88]. Figure adapted from [88]. . . . .	41
1.25	Results of the MLLA+LPHD formalism for the particle ratios $K^\pm/\pi^\pm$ and $p(\bar{p})/\pi^\pm$ in jets as obtained from enhanced parton splitting [88]. Figure adapted from [88]. . . . .	42
1.26	Inclusive $\Lambda/K_S^0$ ratio as measured by the STAR [91] experiment (right side, open markers) and by ALICE at the larger energy of $\sqrt{s_{NN}} = 2.76$ TeV (left side) [92]. Compared are the measurements to model calculations from a hydrodynamical model [93, 94], one describing recombination [95] and the EPOS model [96]. . . . .	43
1.27	$p/\pi$ ratio in d+Au and Au+Au collisions at $\sqrt{s_{NN}} = 200$ GeV measured by PHENIX [99, 100]. Dotted line is the $(p+\bar{p})/(\pi+\bar{\pi})$ ratio from light quark jets in $e^+e^-$ collisions at $\sqrt{s} = 91.2$ GeV [101]. Dashed-and-dotted line is a model calculation by [102, 103] for central Au+Au events. . . . .	44
1.28	Light flavour $R_{AA}$ measurements from Pb–Pb collisions at 2.76 TeV in 0-5% central and 60-80% peripheral events for identified particles and different particle types shows a dependence on the particle mass [110]. For the most central collisions and at intermediate hadron $p_T$ the mesons show a stronger suppression than the baryons. . . . .	45
1.29	Elliptic flow measurement in 40-50% central events for different particle types can be well described by viscous hydrodynamical models [112]. . . . .	46

1.30	Comparison of $p_T$ -dependent baryon-to-meson ratios measured in central (0-10%) Pb–Pb collisions at $\sqrt{s_{NN}} = 2.76$ TeV: $\Lambda/K_S^0$ [92], $p/\pi$ [4, 114] and $p/\phi$ [115]. Figure adapted from [116]. . . . .	47
1.31	$\Lambda/K_S^0$ ratio as a function of the $V^0$ $p_T$ with <i>eta-gap</i> correlation technique that associates $\Lambda$ and $K_S^0$ particles with high- $p_T$ trigger hadrons. (Figure adapted from T.Richert, thesis [117]). . . . .	48
1.32	$(\Lambda+\bar{\Lambda})/2K_S^0$ ratio measured by STAR in di-hadron correlations with identified strange associated particles in 0-60% most central Cu+Cu collisions at $\sqrt{s_{NN}} = 200$ GeV. Figure adapted from [118]. . . . .	49
1.33	$p/\pi$ particle ratio as a function of $p_T$ in charged jets from the interval $10 < p_T^{\text{jet}} < 15$ GeV/c and measured in pp collisions at $\sqrt{s} = 7$ TeV. The result is compared to PYTHIA simulations. Figure adapted from [119, 120].	50
1.34	$(\bar{\Lambda}+\Lambda)/2K_S^0$ ratio in jets in p–Pb collisions (for different values of $R$ ) for $p_T^{\text{jet}} > 10$ GeV/c (left panel) and $p_T^{\text{jet}} > 20$ GeV/c (right panel) and compared to inclusive particle ratio in the 0-10% V0A multiplicity class interval (Pb-Side) in p–Pb collisions (black markers) and to the expectation from a PYTHIA 8 4C simulation at 5.02 TeV (dotted lines, showing spread for the used values of $R$ ) [121, 122]. Figure adapted from [123]. . . . .	50
2.1	LHC complex with injector chain and interaction points (yellow points). Where the two oppositely directed beams intersect, the 4 largest experiments are ALICE, CMS, LHCb and ATLAS are located. Several pre-accelerators are required to reach the final LHC collisional energy [132]. . . . .	54
2.2	Definition of the coordinate system axis and the angles in ALICE [137]. . . . .	56
2.3	The ALICE detector at the CERN LHC. Shown are several sub-detectors of the central barrel at mid-rapidity (ITS, TPC, TRD, TOF, PHOS, EM-Cal and HMPID) and in the forward-rapidity region (PMD, FMD, V0, T0 and ZDC). They are surrounded by a solenoid magnet providing a 0.5 T longitudinal magnetic field. The muon-spectrometer is located in forward direction. . . . .	57
2.4	A Pb–Pb collision event recorded in ALICE at $\sqrt{s_{NN}} = 2.76$ TeV. Several thousand charged particles are produced in one collision that are recorded by the various detector systems. Neutral particles are visible as (blue) calorimeter towers on top, where the Electromagnetic calorimeters are installed. The reconstructed charged particle tracks within the central barrel detector are visible as reddish-yellow trajectories. . . . .	58
2.5	Energy loss distribution in the ITS as a function of the particle momentum [136].	59
2.6	ALICE Time Projection Chamber. Together with the anodes on both sides of the TPC barrel, the central HV electrode (which is on 100 kV w.r.t. the endplates of the TPC barrel) provides the electrical drift field to guide the created ionization to the read-out pads on both sides of the TPC. . . . .	61

2.7	TPC specific energy loss $dE/dx$ as a function of the rigidity $\frac{p}{z}$ . The most probably value for the mean energy loss per particle type and momentum is derived with the ALEPH parametrisation [140] of the Bethe Bloch curve [136].	61
2.8	The left sketch illustrates two heavy-ion nuclei briefly before the collision that is characterised by their impact parameter $\mathbf{b}$ . On the right side the nuclei are colliding inelastically, all nucleons affected by the collisions are called “participants”, those continuing their trajectory bound in the remnant of the original nucleus are called “spectators”. They can serve to estimate the centrality of the event e.g. with help of the ZDC detector signal (Fig. adapted from [57]).	64
2.9	Distribution of the sum of the amplitudes in the VZERO scintillators in Pb–Pb collisions at $\sqrt{s_{NN}}$ 2.76 TeV. By integration of the signal from the right to the left, the different centrality intervals can be defined. The VZERO signal amplitude (corresponding to the charged-particle multiplicity in forward direction) is fitted by a function from a NBD-Glauber model calculation [149]. Figure adapted from [149].	65
2.10	View of a semi-central nucleus-nucleus collision in beam direction. The line connecting the centers of the nuclei and the beam axis (into the paper) defines the reaction plane $\psi_{RP}$ . Figure adapted from [153].	66
2.11	The event reconstruction in the central barrel detector system is done in several steps[136]	67
2.12	Secondary vertex reconstruction in the first two layers of the ITS. The reconstructed charged daughter tracks are drawn as solid lines, the dashed lines are extrapolations to the primary vertex and represent the $V^0$ particles. Also shown is an example for a cascade particle decay ( $\Xi^-$ ) [136]. Figure adapted from [136].	68
3.1	Number of vertex contributors (before the cut is applied) of the analysed events in the analysed data set in Pb–Pb collisions at $\sqrt{s_{NN}} = 2.76$ TeV. All events with less contributing tracks than 2 are rejected.	71
3.2	The nominal primary vertex $z$ position (before cuts) of the analysed events in the analysed data set in Pb–Pb collisions at $\sqrt{s_{NN}} = 2.76$ TeV. Only events with $ z  < 10$ cm are accepted by the physics selection.	72
3.3	The centrality distribution of all events contained in the used 2011 Pb–Pb data set at $\sqrt{s_{NN}} = 2.76$ TeV. Only events with an event centrality of 0-10% are selected for the analysis.	73
3.4	Topological properties of a $V^0$ decay and the selection parameters used for $V^0$ reconstruction.	75

3.5	The $V^0$ candidates separated into different particle types via the Armenteros-Podolanski variables $q_T$ (momentum component perpendicular to mother particle momentum) and $\alpha = \frac{p_L^+ - p_L^-}{p_L^+ + p_L^-}$ . At low $q_T$ one can see $\gamma$ conversions into pairs of electrons. a) The Armenteros-Podolanski plot for $V^0$ candidates in pp events shows a clear separation of the different particle species. b) The $K_S^0$ candidates are separated from a possible contamination of $\Lambda(\bar{\Lambda})$ candidates by the requirement: $q_T^{\text{Arm.}} \geq 0.2  \alpha $ . For the rejection of $\gamma$ conversions, another cut is applied already during the $V^0$ reconstruction. Left Fig. adapted from [158]. . . . .	76
3.6	a) Invariant mass distribution for inclusive $K_S^0$ candidates in $3 \text{ GeV}/c < V^0 p_T < 4 \text{ GeV}/c$ , the signal region is indicated in red. The regions for the background fit are indicated in grey. b) Invariant mass distribution for inclusive $K_S^0$ candidates in $7 \text{ GeV}/c < V^0 p_T < 10 \text{ GeV}/c$ . . . . .	77
3.7	a) Invariant mass distribution for inclusive $\Lambda$ candidates from $3 \text{ GeV}/c < V^0 p_T < 4 \text{ GeV}/c$ , the signal region (defined according to table 3.3) is indicated in red. b) Example of an invariant mass distribution for inclusive $\Lambda$ candidates from $7 \text{ GeV}/c < V^0 p_T < 10 \text{ GeV}/c$ , the two regions for the background fit are indicated in grey. . . . .	78
3.8	Invariant mass distribution for $K_S^0$ (left) and $\Lambda$ (right) candidates in the jet cone (with $R = 0.2$ ) and for $p_T^{\text{jet}} > 10 \text{ GeV}/c$ and $3.0 \text{ GeV}/c < V^0 p_T < 4.0 \text{ GeV}/c$ . . . . .	80
3.9	Two examples for the signal purity as function of the $V^0 p_T$ obtained with the signal extraction for inclusive $K_S^0$ (left panel) and the $K_S^0$ particle in jet cones (right panel). The signal purity is defined as the ratio of the signal yield (in the peak region) over the signal+background sample in the same region. . . . .	80
3.10	Raw $p_T$ spectrum of inclusive $K_S^0$ , $\Lambda$ and $\bar{\Lambda}$ for 0-10% most central events of the 2011 Pb–Pb data at $\sqrt{s_{\text{NN}}} = 2.76 \text{ TeV}$ . . . . .	81
3.11	Comparison of raw $V^0 p_T$ spectra in different selections and event regions (inclusive - black markers, JC - red markers, PC - blue markers, RC - green markers, MCC - brown markers, OC - beige markers, NJ - orange markers). From the shape of the $V^0 p_T$ spectra, already before the subtraction of the $V^0$ contribution from the Underlying Event (UE), a clear different slope of the intra-jet $V^0$ particles w.r.t. the inclusive particles or those from the UE can be seen (compare red markers to the others). . . . .	82
3.12	Analysis workflow . . . . .	83
3.13	Herwig8 generated event together with many randomly placed soft particles is clustered up by the anti- $k_t$ jet algorithm. The resulting areas of this jet finder have circular shapes [161]. . . . .	85
3.14	Resulting areas of the $k_t$ jet algorithm have non-regular shapes [161]. . . . .	86

- 3.15 Dependence of the average background  $p_T$  density  $\rho$  on the uncorrected multiplicity of tracks used for jet finding ( $|\eta| < 0.9$ ) in Pb–Pb collisions at  $\sqrt{s_{NN}} = 2.76$  TeV. The dotted line is a linear fit to the centroids in each multiplicity bin. The insets show the projected distributions of  $\rho$  and raw multiplicity for the 10% most central events. Figure and caption adapted from [163]. . . . . 87
- 3.16  $\delta p_T$  distribution of random cones in the 10% most central Pb–Pb events for three different kind of random cone probes with  $p_T^{min}=0.15$  GeV/c cut. A Gaussian fit to the left-hand-side and its extrapolation to positive  $\delta p_T$  are shown for measured Pb–Pb events ( $\mu^{LHS}$  and  $\sigma^{LHS}$  in GeV/c). The solid line is a fit according to a probability distribution of  $\delta p_T$  which is shifted to zero (see reference for more details). Figure and caption adapted from [163]. 88
- 3.17  $\delta p_T$  distribution obtained from random cones in Pb–Pb events and for different size of the jet cone ( $R = 0.4, 0.3, 0.2$ ). The  $\sigma$  of the  $\delta p_T$  decreases for smaller cone size. Figure adapted from [164]. . . . . 89
- 3.18 Charged jet  $p_T$  spectrum from PbPb events at  $\sqrt{s_{NN}} = 2.76$  TeV, with (open markers) and without (filled markers) leading track  $p_T$  bias. This cuts aim to suppress combinatorial jets at low  $p_T^{jet}$ . . . . . 90
- 3.19 Ratio of the full jet spectra in pp at  $\sqrt{s} = 2.76$  TeV with and without leading constituent  $p_T$  requirement. The ratios are obtained from data (full markers) and MC PYTHIA simulation (open markers). Figure adapted from [84]. . . 91
- 3.20 Jet- $V^0$  particle matching via a geometrical requirement (see definition in Eq. 3.12). . . . . 93
- 3.21 Reconstruction Efficiency of inclusive  $V^0$  particles in  $|\eta_{V^0}| < 0.7$ . . . . . 98
- 3.22 (Upper plot) MC true  $K_S^0$   $\eta$  probability density for different  $V^0$   $p_T$  intervals. The shape of this distribution in  $\eta$  is varying for the different  $p_T$  intervals. (Lower plot) MC generated  $K_S^0$   $\eta$  probability distribution inside a jet cone ( $R = 0.2$ ), for different intervals of the  $V^0$   $p_T$  and for  $p_T^{jet} > 10$  GeV/c. . . . 100
- 3.23 Inclusive  $V^0$  reconstruction efficiency as a function of MC true  $V^0$   $\eta$  for different  $V^0$   $p_T$  intervals. These efficiency distributions are the starting point of the MC "re-weighting" procedure. . . . . 101
- 3.24 Example for signal purity (Signal/Signal+Background) from the inclusive  $V^0$  signal extraction as a function of  $V^0$   $\eta$  (and for the  $V^0$   $p_T$  interval 2-3 GeV/c). . . . . 101
- 3.25 Two examples are shown for the measured  $K_S^0$   $\eta$  distribution inside the jet cone (left plot) and the MC generated  $K_S^0$   $\eta$  distribution (right plot) obtained from the "reweighting" with the shape of the measured distribution. The thus obtained MC truth is used to estimate finally the ("reweighted")  $K_S^0$  reconstruction efficiency in the jet cone. . . . . 102
- 3.26 The "reweighted" reconstruction efficiency for the  $V^0$  particles inside the jet cone (within  $|\eta^{V^0}| < 0.7$ ) is calculated as a function of  $V^0$   $p_T$ . The efficiency includes furthermore the branching ratios of the  $V^0$  types. . . . . 103

3.27	The "reweighted" reconstruction efficiency for the $V^0$ particles in "no-jet" events and as a function of $V^0$ $p_T$ . The efficiency considers the branching ratios as well as the $\eta$ acceptance of the $V^0$ particles. . . . .	104
3.28	Correlation of the mother ( $\Xi$ ) $p_T$ with the daughter ( $\Lambda$ ) $p_T$ obtained from a Monte Carlo simulation of Pb–Pb collisions at $\sqrt{s_{NN}} = 2.76$ TeV and for reconstructed inclusive MC particles. . . . .	105
3.29	The calculated feed-down (FD) fractions obtained by the FD matrix from inclusive particles (black markers) with simulated in pp (PYTHIA8) jets (for $R = 0.2$ in red markers, for $R = 0.3$ in blue markers). . . . .	107
3.30	A PYTHIA simulated jet is embedded into a real Pb–Pb event. The jet finding algorithm reconstructs the embedded PYTHIA jet as well as real jets stemming of the Pb–Pb collision. . . . .	110
3.31	Comparison of the minimum-bias PYTHIA spectrum ("Jets from PYTHIA MB"), used for the embedding and the embedded reference $p_T^{\text{jet}}$ spectrum ("Embedded jets $R = 0.3$ in FastEmbedding" with multiple event selection). . . . .	111
3.32	Distribution of the radial distance between the jet axis from matched ( $R = 0.2$ ) jets to embedded ("particle level") jets. A loose cut of 0.3 is imposed (per default for the method) on the $\Delta R$ distribution of the matched jet (pairs) candidates to minimize the combinations of jet pairs that are the input of the next matching check, the shared $p_T$ fraction (see figure 3.33) of commonly used jet-tracks. . . . .	112
3.33	Fraction of total $p_T$ of matched ( $R = 0.2$ ) jets that is shared with the embedded ("particle level") PYTHIA jets in the overlapping region of both jet cones. Already a loose $\Delta R < 0.3$ is applied for these jet pairs (matched & embedded jet). On this distribution of shared total $p_T$ a cut of 50% is applied to select good candidates for the "matched" jets in the "hybrid" events. . . . .	113
3.34	PYTHIA jets that are reconstructed from all embedded PYTHIA simulated events at $\sqrt{s_{NN}} = 2.76$ TeV . . . . .	114
3.35	The jet matching efficiency (ratio from matched to embedded jets) is finite at very low $p_T^{\text{jet}}$ (up to around 10 - 20 GeV/c) but increases rapidly for jets from 10 GeV/c on and reaches 100 % matching efficiency from around 20 GeV/c on. For a better comparability the matched jet spectrum is plotted versus the corresponding $p_T^{\text{jet}}$ before the embedding (which avoids the $p_T^{\text{jet}}$ "smearing"). . . . .	115
3.36	Charged track $p_T$ spectrum in "signal+embedded" jet cones (light blue markers) for $p_T^{\text{jet}} > 10$ GeV/c and jet resolution parameter $R = 0.2$ , charged track spectrum in perpendicular cones (dark blue), after subtraction of UE (perp. cones) and compared to embedded PYTHIA jet constituents (red markers) . . . . .	116

- 3.37 The  $V^0$  particle  $p_T$  spectra inside the jet cone. Figures a) and b) show the full  $V^0$  particle content (“PYTHIA signal + data bckg” - cyan markers), only the PYTHIA (embedded signal) in red markers. The main interest of this study is the  $V^0$  particle background inside the jet cone (blue markers), coming from the PbPb event (in which the PYTHIA jets have been embedded). The background derived from this embedding study serves to estimate correction factors for the default method (“no-jet” events) that was used so far to subtract the UE  $V^0$  contribution to the jet cone. . . . . 118
- 3.38  $\Lambda$   $p_T$  spectrum in “no-jet” (NJ) events and from perpendicular cones, compared to the spectrum from the UE in embedded PYTHIA jet cones. The ratio (lower panel) is used to calculate a correction factor (CF) for the impact of the UE fluctuations on the  $V^0$  particles inside the jet cone (for  $p_T^{\text{jet}} > 10$  GeV/c (J1) and  $R = 0.2$ ). Used as CF is finally only the first  $p_T$  bin (centered at 2.5 GeV/c) of the ratio shown below the spectra. a) UE  $K_S^0$   $p_T$  spectra and ratio from comparison of UE  $V^0$  Embedding  $p_T$  spectrum to “no-jet”  $V^0$   $p_T$  spectrum. b) UE  $\Lambda$   $p_T$  spectra and ratio. . . . . 119
- 3.39 Ratio of  $V^0$  background from Embedding to the "event-averaged" UE  $V^0$  estimation from sampling  $V^0$  particles in “no-jet” events. a) shows the correction factors for the  $K_S^0$ , b) for the  $\Lambda$  particles. A linear fit together with a constant (through the first data point) serves to estimate a systematic uncertainty to the ratio value in the first  $p_T$  bin that is used as a correction factor (CF) for the default method ("no-jet" events). . . . . 120
- 3.40 UE  $V^0$   $p_T$  spectra from PYTHIA Embedding into all events (default method) compared to the one obtained from Embedding into "no-jet" events. The difference (visible at high  $p_T$ ) gives a hint on the jet contamination of the sampled UE  $V^0$  particles. a) Results for  $K_S^0$  particles. b) Results for  $\Lambda$  particles. 120
- 3.41 Correction factor (CF = Ratio of Embedding UE  $V^0$   $p_T$  spectrum divided by the UE  $V^0$   $p_T$  spectrum measured in “no-jet” events) from the first  $p_T$  bin obtained by Embedding into all events (default method) compared to the one which is obtained from Embedding into “no-jet” events. The difference serves to estimate a systematic uncertainty for a remaining jet contamination of the CF of this first bin. . . . . 121
- 3.42 Corrected  $V^0$   $p_T$  spectra in jets. The  $V^0$  UE contribution is subtracted with the “no-jet” event estimation method (green markers). Compared is the  $K_S^0$   $p_T$  spectrum in jets with the one corrected with the correction factor (CF) derived from the Embedding method (blue markers). a) Results for  $K_S^0$  particles. b)+c) Results for  $\Lambda$  and for  $\bar{\Lambda}$  particles. . . . . 122
- 3.43 Jet  $p_T$  spectrum ( $R = 0.2$ ) for a PYTHIA minimum bias spectrum (magenta markers) and a PYTHIA  $p_T$  hard bin (first  $p_T$  hard bin containing generated jets from 5 GeV/c up to 25 GeV/c, black markers) jet  $p_T$  spectrum. For comparison also the measured  $p_T^{\text{jet}}$  spectrum from the Pb–Pb data is drawn (grey markers). . . . . 123

3.44	Ratio of the $V^0$ background as measured in matched PYTHIA jets by using the PYTHIA MB $p_T^{\text{jet}}$ spectrum and by using the first $p_T$ -hard bin PYTHIA simulation. Left side shows the ratio for $K_S^0$ , right side shows the ratio for $\Lambda$ particles. . . . .	124
3.45	The elliptic flow coefficient $v_2^{\text{part}}$ for charged particles [175], [176] (in orange, green markers), for charged jets in ALICE (black markers) and for full (charged+neutral fragments) jets $v_2^{\text{ch jet}}$ with $R = 0.2$ in ATLAS (blue markers), measured in $\eta < 2.1$ [173]. Note that the centrality intervals used for the different measurements are not the same. Furthermore the same parton $p_T$ corresponds to different single particle $p_T$ or $p_T^{\text{jet}}$ . . . . .	125
3.46	Left side: Ratio of UE $V^0$ $p_T$ spectra from PYTHIA jet embedding in-plane and embedding out-of-plane. Right side: Second term of Eq. 3.38 (the impact of event asymmetry) calculated for all $V^0$ hadron species. The black markers show the combined result for all particle species which gives a negligible deviation ( $\lesssim 4.4 \cdot 10^{-6}$ ). Instead a relative difference of the spectra of 1% is assumed as a conservative estimate. . . . .	127
3.47	a) Variations of the signal extraction for the $V^0$ $p_T$ spectra. b) Impact on the (uncorrected) inclusive $(\Lambda + \bar{\Lambda})/2K_S^0$ particle ratio for 3 different variations. . . . .	132
3.48	Cut variations for the estimation of a relative systematic uncertainty on the efficiency correction of the $V^0$ $p_T$ spectra in jets ( $R = 0.2$ ) and estimated with jets of $p_T^{\text{jet}} > 10$ GeV/c <sup>2</sup> . Left plot shows the results for $K_S^0$ mesons, the right plot the results for $\Lambda$ baryons. . . . .	134
3.49	Two feed-down (FD) estimation approaches allow to calculate a systematic uncertainty for the FD subtraction. The default method is the FD fraction calculated for $\Lambda$ particles as in the inclusive $\Lambda$ analysis [177]. The second approach is the FD fraction derived from a PYTHIA8 simulation. Shown are the FD corrected $\Lambda$ $p_T$ spectra with $p_T^{\text{jet}} > 10$ GeV/c obtained from both approaches. . . . .	135
3.50	Cut variations for the estimation of a relative systematic uncertainty of the $V^0$ reconstruction efficiency on the $(\Lambda + \bar{\Lambda})/2K_S^0$ ratio in charged jets ( $R = 0.2$ ). . . . .	135
3.51	The feed-down fractions from inclusive particle analysis (black markers) and from simulation in PYTHIA8 jets (red markers - $R = 0.2$ , blue markers - $R = 0.3$ ) that have been calculated for the current analysis. . . . .	136
3.52	$(\Lambda + \bar{\Lambda})/2K_S^0$ ratio in jets ( $p_{T,\text{jet}}^{\text{ch}} > 10$ GeV/c and $R = 0.2$ ), corrected with FD fractions from inclusive particle analysis and from simulation in PYTHIA8 jets ( $R = 0.2$ ). . . . .	137
3.53	Left side: Ratio of the inclusive $\Lambda$ and $\bar{\Lambda}$ $p_T$ spectrum measured in the 2011 dataset (for the entire $\eta^{V^0}$ acceptance) shows a deviation from unity. The effect is about 5-10% smaller when only taking $\Lambda(\bar{\Lambda})$ particles with positive $\eta^{V^0}$ (what corresponds to the "A-side" of the detector) shown as open markers. Right side: $\Lambda/\bar{\Lambda}$ ratio as function of $p_T$ in jet cones (uncorrected yields). . . . .	138

3.54	Ratio of inclusive particle $p_T$ spectrum from 2010 data (and respective MC) to those recorded in 2011 (used for this work). Since the ratio of $p_T$ spectra deviates from unity a systematic uncertainty of 10% on this effect is assigned to all data points in the final results. . . . .	138
3.55	Contributions to the total relative systematic uncertainty (black dashed line) for the $K_S^0$ $p_T$ spectra in jets ( $R = 0.2$ ). The various contributions are added linearly, while the total relative systematic uncertainty is calculated according to Eq. 3.43. a) Uncertainty contributions for the $K_S^0$ $p_T$ spectrum. b) Uncertainty contributions for the $\Lambda + \bar{\Lambda}$ $p_T$ spectrum. . . . .	140
3.56	Contributions to the total relative systematic uncertainty (black dashed line) for the $(\Lambda + \bar{\Lambda})/2K_S^0$ in jets (of $R = 0.2$ ). The various contributions are added linearly, while the total relative systematic uncertainty is calculated according to Eq. 3.43. . . . .	140
4.1	a) Corrected inclusive $K_S^0$ and $\Lambda(\bar{\Lambda})$ $p_T$ spectra of the 10% most central events in Pb–Pb collisions. The $\Lambda$ and $\bar{\Lambda}$ $p_T$ spectra are scaled for better visibility and only statistical errors are shown. b) $(\Lambda + \bar{\Lambda})/2K_S^0$ ratio of the 10% most central events in Pb–Pb collisions (only statistical errors are shown) compared to the published [92] inclusive $\Lambda/K_S^0$ ratio from events of the centrality intervals 0-5% (red markers) and 5-10% (black markers). . . .	144
4.2	Upper panel: $(\Lambda + \bar{\Lambda})/2K_S^0$ ratio in jets ( $R = 0.2$ ) for $p_T^{\text{jet}} > 10$ GeV/c and $p_T^{\text{jet}} > 20$ GeV/c. Furthermore the $(\Lambda + \bar{\Lambda})/2K_S^0$ ratio obtained from PYTHIA jets ( $R = 0.2$ ) is shown. Lower panel: The $(\Lambda + \bar{\Lambda})/2K_S^0$ ratio in jets ( $R = 0.2$ ) for $p_T^{\text{jet}} > 10$ GeV/c (red markers) and $p_T^{\text{jet}} > 20$ GeV/c (blue markers) and in the inclusive (i.e. all $V^0$ particles) event (open black markers) obtained from this analysis. Shown are only statistical errors. . . .	146
4.3	Corrected $\Lambda$ , $\bar{\Lambda}$ and $K_S^0$ $p_T$ spectra in ("no-jet") events from Pb–Pb data (left panel). Right panel: Spectra outside (black markers) and inside ( $R = 0.2$ ) jets (red markers) together. Open markers are $K_S^0$ , full markers are $\Lambda$ hadrons. . . .	147
4.4	$(\Lambda + \bar{\Lambda})/2K_S^0$ ratio in jets ( $R = 0.2$ ) for $p_T^{\text{jet}} > 10$ GeV/c (red markers) and $p_T^{\text{jet}} > 20$ GeV/c (blue markers) and in the bulk of the Pb–Pb collision event (green markers) via "no-jet" events. The measured ratios from this analysis are compared to the inclusive, published $\Lambda/K_S^0$ ratio (grey markers) and the inclusive ratio measured in pp collisions at $\sqrt{s} = 7$ TeV and $\sqrt{s} = 0.9$ TeV. . . .	148
4.5	$(\bar{\Lambda} + \Lambda)/2K_S^0$ ratio in jets in p–Pb collisions compared to the ratio measured in this analysis in Pb–Pb collisions. Results in p–Pb collisions adapted from [123]. . . . .	149
4.6	Comparison of results obtained in the current jet analysis and in the high- $p_T$ hadron- $V^0$ correlation study (data adapted from T. Richert, thesis at Lund University [117]). . . . .	151
4.7	Corrected $K_S^0$ and $\Lambda$ spectrum in jets ( $R = 0.2$ ) for $p_T^{\text{jet}} > 10$ GeV/c (upper panels) $p_T^{\text{jet}} > 20$ GeV/c (lower panels), in logarithmic and linear y-axis scale. Jets are selected with a leading track bias $p_T^{\text{leading track}} > 5$ GeV/c. . . .	153

- 4.8 Comparison of the  $V^0$   $p_T$  spectra in jets in Pb–Pb collisions to the prediction of PYTHIA jets (simulating pp events at  $\sqrt{s} = 2.76$  TeV) is made. The left panel shows the  $K_S^0$  and  $\Lambda$   $p_T$  spectrum in jets with  $p_T^{\text{jet}} > 10$  GeV/c. The right panel shows the spectra for jets with  $p_T^{\text{jet}} > 20$  GeV/c. The results from PYTHIA jets (for three different tunes) are smeared in  $p_T^{\text{jet}}$  according to the particle level  $\sigma(\delta p_T^{\text{ch}})$  values [84]. The four panels below show the ratios for data divided by MC simulation (different PYTHIA tunes in different marker colours), for  $K_S^0$  and  $(\Lambda + \bar{\Lambda})$  separately. The ratios (data/MC) are shown separately for the two  $p_T^{\text{jet}}$  intervals and below the corresponding measurement. The PYTHIA simulations are adapted from [172]. . . . . 155
- 4.9 Comparison of the  $K_S^0$  and  $(\Lambda + \bar{\Lambda})$   $p_T$  spectra from this analysis to the spectra measured in p–Pb events at  $\sqrt{s_{\text{NN}}} = 5.02$  TeV. The left panel shows the spectra in jets for  $p_T^{\text{jet}} > 10$  GeV/c. On the right panel the spectra are shown for jets with  $p_T^{\text{jet}} > 20$  GeV/c. The results from the p–Pb data are scaled according to a PYTHIA8 simulation to take into account the effect of the UE fluctuations on  $p_T^{\text{jet}}$  that are present in Pb–Pb events, the leading constituent cut  $p_T^{\text{leading track}} > 5$  GeV/c and the different collision energy. Used are three different tunes of PYTHIA8 (tune "Monash", "Perugia 2011" and "NoCR"). The systematic uncertainties of the PYTHIA tunes are superimposed, they are lightgrey for the  $\Lambda$  baryons and darkgrey for the  $K_S^0$  mesons. Scaled reference is adapted from [172] and based on the measurement from [123]. . . . . 156
- A.1 Top: inclusive  $p_T$  spectrum of charged hadrons in central Au+Au collisions at  $\sqrt{s_{\text{NN}}} = 200$  GeV; data taken from the PHENIX collaboration. Bottom: Ratio of protons to  $\pi^+$  as a function of  $p_T$ . The region below 4 GeV/c is dominated by recombination, the region above 6 GeV/c by parton fragmentation. Figure and caption adapted from [181]. . . . . 190
- F.1 The principle of the UE  $V^0$  estimation of outside cones ('OC') drawn as a sketch. A cone of  $2R$  is placed around selected jets and all  $V^0$  particles outside these cones and inside the  $V^0$  acceptance are collected. For the normalisation of this OC spectrum the areas of the excluded  $2R$ -cones are subtracted from the area of the entire event acceptance. Shown are exaggerated and not true proportions of the geometrical measures. . . . . 216
- F.2 Uncorrected  $K_S^0$   $p_T$  spectra in the Underlying Event and for 5 different estimation methods. The lower plot shows the ratio for each method relative to the default method ('no-jet') events. . . . . 218
- F.3 Uncorrected  $\Lambda$   $p_T$  spectra in the Underlying Event and for 5 different estimation methods. The lower plot shows the ratio for each method relative to the default method ('no-jet') events. . . . . 218

G.1	Comparison of the different $V^0$ $p_T$ spectra from PYTHIA jets of different tunes. Open markers represent spectra for $\sqrt{s_{NN}} = 5.02$ TeV. Closed markers represent spectra for $\sqrt{s_{NN}} = 2.76$ TeV that are including the $p_T^{\text{jet}}$ 'smearing' and the leading track requirement. Figure adapted from [172].	220
G.2	Comparison of the measured $V^0$ $p_T$ spectra in p–Pb collisions (red markers) to the scaled reference spectra (open markers, different colours for the PYTHIA tunes). Figure adapted from [172].	221
H.1	$\Lambda/K_S^0$ ratio in jet cones from <i>hybrid events</i> (green markers) for $p_T^{\text{jet}} > 10$ GeV/c and a jet resolution parameter $R = 0.2$ , and compared to the reference from the ratio in PYTHIA jets (red markers) that are used for the embedding into data.	224
H.2	Left side: $(\Lambda + \bar{\Lambda})/2K_S^0$ ratio as derived from the fully corrected $V^0$ $p_T$ spectra as presented in this thesis. Right side: ALICE Physics preliminary version from May 2015, not including the correction for the impact of the Underlying Event fluctuations (via Embedding of PYTHIA jets into data events).	224



# Appendix A

## Hadronisation mechanisms

The concept of quark recombination and coalescence is an interesting attempt to better understand the hadronisation mechanisms and aims to explain the baryon-to-meson ratio enhancement observed in heavy-ion collisions. This approach (as adapted from [109]) considers hadron production in relativistic heavy-ion collisions at transverse momenta larger than 2 GeV/ $c$  to be a competition of two different hadronisation mechanisms. High- $p_T$  hadrons ( $\gtrsim 5$  GeV/ $c$ ) are dominantly produced via fragmentation of partons that are created perturbatively. For hadrons in the intermediate  $p_T$  range (from around 2-5 GeV/ $c$ ) however the recombination of partons from the medium dominates. This idea of different hadronisation mechanisms was motivated by the baryon anomaly that saw a “lack of suppression” for baryons compared to mesons (see e.g. ALICE measurement of the  $\Lambda/K_S^0$  ratio in Pb–Pb collisions as shown in Fig.1.26). While it is a commonly accepted picture that high- $p_T$  partons traversing the medium are suffering energy loss independent of the later hadronisation process, there is no explanation for the enhancement of baryon production. This phenomenon of baryon-to-meson enhancement might be therefore attributed to the hadronisation itself.

The hadronisation via fragmentation is expected to happen as follows:

- A parton with momentum  $p_T$  is created and leaves the interaction zone being still connected with other partons by a colour string
- The string breaks as the string energy is exceeding a certain limit, breaks and creates new quark-antiquark pairs
- Quark-antiquark pairs combine into final state hadrons
- Hadrons at larger  $p_T$  are distributed according to a perturbative power law function

the hadronisation mechanism via parton recombination is expected as

- Partons created by the hot and dense medium in heavy-ion collisions are very close in phase space
- If they are close enough (which is expected to be the case for the densely populated phase space in the plasma) they can recombine to form a hadron (baryon or meson)

- It is energetically favored to build a baryon, that consists of three quarks, with each quark carrying  $\frac{1}{3} p_{\text{baryon}}$
- Quarks forming a meson need to carry the (larger) momentum fraction  $\frac{1}{2} p_{\text{meson}}$  to form a meson with the same total momentum as the baryon.
- Particles at low  $p_T$  follow a thermal momentum distribution

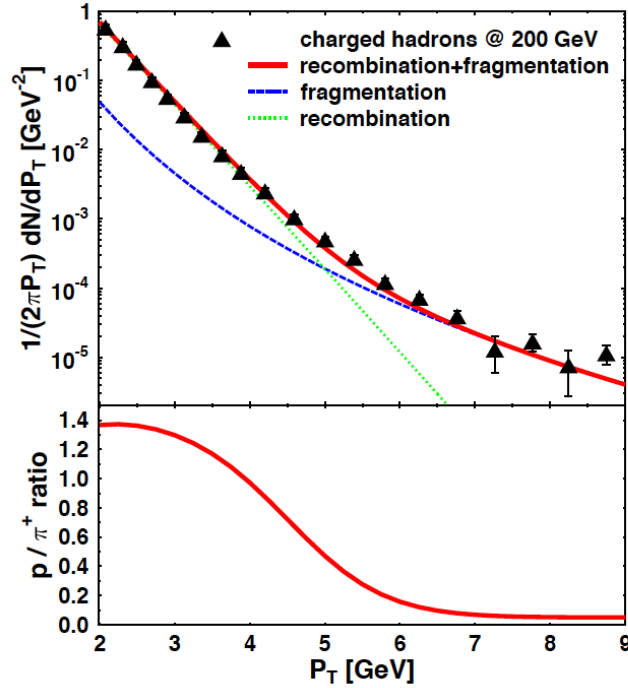


Figure A.1: Top: inclusive  $p_T$  spectrum of charged hadrons in central Au+Au collisions at  $\sqrt{s_{\text{NN}}} = 200$  GeV; data taken from the PHENIX collaboration. Bottom: Ratio of protons to  $\pi^+$  as a function of  $p_T$ . The region below 4 GeV/c is dominated by recombination, the region above 6 GeV/c by parton fragmentation. Figure and caption adapted from [181].

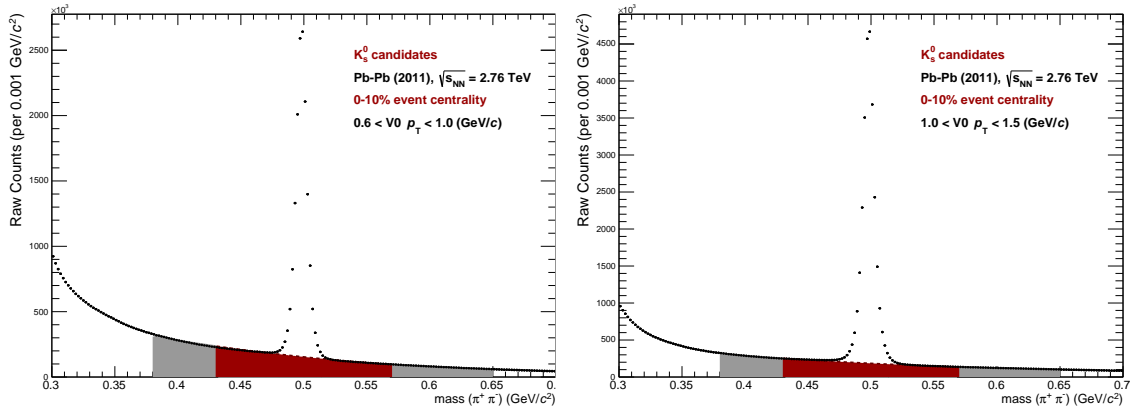
The prediction of the “recombination” model by Fries, Müller and Nonaka [103] is shown in Fig. A.1. The model considers quark recombination for hadrons at low  $p_T$  and fragmentation for hadrons with higher  $p_T$  as the dominant hadronisation mechanism. The combination of these approaches is indicated by the red solid line. The prediction is made for charged hadrons and can well describe a measurement by PHENIX at  $\sqrt{s_{\text{NN}}} = 200$  GeV. The model prediction for the proton-to-pion ratio is shown in the lower panel, it exhibits the characteristic baryon-meson enhancement. The conclusion from this model might be that particle production is dominated by recombination whenever the system of partons is very dense in phase space and has thermal character. Otherwise, for larger hadron transverse momentum, the particles are produced by perturbative string fragmentation.

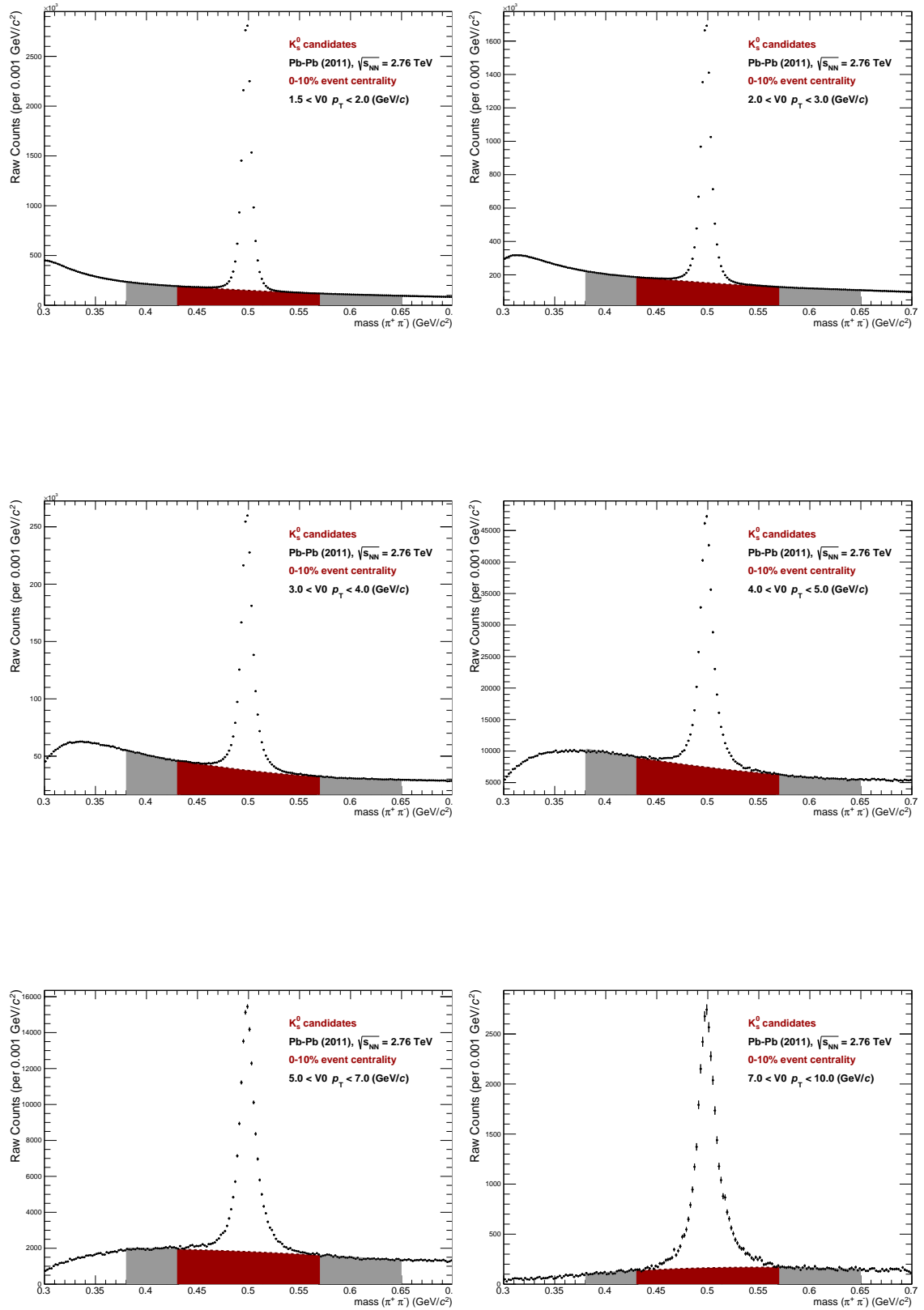
This model gives an explanation of the identified light-flavour observations in heavy-ion collisions made at RHIC and LHC that does not consider energy loss or collective effects in the medium but the way how particles are produced in the hadronisation.

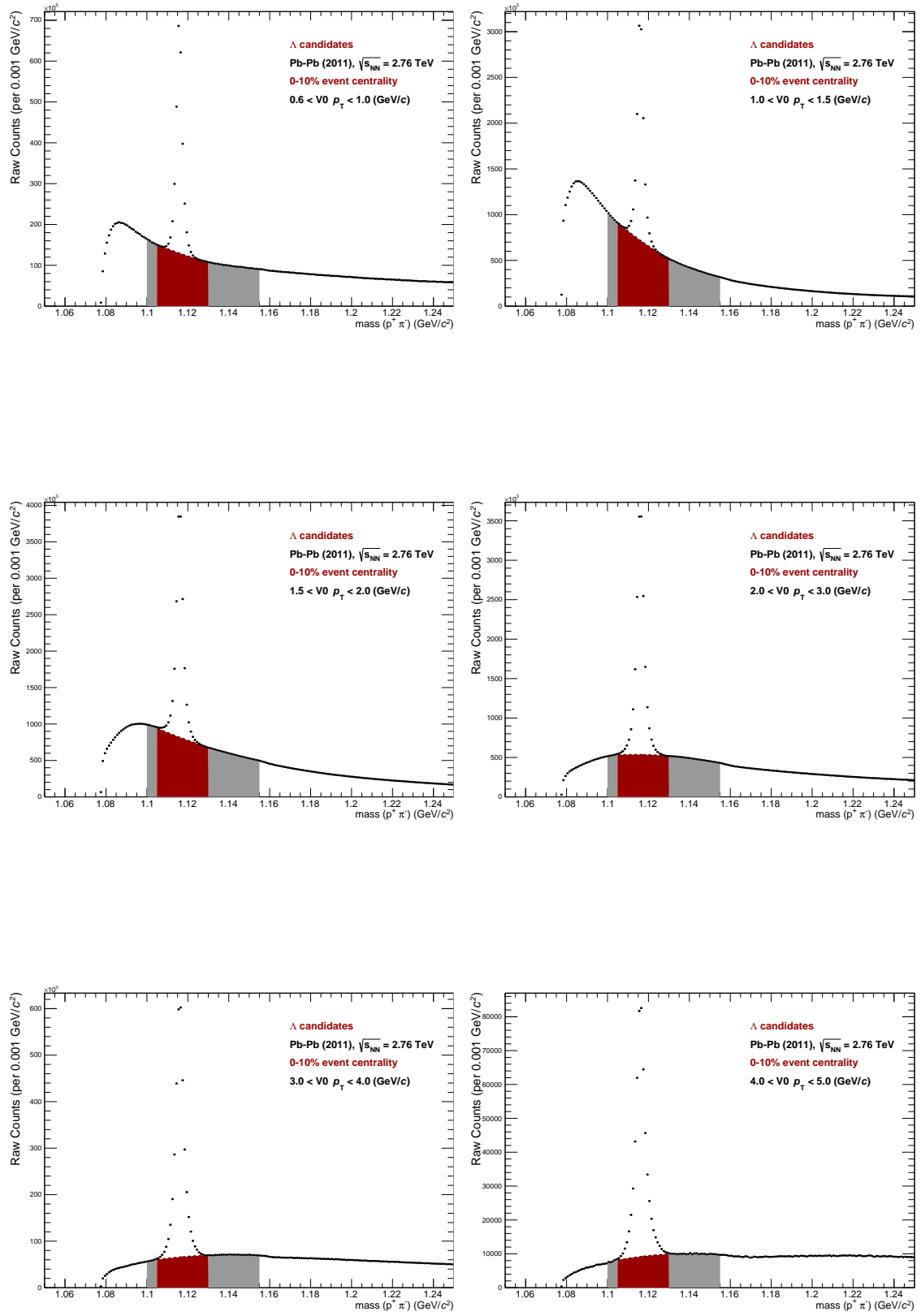
## Appendix B

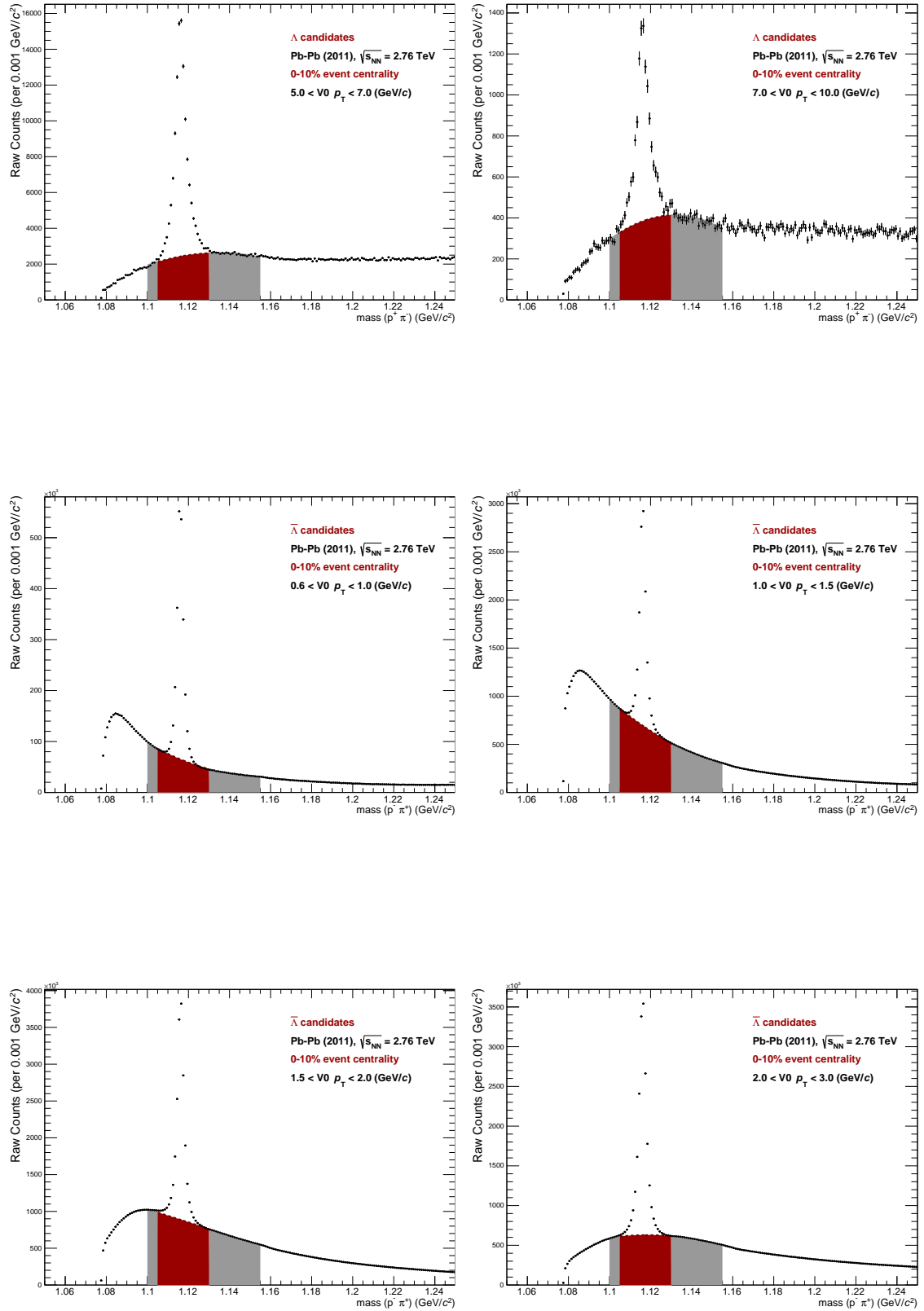
# Signal extraction for inclusive $V^0$ particles

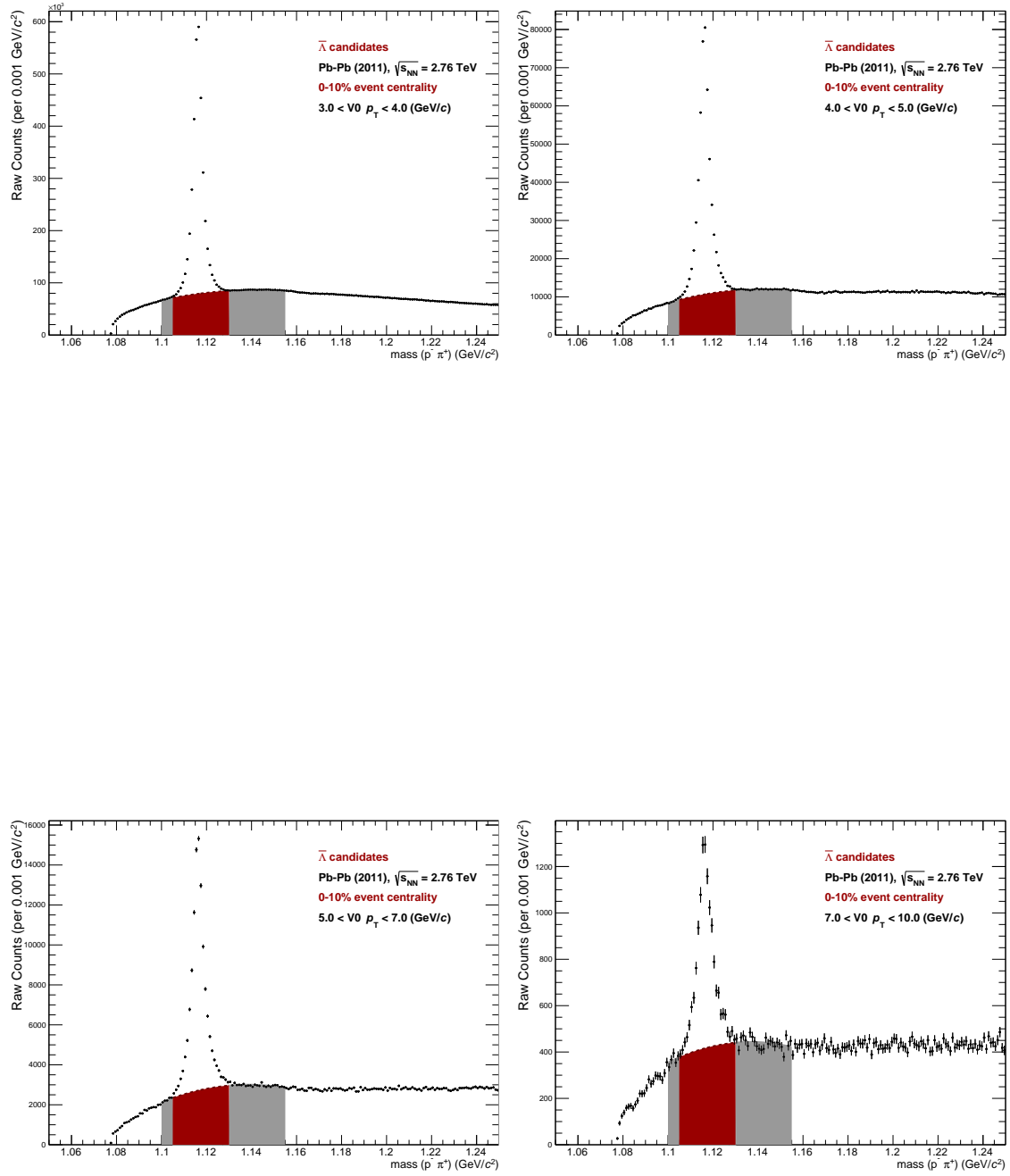
In the following the invariant mass distributions for the inclusive (i.e. all candidates in the event acceptance)  $V^0$  candidates are shown. The distributions are drawn together with the fit function that is used to estimate the combinatorial background below the signal peak. Each plot is labeled with the  $V^0$  hadron species and the  $p_T$  interval in which the  $V^0$  candidates are reconstructed. All invariant mass distributions show  $V^0$  candidates from the 0-10% most central events of the (in 2011 recorded) Pb–Pb data at  $\sqrt{s_{NN}} = 2.76$  TeV. The signal range is indicated as a red area (the “peak region”) and the background ranges (used for the fitting) are marked as gray areas on both sides of the signal peak. The background is estimated using the integral of the fit function under the peak (in the region marked as red area) and subtracted from the number of (signal+background) candidates in the “peak region”. More details about the signal extraction procedure can be found in section 3.1.5.













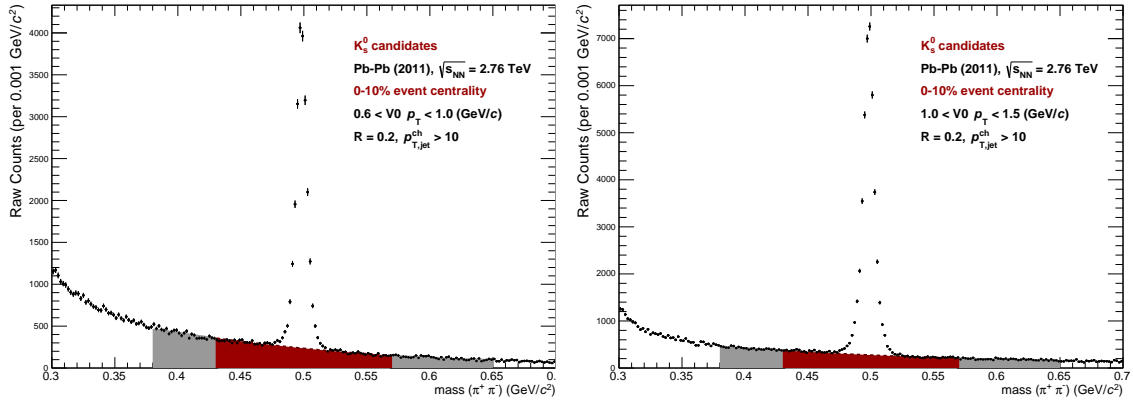
# Appendix C

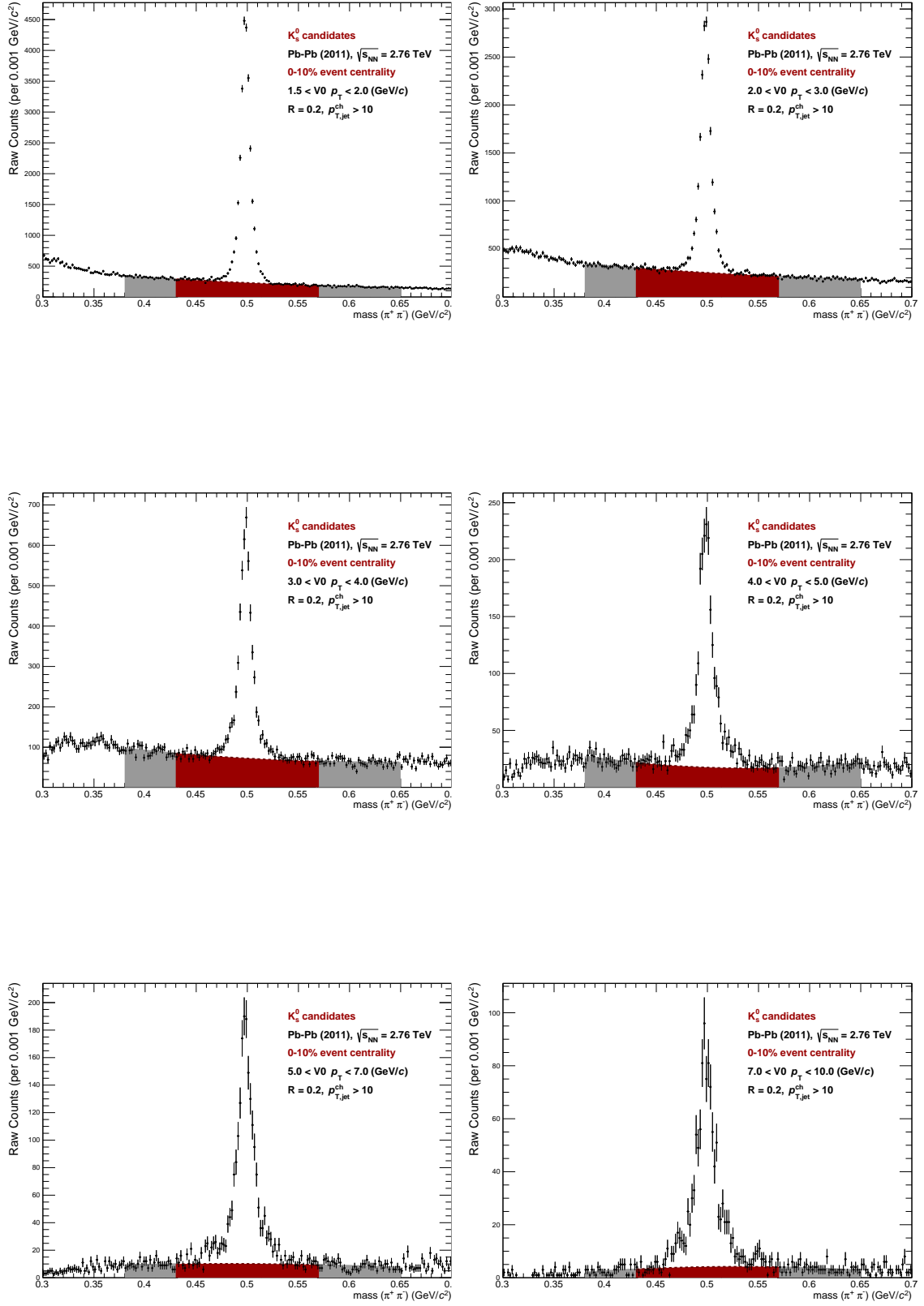
## Signal extraction in jet cones

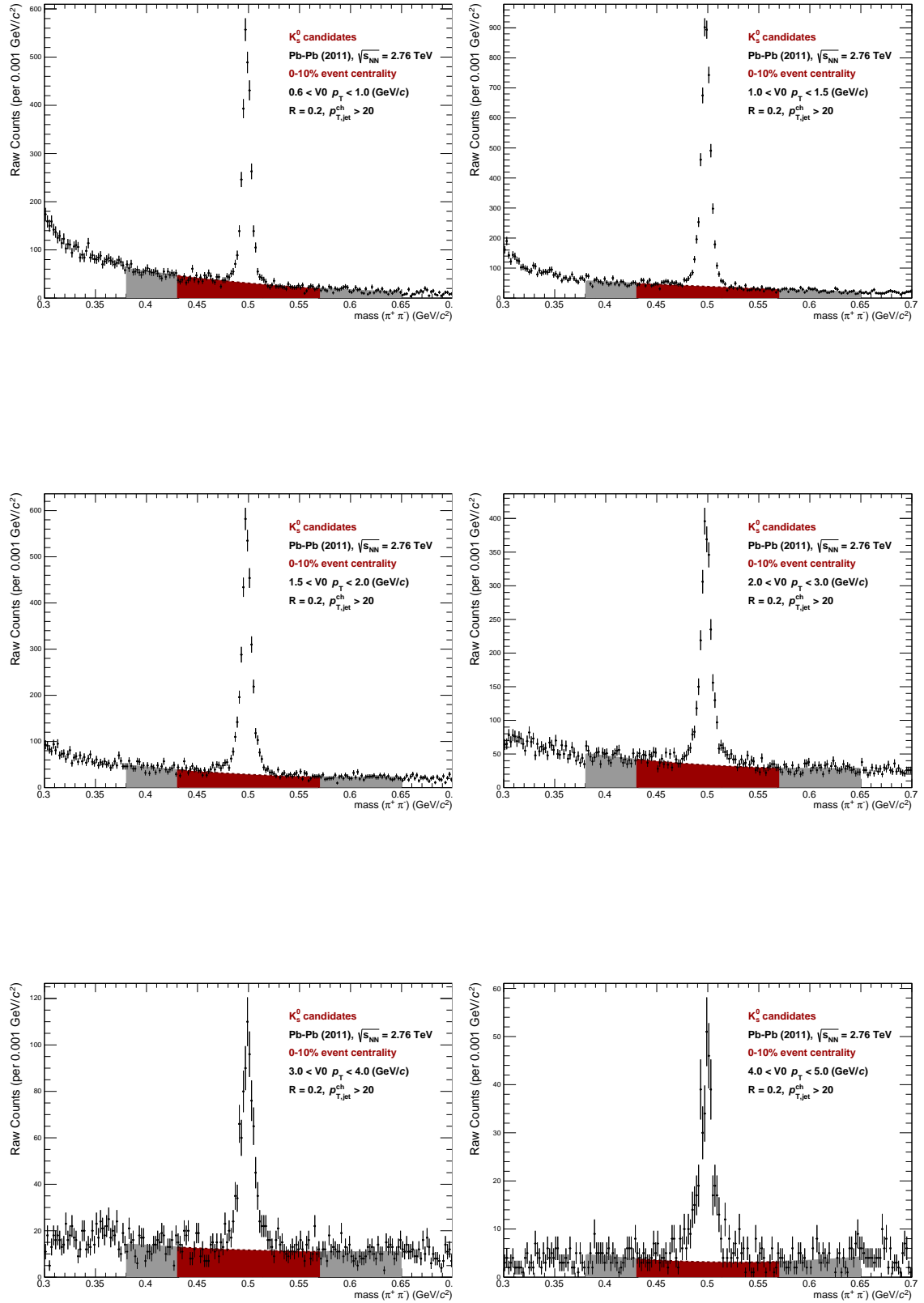
In the following the invariant mass distributions for the  $V^0$  candidates in the ( $R = 0.2$ ) jet cones are shown.

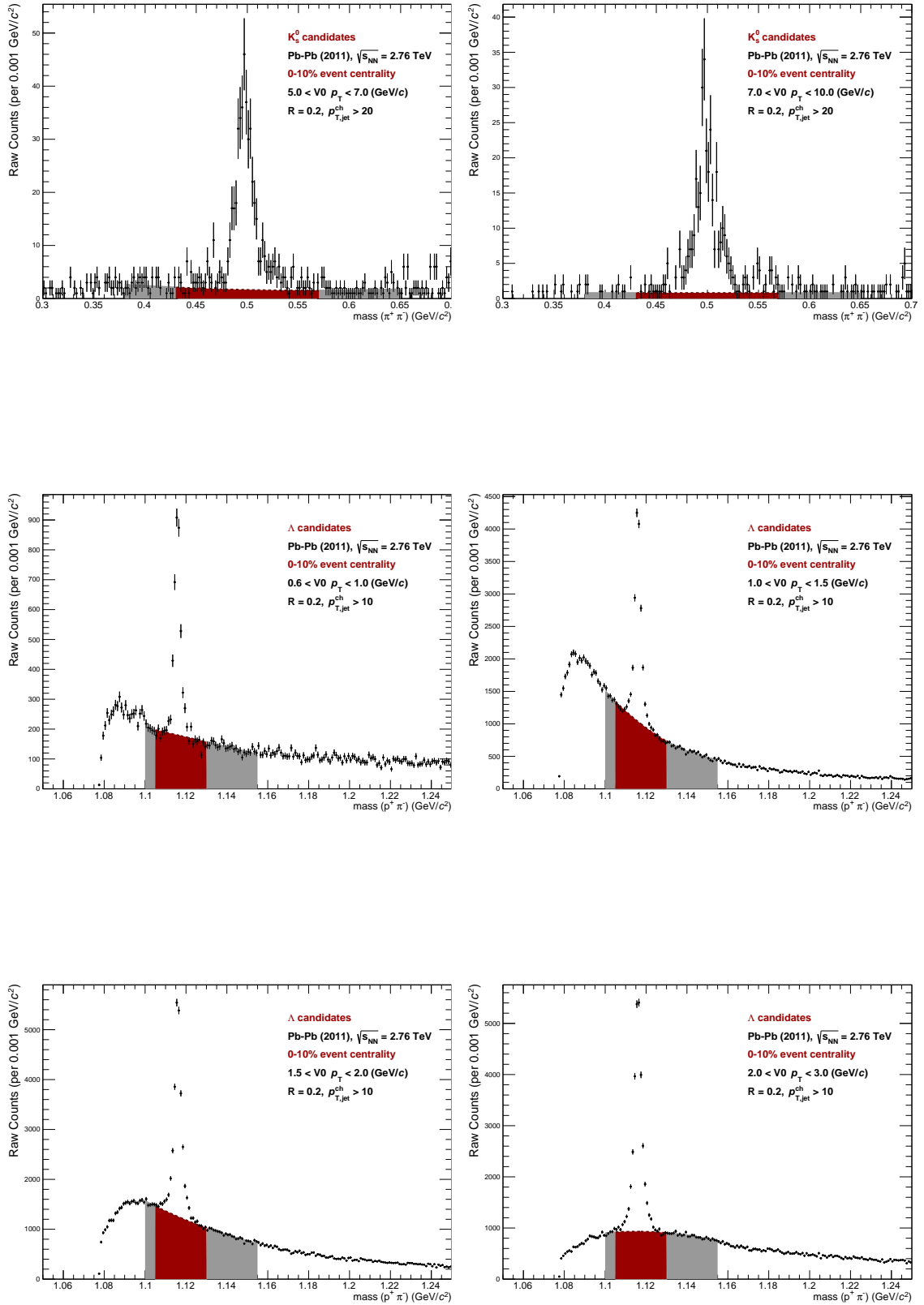
The distributions are drawn together with the fit function that is used to estimate the combinatorial background below the signal peak. Each plot is labeled with the corresponding hadron species, the hadron  $p_T$  interval and the jet  $p_T$  interval in which the  $V^0$  candidates are reconstructed. All invariant mass distributions show  $V^0$  candidates from the 0-10% most central events of the (in 2011 recorded) Pb–Pb data at  $\sqrt{s_{NN}} = 2.76$  TeV.

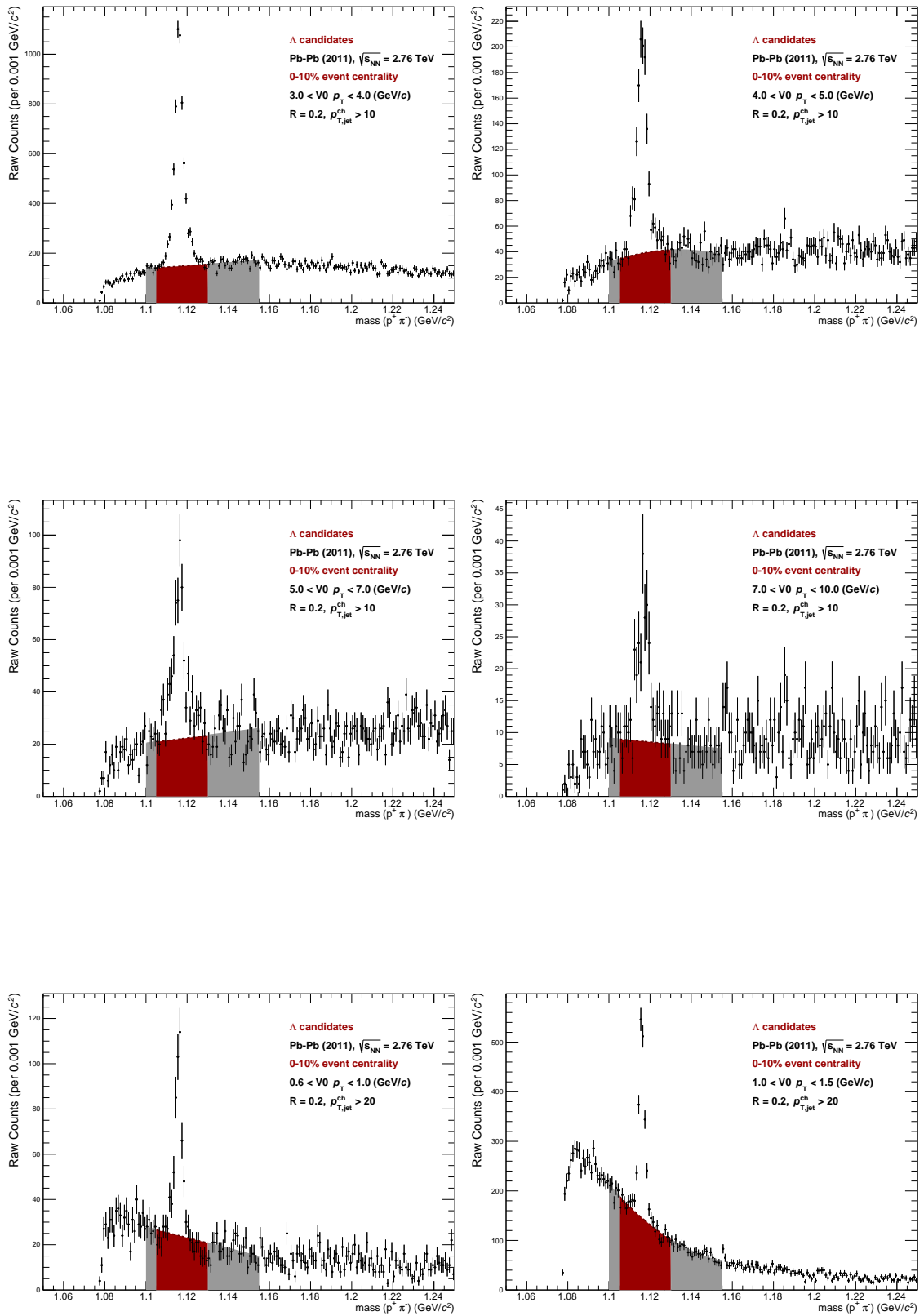
The signal range is indicated as a red area (the “peak region”) and the background ranges (used for the fitting) are marked in gray areas on both sides of the signal peak. The background is estimated using the integral of the fit function under the peak (in the region marked as red area) and subtracted from the number of (signal+background) candidates in the “peak region”. More details about the signal extraction procedure can be found in section 3.1.5.

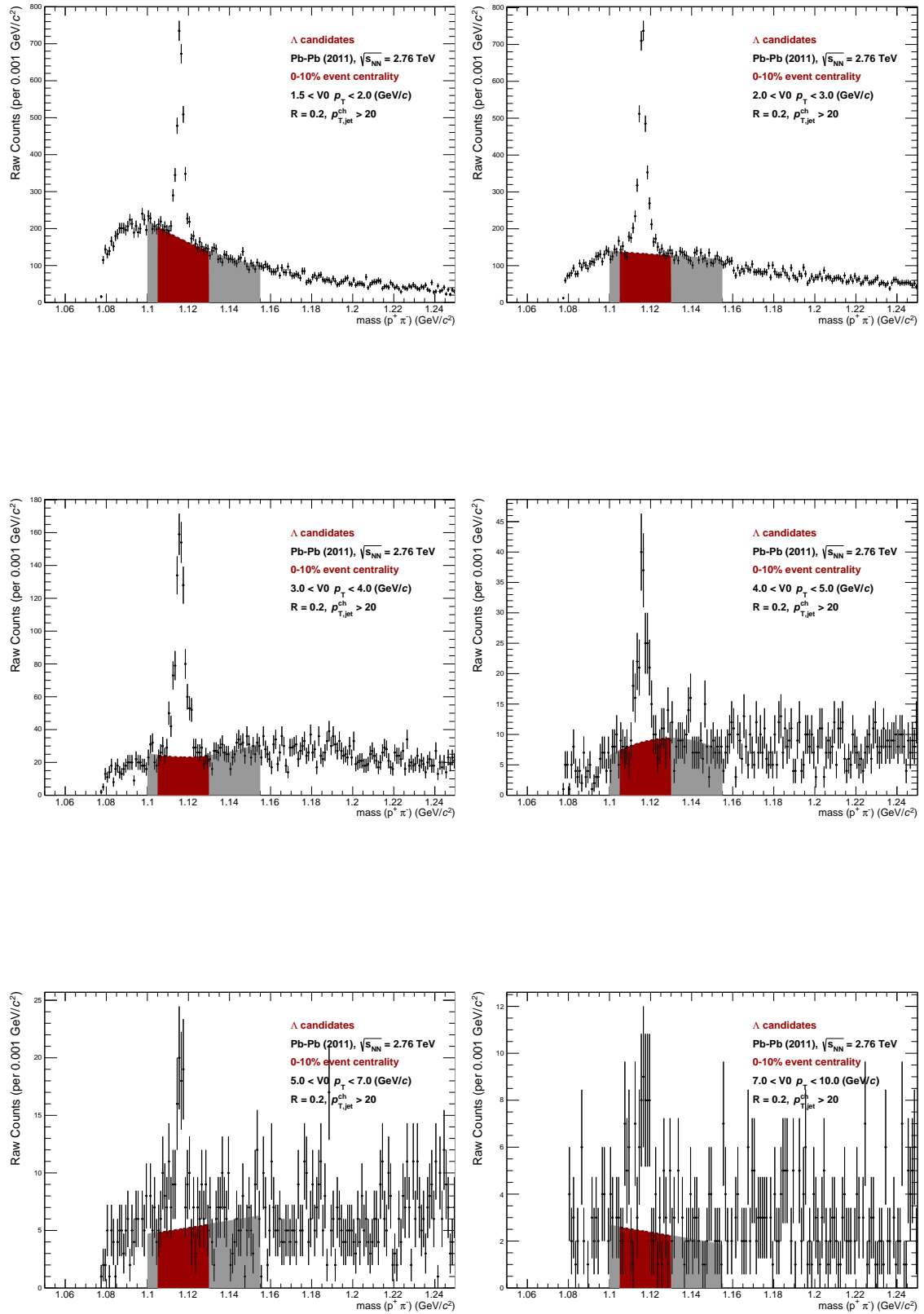


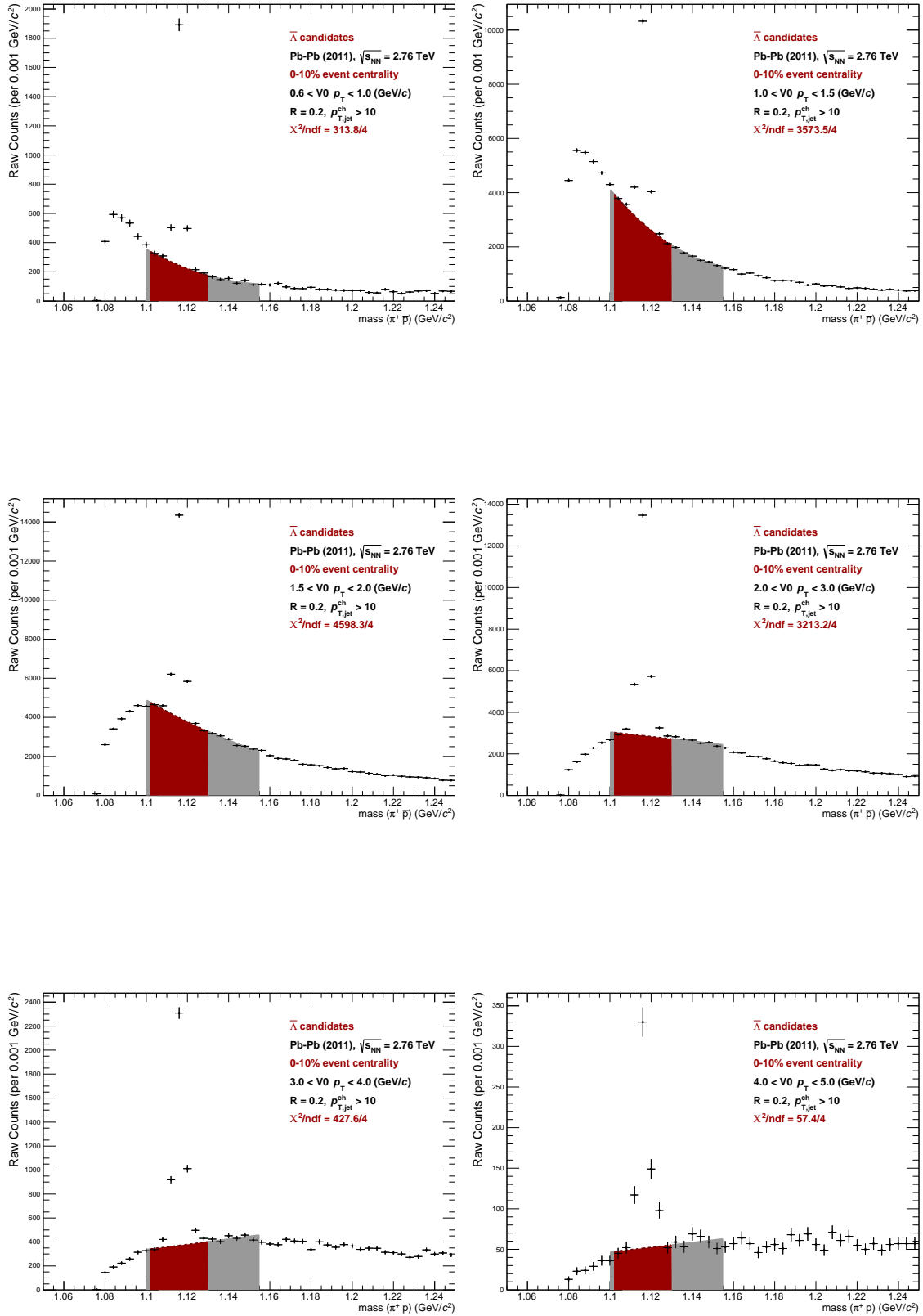


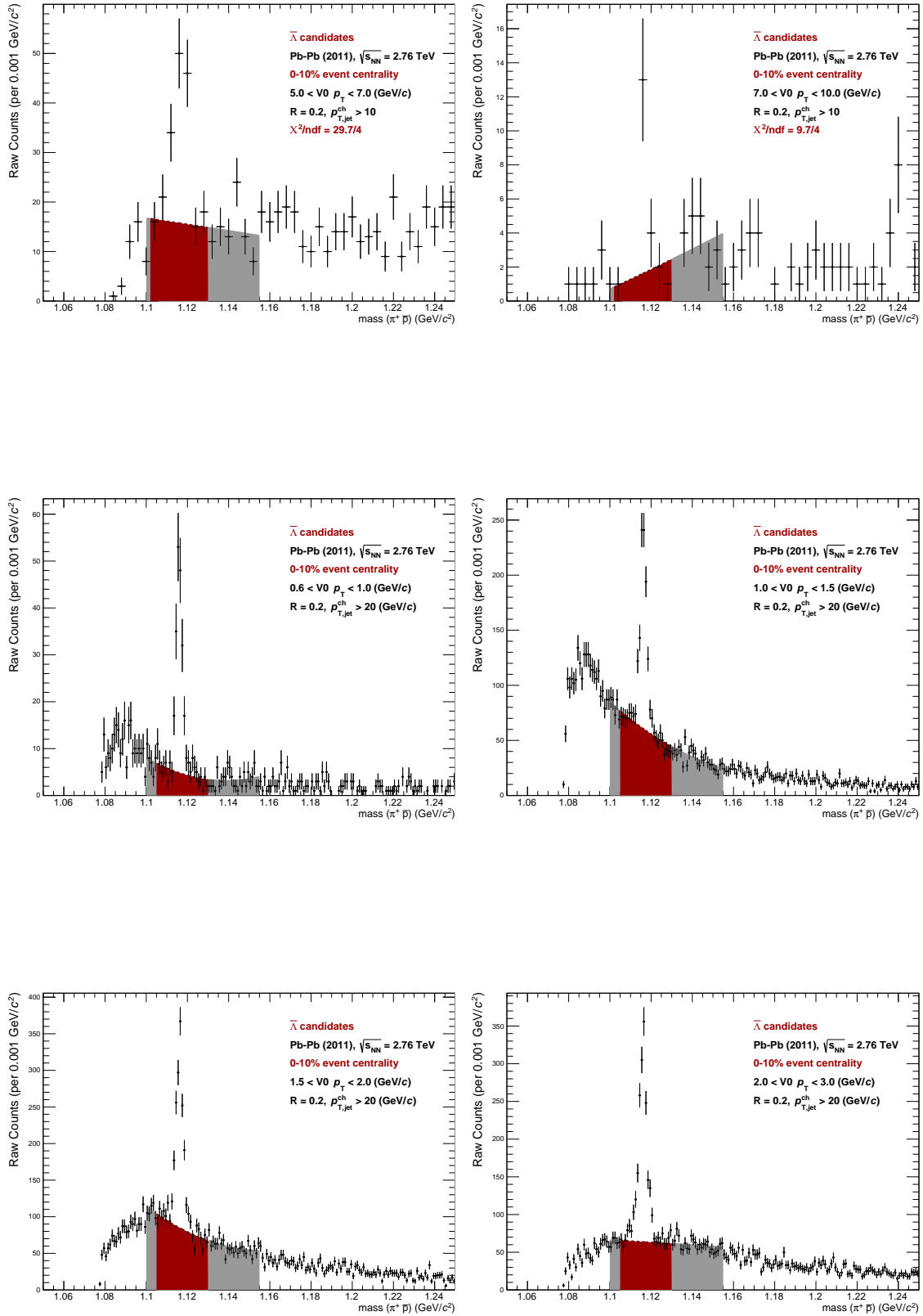


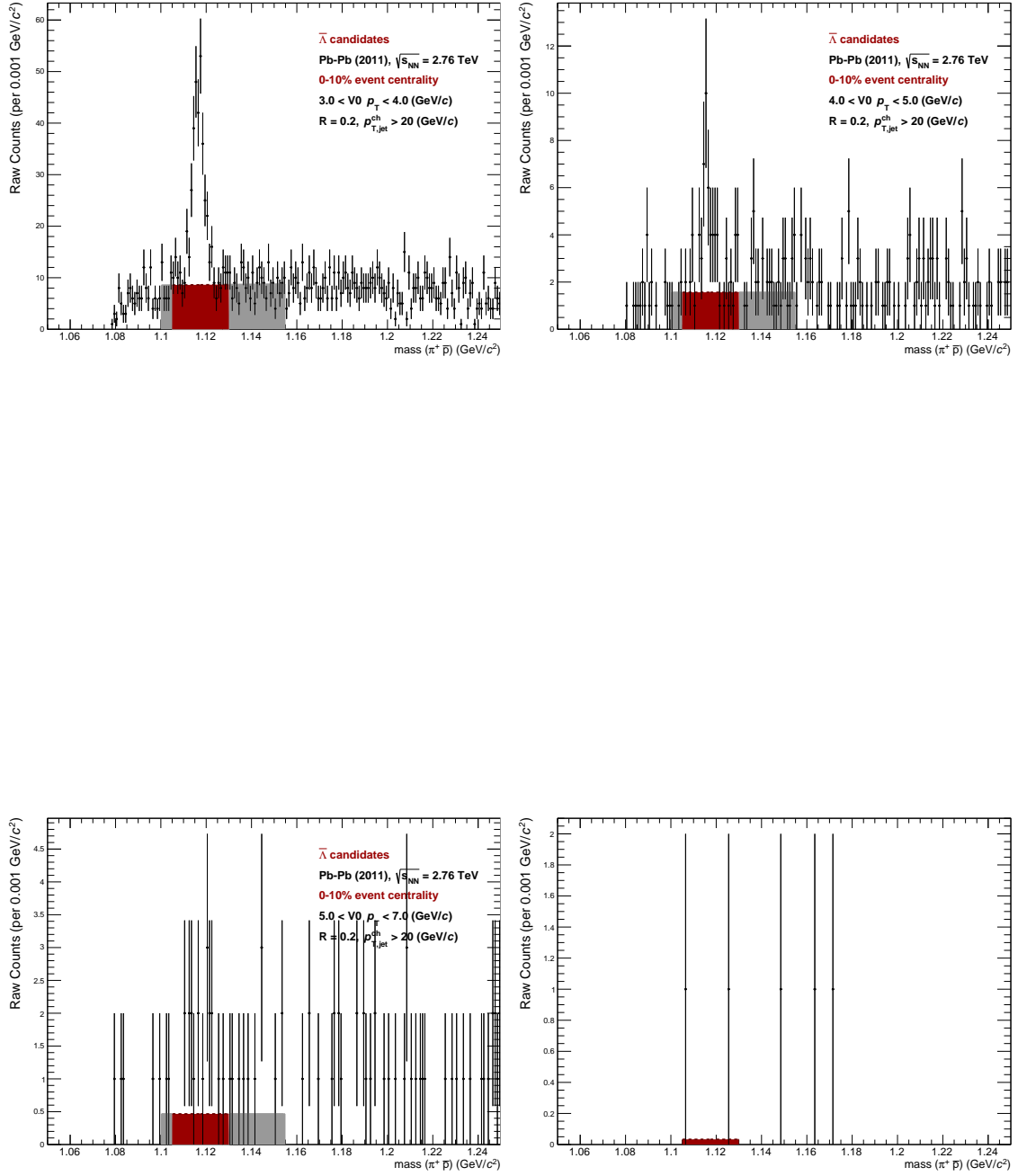














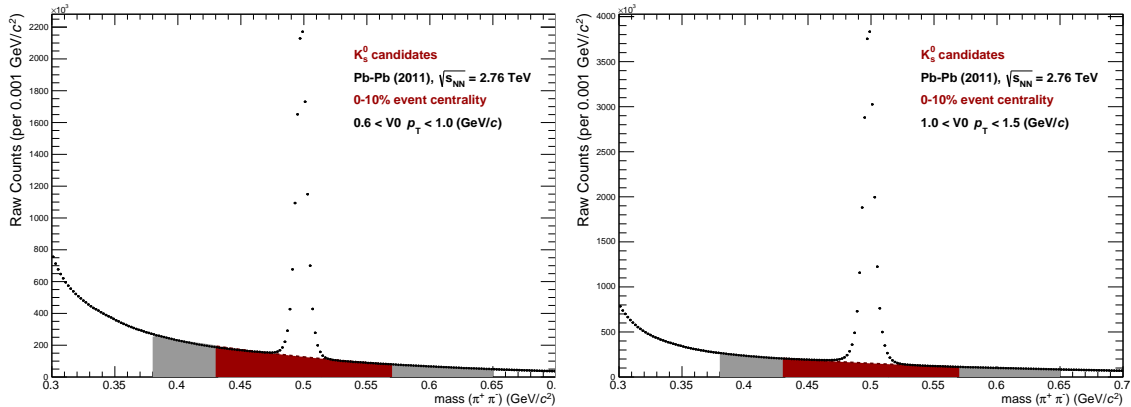
## Appendix D

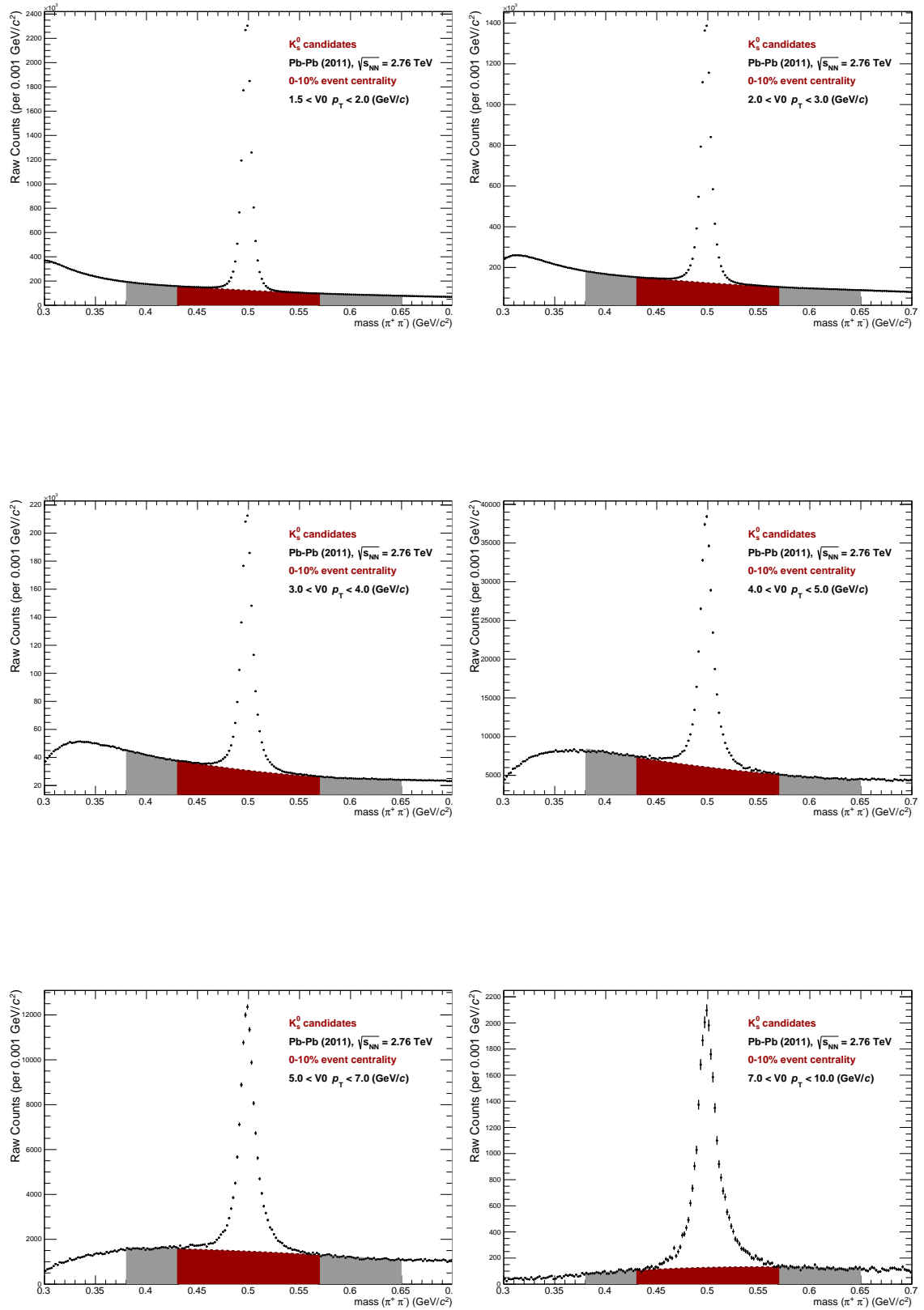
# Signal extraction in the Underlying Event

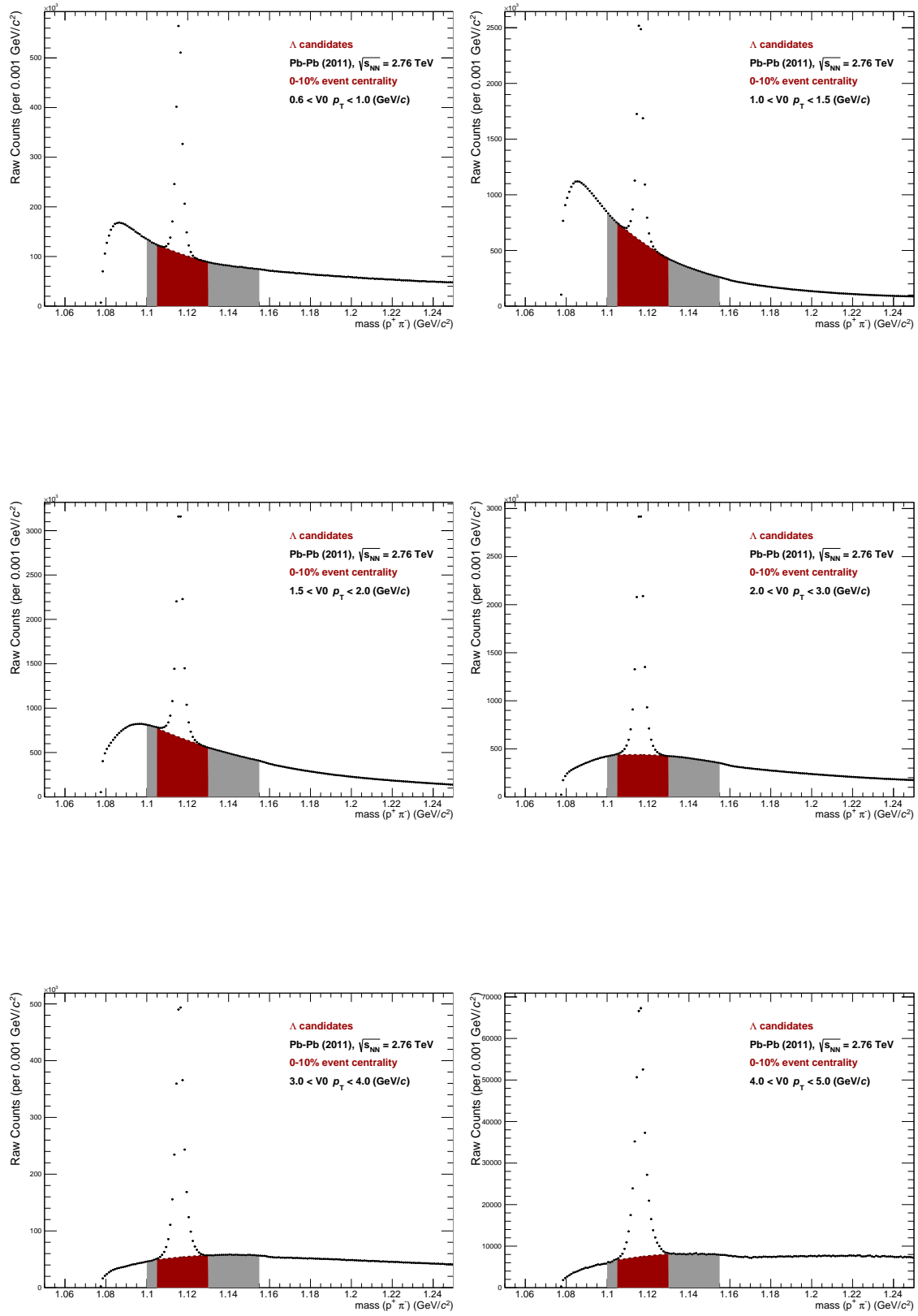
In the following the invariant mass distributions for the  $V^0$  candidates in 'no-jet' events (i.e. events in which no jet was selected) are shown. The  $V^0$  hadrons from 'no-jet' events serve as an estimate of UE  $V^0$ s contributing to the particle content of jet cone.

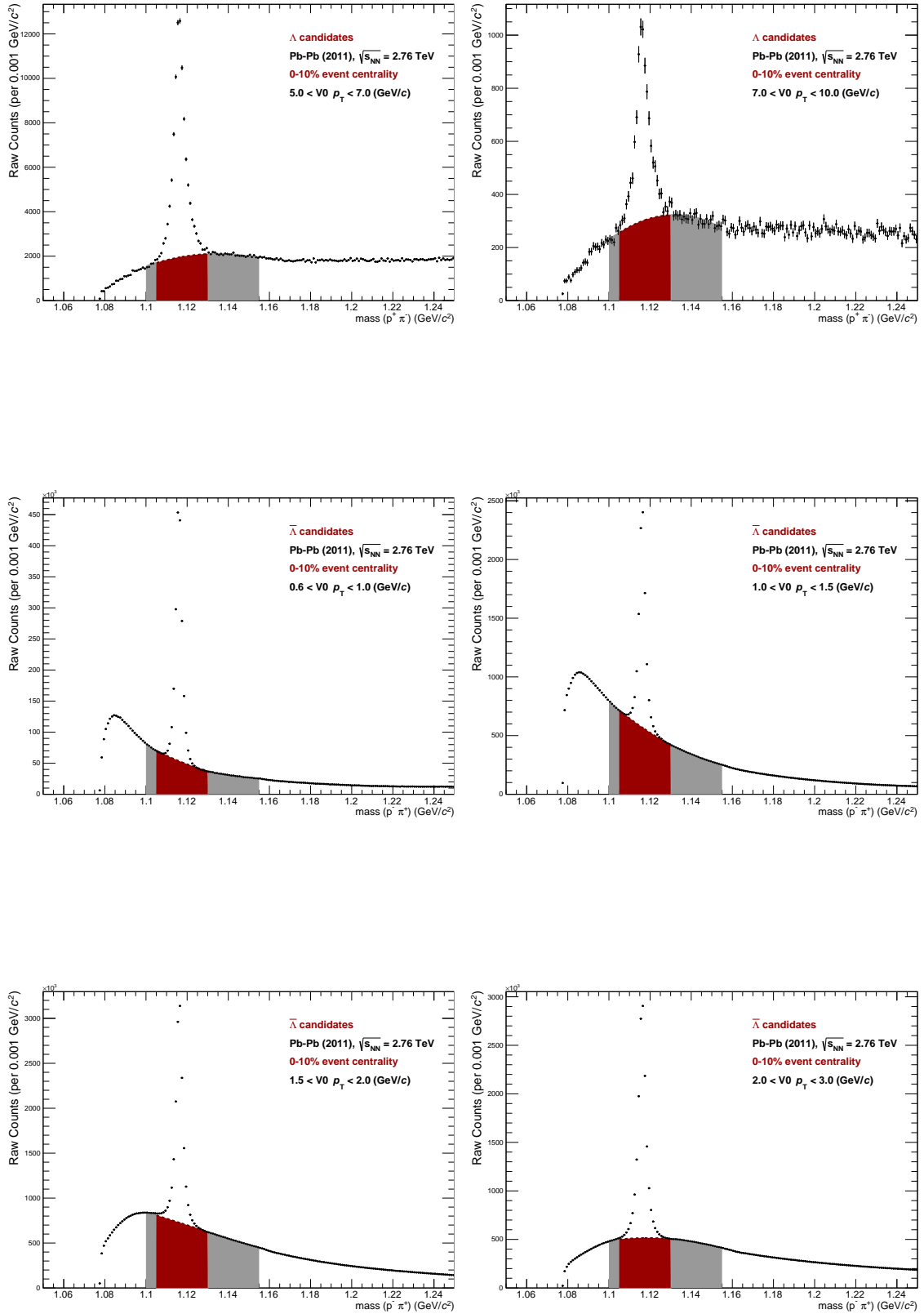
The invariant mass distributions are drawn together with the fit function that is used to estimate the combinatorial background below the signal peak. Each plot is labeled with the  $V^0$  hadron species and the  $p_T$  interval in which the  $V^0$  candidates are reconstructed. All invariant mass distributions show  $V^0$  candidates from the 0-10% most central events of the (in 2011 recorded) Pb–Pb data at  $\sqrt{s_{NN}} = 2.76$  TeV.

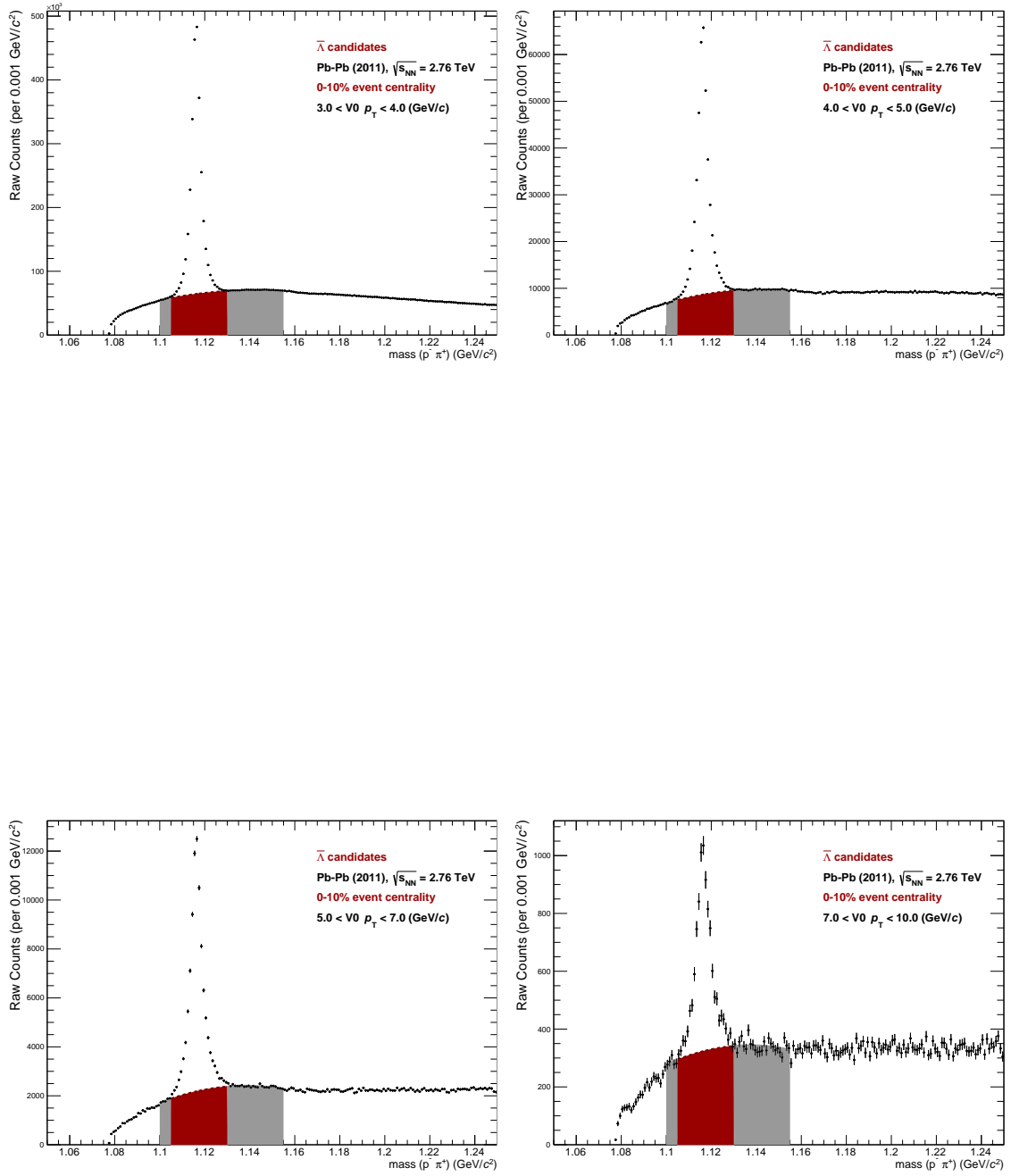
The signal range is indicated as a red area (the “peak region”) and the background ranges (used for the fitting) are marked as gray areas on both sides of the signal peak. The background is estimated using the integral of the fit function under the peak (in the region marked as red area) and subtracted from the number of (signal+background) candidates in the “peak region”. More details about the signal extraction procedure can be found in section 3.1.5.













# Appendix E

## Technical details jet reconstruction

### E.1 Cut selection on tracks used for jet reconstruction

To ensure good tracking quality, track uniformity and an high  $p_T$  resolution for the charged tracks that are used by the *anti* -  $k_t$  jet finding algorithm all tracks have to fulfill the so-called “hybrid track” cut selection. The criteria for the selection (of the data set from 2011) are listed in the following. They aim furthermore to select primary tracks and reject secondary tracks (e.g.  $V^0$  daughters) from the reconstructed jets.

There are basically two track selection classes, the "good global tracks" and the "complementary tracks" which are both used to select tracks, therefore this track selection is also called "hybrid track" cut selection.

- Use good global tracks when they are available, otherwise use constrained tracks (which are constrained to the primary vertex of the event to ensure a good track momentum resolution)
- Cuts for good global tracks:
  - At least one hit in SPD
  - Require ITS refit
  - Number TPC crossed rows  $\geq 70$
  - Ratio crossed rows over findable TPC  $\geq 0.8$
  - $\chi^2$  per TPC cluster in first iteration  $\leq 4$
  - No kink daughter tracks are accepted
  - Require TPC refit
  - Fraction of shared TPC clusters  $< 0.4$
  - $\chi^2$  per ITS cluster  $< 36$
  - $DCA_z < 2$  cm
- Cuts for constrained tracks (imposed on tracks not passing requirements for “good global” tracks)

- Same cuts as for the good global tracks shown above
- Constrained to primary vertex to improve  $p_T$  resolution

## E.2 Jet reconstruction settings

The jet reconstruction is performed by the AliRoot analysis task `$ALICE_ROOT/JETAN/AliAnalysisTaskJetCluster.cxx` [182].

The following settings are chosen for the jet finding in this analysis:

- algorithm: anti- $k_t$  (signal jet),  $k_t$  (background estimation)
- parameters:
  - resolution parameter:  $R = 0.2$
  - algorithmic strategy for clustering: automatic selection (`fastjet::Best`)
- recombination scheme: boost-invariant  $p_T$  scheme (`fastjet::BIpt_scheme`)

The following settings are chosen for the jet finding in this analysis:

- algorithm: anti- $k_t$  (signal jet),  $k_t$  (background estimation)
- parameters:
  - resolution parameter:  $R = 0.2$
  - algorithmic strategy for clustering: automatic selection (`fastjet::Best`)
- recombination scheme: boost-invariant  $p_T$  scheme (`fastjet::BIpt_scheme`)

For the reconstruction of the signal jets the anti- $k_t$  jet finder is used, for the estimation of the average contribution of charged tracks to the jets, the  $k_t$  jet finder as described in section 3.2.2.

In order to estimate the  $p_T$ -density of background particles, it is needed to determine areas of reconstructed jets  $A_{\text{jet}}$ . This is calculated by FastJet using the following jet-area definition:

- type: `fastjet::active_area`
- ghost acceptance:  $|\eta_{\text{ghost}}|^{\text{max}} = 0.9$
- ghost area: 0.005

## Appendix F

# Methods to estimate $V^0$ $p_T$ spectrum in the Underlying Event

In the following several different estimation methods for the  $V^0$  contribution from the Underlying Event to the  $V^0$  yield in the jet cone are presented. They have been studied to access the UE contribution in different ways, acting on different event samples and different regions inside the event. Since it was seen that the methods agree with each other at low  $V^0$   $p_T$  (where most of the statistics is available) the method with the largest statistics, the “no-jet” events, was chosen. That is essential in order to avoid large statistical uncertainty of the final results.

Table F.1 gives an overview about the features of the different UE estimation methods. In addition to the no-jet events, the  $V^0$ s inside two perpendicular cones are sampled. These cones are placed (w.r.t. the selected jet) in  $\phi_{PC} = \phi_{jet} \pm \pi/2$  and at the same  $\eta_{PC} = \eta_{jet}$ . The resulting  $V^0$   $p_T$  spectrum is the average of both perpendicular cones.

The third method are random cones (RC) that are placed into events, in which at minimum one jet has been selected. They are placed into each selected event with a randomly chosen  $\phi_{RC} \in [0, 2\pi]$  and  $|\eta_{RC}| < |\eta_{jet}|^{\max}$  value. It is checked that the RC do not overlap with any selected-jet cone in the same event and if yes, the random cone is discarded and a new RC is placed, checked and analysed or once more discarded (if needed up to 10 random cones are tried, before the last RC is finally accepted or discarded).

The fourth method are the outside cones (OC) which are  $V^0$  particles in the area that remains after excluding a cone with  $r^{OC} = 2R$  around each selected jet (see also sketch in figure F.1).

The last method, called median cluster cone (MCC), uses the  $k_t$  cluster algorithm to select a median cluster in the event and sample the  $V^0$  particles inside a cone around the axis of this median cluster. Therefore the  $k_t$  cluster finder is carried out in every event, in which selected jets are found. It starts to cluster up the low momentum particles, sorts them in a list in dependence of their  $p_T^{\text{jet}}/A_{\text{jet}}$  and excludes afterwards the first two leading clusters (to exclude possible true jets from this median cluster method). In the remaining list the median cluster is taken and with the usual geometrical condition to collect the particles inside the cone, the MCC  $p_T$  spectrum is measured. In case it does not fall into the  $V^0$  acceptance  $|\eta_{MCC}| < |\eta_{jet}|^{\max}$ , the MCC is discarded for the event.

Subtraction method	Principle of operation	Active area per event
'No-jet' events (NJ)	Events with no selected jet, serves as the default estimation method.	Full $V^0$ particle acceptance $A_{\text{NJ}} =  \eta_{V0}  \times  \phi_{V0} $
Perpendicular cone (PC)	$\eta_{\text{PC}} = \eta_{\text{jet}}; \phi_{\text{PC}} = \phi_{\text{jet}} \pm \pi/2; p_{\text{T}}^{\text{PC}} = p_{\text{T}}^{\text{jet}}$	$A_{\text{PC}} = \pi \dot{R}^2$
Outside cones (OC)	Outside $2\dot{R}$ of selected jets	$A_{\text{OC}} =  \eta_{V0}  \times  \phi_{V0}  - \sum_{n_{\text{jets}}} A_{\text{jets}}$
Random cones (RC)	Cone with randomly selected $ \eta_{\text{RC}}  <  \eta_{\text{jet}} ^{\text{max}}$ and $\phi_{\text{RC}} \in [0, 2\pi]$ ; no overlap with selected jets	$A_{\text{RC}} = \pi \dot{R}^2$
Median cluster cones (MCC)	Cone around median cluster aXeis (using $k_t$ algorithm, list of $k_t$ jets sorted by $p_{\text{T}}^{\text{jet}}/A_{\text{jet}}$ ); $ \eta_{\text{MCC}}  <  \eta_{\text{jet}} ^{\text{max}}$	$A_{\text{MCC}} = \pi \dot{R}^2$

Table F.1: The 5 different methods to estimate the  $V^0$  contribution to the jet cone from the UE.

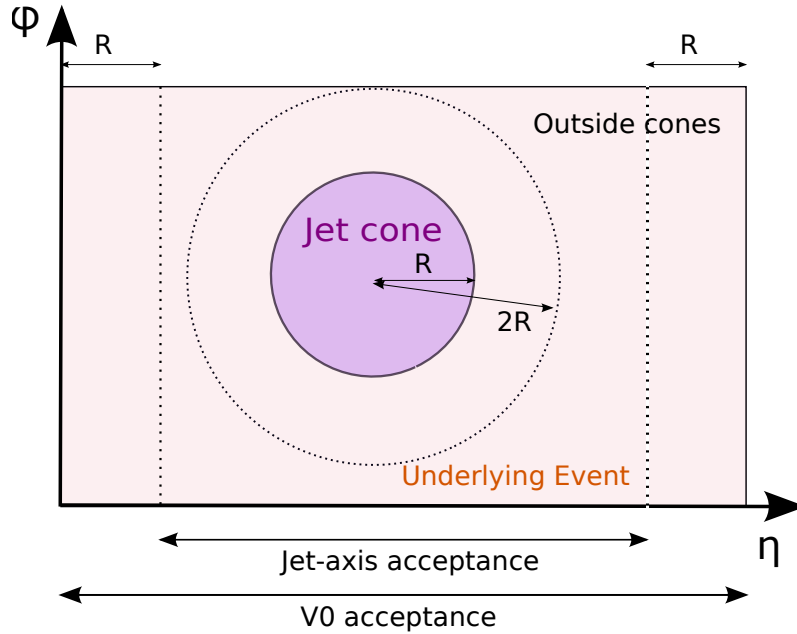


Figure F.1: The principle of the UE  $V^0$  estimation of outside cones ('OC') drawn as a sketch. A cone of  $2R$  is placed around selected jets and all  $V^0$  particles outside these cones and inside the  $V^0$  acceptance are collected. For the normalisation of this OC spectrum the areas of the excluded  $2R$ -cones are subtracted from the area of the entire event acceptance. Shown are exaggerated and not true proportions of the geometrical measures.

The normalization factors for the jet cone (JC) measurement and those in the Underlying Event (UE) are calculated as follows.

$$A_{\text{active}}^{\text{JC,norm.}} = N_{\text{jets}}(p_{\text{T}}^{\text{jet}}) \cdot \pi R^2$$

is the number of jets times the jet area.

$$A_{\text{active}}^{\text{NJ,norm.}} = N^{\text{“no-jet” events}} \cdot \pi(\eta_{\text{max}})^2$$

is the normalization factor for the “no-jet” events and

$$A_{\text{active}}^{\text{OC,norm.}} = N_{\text{jets}} \cdot (\pi(\eta_{\text{max}})^2 - (A_{\text{jet,miss.}}))$$

for the outside-cones.

$A_{\text{jet,miss.}}$  is the area of jets which exceeds the  $\eta_{V^0}$  acceptance and also needs to be subtracted from the full event acceptance, to obtain the real area that is used for the OC  $V^0$  particle sampling.

$$A_{\text{active}}^{\text{RC,norm.}} = N_{\text{RC}}(p_{\text{T}}^{\text{jet}}) \cdot \pi R^2$$

is the number of RC events times the jet cone area, (since random cones are chosen to have the same size as the jet cones).

$$A_{\text{active}}^{\text{MCC,norm.}} = N_{\text{MCC}}(p_{\text{T}}^{\text{jet}}) \cdot \pi R^2$$

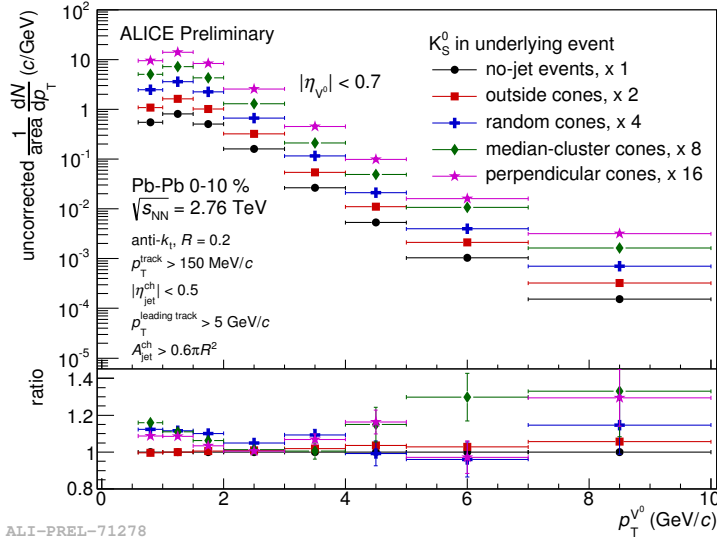
is the number of MCC events multiplied with the jet cone area, (since also the MCC are chosen to have the same size like the jet cones).

$$A_{\text{active}}^{\text{PC,norm.}} = N_{\text{jets}}(p_{\text{T}}^{\text{jet}}) \cdot \pi R^2$$

is the number of PC (selected jet) events times the jet cone area, (The perpendicular cone is placed at  $\eta_{\text{jet}}$  and is rotated in the azimuthal direction w.r.t the selected jet by  $\Delta\phi = \pm\pi/2$ ).

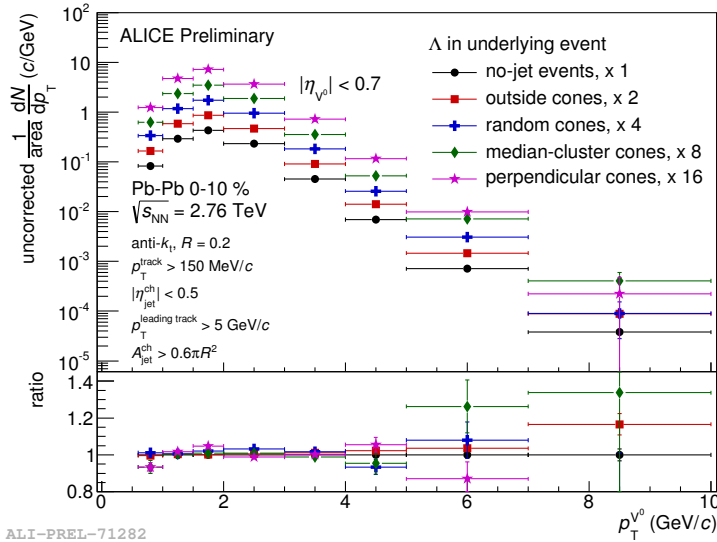
Figure F.2 and F.3 show the uncorrected  $V^0$   $p_{\text{T}}$  spectra in the UE and for the 5 different methods. In the lower panels, the ratio of the spectra obtained with each method and divided by the default spectrum (‘no-jet’ events). After the efficiency correction is applied, the different spectra agree around intermediate  $p_{\text{T}}$  (in the relevant range for measuring the characteristic baryon enhancement which is around 2-4 GeV/c) within 5 %, however for higher  $p_{\text{T}}$  values the statistical uncertainties are larger and one cannot check accurately how well they agree.

One has to keep in mind, that all these different methods don’t correct for the impact of the UE fluctuations on the UE  $V^0$   $p_{\text{T}}$  spectrum. To correct for this PYTHIA jets have been embedded into Pb–Pb data events and a correction factor was applied as described in section .



ALI-PREL-71278

Figure F.2: Uncorrected  $K_S^0$   $p_T$  spectra in the Underlying Event and for 5 different estimation methods. The lower plot shows the ratio for each method relative to the default method ('no-jet') events.



ALI-PREL-71282

Figure F.3: Uncorrected  $\Lambda$   $p_T$  spectra in the Underlying Event and for 5 different estimation methods. The lower plot shows the ratio for each method relative to the default method ('no-jet') events.

## Appendix G

# Scaling of reference measurement in p–Pb collisions

For the comparisons shown in Fig. 4.9 the measured spectra in p–Pb data had to be scaled in order to account for the differences between the analyses and the different collision systems. This scaling reference is based on the measured  $V^0$   $p_T$  spectra in jets in p–Pb collisions [123] and a scaling procedure [172] that uses a Monte Carlo simulation of pp events.

These differences among both analysis (using Pb–Pb and p–Pb events) are

- the impact of the Underlying Event fluctuations on the measured  $V^0$  spectra in jets in Pb–Pb events
- the fact that each jet in a Pb–Pb event is required to have at least one track with  $p_T^{\text{lead., const}} > 5$  GeV/c but no such selection is done in the p–Pb events (due to the much smaller UE)
- the impact of the different collisional energy ( $\sqrt{s_{\text{NN}}} = 2.76$  TeV for Pb–Pb and  $\sqrt{s_{\text{NN}}} = 5.02$  TeV for p–Pb data) on the shape of the jet spectrum.

The scaling correction is derived from a PYTHIA Monte Carlo (MC) simulation of pp events. Two sets of MC events are simulated by using the true particle observables (i.e. no detector effects are considered in this simulation, like it is done usually e.g. for the reconstruction efficiency estimation). The first set of events reflects the conditions in the p–Pb analysis: It simulates events at  $\sqrt{s_{\text{NN}}} = 5.02$  TeV, for the jet finding no leading track requirement is used. The second set of events simulates the conditions in the Pb–Pb analysis: pp events, that are containing the true particle information, are simulated at  $\sqrt{s_{\text{NN}}} = 2.76$  TeV. On both MC sets the jet finding algorithm is applied and the jets that are found in the sample which is representing the 'Pb–Pb-conditions' are 'smeared' in order to take into account the impact of the UE fluctuations on the reconstructed  $p_T^{\text{jet}}$ . The  $p_T^{\text{jet}}$ - 'smearing' is done according to the  $\sigma$  value of the (true)  $\delta p_T$  distribution for jets (selected using the same criteria) that was estimated to be  $\sigma(\delta p_T) \sim 5.10$  GeV/c as reported in [84].

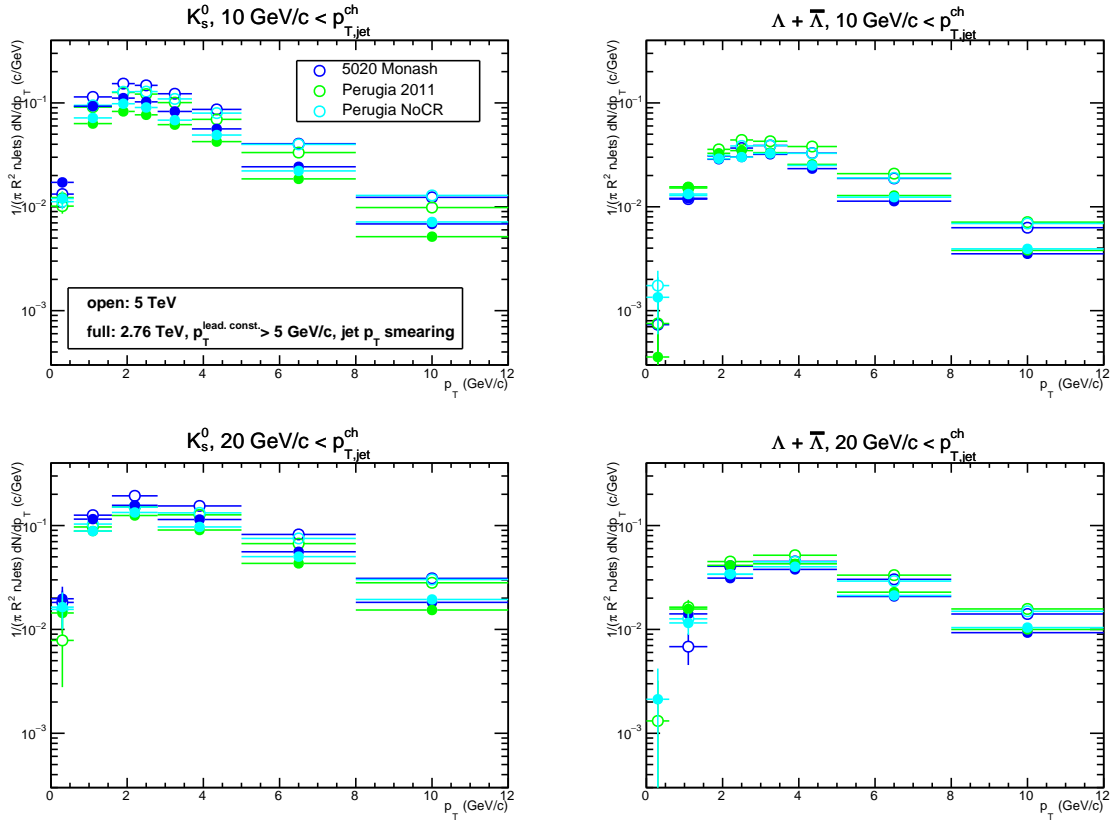


Figure G.1: Comparison of the different  $V^0$   $p_T$  spectra from PYTHIA jets of different tunes. Open markers represent spectra for  $\sqrt{s_{NN}} = 5.02$  TeV. Closed markers represent spectra for  $\sqrt{s_{NN}} = 2.76$  TeV that are including the  $p_T^{\text{jet}}$  ‘smearing’ and the leading track requirement. Figure adapted from [172].

Then the  $p_T$  spectra of the identified  $V^0$  particles inside the jet cones ( $R = 0.2$ ) and for the different PYTHIA tunes are obtained as presented in Fig. G.1. Open markers represent the spectra for a PYTHIA simulation (of different PYTHIA tunes) at  $\sqrt{s_{NN}} = 5.02$  TeV. The closed markers represent the spectra for the PYTHIA simulation at  $\sqrt{s_{NN}} = 2.76$  TeV that are including the  $p_T^{\text{jet}}$  ‘smearing’ and the leading track requirement. By calculating the ratio of these two kind of spectra one obtains the scaling weights separately for each  $p_T$ -interval. The scaling weights are multiplied by the corresponding measured  $V^0$   $p_T$  spectrum from the p–Pb collisions.

Figure G.2 shows a comparison of the measured  $V^0$   $p_T$  spectra in p–Pb collisions (red markers) to the scaled reference spectra (shown as open markers). The different colours represent the scaled reference obtained by using the Monte Carlo event generators PYTHIA8 tune “Monash” (blue markers), PYTHIA6 tune “Perugia 2011” and tune “Perugia NoCR” (no colour reconnection). From the difference of the original measured spectra to the different scaled reference spectra one can see that the change in collision energy, the impact of the background fluctuations on the  $p_T^{\text{jet}}$  and the leading track requirement (for the jet selection) shifts the spectrum downwards in yield and also makes the spectra softer (i.e. falling steeper with increasing  $V^0$   $p_T$ ). Among the scaled references obtained

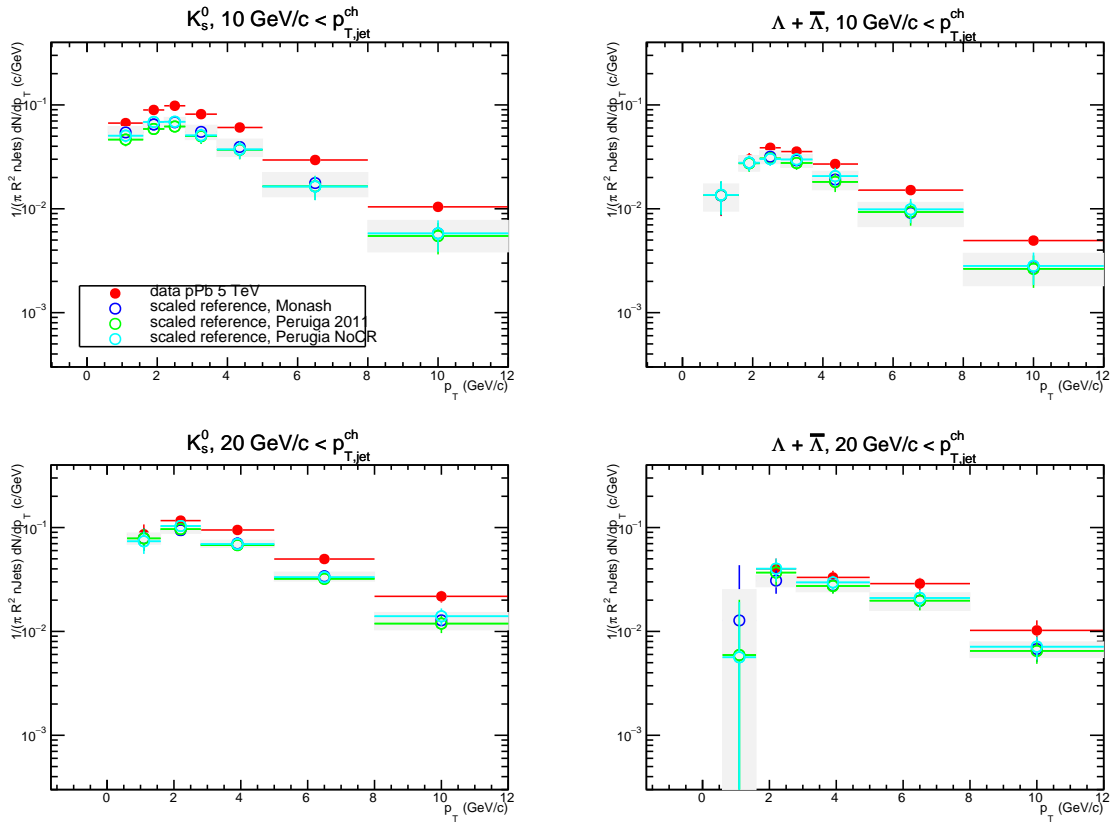


Figure G.2: Comparison of the measured  $V^0$   $p_T$  spectra in p–Pb collisions (red markers) to the scaled reference spectra (open markers, different colours for the PYTHIA tunes). Figure adapted from [172].

by using different PYTHIA tunes almost no deviation in the resulting reference is visible. This indicates the stability of the used scaling method.



## Appendix H

# Preliminary version of the $(\Lambda + \bar{\Lambda})/2K_S^0$ ratio

From the  $(\Lambda + \bar{\Lambda})/2K_S^0$  ratio a ALICE preliminary version (as shown on right panel in Fig. H.2) was accepted for public presentation in May 2015. The preliminary result did not include the correction for the impact of the Underlying Event (UE) on the  $V^0$   $p_T$  spectra inside the jet. However for the preliminary version it could be shown from a Monte Carlo study (that embedded PYTHIA jets into real events and studied the change of the reconstructed particle ratio inside the jet cone), that any impact of the UE would act in the same way on the  $K_S^0$  and the  $\Lambda + \bar{\Lambda}$   $p_T$  spectra. The PYTHIA Embedding study is described in detail in section 3.5. The result of this comparison is shown in Fig. H.1. The embedded PYTHIA jet reference is shown in red markers while the reconstructed PYTHIA signal in the jet cones from the *hybrid* events<sup>38</sup> is given by the green markers. Therefore no sizable impact on the particle ratio could be expected. The particle ratio as obtained from the fully corrected  $p_T$  spectra and presented in this thesis is shown on the left panel.

As can be seen from both particle ratios (on the left and right panel) and within uncertainties no sizable difference was caused on the particle ratio by the correction (more details on this correction procedure is described in section ) for the UE fluctuations. One has to note that the systematic uncertainty for the feed-down subtraction is included into the total uncertainty of the new derived plot (on the left panel) while it is drawn as an extra (shaded band) uncertainty for the Preliminary result.

---

<sup>38</sup>The hybrid events are obtained by combining the data event and PYTHIA event tracks into one combined event. Afterwards the analysis is performed as for usual real data. The UE contribution to the jet cone is subtracted using  $V^0$ s from 'no-jet' events.

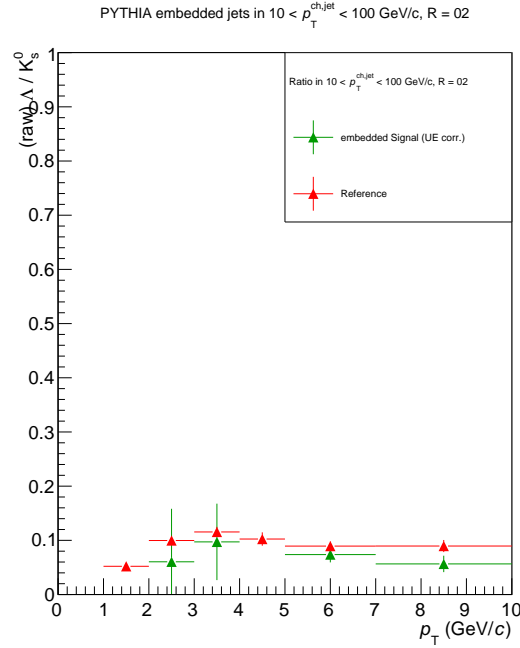


Figure H.1:  $\Lambda/K_S^0$  ratio in jet cones from *hybrid events* (green markers) for  $p_T^{\text{jet}} > 10$  GeV/c and a jet resolution parameter  $R = 0.2$ , and compared to the reference from the ratio in PYTHIA jets (red markers) that are used for the embedding into data.

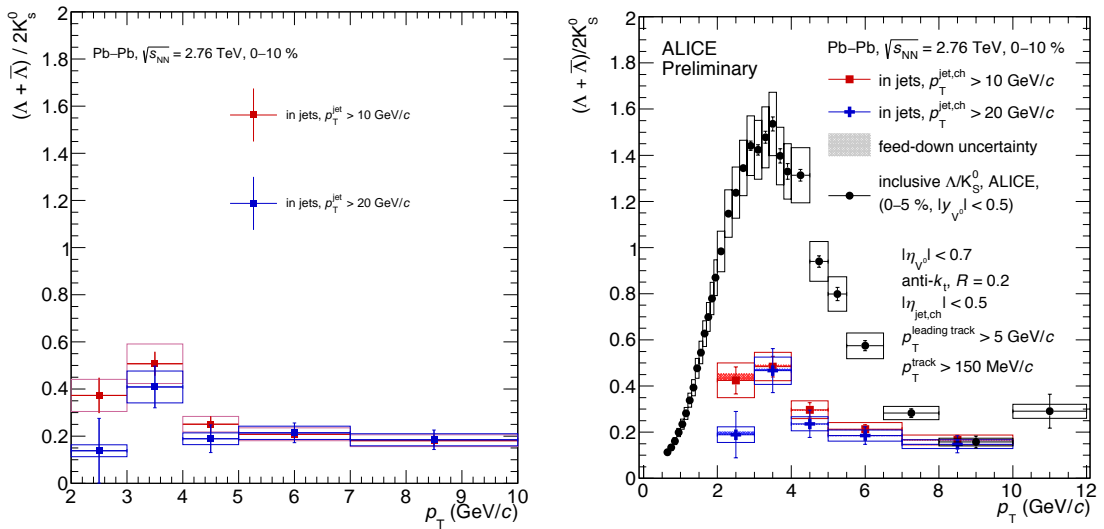


Figure H.2: Left side:  $(\Lambda + \bar{\Lambda})/2K_S^0$  ratio as derived from the fully corrected  $V^0$   $p_T$  spectra as presented in this thesis. Right side: ALICE Physics preliminary version from May 2015, not including the correction for the impact of the Underlying Event fluctuations (via Embedding of PYTHIA jets into data events).

# Acknowledgements

I would like to thank my supervisor Prof. Dr. Johanna Stachel for giving me the opportunity to realise my doctoral thesis in her group in Heidelberg and the opportunity of staying at CERN. I appreciate her permanent support and advice during the past years.

Many thanks are dedicated to my supervisor Dr. Oliver Busch who always supported me with his valuable advice. Without our frequent discussions, Oliver's numerous ideas, constructive hints and support, during working days and weekends, this analysis would not have been possible.

I would like to thank my colleagues from the ALICE collaboration that were supporting me with their scientific expertise and their experience, especially Dr. Marco van Leuwen, Dr. Jana Bielcikova, Dr. Mateusz Ploskon, Dr. Leticia Cunqueiro, Dr. Iouri Belikov, Dr. Antonin Maire, Dr. Marian Ivanov, Alexander Bertens, Dr. Jochen Klein, Dr. Jeremy Wilkinson and many others.

I would like to thank especially Vít Kučera, Dr. Xiaoming Zhang and Yonghong Zhang for their excellent collaboration on the field of our jet analyses.

Furthermore I warmly thank all the members of the ALICE collaboration group in Heidelberg, especially Dr. Xianguo Lu, for many productive discussions, and the crew at Point 2, where we spent many days and nights on the shifts to experience this great experiment in action. Many thanks go to Dr. Bastian Bathen who introduced me into the TRD OnCall operations and to Dr. Jorge Mercado which was supporting me during my service task at Point 2.

Many thanks go to the proof-readers of my thesis: Dr. Oliver Busch, Dr. Michael Knichel, Dr. Klaus Reygers, Dr. Marco Leoncino, Kambiz Veshgini, Dr. Hans Beck, Dr. Yvonne Pachmayer and Dr. Jörn Putschke.

I would like to thank the Heidelberg Graduate School of Fundamental Physics (HGSFP) and the Helmholtz Graduate School (HGS-HIRE) for their student support that enabled my attendance of various conferences and workshops abroad.

I owe many thanks to my parents and my sister Iris, which awoke my interest for natural science. For their permanent support and understanding. I would like to thank Marco for his encouragement, support, advice and understanding during the past months.

Special thanks also go to my friends, Anne, Dominik, Kambiz and Dmitry, for their friendship and mental coaching.

# Erratum

zur Dissertation "Production of strange hadrons in charged jets in Pb-Pb collisions measured with ALICE at the LHC" vorgelegt von Alice Zimmermann, Oktober 2016.

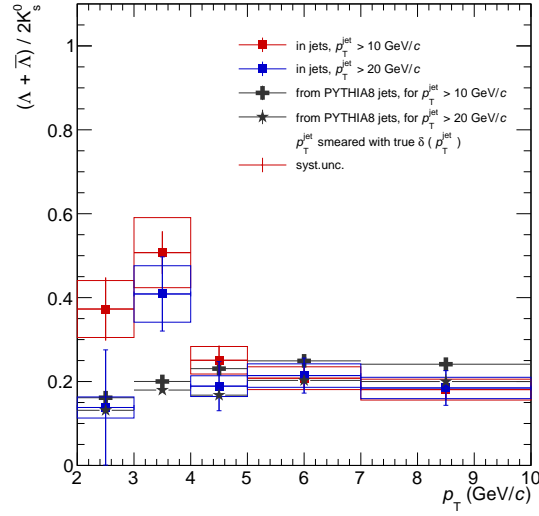


Figure 4.2: Upper panel:  $(\Lambda + \bar{\Lambda})/2K_S^0$  ratio in jets ( $R = 0.2$ ) for  $p_T^{\text{jet}} > 10$  GeV/c and  $p_T^{\text{jet}} > 20$  GeV/c. Furthermore the  $(\Lambda + \bar{\Lambda})/2K_S^0$  ratio obtained from PYTHIA jets ( $R = 0.2$ ) is shown.

## 1 Erratum to chapter 4: Results and discussion

Figure 4.2 shows the comparison of the measured  $(\Lambda + \bar{\Lambda})/2K_S^0$  ratio in jets ( $R = 0.2$ ) (for both jet  $p_T$  intervals) to a PYTHIA simulation of the ratio in jets. The PYTHIA simulated reference shown in the thesis includes an error in the way the  $\Lambda$  and  $\bar{\Lambda}$   $p_T$  spectra from the reference have been added and therefore the ratio is missing a factor of 0.5. This corrected version replaces Fig. 4.2 (upper panel) that is shown on page 146 in the thesis.

Figure 4.8 shows the comparison of the measured  $(\Lambda + \bar{\Lambda})/2 p_T$  spectrum and the  $K_S^0 p_T$  spectrum in jets in Pb–Pb collisions to the prediction of PYTHIA jets (using different PYTHIA versions and tunes). The  $\Lambda$  and  $\bar{\Lambda}$  baryons from the PYTHIA simulation as shown in the thesis are missing the same factor of 0.5 as mentioned already for the previous Fig. 4.2. Therefore Fig. 4.8 as shown on page 155 has to be replaced by these plots in which the reference is corrected for the missing factor. The  $K_S^0$  containing  $p_T$  spectra from the PYTHIA simulations are not affected.

Figure 4.9 shows the comparison of the measured  $(\Lambda + \bar{\Lambda})/2$  and the  $K_S^0 p_T$  spectrum to a scaled reference measurement from p–Pb collisions. Also here the factor of 0.5 for the  $(\Lambda + \bar{\Lambda})/2 p_T$  spectra of the reference is corrected and replaces Fig. 4.9 (shown on page 156) in the thesis.

## 2 Erratum to chapter 5: Conclusions

The conclusion from the comparison of the measured  $(\Lambda + \bar{\Lambda})/2 p_T$  spectra to the prediction from PYTHIA simulated jets as shown in Fig. 4.8 (page 158, fourth paragraph) has to be changed from "At high- $p_T$  the measured  $\Lambda$  yields are significantly lower compared to the PYTHIA simulations" to "At high- $p_T$  the measured  $(\Lambda + \bar{\Lambda})/2$  yields are in agreement with the PYTHIA simulations". Furthermore the conclusion from the comparison shown in Fig. 4.9 has to be changed

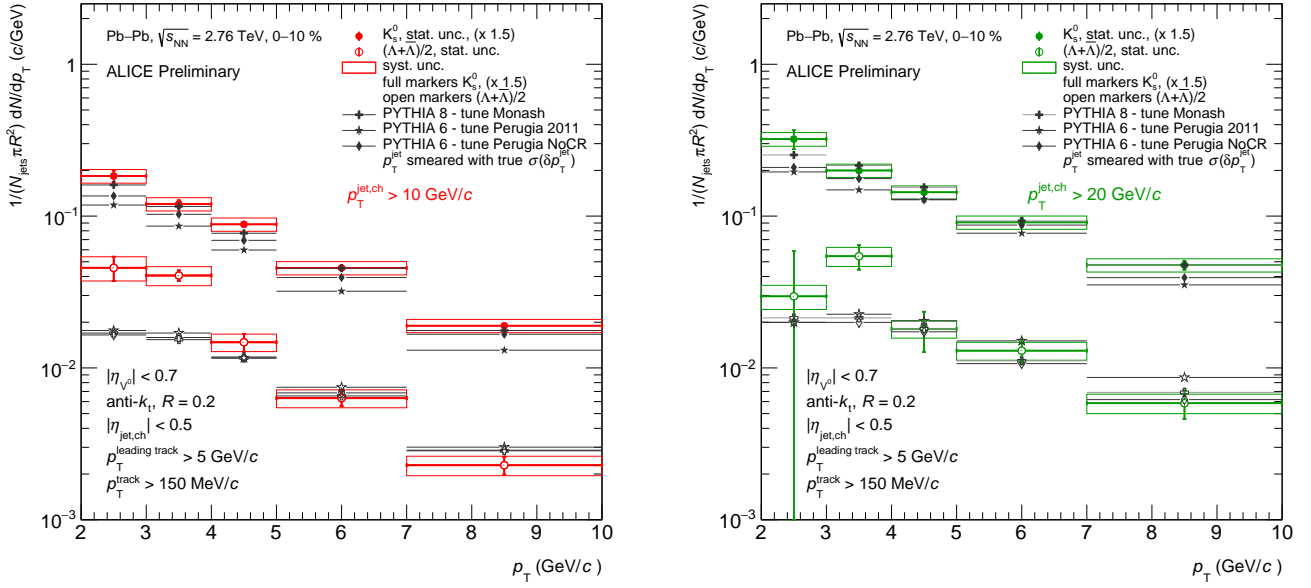


Figure 4.8: Comparison of the  $V^0$   $p_T$  spectra in jets in Pb–Pb collisions to the prediction of PYTHIA jets (simulating pp events at  $\sqrt{s} = 2.76$  TeV) is made. The left panel shows the  $K_S^0$  and  $\Lambda$   $p_T$  spectrum in jets with  $p_T^{\text{jet}} > 10$  GeV/c. The right panel shows the spectra for jets with  $p_T^{\text{jet}} > 20$  GeV/c. The results from PYTHIA jets (for three different tunes) are smeared in  $p_T^{\text{jet}}$  according to the particle level  $\sigma(\delta p_T^{\text{ch}})$  values [84]. The four panels below show the ratios for data divided by MC simulation (different PYTHIA tunes in different marker colours), for  $K_S^0$  and  $(\Lambda + \bar{\Lambda})$  separately. The ratios (data/MC) are shown separately for the two  $p_T^{\text{jet}}$  intervals and below the corresponding measurement. The PYTHIA simulations are adapted from [172].

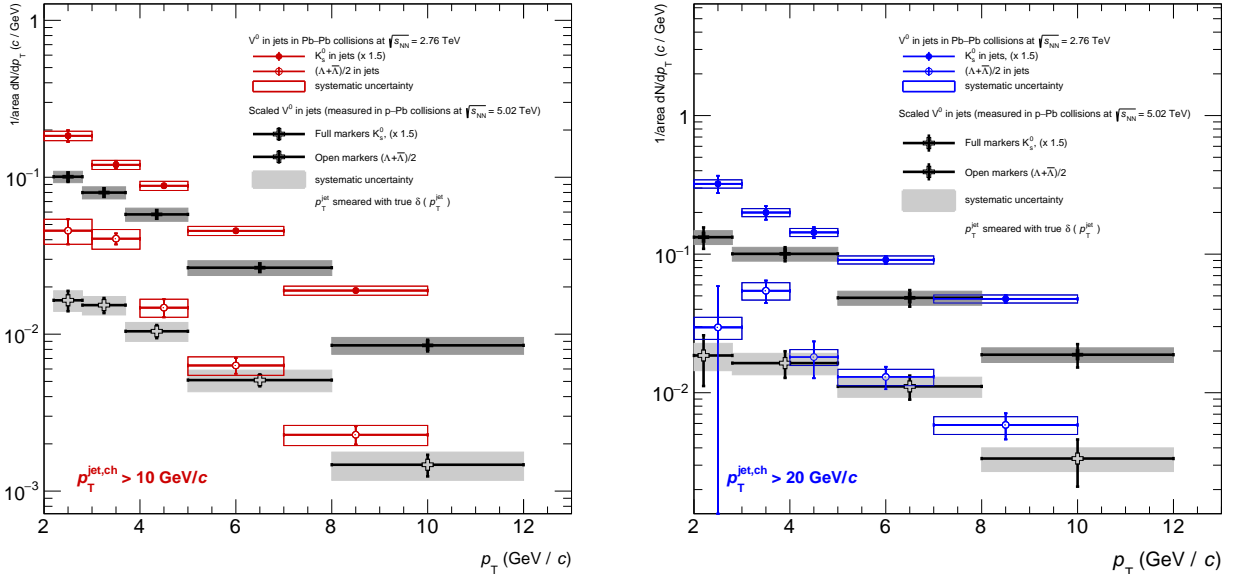


Figure 4.9: Comparison of the  $K_S^0$  and  $(\Lambda + \bar{\Lambda})$   $p_T$  spectra from this analysis to the spectra measured in p–Pb events at  $\sqrt{s_{NN}} = 5.02$  TeV. The left panel shows the spectra in jets for  $p_T^{\text{jet}} > 10$  GeV/c. On the right panel the spectra are shown for jets with  $p_T^{\text{jet}} > 20$  GeV/c. The results from the p–Pb data are scaled according to a PYTHIA8 simulation to take into account the effect of the UE fluctuations on  $p_T^{\text{jet}}$  that are present in Pb–Pb events, the leading constituent cut  $p_T^{\text{leading track}} > 5$  GeV/c and the different collision energy. Used are three different tunes of PYTHIA8 (tune "Monash", "Perugia 2011" and "NoCR"). The systematic uncertainties of the PYTHIA tunes are superimposed, they are lightgrey for the  $\Lambda$  baryons and darkgrey for the  $K_S^0$  mesons. Scaled reference is adapted from [172] and based on the measurement from [123].

from "The  $\Lambda$  yields at low hadron  $p_T$  indicate an enhancement while for higher hadron  $p_T$  they seem to be slightly lower" to "The  $(\Lambda+\bar{\Lambda})/2$  yields at low hadron  $p_T$  indicate an enhancement while for higher hadron  $p_T$  they seem to be slightly higher". The results and conclusions from the measured  $V^0$   $p_T$  spectra in jets in Pb–Pb collisions as obtained from the analysis in this thesis are not affected by this erratum.